

STATE OF CALIFORNIA DEPARTMENT OF TRANSPORTATION  
**TECHNICAL REPORT DOCUMENTATION PAGE**  
 TR0003 (REV. 10/98)

1. REPORT NUMBER <b>CA12-2242</b>	2. GOVERNMENT ASSOCIATION NUMBER	3. RECIPIENT'S CATALOG NUMBER
4. TITLE AND SUBTITLE <b>EFFECT OF VERTICAL GROUND MOTIONS ON SHEAR DEMAND AND CAPACITY IN BRIDGE COLUMNS</b>		5. REPORT DATE March 2012
7. AUTHOR(S) Hyerin Lee, Pardeep Kumar, Selim Gunay, Khalid Mosalam, Sashi Kunnath		6. PERFORMING ORGANIZATION CODE
9. PERFORMING ORGANIZATION NAME AND ADDRESS Department of Civil & Environmental Engineering University of California at Davis, One Shields Ave, CA 95616 University of California at Berkeley, 760 Davis Hall, CA 74720		8. PERFORMING ORGANIZATION REPORT NO. UCD-UCB-SESM-12-01
12. SPONSORING AGENCY AND ADDRESS California Department of Transportation Division of Research and Innovation, MS-83 1227 O Street Sacramento CA 95814		10. WORK UNIT NUMBER
		11. CONTRACT OR GRANT NUMBER 59A0688
		13. TYPE OF REPORT AND PERIOD COVERED Final Technical Report (2008-2011)
		14. SPONSORING AGENCY CODE

15. SUPPLEMENTAL NOTES

16. ABSTRACT  
 The objective of this project was to examine the effects of axial force variation in bridge columns due to strong vertical ground motions and the influence of these axial force fluctuations on shear strength degradation.

Two quarter scale specimens (SP1 and SP2) with different transverse reinforcement ratios were constructed and tested on the UC-Berkeley shaking table at the Richmond Field Station. As a result of an extensive numerical investigation and preliminary fidelity tests, the 1994 Northridge earthquake acceleration recorded at the Pacoima Dam was selected as an input motion for the shaking table study. The chosen ground motion was applied to the test specimens at various intensity levels ranging from 5% to 125% of the actual recorded motion.

As part of the computational modeling, a new shear spring model which incorporates shear strength estimations based on ACI and Caltrans SDC equations is developed and implemented in the computational platform, OpenSees [28]. The models are reasonably successful in capturing the shear-force and displacement histories measured during the tests.

The study indicates that strong vertical excitations can induce axial tension in the column which causes marginal degradation of the shear strength (mainly due to the degradation of the concrete contribution to shear strength). The degradation did not adversely affect the performance of the column. Since the vertical frequency of bridge columns is much higher than the transverse or longitudinal frequency, the imposed axial tension is sustained for very short durations.

The present study of a single column bent suggests that ignoring the concrete contribution to shear capacity when the column is in tension is conservative. Given the fact that the shear capacity expression in SDC is specified to deal with cases of sustained axial tension, attention should be paid to the use of SDC expression in cases where axial tension occurs only due to vertical excitation.

17. KEY WORDS Bridge column; experimental study; shaking table test; shear demand; shear capacity; vertical ground motion	18. DISTRIBUTION STATEMENT No restrictions. This document is available to the public through the National Technical Information Service, Springfield, VA 22161	
19. SECURITY CLASSIFICATION (of this report) <b>Unclassified</b>	20. NUMBER OF PAGES <b>180</b>	21. PRICE

---

# EFFECT OF VERTICAL GROUND MOTIONS ON SHEAR DEMAND AND CAPACITY IN BRIDGE COLUMNS

A Technical Report Submitted to the California Department of Transportation  
under Contract 59A0688

Hyerin Lee<sup>+</sup>  
Pardeep Kumar<sup>+</sup>  
Selim Gunay<sup>+</sup>  
Khalid Mosalam<sup>+</sup>  
Sashi K. Kunnath\*

March 2012



Department of Civil and Environmental Engineering

<sup>+</sup>University of California at Berkeley

\*University of California at Davis





## **Disclaimer**

This document is disseminated in the interest of information exchange. The contents of this report reflect the views of the authors who are responsible for the facts and accuracy of the data presented herein. The contents do not necessarily reflect the official views or policies of the State of California or the Federal Highway Administration. This publication does not constitute a standard, specification or regulation. This report does not constitute an endorsement by the Department of any product described herein.

For individuals with sensory disabilities, this document is available in Braille, large print, audiocassette, or compact disk. To obtain a copy of this document in one of these alternate formats, please contact: the Division of Research and Innovation, MS-83, California Department of Transportation, P.O. Box 942873, Sacramento, CA 94273-0001.



## **Acknowledgements**

Funding for this study provided by the California Department of Transportation (Caltrans) under Contract No.59A0688 is gratefully acknowledged. Input and comments from Li-Hong Sheng, Mark Yashinsky, Mark Mahan and Fadel Alameddine are sincerely appreciated. The Pacific Earthquake Engineering Research (PEER) Center staff assistance, especially those of Mr. Wesley Neighbour, Mr. Nathaniel Knight, and Mr. David Maclam, was essential for the experimental study. Perse Construction Company has greatly donated and helped with the design and fabrication of the repair of the test specimens and application of Carbon and Glass FRP repairs. Special thanks are due to the lead installer Mr. Seyed a. Abbasi and his team.



# Table of Contents

1	Introduction .....	1
1.1	Motivation .....	1
1.2	Objectives and Scope of the Research .....	2
1.3	Previous Studies on Vertical Ground Motions and its Effect on Bridge Columns .....	3
1.3.1	Ground Motion Characteristics .....	3
1.3.2	Experimental and Numerical Studies .....	4
1.4	Overview of Shear Strength Assessment .....	6
1.4.1	ACI 318-08 .....	6
1.4.2	A Note about Size Effect .....	7
1.4.3	AASHTO (2010) .....	8
1.4.4	Canadian Code (2004) .....	10
1.4.5	Eurocode (2004) .....	12
1.4.6	Priestley et al. (1996) .....	13
1.4.7	Caltrans SDC (2010) .....	14
2	Selection of Ground Motions and Model Bridge Configuration .....	16
2.1	Selection of Ground Motion .....	16
2.2	Prototype Model for Parametric Study .....	17
2.2.1	Amador Creek Bridge .....	17
2.2.2	Interlocking Spiral Section and Effective Circular Section .....	20
2.2.3	Comparison of Responses of the Bridge Systems with the Interlocking and the Effective Circular Cross-Sections .....	21
2.3	Parametric Study .....	23
2.3.1	Ground Motion Components .....	23
2.3.2	Mass Moment of Inertia .....	23
2.3.3	Aspect Ratio .....	23
2.3.4	Computational Models .....	23
2.3.5	Comparison of Responses of Bridge System vs. Single Column Models .....	26
2.4	Results of the Parametric Study .....	28
2.5	Investigation of the Effect of Axial Force on Shear Capacity .....	28
2.5.1	Comparison of Shear Demand and Capacity .....	28
2.5.2	Observations .....	35
2.6	Summary .....	35
3	Design of Shaking Table Tests .....	37
3.1	Introduction .....	37
3.2	Description of the Shaking Table .....	37
3.3	Selection of Input Motion: Fidelity Tests .....	37
3.3.1	Fidelity Test Setup .....	38
3.3.2	Input Ground Motion Candidates and Scale Factors .....	40
3.3.3	Fidelity Test Results .....	41
3.3.4	Further Discussion about GM7 .....	48
3.4	Specimen Design .....	48
3.4.1	Cross-Section Properties .....	50
3.4.2	Mass and Mass Moment of Inertia .....	50

3.4.3	Material Properties.....	52
3.5	Experimental Setup and Test Program.....	56
3.5.1	Dimensional Analysis.....	56
3.5.2	Column.....	56
3.5.3	Base Plate, Footing, and Top Steel Beams.....	57
3.5.4	Mass Blocks.....	59
3.5.5	Instrumentation.....	60
3.5.6	Internal Instrumentation.....	60
3.5.7	External Instrumentation.....	61
3.5.8	Test Sequence.....	62
3.6	Summary.....	62
4	Results of Shaking Table Tests: Global Responses.....	64
4.1	Introduction.....	64
4.2	Stiffness, Natural Frequency, and Viscous Damping.....	66
4.2.1	Pullback Tests.....	66
4.2.2	Free Vibration Tests.....	67
4.2.3	Estimation of the Vertical Period.....	68
4.3	Table Accelerations.....	71
4.3.1	Rotation of the Mass Blocks.....	74
4.4	Forces.....	75
4.4.1	Shear and Axial Forces.....	75
4.4.2	Bending Moments.....	81
4.5	Lateral Displacements.....	84
4.6	Force-Displacement Responses.....	89
4.7	Crack Propagation.....	94
4.8	Local Member Responses.....	101
4.8.1	Section Curvatures.....	102
4.8.2	Moment-Curvature Response.....	104
4.8.3	Longitudinal Strains.....	106
4.8.4	Transverse (Hoop) Strains.....	109
4.9	Summary.....	111
5	Testing of Repaired Columns.....	113
5.1	Details of Repaired Test Specimens and Repair Procedure.....	113
5.1.1	Unidirectional Glass Fiber Fabric.....	116
5.1.2	Unidirectional Carbon Fiber Fabric.....	116
5.2	Instrumentation.....	116
5.3	Loading Protocol.....	117
5.4	Experimental Results.....	118
5.4.1	Test Specimen SP1.....	118
5.4.2	Test Specimen SP2.....	122
6	Development and Evaluation of Computational Models.....	127
6.1	Development of OpenSees Element.....	127
6.2	Simulation Model of Bridge Column.....	129
6.2.1	Material Modeling.....	130
6.2.2	Fiber Section Modeling.....	132

6.3	Model Adjustment due to Shaking Table Effect.....	133
6.4	Other Considerations and Parameters for Numerical Simulations.....	134
6.5	Comparison of Numerical and Experimental Results.....	136
6.5.1	Shear Force Demands.....	137
6.6	Lateral Displacement Demands.....	145
6.7	Summary.....	150
7	Concluding Remarks.....	151
7.1	Summary of Findings.....	151
7.1.1	Experimental Findings.....	151
7.1.2	Findings from Numerical Simulations.....	152
7.2	Shear Demand versus Shear Capacity.....	152
7.3	Shear Demands in Two-Column Bents.....	156
7.4	Final Comments and Recommendations.....	158
	References.....	160



# List of Figures

Figure 1-1: Outline of research project.....	2
Figure 1-2: Parameters $b_v$ , $d_v$ and $d_e$ for a circular column (AASHTO 2010 [6]).....	10
Figure 1-3: Shear parameters, AASHTO (2010) [6].....	10
Figure 1-4: Contribution of axial forces to shear strength, Priestley et al. (1996) [38].....	14
Figure 2-1: Bent elevation and column cross-section of the Amador Creek Bridge.....	18
Figure 2-2: OpenSees model of the Amador Creek Bridge.....	20
Figure 2-3: Responses of the Amador Creek Bridge at column H2 with interlocking spiral and effective circular cross-sections.....	22
Figure 2-4: Models for the parametric study.....	24
Figure 2-5: Line representations of the considered models.....	25
Figure 2-6: Responses of the bridge system and the single column models.....	27
Figure 2-7: Shear demand and capacity with ground motion #9.....	31
Figure 2-8: Demand to capacity ratio ( $Maxdcr$ ) and reduction in shear strength ( $Red$ ) considering ACI equation for Type 2 and the selected 61 ground motions.....	32
Figure 2-9: Demand to capacity ratio ( $Maxdcr$ ) and reduction in shear strength ( $Red$ ) considering SDC equation for Type 2 and the selected 61 ground motions.....	33
Figure 2-10: Demand to capacity ratio ( $Maxdcr$ ) and reduction in shear strength ( $Red$ ) considering ACI equation for Type 2 and the 293 ground motions with $PGA_h > 0.25g$ .....	34
Figure 3-1: Schematic of the fidelity test setup.....	39
Figure 3-2: Photograph of the fidelity test setup.....	39
Figure 3-3: Shaking table plan, axes, and instrumentation for the fidelity tests.....	40
Figure 3-4: GM1 yield level.....	43
Figure 3-5: GM1 MCE level.....	44
Figure 3-6: GM7 0.5-yield level.....	45
Figure 3-7: GM7 yield level.....	46
Figure 3-8: GM7 MCE level.....	47
Figure 3-9: Column cross-sections of the Plumas-Arboga Overhead Bridge (units: mm).....	49
Figure 3-10: Prototype and test specimen column cross-sections.....	50
Figure 3-11: Concrete strength maturity curve.....	54
Figure 3-12: Example concrete stress-strain relationship on the 72 <sup>nd</sup> day (1 <sup>st</sup> cylinder).....	54
Figure 3-13: Testing longitudinal and transverse reinforcing bars (sample results and setup).....	55
Figure 3-14: Specimen location on the shaking table and the catching safety system (a) Plan view, (b) Elevation view.....	58
Figure 3-15: Final mass configuration.....	59
Figure 3-16: Final test setup.....	60
Figure 4-1: Horizontal (X) and vertical components (Z) of 100% Northridge earthquake.....	64
Figure 4-2: Photographs of the pullback tests without (left) and with (right) total mass.....	66
Figure 4-3: Estimation of lateral stiffness.....	67
Figure 4-4: Absolute displacement measured in the free vibration tests.....	68
Figure 4-5: Dominant frequencies of vertical acceleration measurements in free vibration tests.....	69
Figure 4-6: Response spectra using the measured vertical accelerations.....	70

Figure 4-7: Shaking table acceleration history in SP1 tests.....	72
Figure 4-8: Shaking table acceleration history in SP1 tests (continued) .....	73
Figure 4-9: Comparison of measured and derived accelerations (specimen SP1, run 1-9).....	76
Figure 4-10: Axial force and shear force history .....	78
Figure 4-11: Axial force and shear force history (continued).....	79
Figure 4-12: Positive peak axial and shear forces with increasing intensity of shaking .....	80
Figure 4-13: Bending moment history at the top and base of the test specimens.....	82
Figure 4-14: Bending moment history at the top and base of the test specimens (continued) .....	83
Figure 4-15: Peak bending moments at the top and base of the test specimens .....	84
Figure 4-16: Relative lateral displacement history .....	86
Figure 4-17: Relative lateral displacement history (continued).....	87
Figure 4-18: Peak relative lateral displacement at the top of the test specimens .....	88
Figure 4-19: Shear force-lateral displacement response.....	90
Figure 4-20: Shear force-lateral displacement response (continued) .....	91
Figure 4-21: Axial force-vertical displacement response .....	92
Figure 4-22: Axial force-vertical displacement response (continued).....	93
Figure 4-23: Crack propagation of SP1 .....	95
Figure 4-24: Crack propagation of SP1 (continued).....	96
Figure 4-25: Crack propagation of SP1 (continued).....	97
Figure 4-26: Crack propagation of SP2 .....	98
Figure 4-27: Crack propagation of SP2 (continued).....	99
Figure 4-28: Crack propagation of SP2 (continued).....	100
Figure 4-29: Test photographs of the top and base of column, after 125%-scale tests (Runs 1-11, 2-11).....	101
Figure 4-30: Curvature response history at column bottom ( $h=10''$ ) and top ( $h=60''$ ) .....	103
Figure 4-31: Moment-curvature response at $h=10''$ and $h=60''$ .....	105
Figure 4-32: Peak-to-peak strain amplitudes recorded at north-south sides in the 125%-scale tests .....	107
Figure 4-33: Peak tensile strains recorded at north-south sides in the 125%-scale tests.....	107
Figure 4-34: Schematic deflected shapes of the test specimens at shear peaks.....	108
Figure 4-35: Peak-to-peak amplitudes of recorded strains on east-west sides in the 125%-scale tests .....	108
Figure 4-36: Peak tensile strains recorded on east-west sides in the 125%-scale tests .....	109
Figure 4-37: Peak-to-peak hoop strain amplitudes on the north-south sides in the 125%-scale tests .....	110
Figure 4-38: Peak tensile strains on the north-south side of specimens in the 125%-scale tests ..	110
Figure 5-1: Repair of test specimen SP1.....	114
Figure 5-2: Repair of test specimen SP2.....	115
Figure 5-3: Force-deformation response of repaired specimen SP1 (above) and comparison to as-built specimen (below) for 2 excitations: EQ3 (left) and EQ5 (right) .....	119
Figure 5-4: Force-deformation response of repaired specimen SP1 (above) and comparison to as-built specimen (below) for 2 excitations: EQ9 (left) and EQ10 (right) .....	119
Figure 5-5: Local responses of repaired SP1: (a) strain profile from strain gages on the North face, (b) displacement profiles from wire-potentiometers along the height, (c) strain profile from the curvature data obtained using vertical transducers, (d) curvature.....	120

Figure 5-6: Strain profiles of repaired SP1 based on jacket strain gages corresponding to time when maximum strain occurs along the column height: EQ5 (left) and EQ6 (right).....	121
Figure 5-7: Strain profiles of repaired SP1 based on jacket strain gages corresponding to time when maximum strain occurs along the column height: EQ9 (left) and EQ10 (right).....	122
Figure 5-8: Force-deformation response of repaired specimen SP2 (above) and comparison to as-built specimen (below) for 2 excitations: EQ3 (left) and EQ4 (right) .....	123
Figure 5-9: Force-deformation response of repaired specimen SP2 (above) and comparison to as-built specimen (below) for 2 excitations: EQ5 (left) and EQ6 (right) .....	123
Figure 5-10: Force-deformation response of repaired specimen SP2 (above) and comparison to as-built specimen (below) for 2 excitations: EQ9 (left) and EQ10 (right) .....	124
Figure 5-11: Local responses of repaired SP2: (a) strain profile from strain gages on the North face, (b) displacement profiles from wire-potentiometers along the height, (c) strain profile from the curvature data obtained using vertical transducers, (d) curvature ...	125
Figure 5-12: Strain profiles of repaired SP2 based on jacket strain gages corresponding to time when maximum strain occurs along the column height: EQ5 (left) and EQ6 (right)..	126
Figure 5-13: Strain profiles of repaired SP2 based on jacket strain gages corresponding to time when maximum strain occurs along the column height: EQ9 (left) and EQ10 (right) .....	126
Figure 6-1: “Beam With Hinges” element [28] .....	129
Figure 6-2: Specimen modeling.....	130
Figure 6-3: Concrete02 model: material parameters [34].....	131
Figure 6-4: Steel02 model: material parameters [34] .....	132
Figure 6-5: Fiber section modeling.....	133
]Figure 6-6: Axial force difference between numerical simulation and test data measured at the base of model SP1 under the 125%-scale ‘1st X+Z’ motion.....	134
Figure 6-7: 2-DOF analysis for the shaking table and test specimen responses.....	135
Figure 6-8: Comparison of the numerical simulation and test results for free-vibration test.....	136
Figure 6-9: Comparison of shear force demand and shear strength estimation using ACI and SDC based on the data from 50%, 70%, and 95%-scale runs .....	138
Figure 6-10: Comparison of shear force demand and shear strength estimation using ACI and SDC based on the data from 125%-scale runs.....	139
Figure 6-11: Comparison of simulated versus recorded shear force histories of SP1 subjected to 50%, 70%, and 95%-scale motions .....	140
Figure 6-12: Comparison of simulated versus recorded shear force histories of SP1 subjected to 125%-scale motions.....	141
Figure 6-13: Comparison of recorded versus simulated shear force histories of SP2 subjected to 50%, 70%, and 95%-scale motions .....	143
Figure 6-14: Comparison of recorded versus simulated shear force histories of specimen SP2 subjected to 125%-scale motions.....	144
Figure 6-15: Comparison of the computed to observed shear demands at the 3rd peak for both specimens using ACI and SDC models under the 125%-scale motions.....	145
Figure 6-16: Comparison of computed and observed lateral displacement histories of SP1 subjected to 50%, 70%, and 95%-scale motions .....	146
Figure 6-17: Comparison of computed and observed lateral displacement histories of SP1 subjected to 125%-scale motions.....	147

Figure 6-18: Comparison of computed and observed lateral displacement histories of SP2 subjected to 50%, 70%, and 95%-scale motions .....	148
Figure 6-19: Comparison of computed and observed lateral displacement histories of SP2 subjected to 125%-scale motions.....	149
Figure 7-1: Axial force, shear force and ductility demands on specimen SP1 during the maximum intensity horizontal + vertical motions (Left: Run 1-9; Right: 1-11) .....	153
Figure 7-2: Variation of control parameters in SDC shear capacity expression during the maximum intensity horizontal + vertical motions imposed on specimen SP1 (Left: Run 1-9; Right: 1-11) .....	153
Figure 7-3: Axial force, shear force and ductility demands on specimen SP2 during the maximum intensity horizontal + vertical motions (Left: Run 2-9; Right: 2-11) .....	154
Figure 7-4: Variation of control parameters in SDC shear capacity expression during the maximum intensity horizontal + vertical motions imposed on specimen SP2 .....	154
Figure 7-5: Shear demands in columns at instants of peak axial compression and tension: (a) Specimen SP1; (b) Specimen SP2 (Note: Solid line = contribution of shear reinforcement only).....	155
Figure 7-6: Shear demands in columns as a function of lateral displacement ductility: (a) Specimen SP1; (b) Specimen SP2 (Note: <i>Shear capacity was estimated assuming Factor2=1</i> ).....	155
Figure 7-7: Configuration of two-column bent system investigated in the final phase of study..	156
Figure 7-8: Simulation model of two-column bent.....	156
Figure 7-9: Mean spectrum of scaled ground motions .....	157
Figure 7-10: Shear demand versus capacity as a function of peak axial force and ductility demand.....	158

## List of Tables

Table 1-1: V/H Ratios for several earthquakes.....	3
Table 2-1: Properties of superstructure and springs used to model the soil-foundation system for the Amador Creek Bridge .....	19
Table 2-2: Column cross-section properties of the Amador Creek Bridge .....	21
Table 2-3: Modal properties of the Amador Creek Bridge.....	21
Table 2-4: Modal properties of single column models .....	25
Table 2-5: Vertical periods of bridge system model with effective circular cross-section .....	25
Table 2-6: Selected ground motions for the experimental study .....	36
Table 3-1: Properties of superstructure and springs used to model the soil-foundation system for the Amador Creek Bridge .....	38
Table 3-2: Properties of the finally selected four ground motions for the fidelity tests .....	41
Table 3-3: GM7 Information .....	42
Table 3-4: Cross-section properties of the Plumas-Arboga Overhead Bridge superstructure.....	49
Table 3-5: Column cross-section properties of the Plumas-Arboga Overhead Bridge .....	49
Table 3-6: Cross-section properties .....	51
Table 3-7: Mass of the ¼-scale test specimen .....	52
Table 3-8: Concrete mix specifications .....	53
Table 3-9: Strength properties of concrete.....	53
Table 3-10: Average properties of the reinforcing bars.....	56
Table 4-1: Test sequence .....	65
Table 4-2: Stiffness from pullback tests .....	66
Table 4-3: Estimation of the periods of vibration of the test specimens .....	71
Table 4-4: Comparison of axial force at the maximum positive shear force.....	80
Table 4-5: Comparison of the maximum bending moment at the base and top of the column ....	81
Table 5-1: Ground motions for shaking table testing .....	117
Table 5-2: Maximum responses during testing specimen SP1 .....	121
Table 5-3: Maximum responses during testing repaired specimen SP2.....	125
Table 6-1: Concrete model parameters for numerical simulations.....	131
Table 6-2: Steel model parameters for numerical simulations .....	132
Table 6-3: Measured damping ratio.....	136
Table 7-1: Selected ground motions for study of two-column bent .....	157



# 1 Introduction

## 1.1 Motivation

Current provisions in SDC (2006) [13] do not provide adequate guidelines on when and how to consider the adverse consequences of vertical accelerations in seismic design of ordinary bridges. While previous studies have uncovered several critical issues, additional experimental testing and analytical simulations are still needed to gain further insight into the effects of strong vertical motions on the imposed demands on bridge components. This project is particularly concerned with investigating the effects of varying axial forces induced by vertical motions on shear demand and shear capacity in bridge columns.

The expressions given in current codes and the Seismic Design Criteria (SDC) employed by Caltrans in the design of bridge structures (SDC-2006) suggest that the shear capacity of reinforced concrete (RC) members are associated with the axial force demand on the member. An increase (or decrease) in the axial force demand results in an increase (or decrease) in the concrete contribution to the shear capacity of a reinforced concrete member,  $V_C$ . For RC members in axial tension, both guidelines suggest that the concrete contribution should be ignored and the shear capacity of the RC member should be taken to be equal to the steel contribution,  $V_s$ . However, the effect of axial force demands on shear capacity is a fairly complex issue to fully comprehend and evaluate since the shear demand in an RC bridge column is affected by the variations in the axial force in the member. At the limit state, the maximum probable shear demand in a structural member is equal to  $V = (M_y^i + M_y^j)/L$ , where  $M_y^i$  and  $M_y^j$  are the moment capacities of the member at ends and  $L$  is the length of the member. The moment capacity of a RC section also depends on the axial force on the section. Hence, variations in the axial force on the section results in a variation in the moment capacity of the section which in turn results in a variation in the maximum probable shear demand on the section. Accordingly, the shear force demand in an RC member may increase when the compressive force on the member increases significantly. This is an indirect effect. On the other hand, vertical motions leading to axial tension in the column can directly impact the shear capacity of the element.

The issues listed above are further complicated by the fact that the frequency of vertical motion is higher than the frequency of the horizontal motion. Hence it is necessary to gain additional insight into high frequency axial variations on shear demand and shear capacity of typical bridge columns that are vulnerable to vertical effects of strong ground shaking.

## 1.2 Objectives and Scope of the Research

The main objective of this study is to investigate the effect of axial force, produced by the vertical component of the ground motion, on the behavior of bridge columns, especially on shear strength degradation. Outline of the research activities is presented in Figure 1-1.

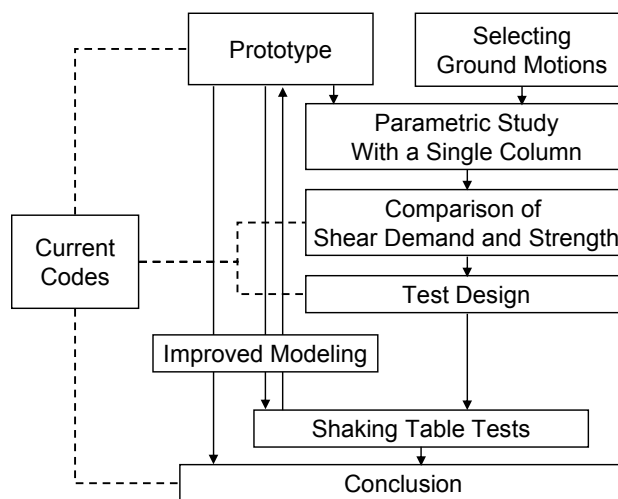


Figure 1-1: Outline of research project

This study consists of four parts. In the first part, a parametric study is conducted on a single column model which is based on a representative bridge prototype. Using a sub-set of ground motions from the Pacific Earthquake Engineering Research (PEER) Center's Next Generation Attenuation (NGA) ground motion database, with strong influence of the vertical acceleration, shear demand is compared to capacity suggested in current codes. The findings from this phase of study facilitate both the selection of the appropriate ground motion as well as the design of the model specimen for the shaking table study.

The second part of the study is concerned with the dynamic tests of the model specimens. The specimens, which are  $\frac{1}{4}$ -scale models of the prototype columns, are designed based on the Caltrans SDC requirements. Corresponding mass and mass moment of inertia are determined from the prototype. Fidelity tests are used to choose the most suitable motion which can be replicated by the shaking table at the UC-Berkeley Richmond Field Station. Dynamic tests of two specimens are conducted and pertinent results are summarized.

The third part describes the retrofit and retesting of the damaged model columns. The retrofit consisted of wrapping the damaged regions with glass and carbon fiber reinforced polymer

jackets in conjunction with a special commercial epoxy system. The same ground motions used on the original specimen are applied to the retrofitted model.

In the fourth and final part, analytical simulations are carried out so as to calibrate a simulation model of the model column. A new OpenSees shear spring element is developed since existing elements do not consider the ductility-axial-shear coupled behavior. Current code equations are evaluated and compared to the analysis results.

## 1.3 Previous Studies on Vertical Ground Motions and its Effect on Bridge Columns

### 1.3.1 Ground Motion Characteristics

One of the sources of axial load on bridge columns is attributed to the effect of the vertical component of the earthquake acceleration. Vertical excitation has been neglected in most design provisions for ordinary bridges for several decades. In many codes, vertical earthquake motion is represented by scaling a single design spectrum derived for horizontal components. This procedure was devised by Newmark et al. (1973) [33] and has been widely used. Generally, the scaling factor, i.e. the vertical-to-horizontal ratio, has been taken as 2/3. The weakness of this procedure is the assumption that horizontal and vertical components have the same frequency content which does not reflect either the frequency content of ground motion or the actual structural responses of bridge systems. In addition, the ratio of peak vertical-to-horizontal ground accelerations (V/H) may often exceed 2/3, which is the value usually considered in current design codes, in the near-source region. In Table 1-1, V/H ratios from various earthquakes which are greater than 2/3 are presented.

**Table 1-1: V/H Ratios for several earthquakes**

Earthquake	Station	PGA [g]		V/H
		Horizontal	Vertical	
Nahanni 1985	Site 1	1.06	2.09	1.98
Gazli 1976	Karakyr	0.644	1.26	1.96
Kobe 1995	Port Island	0.315	0.562	1.78
Kobe 1995	Kobe University	0.310	0.380	1.23
Landers 1992	Lucerne	0.721	0.819	1.14
Loma Prieta 1989	LGPC	0.784	0.886	1.13
Northridge 1994	Jensen Filter Plant	0.764	0.825	1.08

Current provisions in SDC [13] do not provide guidelines considering the adverse consequences of vertical accelerations in seismic design of ordinary bridges where the site peak rock acceleration is smaller than 0.6g. Also, when this acceleration is 0.6g or greater, only equivalent static methods are required.

To consider the effect of vertical ground motion appropriately, some recent studies have focused on constructing vertical design spectra. In particular, references [15] and [18] proposed a vertical design acceleration spectrum which consists of a flat portion at short periods (0.05 to 0.15 sec) and a decaying spectral acceleration for  $T \geq 0.15$ sec. Elgamal and He (2003) [17] studied the characteristics of vertical ground motion with 111 free field records and down-hole array records. They found that significant high frequency (about 8 Hz or higher) prevailed in all vertical records and that site distance from source affects the spectral shape. They also discovered that the spectra of Elnashai and Papazoglou proposed in [19] with corner periods of 0.05 sec and 0.15 sec are quite representative for near-field sites. From the scarce available down-hole array records, they found little variation with depth in spectral shape and concluded that using the surface spectral shape for a spectrum at any depth may be acceptable, but the values should be gradually reduced by 1/2 to 2/3 as the depth reaches the range of 20 m.

Bozorgnia and Campbell (2004) [11] studied the characteristics of vertical ground motion extensively and proposed a ground motion model for the vertical-to-horizontal ratio (V/H) of the peak ground accelerations. Based on a study of over 400 near-source accelerations with large  $M_w$  (i.e.  $4.7 \leq M_w \leq 7.7$ ), they found no bias in the V/H estimates from independent analyses of vertical and horizontal response spectra. In addition, V/H was found to be a strong function of natural period, local site conditions, and source-to-site distance and a relatively weaker function of magnitude, faulting mechanism, and sediment depth. V/H exhibits its greatest differences at long periods on firm rock (NEHRP: BC), where it has relatively low amplitudes, and at short periods on firm soil (NEHRP: D), where it has amplitudes that approach 1.8 at large magnitudes and short distances.

As discussed in [15], [27], the arrival time interval is an important parameter which affects the interaction between horizontal and vertical responses. In these studies, the interval between the peak acceleration of horizontal component and that of vertical one is utilized as the arrival time interval. Collier and Elnashai (2001) [15] pointed out that a maximum interaction effect between the horizontal and vertical motions occurs when the arrival time interval is less than 0.5 sec. They also showed that there is no interaction effect when the arrival time is longer than 4.0 sec.

### **1.3.2 Experimental and Numerical Studies**

Sakai and Unjoh (2007) [40] conducted shaking table experiments with combined horizontal and vertical excitations. The specimen was a 1/4-scale circular column which had 3 m height and 600 mm diameter, corresponding to an effective aspect ratio of 5. The test had two phases, one for dynamic response in elastic range and the other for nonlinear response. The amplitudes in all the three directions were scaled by 20% and 400% for each phase. The lateral period was 0.3 sec and

the vertical period was 0.08 sec. Because the predominant natural period in the vertical direction was 25% of that in the lateral directions, the lateral response and axial force rarely reached their maximum values simultaneously. Hence, the lateral response was not significantly affected by the fluctuation of the axial force.

To investigate the effect of vertical ground motion on RC bridges and buildings, Kim and Elnashai (2008) [27] performed extensive analytical and experimental investigations. For RC bridges, they assessed the effect of various peak vertical-to-horizontal acceleration ratios and studied the effect of time intervals between the arrival of vertical and horizontal peaks of given earthquake records. Some observations from their analytical study are as follows:

- The ratio of vertical seismic force to gravity load of pier was higher for the bridge with shorter span because the fundamental period of short span bridge was close to the dominant period of vertical motion.
- The shear capacity decreased due to vertical excitation.
- The contribution of vertical ground motion to axial force variation increased as the span ratio (i.e. the ratio between the two adjacent span lengths) increased. Therefore, shear capacity was reduced as well, but the effect of vertical ground motion on shear demand varied irregularly.
- The shear capacity of shorter column height was significantly reduced with vertical excitation while shear demand decreased as the height increased.

It was concluded that the effect of arrival time was minimal on the periods of vibration, axial force variation, and moment and shear demands. On the other hand, it was shown that the time interval had an effect on the shear capacity. In summary they stated that vertical ground motion should be considered in assessing the shear capacity and in the demand assessment when V/H is likely to be high and the arrival time interval is near zero or very short.

Kim and Elnashai [27] also conducted SPSD tests and cyclic static tests with different axial loads using the Multi-Axial Full-Scale Sub-Structured Testing and Simulation (MUST-SIM) facility at University of Illinois at Urbana-Champaign. Due to the capacity limitations of the MUST-SIM facility, a 1/2-scale model was constructed. Two SPSD tests were conducted to investigate the effect of vertical ground motion, one under horizontal ground motion only (IPH) and the other under horizontal and vertical ground motions (IPV). To investigate the effect of axial force, two specimens were used for static cyclic tests, one subjected to tension (ICT) and the other subjected to compression (ICC). The damage in IPV was more severe than that of IPH. At mid height of IPV, severe shear damage was observed. Although the effect of vertical ground motion on the longitudinal strain distribution was not significant, that on the spiral strain was significant. The maximum spiral strain in IPH and IPV was detected at 20% and 55% of the pier height, respectively, and the spiral strain at the same level increased by 160% due to the vertical ground motion. Considering trends of the strain distribution and the maximum spiral strains measured from both piers, it was estimated that the spiral strain increased up to about 200% when the vertical ground motion was included. In summary, it was concluded that including the vertical ground motion reduced the shear capacity of the pier. In specimen ICT, a flexure-dominated behavior was clearly observed. There was no significant strength degradation until the loading

reached the lateral displacement where the maximum lateral force was recorded. ICC experienced brittle shear failure with rupture of the spiral. On the other hand, ICT subjected to moderate tension was severely damaged with significant flexural and inclined cracks as well as large opening of diagonal cracks near the bottom of the pier. However, there was no strength degradation in ICT.

Kim and Elnashai [27] also compared the shear strength evaluated by employing the design code methods and a predictive approach, with the observed values from the experiments. ACI 318-05 [3] and AASHTO LRFD (2005) [1] were used as conventional design code methods and Priestley et al. (1994) [37] as the predictive approach. They concluded that the approaches except that in [37] were conservative for IPH, IPV, and ICC considering the observed spiral strain histories and damage state of the specimens. ICT showed higher shear strength than that predicted by all approaches.

## 1.4 Overview of Shear Strength Assessment

Estimating the shear strength of RC members is still contentious and there is obvious divergence of opinions, design approaches, and code equations. In particular, the influences of axial load, flexural ductility, and size of members and aggregates are not well agreed upon within different codes. The following code equations and an analytical approach are widely used methods to estimate the shear strength of RC members, e.g. columns.

### 1.4.1 ACI 318-08

According to ACI 318-08 [4], the nominal shear strength is computed by:

$$V_n = V_c + V_s \quad (1.1)$$

where  $V_c$  and  $V_s$  are the nominal shear strength provided by concrete and shear reinforcement, respectively. When shear reinforcement perpendicular to the axis of the member is used, one can use

$$V_s = \frac{A_v f_y d}{s} = \frac{A_v f_y (0.8D)}{s} \quad (1.2)$$

where  $A_v$  is the cross-sectional area of the spiral reinforcement within spacing  $s$  and  $D$  is the diameter of the concrete section. For circular members with circular ties, hoops or spirals used as shear reinforcement, it is permitted to take the effective depth,  $d$ , as 0.80 times the diameter of the concrete section and  $A_v$  can be taken as two times the area of the bar cross-section used as the spiral. Finally,  $f_y$  is the specified yield strength of the spiral reinforcement.

For members subjected to axial compression,

$$V_c = 2 \left( 1 + \frac{N_u}{2000A_g} \right) \sqrt{f'_c} b_w d \quad (1.3)$$

and for members subjected to significant axial tension,

$$V_c = 2 \left( 1 + \frac{N_u}{500A_g} \right) \sqrt{f'_c} b_w d \quad (1.4)$$

where  $N_u$  is positive for compression and negative for tension. In the above two equations,  $N_u/A_g$  and the concrete compressive strength of the standard specimen  $f'_c$  have psi units, and  $A_g$  is the gross cross-sectional area with web width  $b_w$  and effective depth  $d$ .

For circular members, the area used to compute  $V_c$  can be taken as the product of the diameter and effective depth of the concrete section. Hence, the following  $V_c$  can be used,

$$V_c = 2 \left( 1 + \frac{N_u}{2000A_g} \right) \sqrt{f'_c} (0.8D^2) \text{ for members subjected to axial compression} \quad (1.5)$$

$$V_c = 2 \left( 1 + \frac{N_u}{500A_g} \right) \sqrt{f'_c} (0.8D^2) \text{ for members subjected to axial tension} \quad (1.6)$$

where  $A_g = \frac{\pi D^2}{4}$ .

## 1.4.2 A Note about Size Effect

Unfortunately, ‘size effect’ is not considered in Eqs. (1.3) to (1.6) for  $V_c$ . Size effect is the phenomenon that the failure shear stress for members without web reinforcement decreases as the member depth increases. Eqs. (1.3) to (1.6) were obtained from specimens with average height of 340 mm (13.4 in) and as a result, the ACI expressions offer a continuous and linear increase in the contribution of concrete to shear capacity as the member depth increases. This means that these expressions are not suitable for deeper members without web reinforcement.

The Modified Compression Field Theory (MCFT) [45] provides analytical model which is capable of predicting the load-deformation response of RC elements subjected to in-plane shear and normal stresses. It is developed from the compression-field theory for RC members subjected to torsion and shear. While the compression-field theory did not take into account tension in the cracked concrete, the MCFT reflects tensile stresses between cracks. Also, in the MCFT, the size effect is related to the crack spacing in the web and the crack width.

Cracking usually occurs along the interface between the cement paste and the aggregate particles and the rough cracks can transfer shear by aggregate interlocking. Based on Walraven’s experimental study [46], the relationship between the shear transfer across the crack and the

crack width was derived. Roughly, the larger crack width which occurs in a larger member reduces aggregate interlocking and accordingly reduces the shear transfer. In other words, the shear stress decreases as the crack width increases and as the relative maximum aggregate size (compared to the member size) decreases. Therefore, the shear stress limit of a large member is lower than that of a small member. The crack width is the average crack width over the crack surface and it can be taken as the product of the principal tensile strain and the crack spacing. It means that crack widths increase linearly with both the tensile strain in the reinforcement and the spacing between cracks.

The AASHTO LRFD [2] and the 2004 Canadian Standards Association (CSA) [16] are based on the Simplified Modified Compression Field Theory (SMCFT) [10], but has been further simplified. Simple expressions have been developed for the factor determining the ability of diagonally-cracked concrete to transmit tension,  $\beta$ , the crack angle,  $\theta$ , and the longitudinal strain in the web,  $\varepsilon_x$ , thereby eliminating the need to iterate to solve for these values.

### 1.4.3 AASHTO (2010)

AASHTO LRFD Bridge Design Specification [2] defines the shear resistance of a concrete member as the sum of resistance due to shear stress of concrete,  $V_c$ , tensile stress in the transverse reinforcement,  $V_s$ , and the vertical component of prestressing force, if any,  $V_p$ , as follows,

$$V_n = V_c + V_s + V_p \quad (1.7)$$

The contribution of concrete is determined in N-mm units as follows:

$$V_c = 0.083\beta\sqrt{f'_c}b_vd_v \quad (1.8)$$

where  $b_v$  is the effective web width taken as the minimum web width with the depth  $d_v$ . For a circular section,  $b_v = D$ ,  $d_v = 0.9d_e$  can be used, where  $d_e = \frac{D}{2} + \frac{D_r}{\pi}$  as shown in Figure 1-2.

The value of  $\beta$ , factor to determine the ability of diagonally-cracked concrete to transmit tension, is defined as follows:

$$\beta = \frac{4.8}{1 + 750\varepsilon_s} \quad (1.9a)$$

$$\beta = \left( \frac{4.8}{1 + 750\varepsilon_s} \right) \left( \frac{51}{39 + s_{xe}} \right) \quad (1.9b)$$

Eq. (1.9a) is for sections containing at least the minimum amount of transverse reinforcement and Eq. (1.9b) is for the rest. The minimum amount of transverse reinforcement is defined as  $A_v \geq 0.05b_w s / f_y$ , where  $b_w$  is the width of web. In addition, the crack spacing parameter is calculated as follows:

$$s_{xe} = s_x \frac{1.38}{a_g + 0.63} \quad (1.10)$$

where  $a_g$  is the maximum aggregate size in mm, and  $s_x$  is the lesser of either  $d_v$  or the maximum distance between layers of longitudinal crack control reinforcement.  $s_{xe}$  should be between 12 in (305 mm) and 80 in (2032 mm). If there is no prestressing tendon, the net longitudinal tensile strain in the section at the centroid of the tension reinforcement,  $\varepsilon_s$ , is defined as follows:

$$\varepsilon_s = \frac{\left( \frac{|M_u|}{d_v} + 0.5N_u + |V_u| \right)}{E_s A_s} \quad (1.11)$$

where  $N_u$ ,  $M_u$ , and  $V_u$  are the factored axial force, bending moment, and shear force, respectively, and  $A_s$  and  $E_s$  are the cross-sectional area and modulus of elasticity for the longitudinal tension reinforcement.

The contribution of transverse reinforcement is determined as follows:

$$V_s = \frac{A_v f_y d_v (\cot \theta + \cot \alpha) \sin \alpha}{s} \quad (1.12)$$

$$\theta = 29^\circ + 3500\varepsilon_s \quad (1.13)$$

The parameter  $\alpha$  is the angle of inclination of transverse reinforcement (with cross-sectional area,  $A_v$ , yield stress,  $f_y$ , and spacing,  $s$ ) to the longitudinal axis of the member, and  $\theta$  is the angle of inclination of the diagonal compressive stress. The factors  $\beta$  (Eq. (1.9)) and  $\theta$  (Eq. (1.13)) depend on the applied loading and the properties of the cross-section.

Prior to the 2008 interim revisions, AASHTO provided the procedure for shear design, which was iterative and required the use of tables for the evaluation of  $\beta$  and  $\theta$ . With the 2008 revisions, this design procedure was modified to be non-iterative and algebraic equations were introduced for the evaluation of  $\beta$  and  $\theta$ . These equations are functionally equivalent to those used in the Canadian code (CSA 2004), which was also derived from the SMCFT [10]. Since Eq. (1.8) and Eq. (1.16) are equivalent, only CSA equations will be used in Chapter 2.

The longitudinal strain,  $\varepsilon_s$ , is affected by diagonal compressive stresses. After diagonal cracks have formed in the web, the shear force applied to the web concrete,  $V_u$ , is primarily carried by diagonal compressive stresses in the web concrete. These stresses result in a longitudinal compressive force in the web concrete of  $V_u \cot \theta$  (Figure 1-3). Equilibrium requires that this longitudinal compressive force in the web needs to be balanced by tensile forces in the two flanges, with half the force, that is  $0.5V_u \cot \theta$ , being taken by each flange. For simplicity, the longitudinal demand due to shear in the longitudinal tension reinforcement may be taken as  $V_u$  without significant loss of accuracy. After the required axial forces in the two flanges are

calculated, the resulting axial strains in the steel reinforcement and concrete,  $\epsilon_s$  and  $\epsilon_c$ , respectively, can be calculated based on the axial force-axial strain relationships.

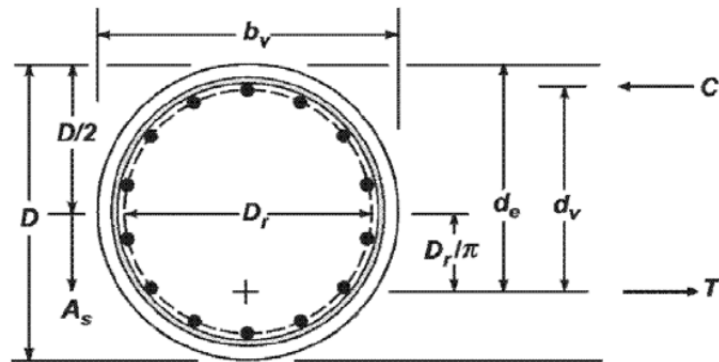


Figure 1-2: Parameters  $b_v$ ,  $d_v$  and  $d_e$  for a circular column (AASHTO 2010 [6])

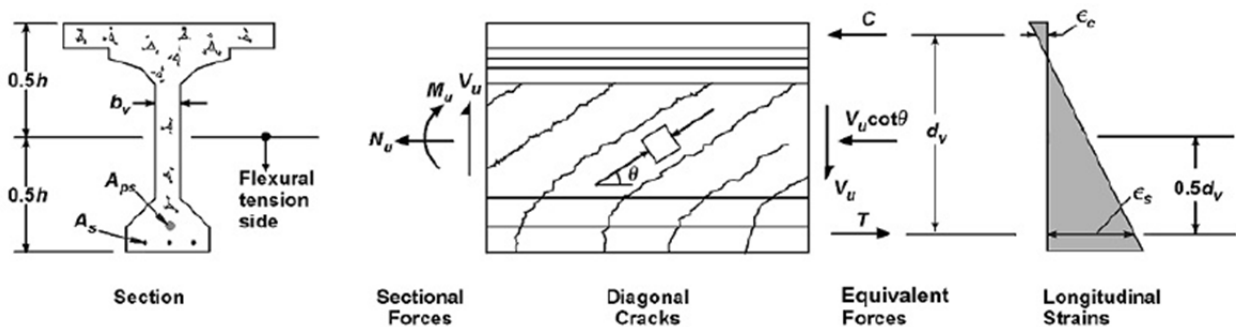


Figure 1-3: Shear parameters, AASHTO (2010) [6]

#### 1.4.4 Canadian Code (2004)

2004 CSA A23.3 [16] shear provisions for RC are based on the MCFT like the AASHTO [2]. In CSA, the shear strength is assumed to be the sum of  $V_c$ ,  $V_s$ , and  $V_p$  (Eq. (1.7)) as in other codes where  $V_c$  is the shear resistance from concrete, which is due to the shear stress transfer across the crack itself, usually called aggregate interlocking stresses,  $V_s$  is from the transverse reinforcement, specifically due to the yielding stirrup legs that cross the diagonal crack, and  $V_p$  is the vertical component of the prestressing force, if any. Since the vertical force from dowel action is ignored in the MCFT, it is ignored in the CSA as well.

The aggregate interlocking resistance of the complex crack geometry may be estimated at only one depth in the member, e.g. mid-height, and this can represent the entire crack surface. The

shear stress resistance of the flexural compression region is larger than that of the cracked region, and thus the ability of the cracks to resist shear stresses controls the member strength for members without stirrups.

The shear resistance from transverse reinforcement is defined as follows:

$$V_s = \frac{A_v f_y d_v \cot \theta}{s} \quad (1.14)$$

$$\theta = 29^\circ + 7000 \varepsilon_x \quad (1.15)$$

$$V_c = \beta \sqrt{f'_c} b_v d_v \quad (1.16)$$

$$\beta = \left( \frac{0.4}{1 + 1500 \varepsilon_x} \right) \left( \frac{1300}{1000 + s_{ze}} \right) \quad (1.17)$$

where  $A_v$  is the cross-sectional area of the spiral reinforcement,  $f_y$  is the yield strength of the spiral reinforcement material,  $s$  is the spacing of the spiral reinforcement, and  $f'_c$  is the compressive strength of concrete and its unit is MPa. The parameters which define  $\beta$  and  $\theta$  for the determination of  $V_c$  and  $V_s$ , respectively, are similar to the case of AASHTO, except the longitudinal strain. In CSA, the longitudinal strain at the centroid,  $\varepsilon_x$ , is used rather than the longitudinal strain at the centroid of the tension reinforcement,  $\varepsilon_s$ .

Since the aggregate interlocking relationship directly depends on the crack width, the calculation of such crack width is needed to determine  $V_c$ . Approximately, the crack width can be estimated as the product of average crack strain perpendicular to the crack and the average crack spacing in this direction. Previous studies demonstrated that the crack patterns are consistent from one size to another, and the crack spacing increases as the RC member (without shear reinforcement) is scaled to a larger size. Since wider cracks carry less shear stresses, larger member's shear stress related to  $V_c$  cannot exceed that of a smaller member. However, members with transverse reinforcement do not follow this trend because transverse reinforcement controls the crack spacing. Therefore, such RC members (with shear reinforcement) do not show a significant size effect. Hence, the basic crack spacing  $s_z$  is taken as 300 mm (11.8 in) for the members with stirrups or transverse reinforcement, rather than  $s_z = d_v = 0.9D$  (where  $D$  is the diameter of the column) which is used by CSA 2004 for the members without stirrups.

The effective crack spacing parameter,  $s_{ze}$ , reflects the effect of different coarse aggregate sizes in mm,  $a_g$ , and it is calculated as follows:

$$s_{ze} = \frac{35s_z}{15 + a_g} \geq 0.85s_z \quad (1.18)$$

In case of a member with transverse reinforcement and 19 mm (0.75 in) coarse aggregate,  $s_{ze} = 308.8$  mm (12.2 in). For a circular section,  $d_v = 0.72D$  in CSA 2004. Also, nominal shear strength should not be taken larger than the following:

$$V_{n,max} = 0.25f'_c b_v d_v \quad (1.19)$$

### 1.4.5 Eurocode (2004)

Eurocode 2 [21] suggests the use of Eq. (1.1) with following definitions:

$$V_s = \min \left( \frac{A_v z f_y \cot \theta}{s}, \frac{\alpha_c b_w z v f'_c}{\cot \theta + \tan \theta} \right) \quad (1.20)$$

$$V_s = \frac{A_v z f_y \cot \theta}{s} = \frac{A_v f_y (0.72D)}{s} \quad (1.21)$$

where  $z$  is the lever arm and  $\theta$  is the angle of the inclined struts. The recommended limiting values are:  $1 \leq \cot \theta \leq 2.5$ , i.e.  $22^\circ \leq \theta \leq 45^\circ$ . In this study,  $\cot \theta = 1$ , i.e.  $\theta = 45^\circ$ , is used unless otherwise noted. The parameter  $\alpha_c$  is a coefficient which takes into account the effect of normal stresses on the shear strength and its recommended value is as follows:

$$\left( \begin{array}{l} \text{non-prestressed : } \alpha_c = 1 \\ 0 < \sigma_c \leq 0.25 f'_c : \alpha_c = 1 + \sigma_c / f'_c \\ 0.25 < \sigma_c \leq 0.50 f'_c : \alpha_c = 1.25 \\ 0.50 < \sigma_c \leq 1.0 f'_c : \alpha_c = 2.5 (1 - \sigma_c / f'_c) \end{array} \right) \quad (1.22)$$

where  $\sigma_c$  is the compressive stress in concrete from axial load or prestressing. The parameter  $v$  is a coefficient that takes into account the increase of fragility and the reduction of shear transfer by aggregate interlocking with the increase of the compressive concrete strength. It may be taken to be 0.6 for  $f'_c \leq 60$ MPa, and  $0.9 - f'_c / 200 > 0.5$  for high-strength RC members.

$$V_c = \frac{\pi D_c^2}{4} \left[ \tau_{rd} k (1.2 + 40 \rho_l) + 0.15 \sigma_{cp} \right] \quad (1.23)$$

$$D_c = D - 2c_c - 2d_{bw} \quad (1.24)$$

where  $d_{bw}$  is the diameter of the spiral reinforcement and  $c_c$  is the concrete cover outside the spiral.

$$\tau_{rd} = 0.25 \left( 0.7 \sqrt{f'_c} \right) \quad (1.25)$$

$$k = 1 \quad (1.26)$$

$$\sigma_{cp} = \frac{N}{A_c} \quad (1.27)$$

where  $N$  is the axial load and  $A_c = \frac{\pi D_c^2}{4}$ .

### 1.4.6 Priestley et al. (1996)

Priestley et al. (1996) [38] suggested the following equations to calculate the nominal shear strength of RC columns. In this approach,  $V_c$  is calculated for the plastic hinge zone considering the effect of displacement ductility and  $V_s$  is calculated based on the truss model for circular columns. The shear strength enhancement resulting from axial compression,  $V_p$ , is considered as an independent compression strut. Accordingly, Eq. (1.7) is used in this model.

The contribution of transverse reinforcement to the shear strength is based on the truss mechanism using  $\theta$  as the angle of inclination between the shear cracks and the vertical column axis. Accordingly, one obtains,

$$V_s = \frac{\pi A_v f_y D'}{2s} \cot \theta \quad (1.28)$$

where  $A_v$  is the total transverse reinforcement cross-sectional area and  $D'$  is the distance between centers of the peripheral hoop in the direction parallel to the applied shear force. The angle of the critical inclined flexure shear cracking to the column axis is taken as  $\theta = 30^\circ$  unless limited to larger angles by the potential corner-to-corner crack. The contribution of concrete is given as follows:

$$V_c = k \sqrt{f'_c} A_e \quad (1.29)$$

where  $A_e = 0.8A_g$  is the effective shear area and  $k$  depends on the instantaneous displacement or ductility. In case of displacement ductility and when subjected to biaxial ductility demand,  $\mu_\Delta$ ,  $k$  is defined as follows when the concrete strength and the effective shear area are respectively in MPa and  $\text{mm}^2$  units:

$$\left( \begin{array}{l} \mu_\Delta \leq 1 : k = 0.29 \\ 1 < \mu_\Delta \leq 3 : k = 0.10 + 0.19(3 - \mu_\Delta)/2 \\ 3 < \mu_\Delta \leq 7 : k = 0.05 + 0.05(7 - \mu_\Delta)/4 \\ 7 < \mu_\Delta : k = 0.05 \end{array} \right) \quad (1.30)$$

The shear strength increase by axial force is calculated as a result of an inclined compression strut given as follows:

$$V_p = P \tan \alpha = \frac{D - c}{2a} P \quad (1.31)$$

where  $D$  is cross-section height or diameter,  $c$  is the compression zone depth and it is determined from flexural analysis. The parameter  $a$  is the shear span which is  $L/2$  for a column in double curvature and  $L$  for a column in single curvature, Figure 1-4.

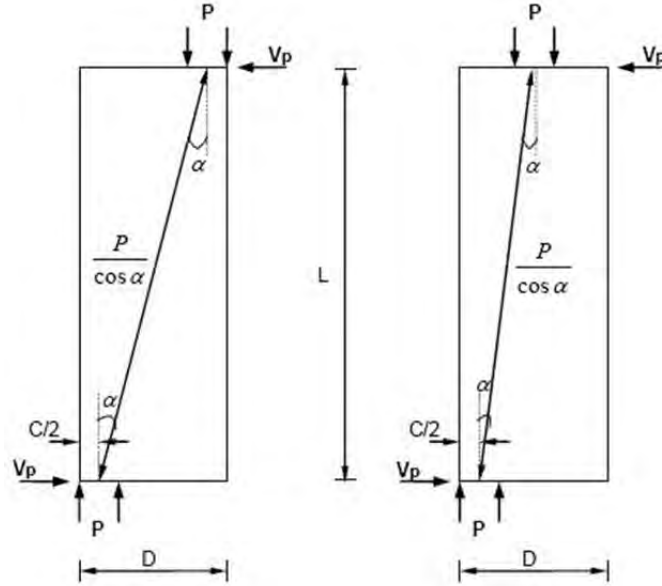


Figure 1-4: Contribution of axial forces to shear strength, Priestley et al. (1996) [38]

### 1.4.7 Caltrans SDC (2010)

Caltrans SDC (2010) [13] suggests the use of Eq. (1.1) with following definitions for the shear strength of ductile concrete circular members.

$$V_s = \frac{A_v f_y D'}{s} \quad (1.32)$$

$$A_v = n \left( \frac{\pi}{2} \right) A_b \quad (1.33)$$

$$V_c = v_c A_e \quad (1.34)$$

where  $n$  is the number of branches of the transverse reinforcement crossed by the diagonal shear cracks,  $A_b$  is the cross-sectional area of the bar used as transverse reinforcement,  $A_e = 0.8A_g$  is the effective shear area and  $v_c$  is determined by the location of the cross-section, transverse reinforcement, and ductility demand ratio as follows:

Inside the plastic hinge zone, 'Factor1' is included in calculating  $v_c$ .

$$v_c = \text{Factor1} \times \text{Factor2} \times \sqrt{f'_c} \leq 4\sqrt{f'_c} \quad (\text{psi units}) \quad (1.35)$$

Outside the plastic hinge zone, the constant, 0.25, is used instead of 'Factor1'.

$$v_c = 3 \times \text{Factor2} \times \sqrt{f'_c} \leq 4\sqrt{f'_c} \quad (\text{psi units}) \quad (1.36)$$

The factors in the above equations are defined as follows:

$$0.3 \leq \text{Factor1} = \frac{\rho_s f_{yh}}{0.15 \text{ksi}} + 3.67 - \mu_d \leq 3 \quad (1.37)$$

where  $f_{yh}$  is transverse reinforcement (e.g. hoop) yield strength in ksi units and  $\rho_s f_{yh}$  (where  $\rho_s$  is the volumetric ratio of the transverse reinforcement) is limited to 0.35 ksi.

$$\text{Factor2} = 1 + \frac{P_c}{2000 A_g} < 1.5 \quad (1.38)$$

where  $P_c$  is the axial load in lb and  $A_g$  is in  $\text{in}^2$ . As defined above, ‘Factor1’ is affected by the transverse reinforcement and lateral displacement ductility,  $\mu_d$ , and ‘Factor2’ is affected by the axial pressure. It should be noted that  $v_c = 0$  for members whose net axial load is in tension.

Except that it takes account of displacement ductility instead of curvature ductility in the estimation of the shear strength, Caltrans SDC (2010) [13] adopts the approach of Priestley et al. (Section 1.2.6) [38] for ductility and combines it with the approach of ACI [4] and Eurocode [21] for axial pressure. Another unique feature of the SDC approach is that it provides different estimation along the member. ‘Factor1’, which is determined by the transverse reinforcement and displacement ductility, is only effective inside the plastic hinge zone and it ranges from 0.025 to 0.25. Since 0.25 is applied instead of ‘Factor1’,  $V_c$  of the cross-section outside the plastic hinge zone is equal or larger than that inside the plastic hinge zone.

## 2 Selection of Ground Motions and Model Bridge Configuration

This chapter presents the analyses conducted prior to the shaking table tests on the PEER earthquake simulator of University of California, Berkeley. Results of these analyses were utilized as a guidance to select the ground motions, column geometry and reinforcement, and the setup of the shaking table tests. First, the method used for selecting a smaller number of critical ground motions from a larger set is presented. Subsequently, the possible representative bridge prototypes are described. Finally, a parametric study conducted for a single column based on one of the prototypes is described and the results of this parametric study are presented.

### 2.1 Selection of Ground Motion

PEER NGA database [37] provides 3,551 earthquake acceleration records and their meta-data. Of these, 3,466 ground motions, with all three components available, are selected from the database. Since only strong ground motions with the potential to impose large inelastic demands is of interest, ground motions with peak ground acceleration (PGA) of either horizontal components less than 0.25g are eliminated. After this elimination, the ground motion set is reduced from 3,466 to only 293 ground motions.

A secondary study based on the ratio of the pseudo-spectral acceleration of the vertical component ( $PSa_v$ ) to the corresponding horizontal components ( $PSa_{h1}$ ,  $PSa_{h2}$ ) was also carried out. For each of the 293 ground motions, pseudo-spectral accelerations of the vertical component are calculated corresponding to the vertical periods ( $T_v$ ) of 0.05, 0.1, 0.15, and 0.2 seconds and pseudo-spectral accelerations of the horizontal components are calculated corresponding to the horizontal periods ( $T_h$ ) of 0.4, 0.5, 0.6, 0.7, and 0.8 seconds. The chosen  $T_v$  and  $T_h$  values result in 20  $T_v$ ,  $T_h$  pairs. Since each ground motion has two horizontal components, there are two spectral ratios, namely  $PSa_v/PSa_{h1}$  and  $PSa_v/PSa_{h2}$ , for each pair. The following observations are noted:

- As  $T_v$  increases, the ratio  $PSa_v/PSa_{h1}$  tends to decrease.
- As  $T_h$  increases, the ratio  $PSa_v/PSa_{h1}$  tends to increase.
- There are many ground motions which have small  $PGA_{h1}$ ,  $PGA_v$ , and  $PGA_v/PGA_{h1}$ , but large ratios of  $PSa_v/PSa_{h1}$ . Among them, ground motions with small  $PGA_{h1}$  are not useful since they will not lead to inelastic behavior.

After elimination of the ground motions with small  $PSa_v/PSa_h$  ratios, a smaller subset of 80 records which were considered suitable for the present study. Arrival time of the peak vertical component of the acceleration trace is also an important criterion. As discussed in [15], [27], the

interval between the horizontal and the vertical peak accelerations affects the interaction of the horizontal and the vertical responses. Hence the final criterion used in selecting the ground motion for the study was the interval between the peaks of the horizontal and vertical component of the accelerogram.

Finally, after the frequency content of the ground motions and the arrival time interval between the peaks of the horizontal and vertical were considered, this set was reduced to 61 motions. Some of the following parametric studies used all 293 ground motions while other studies (as indicated in relevant sections of this report) considered only the smaller subset of 80 or 61 motions.

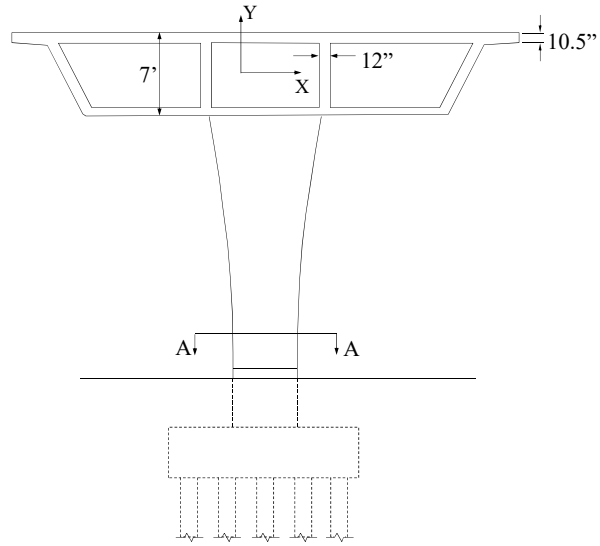
## 2.2 Prototype Model for Parametric Study

Kunnath et al. (2008) [28] considered two types of bridges: single bent, two span overpass and single-column bent, multi-span bridge. For the overpass system, a segment of El Camino Del Norte Bridge was selected as the prototype bridge whereas the Amador Creek Bridge (ACB) was used as the prototype bridge for the multi-span system. The selected overpass represents short-span RC bridges whereas the multi-span system represents long-span PC bridges. According to the analyses in [28], the effect of the vertical acceleration was more significant in El Camino Del Norte Bridge, which had shorter spans, smaller aspect ratio and was comprised of a multi-column bridge bent. Even though the effect of axial force might be more significant in two-column bridge bents, it is difficult to represent this effect in shaking table testing. Moreover, the complexity of the behavior of multi-column bridge bents due to other factors beyond the effect of vertical acceleration makes shaking table testing of single-column bridge bents for understanding the effect of vertical acceleration more realistic. However, as discovered later during testing, the flexibility of table had a significant effect on the vertical response. This flexibility is analogous to the effect of the bridge girders in elongating the vertical period of the bridge system compared to the period of a single bridge column.

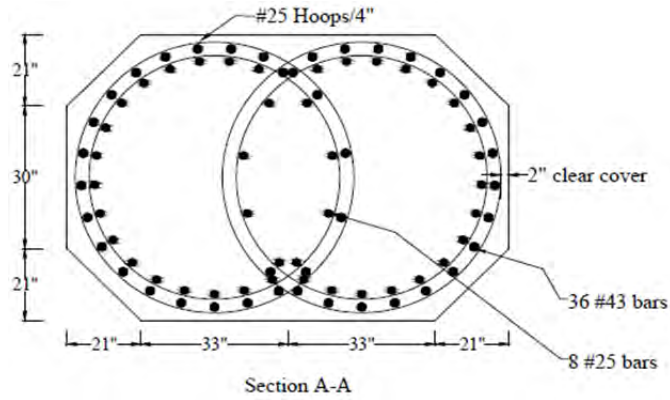
### 2.2.1 Amador Creek Bridge

The Amador Creek Bridge (ACB) is a three-bent, four-span RC bridge and its total length is 685 ft (207.6 m). The spans are 133.0 ft (40.5 m), 177.1 ft (53.7 m), 177.1 ft (53.7 m), and 133.0 ft (40.5 m). The bents of the bridge consist of single double-spiral columns. Figure 2-1 shows the elevation view and cross-sectional details of the columns of this bridge. The column heights are 64.8 ft (19.75 m), 91.9 ft (28.0 m), and 83.7 ft (25.25 m).

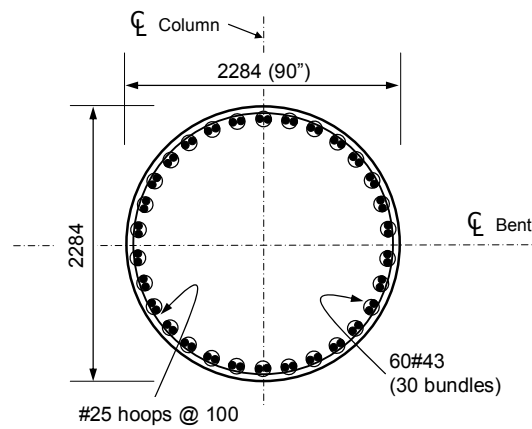
The bridge is modeled (Figure 2-2) as an elastic superstructure supported on nonlinear columns founded on elastic foundation using OpenSees [34]. The assumption of elastic superstructure is based on the capacity design approach employed by Caltrans via SDC-2010 [13]. Area  $A$ , moment of inertia  $I_x$ ,  $I_y$ , and polar moment of inertia,  $J$ , properties of the superstructure cross-section of the ACB are presented in Table 2-1.



(a) Elevation



(b) Interlocking spiral section (original section, units: in)



(c) Effective circular section (units: mm)

**Figure 2-1: Bent elevation and column cross-section of the Amador Creek Bridge**

The compressive strength of unconfined concrete and the yield strength of longitudinal reinforcement are specified to be 4 ksi (27.6 MPa) and 60 ksi (413.7 MPa), respectively, as designated on the design drawings. The compressive strength and ultimate strain of confined concrete were computed as 5.83 kips (25.9 kN) and 0.0157 using Mander’s model [29]. “Concrete01” material in OpenSees is used for both confined and unconfined concrete. A bilinear model with a post-yield stiffness of 1% of the initial stiffness is used to model the reinforcing steel. The columns of the bridge rest on shallow foundations. Therefore, six elastic springs in 3 translational and 3 rotational directions are used to model the soil-foundation system for each column. The approximate expressions in FEMA-356 (FEMA 2000) [22] are used to compute the properties of the corresponding springs. Table 2.1 also lists the values of the spring stiffness representing the foundation system.

**Table 2-1: Properties of superstructure and springs used to model the soil-foundation system for the Amador Creek Bridge**

Component	Parameter	Value
Superstructure	$A$	6.73 m <sup>2</sup>
	$I_x$	4.56 m <sup>4</sup>
	$I_y$	73.75 m <sup>4</sup>
	$J$	78.31 m <sup>4</sup>
Soil-foundation	Translation, X	5.18×10 <sup>6</sup> kN/m
	Translation, Y	6.01×10 <sup>6</sup> kN/m
	Translation, Z	4.99×10 <sup>6</sup> kN/m
	Rotation, X	1.05×10 <sup>8</sup> kN-m/rad
	Rotation, Y	1.16×10 <sup>8</sup> kN-m/rad
	Rotation, Z	5.30×10 <sup>7</sup> kN-m/rad

Seat type abutments are used at both ends of the bridge. Spring systems are used to model the stiffness of the abutments. In the transverse direction, shear keys are designed to break off during a strong ground motion. Hence, stiffness in the transverse direction is neglected. In the vertical direction, the movement of the bridge is prevented at the abutments in both upward and downward directions. Thus, the abutments are modeled as restraining supports in the vertical direction. In the longitudinal direction, the bridge is free to move in the opposite direction of the abutment at each end. Towards the abutment, there is a certain amount of gap before the superstructure makes contact with the abutment. When the superstructure and the abutment are in contact, the stiffness of the abutment is computed as  $K_{abut} = K_i w(h/5.5)$  [13], where  $K_i$  is the initial stiffness of the abutment and is taken as 20.0 k/in per ft of abutment width (11.49 kN/mm per m) and  $w$  and  $h$  are the projected width and height (in feet) of the abutment taken as 22.8 ft and 82.0 ft, respectively. Accordingly, a spring which has no stiffness in tension and elastic in compression with spring stiffness of 6785 kip/ft (99,019.6 kN/m) and with a 4 in (101.6 mm) gap is used to model the abutment behavior in the longitudinal direction.

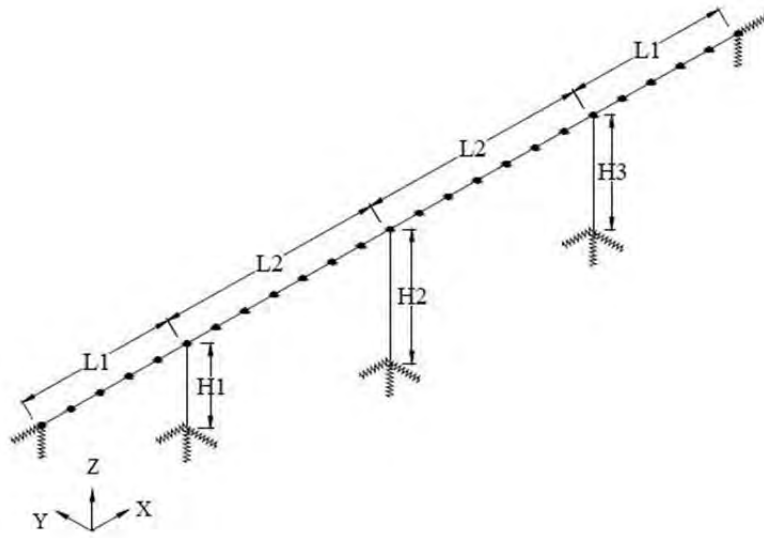


Figure 2-2: OpenSees model of the Amador Creek Bridge

## 2.2.2 Interlocking Spiral Section and Effective Circular Section

As mentioned previously, the objective of the parametric study is to provide guidance about the ground motion, column configuration and setup of the shaking table tests. Since the objective of the tests is to observe the effect of vertical excitation, a symmetric circular cross-section is more suitable than an asymmetric interlocking spiral cross-section. In this way, the effect of the difference of the cross-section moment of inertia and capacity in the two main orthogonal directions, an unnecessary complication affecting the results, is avoided. In addition, a circular section is more suitable from a practical point of view for test specimen detailing and construction. Due to the shaking table limitations, the test specimen should at most be a 1/4-scale of the prototype dimensions. Under these conditions, if interlocking spiral reinforcement is used it should be installed in a small cross-section with unknown influence of this reduced scale on the role of the interlocking spiral. Considering these reasons, the interlocking spiral section which has different properties in each direction is replaced by an effective circular cross-section.

To determine the size and number of longitudinal reinforcing bars and size (i.e. radius) of the effective circular column, flexural and axial capacities are considered. Since the original (interlocking spiral) cross-section has different moment capacities in each direction, the weak axis properties are chosen as the properties to be matched. Resulting area and moment of inertia values for the effective cross-section in comparison with the original interlocking spiral cross-section are listed in Table 2.2. The spacing and diameter of the spiral reinforcement used in the interlocking spiral column are directly employed for the effective circular cross-section.

A series of elastic modal analyses were carried out on both systems (with interlocking spiral and with effective circular cross-sections) to calibrate the inertial properties of the superstructure of

the OpenSees model. Table 2.3 presents the fundamental elastic mode shapes in longitudinal, transverse, vertical, and torsional directions.

**Table 2-2: Column cross-section properties of the Amador Creek Bridge**

Parameter	Interlocking spiral section	Effective circular section
$A$	5.03 m <sup>2</sup>	4.10 m <sup>2</sup>
$I_x$	1.40 m <sup>4</sup>	1.40 m <sup>4</sup>
$I_y$	3.13 m <sup>4</sup>	1.40 m <sup>4</sup>
$J$	4.53 m <sup>4</sup>	2.80 m <sup>4</sup>

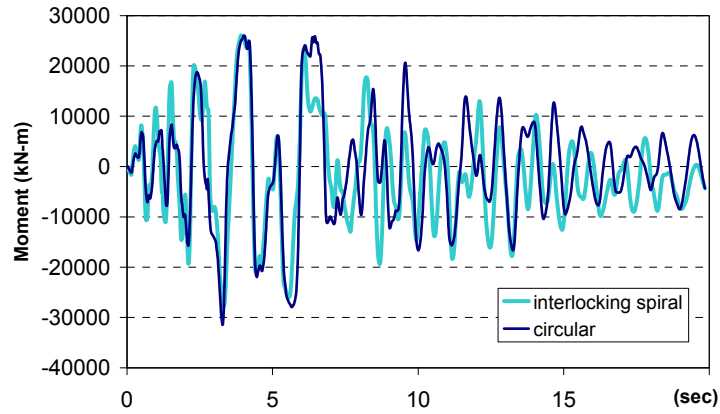
**Table 2-3: Modal properties of the Amador Creek Bridge**

Cross-Section	Mode number	Period [sec]
Interlocking spiral	1	2.29 (X)
	2	1.85 (Y)
	3	1.35 (coupled)
	4	0.80 (coupled)
	5	0.53 (Z)
	6	0.40 (coupled)
Circular	1	2.76 (Y)
	2	2.21 (X)
	3	1.86 (coupled)
	4	0.83 (coupled)
	5	0.68 (coupled)
	6	0.52 (Z)

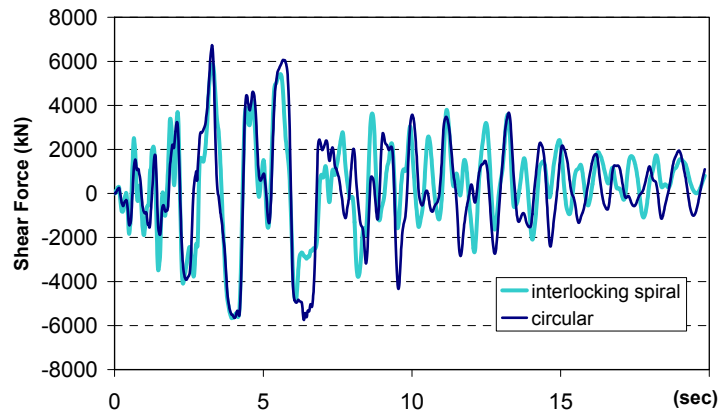
### 2.2.3 Comparison of Responses of the Bridge Systems with the Interlocking and the Effective Circular Cross-Sections

Figure 2-3 compares responses at the second column of the ACB (Column H2) with the interlocking cross-section and the corresponding effective circular cross-section as described above. These results are provided for the bridge response under the three components of the ground motion #40 in Appendix A (RSN 1063 in PEER NGA database [37], Rinaldi receiving station, Northridge earthquake). Figure 2-3(a), (b), and (c) show comparisons of moment at the base,  $M_x$ , base shear force,  $F_y$ , and axial force,  $F_z$ , respectively, for column H2 of the ACB using OpenSees line model. Although the interlocking spiral and the circular cross-sections do not have the same response, the discrepancy is less than 20% when considering the maximum values. Therefore, using the effective circular cross-section instead of the interlocking spiral

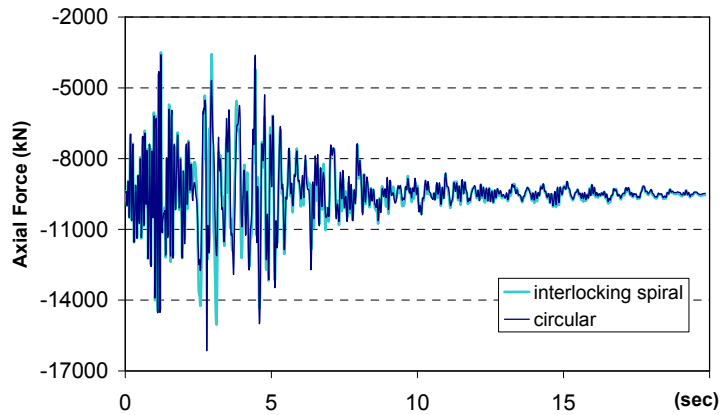
cross-section is an efficient option to reduce complexity of this study and the shaking table experiments.



(a) Moment,  $M_x$



(b) Shear force,  $F_y$



(c) Axial force,  $F_z$

**Figure 2-3: Responses of the Amador Creek Bridge at column H2 with interlocking spiral and effective circular cross-sections**

## 2.3 Parametric Study

Using a single column model with effective circular cross-section from the ACB, the following parametric study is conducted. Considered parameters are ground motion, number of components of ground motions, aspect ratio, and existence of mass moment of inertia.

### 2.3.1 Ground Motion Components

All 293 ground motions with PGA larger than 0.25g are considered in this parametric study. To study the effect of vertical motions, the responses with and without vertical ground motion are compared. In this comparison, three cases are utilized, which are stated below.

- X, Y, and Z components versus X and Y components (effect of vertical excitation when both horizontal components are present)
- X and Z components versus X component (effect of vertical excitation when one of the horizontal components only is present)
- Y and Z components versus Y component (effect of vertical excitation when the other horizontal component is present only)

### 2.3.2 Mass Moment of Inertia

To represent a bridge system which is idealized with free rotation at the connection between the column and the bridge superstructure, a model with no mass moment of inertia on top of the column is adopted. However, mass moment of inertia can be added on top of the column corresponding to the more realistic connection in the bridge system. Note that the value of the mass moment of inertia was calibrated to obtain the same period in the bridge transverse direction,  $T_T$ , for both the bridge system (with the bridge superstructure modeled) and the single column cases.

### 2.3.3 Aspect Ratio

As the aspect ratio (AR), i.e. height to diameter ratio, of a column, i.e.  $H/D$ , gets large, the column becomes less likely to experience shear failure. To study this important parameter, 6 aspect ratios of values 2.5, 3.0, 3.5, 4.0, 4.5, 5.0, were considered in the parametric study. Note that  $H$  is taken as the height of the column itself, which does not include the rigid end zone lengths due to the physical size of the added mass on top of the column as discussed in the following section or due to the footing size.

### 2.3.4 Computational Models

To represent the full-scale single column, the following models are used. Type 1 and Type 2 represent the cases without and with mass moment of inertia, respectively (Fig. 2.4). For both Types, the suggested equivalent circular cross-section is considered and the column is modeled using ‘beam with hinges’ (BWH) element in OpenSees. For Type 1, mass blocks are installed

below the column top to lower the center of mass to the pin location. Since the system can become unstable during shaking, a catching system needs to be utilized for safety purposes but it is not included in the analytical model. For Type 2, regular mass blocks are employed as shown in Figure 2-4. In addition, a third type, designated as Type 2-1 is utilized which is derived from Type 2 model by employing the mass blocks of the Type 1 model to lower the center of mass. Line representations of the three types are presented in Figure 2-5.

Mass was determined from the gravity load of the full-scale prototype bridge system and mass moment of inertia was determined to match the periods of the bridge system.. However, it is not possible to match the vertical period of the single column to that of the bridge system, mainly because of the lack of the additional flexibility introduced by the bridge superstructure in the single-column model. Instead, it is reasonable and practical to match the vertical response of the single column model to that of the corresponding column which is a part of the whole bridge system model. The horizontal and vertical periods of the two models Types 1 and 2 are shown in Table 2.4. The periods of Type 2 are larger than those of Type 1 which is due to the added mass moment of inertia and the difference in height. The differences between the periods of models Type 2-1 and Type 1 are smaller than the differences between the periods of models Type 2 and Type 1 since models Type 1 and Type 2-1 have the same heights.

Table 2.5 presents the vertical periods of the bridge system, which can be compared to those of Type 2 or Type 2-1 single column model listed in Table 2.4. Vertical periods of the bridge system can be as high as 8.5 times of those of the single column model. The difference is basically due to the effect of the flexibility of the superstructure in the bridge system, which is not considered in the single column model, as mentioned above. Note that the vertical periods do not significantly change due to the properties of the springs at the column base, representing flexible foundation. Since the vertical response is expected to have an influence on the shear strength and is closely related to the vertical period, these differences cannot be neglected.

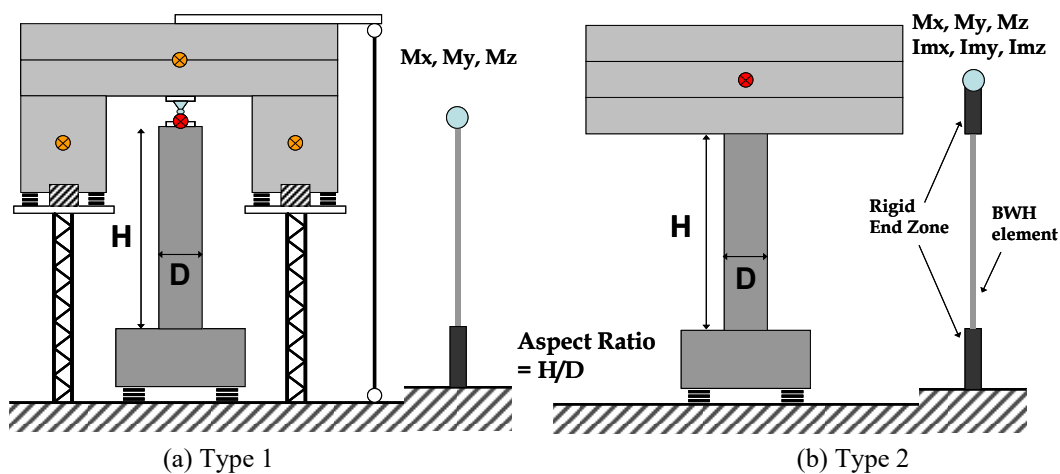


Figure 2-4: Models for the parametric study

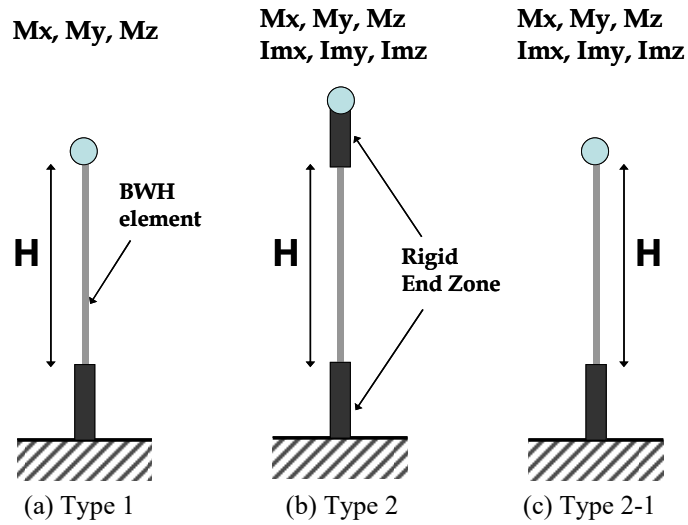


Figure 2-5: Line representations of the considered models

Table 2-4: Modal properties of single column models

AR	Type 1		Type 2		Type 2-1	
	$T_h$ [sec]	$T_v$ [sec]	$T_h$ [sec]	$T_v$ [sec]	$T_h$ [sec]	$T_v$ [sec]
2.5	0.320	0.046	0.469	0.054	0.372	0.046
3.0	0.429	0.051	0.584	0.058	0.475	0.051
3.5	0.549	0.055	0.716	0.062	0.597	0.055
4.0	0.687	0.059	0.860	0.066	0.731	0.059
4.5	0.835	0.063	1.014	0.069	0.876	0.063
5.0	0.993	0.067	1.179	0.073	1.032	0.067

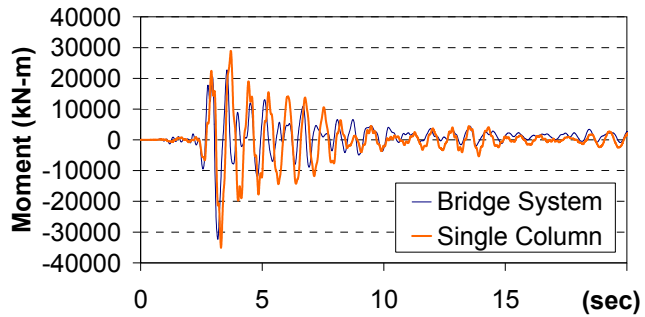
Table 2-5: Vertical periods of bridge system model with effective circular cross-section

AR	$T_v$ [sec]	
	Fixed	With springs at the base
2.5	0.385	0.392
3.0	0.386	0.393
3.5	0.389	0.395
4.0	0.392	0.397
4.5	0.395	0.400
5.0	0.397	0.402

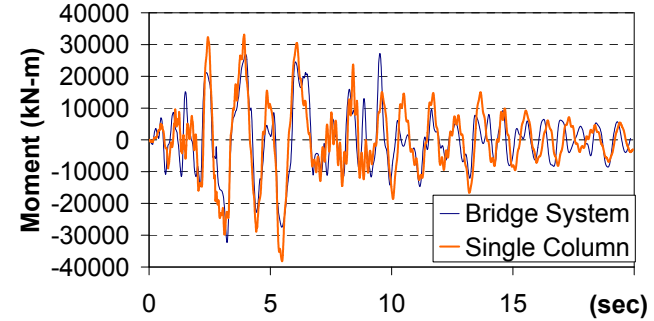
### 2.3.5 Comparison of Responses of Bridge System vs. Single Column Models

Ideally, responses of the single column model are preferred to be identical to those of the bridge system, but for practical purposes, differences within  $\pm 20\%$  are considered to be acceptable. Fig.2.6 presents the bending moment and axial force of the single column model, specifically Type 2 with AR = 4.0, and those of the corresponding system model using all three components of ground motions #60 (Whittier Narrows earthquake record at LA Obregon Park) and #7 (Northridge earthquake record at Rinaldi Receiving Station) (refer to Appendix A for further details about these records). In case of ground motion #60, the bending moment history is similar in the two models and the amplitude of axial force is also similar, even though the frequency is quite different from each other, which is due to the fact that the vertical period of the bridge system is longer than that of the single column. However, ground motion #7 produces very different results. Although the bending moment history is similar in the two models for ground motion #7 as in the case of ground motion #60, the amplitude of the axial force of the bridge system is less than 40% of that of the single column. This means that in this case, the axial response of the single column which may be used in the shaking table tests cannot represent the real axial response of the bridge system. Since the axial force and accordingly the axial strain are considered as main parameters in estimating the shear strength, this situation can cause underestimation of the shear strength and as a result overestimation of the effect of the vertical component of the ground motion.

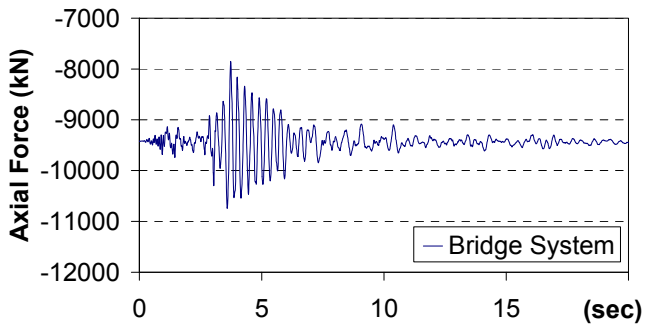
Due to the limitations of the shaking table, it is not possible to construct the complete bridge system. Even though the discrepancy is related to the properties of ground motion, demonstrated by comparing responses of ground motions #60 and #7 as discussed above, modifying input excitations may not be an effective way to resolve this discrepancy within the shaking table limitations. In that regard, the experimental effort on a single column model, even with this discrepancy in comparison with the bridge system model, can be viewed as a means to generate benchmark experimental data sets for developing and calibrating accurate analytical shear strength models for further use in computational modeling of the full bridge system. Finally, it is expected that the effect of the vertical excitation on the seismic response of the bridge system can be computationally assessed using these accurate analytical shear strength models of the RC bridge columns.



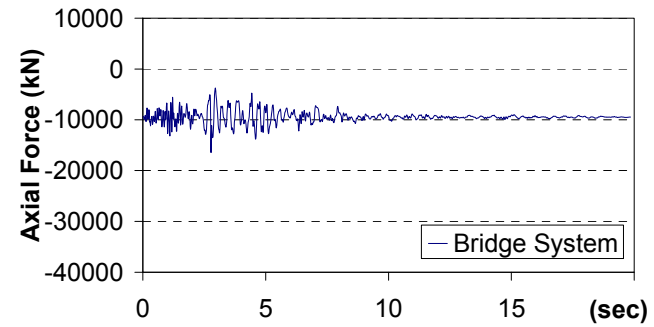
(a) Bending moments at the base due to #60 ground motion



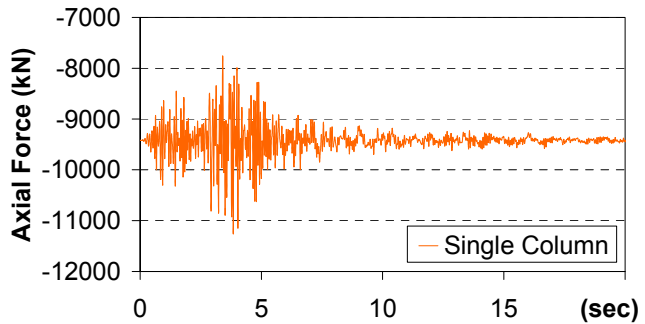
(b) Bending moments at the base due to #7 ground motion



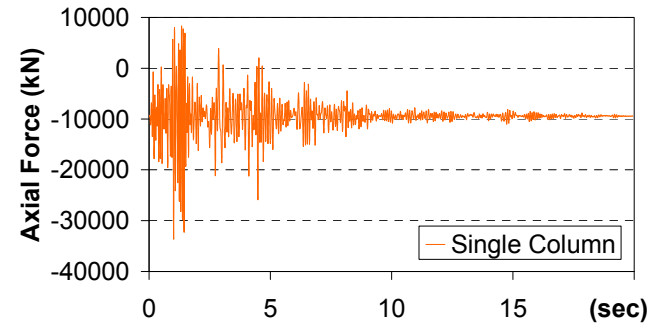
(c) Axial force in the bridge system due to #60 ground motion



(d) Axial force in the bridge system due to #7 ground motion



(e) Axial force in the single column due to #60 ground motion



(f) Axial force in the single column due to #7 ground motion

**Figure 2-6: Responses of the bridge system and the single column models**

## 2.4 Results of the Parametric Study

The main observations for the results discussed above can be summarized as follows:

- The presence of one or both of the horizontal components does not produce significant differences.
- Except for the axial displacement and force, the difference in other response quantities due to vertical excitation is not significant, less than 5%, in general.
- For both setups, Types 1 and 2, the effect of vertical excitation is significant on the axial force demands with a potential to affect their shear strength.
- The difference in axial displacement and axial force of Type 1 and Type 2 is relatively small. For other response parameters, the difference between Type 1 and Type 2 cannot be ignored and becomes larger as the column has a smaller aspect ratio. However, since the axial force is the only important (from the point of view of the present study) parameter that is significantly affected from the vertical excitation, it can be concluded that the differences between Types 1 and 2 are not important for the purposes of this study. These differences are even less important between Types 1 and 2-1.

## 2.5 Investigation of the Effect of Axial Force on Shear Capacity

### 2.5.1 Comparison of Shear Demand and Capacity

In Section 2.4, the change of demand due to vertical excitation is discussed using three different modeling types, several aspect ratios, and various ground motions. It is observed that axial force is the only force parameter that is affected by the presence of vertical excitation. In this section, effect of axial force on the shear strength is investigated in greater detail using different shear strength equations presented in Chapter 1. Moreover, the shear demand is compared with the shear capacity.

Figure 2-7 presents comparison of the shear strength calculated using equations given in ACI (Section 1.2.1), CSA (Section 1.2.4), Eurocode (Section 1.2.5) and Caltrans SDC (Section 1.2.7) and the shear demand using ground motion #9 (Landers earthquake recorded at Lucerne station) (refer to Appendix A for further details about the record) with one of the horizontal components and with and without the vertical component (designated as 'xz' and 'x', respectively). It can be observed that ACI, CSA, Eurocode, and SDC do not provide consistent results in estimating the shear strength. Before the ground motion is applied (i.e. under the presence of only gravity loading), ACI offers the most conservative estimation, but once the dynamic excitation is included, the estimates change significantly for all the methods. In general, the prediction of CSA changes more dramatically than ACI, Eurocode, or SDC during dynamic excitation. Another observation is that the possibility of shear failure increases when vertical excitation is present. For example, including the Z-component produces shear strength which is much closer to the shear demand compared to the shear strength without the Z-component.

The maximum ratio of the shear demand and shear strength,  $Maxdcr$ , and the reduction of the shear strength due to the earthquake excitation,  $Red$ , are calculated using Eq. (2.3) and Eq. (2.4), respectively.

$$Maxdcr = \max\left(\frac{\text{shear demand at each time step}}{\text{shear strength at each time step}}\right) \quad (2.3)$$

$$Red = \frac{\min(\text{shear strength})}{\text{shear strength before excitation}} \quad (2.4)$$

$Maxdcr$  and  $Red$  using ACI are shown in Figure 2-8. All the aspect ratios are considered for the subset of 61 ground motions. Ground motion parameters are listed in Appendix A – *note that the ground motions are ordered from highest to lowest vertical PGA ( $PGA_v$ )*. Only the results of the case, ‘X+Y+Z and X+Y’ (effect of vertical excitation when both horizontal components are present) applied to Type 2 model, are shown. Almost all of the  $Maxdcr$  values are between 0.1 and 0.6 and as expected, small aspect ratios have large values of  $Maxdcr$ . Although  $Maxdcr$  values do not significantly change by adding the vertical earthquake component, there are differences in some of the ground motions. For example,  $Maxdcr$  for  $AR = 2.5$  increases from 0.564 to 0.617 under ground motion #3. Another observation is that  $Red$  values change significantly with relatively large vertical acceleration (ground motions #1 to approximately #20), as expected. Also,  $Maxdcr$  values decrease with reduction in the vertical PGA.

In Figure 2-9(a) and (b),  $Maxdcr$  values based on SDC without and with Z-component, respectively, are shown. In Figure 2-9(c) and (d),  $Red$  values based on SDC without and with Z-component, respectively, are shown. ACI and SDC provide similar  $Maxdcr$  and  $Red$  values with relatively small vertical acceleration (ground motions #20 or above). However, with the ground motions below #20, there is a great disparity between  $Maxdcr$  and  $Red$  of SDC and those of ACI.

In the case of using SDC, there are several ground motions which have significant reduction caused by lateral displacement ductility even without Z-component. It is important to note that there are more than 20 ground motions causing the same  $Red$  around 0.53 with Z-component included. Since the shear strength contribution of concrete,  $V_c$ , from SDC is zero under tension, only the shear strength of transverse reinforcement remains. It should be noted that  $V_c$  is zero using SDC, regardless of how large the tension is. That is why for all the ground motions that result in tension,  $red$  becomes equal to  $V_c$  divided by the sum of  $V_c$  and  $V_s$ , which is equal to 0.53. Zeroing the concrete contribution to shear strength under tension in SDC makes a significant difference between ACI and SDC estimates.  $Maxdcr$  and the minimum of shear strength may not occur simultaneously in case of ACI estimates. Therefore,  $Maxdcr$  using ACI may not increase significantly even if there is noticeable reduction in  $Red$  using ACI. On the contrary,  $Red$  using SDC may occur several times during the excitation and in general  $Maxdcr$  may occur during one of these times. Consequently,  $Maxdcr$  based on SDC equations increases significantly with the inclusion of the Z-component.

Though not shown for all codes, it was observed that *Red* decreases when the vertical component is included. This means that the capacity decreases with the inclusion of the vertical excitation. This is expected because ACI, SDC, and Eurocode have an axial force term and CSA has an axial strain term. With vertical excitation, both demand and capacity fluctuate significantly. Due to the discrepancy of the variation of the axial force of the cross-section and that of the axial strain at the centroid (which is affected not only by the cross-section axial force but also by the cross-section bending moment), the shear strength estimate by CSA is quite different from those by ACI, SDC, and Eurocode.

Finally Figure 2-10 presents *Maxdcr* and *Red* for the whole set of 293 ground motions whose horizontal PGA's are larger than 0.25g. Based on the simulations it was observed that ground motions #1, #2, #3, #4, #7, and #10 (see Appendix A for details) have significant decrease in *Red* with the inclusions of the vertical (Z) excitation.

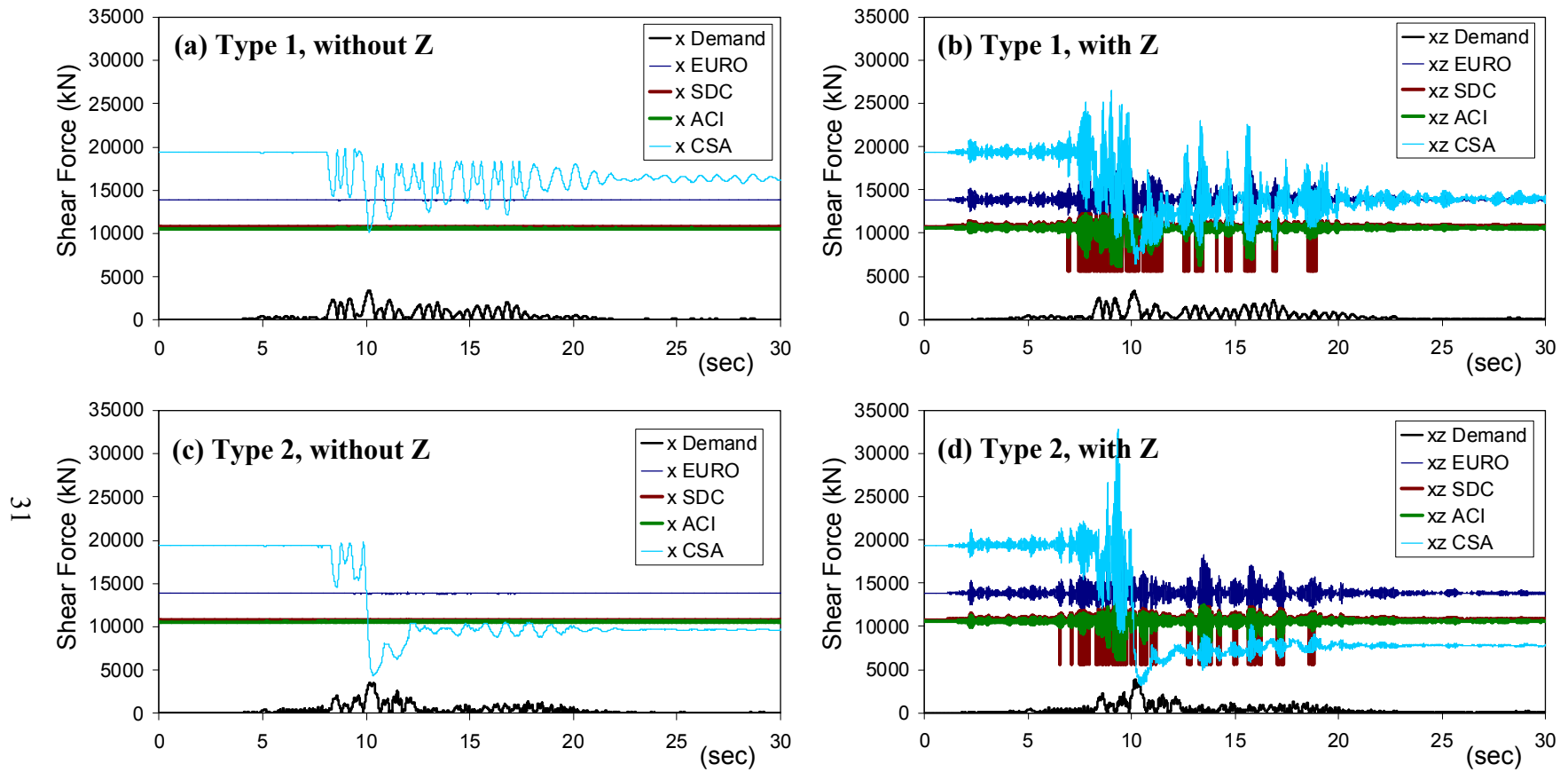


Figure 2-7: Shear demand and capacity with ground motion #9

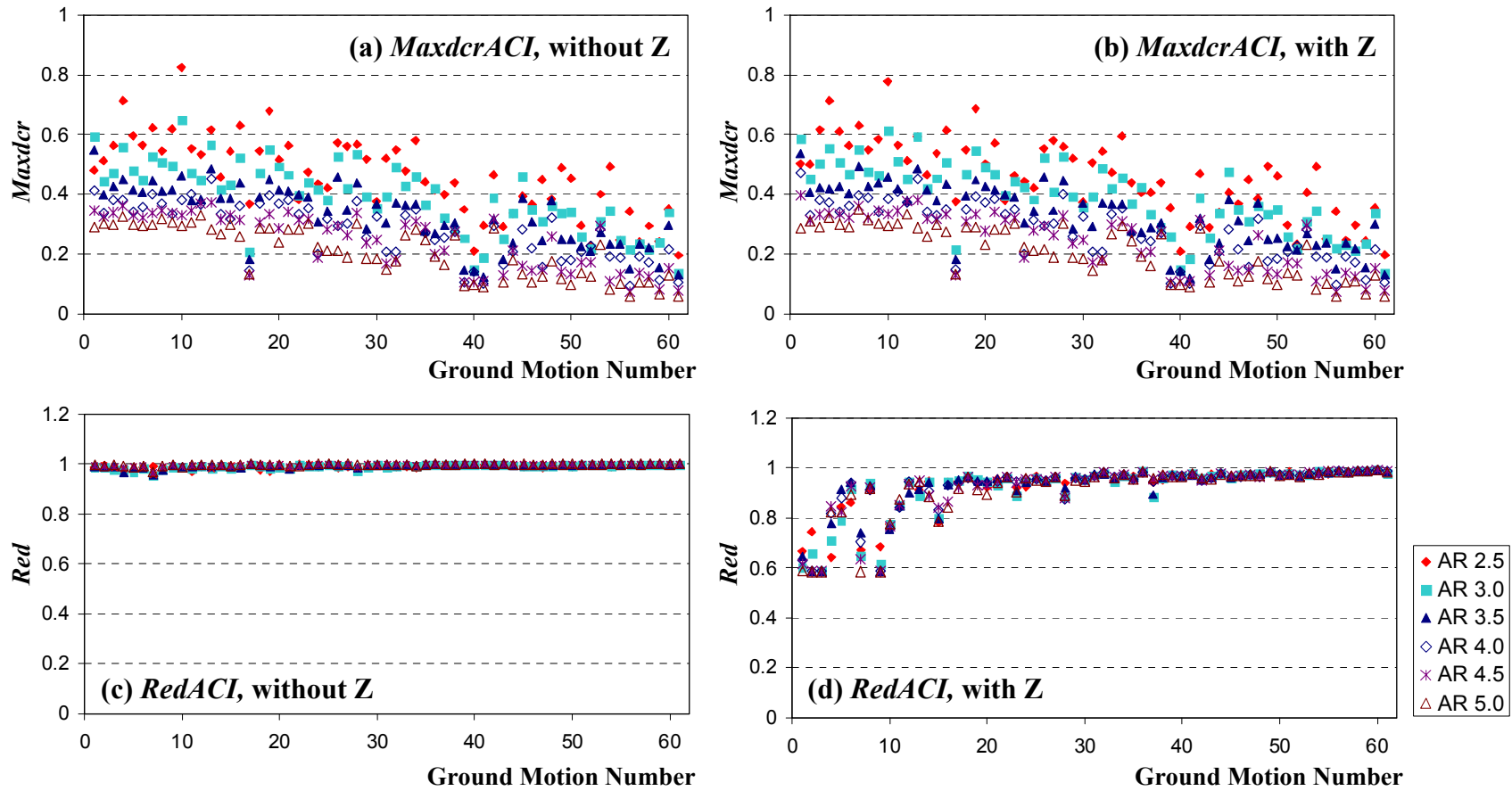


Figure 2-8: Demand to capacity ratio ( $Maxdcr$ ) and reduction in shear strength ( $Red$ ) considering ACI equation for Type 2 and the selected 61 ground motions

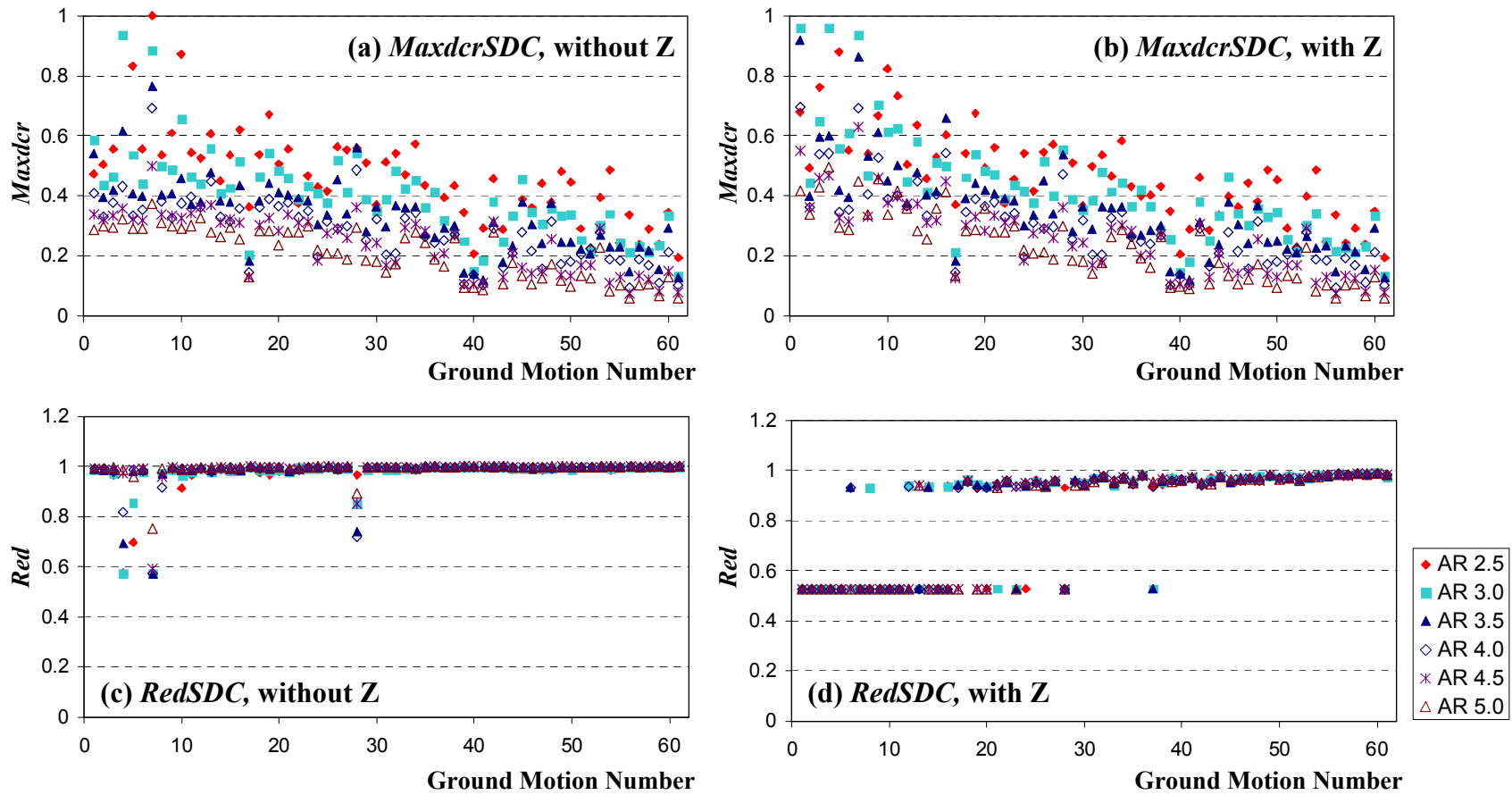


Figure 2-9: Demand to capacity ratio (*Maxdcr*) and reduction in shear strength (*Red*) considering SDC equation for Type 2 and the selected 61 ground motions

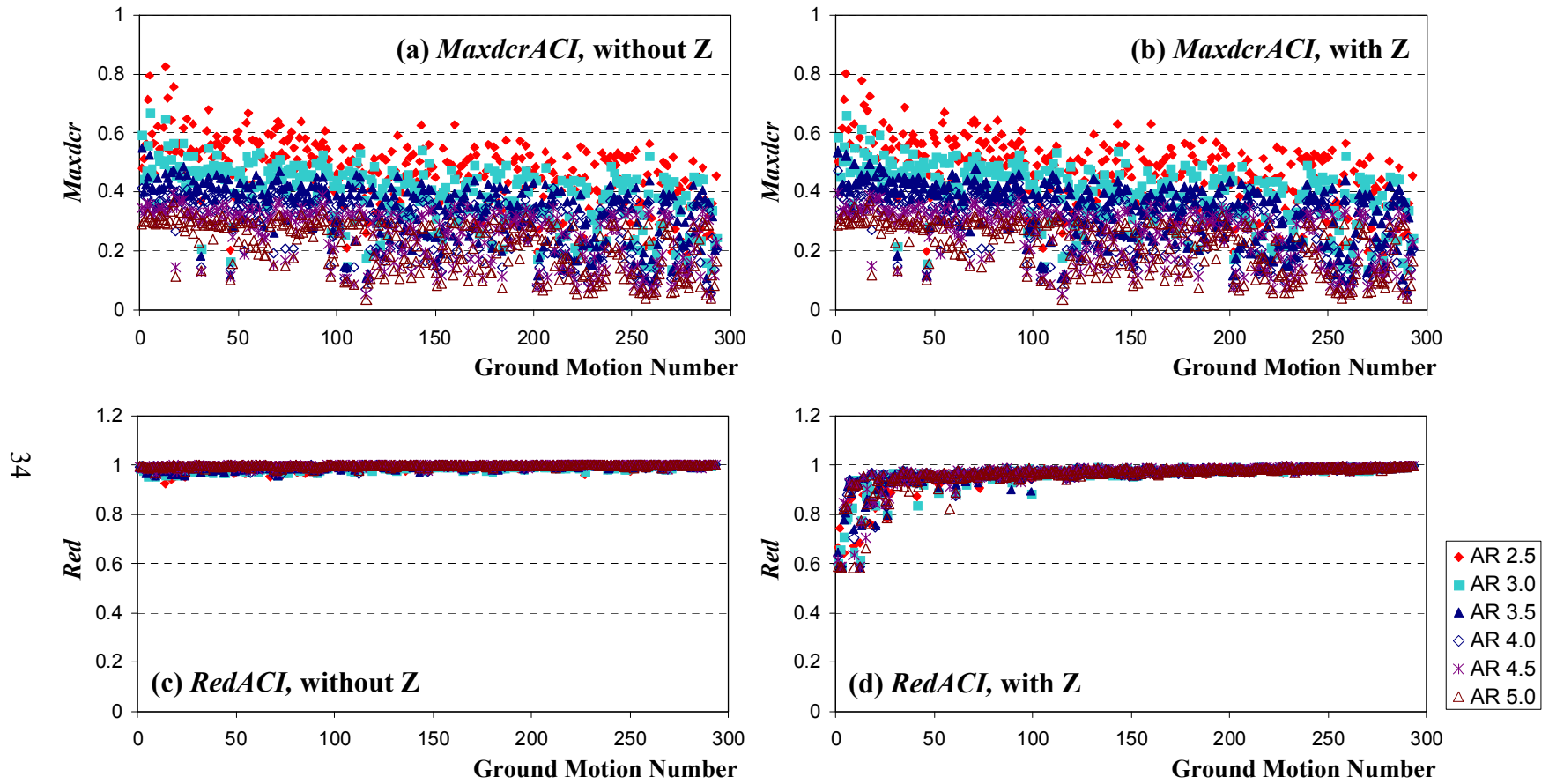


Figure 2-10: Demand to capacity ratio (*Maxdcr*) and reduction in shear strength (*Red*) considering ACI equation for Type 2 and the 293 ground motions with  $PGA_h > 0.25g$

## 2.5.2 Observations

Based on the results and discussions above, the following observations emerge from the parametric study (Note that X and Y refer to the two orthogonal lateral directions and Z refers to the vertical or axial direction of the column):

- Shear strength demand to capacity ratio ( $Maxdcr$ ) values vary, on average, for the different codes as follows: Eurocode < ACI  $\leq$  SDC < CSA.
- For shear strength reduction ( $Red$ ) values, the variation, on average, for different codes is CSA < SDC < ACI  $\approx$  Eurocode.
- A smaller aspect ratio tends to have a larger  $Maxdcr$  and a larger aspect ratio tends to produce less reduction in shear strength.
- The pattern of reduction factors of ACI, SDC, and Eurocode depends moderately on the vertical excitation. The ground motions which make noticeable changes are #1, #2, #3, #4, #7, and #10 (descending order of  $PGA_v$ ) in Appendix A. SDC has a unique pattern because its  $V_c$  is zero, under tension regardless of the value of the tension.
- The reduction factors of CSA do not depend on the vertical excitation as much as ACI, SDC and Eurocode. Their reduction pattern does not change significantly, with or without the vertical component.
- ACI, SDC, and Eurocode explicitly consider the axial force. Therefore, in the case without vertical excitation, their capacity predictions do not differ from ground motion to ground motion or from aspect ratio to aspect ratio, compared to those from CSA.
- CSA takes the effect of axial force into consideration by using axial strain at the centroid of the section, which results in differences in the shear capacity predictions for different ground motions and different aspect ratios in the case without vertical excitation, since the axial strain at the centroid of the section is not only affected by the axial force but also by the bending moment.

## 2.6 Summary

Among 3,551 earthquake acceleration records in the PEER NGA database, 61 ground motions are selected as input candidates based on three criteria. The 1<sup>st</sup> is the horizontal peak ground acceleration where at least one of the horizontal components should have the peak ground acceleration larger than 0.25g. The 2<sup>nd</sup> criterion is based on the ratio of the pseudo-spectral acceleration corresponding to the vertical component ( $PSa_v$ ) to those corresponding to the horizontal components ( $PSa_{h1}$ ,  $PSa_{h2}$ ) where for the 20 pairs of periods  $T_h-T_v$  ( $T_v=0.05, 0.1, 0.15,$  and  $0.2$  seconds and  $T_h=0.4, 0.5, 0.6, 0.7,$  and  $0.8$  seconds),  $PSa_v/PSa_{h1}$  or  $PSa_v/PSa_{h2}$  were calculated. The 3<sup>rd</sup> criterion is the arrival time interval between horizontal and vertical peak accelerations which affects the interaction of the horizontal and the vertical responses. The cut-off interval was selected to be 1 sec. Finally, after removing motions with only low frequency content, 61 ground motions are selected.

A parametric study was conducted to identify the most influential ground motions on the columns with the modified effective circular section of Prototype 1 (Amador Creek Bridge) from the perspective of the effect of vertical excitation. The following parameters were varied: ground motion, number of components, existence of mass moment of inertia, and aspect ratio. The following remarks can be made from the findings of the parametric study. First, the presence of two or one of the horizontal components does not produce significant differences. Second, vertical excitations had an effect primarily on axial deformation and axial force demands in the column. Next, the difference in axial deformation and axial force estimates between Model Types 1 and 2 is relatively small. For other response parameters, the discrepancy between Types 1 and 2 cannot be ignored and becomes larger as the aspect ratio decreases. However, since the axial force is the only parameter that is significant from the perspective of vertical excitations (the focus of this study), it can be concluded that the differences between Types 1 and 2 (especially Type 2-1) may not be important for the purpose of this study.

The effect of axial force on the shear strength is investigated using different shear strength code approaches (ACI, SDC, Eurocode and Canadian Code). The maximum shear demand to shear capacity as well as the maximum reduction in shear capacity due to axial force fluctuations is calculated. Pertinent observations are noted in the previous section.

Finally, as a result of the findings reported in this chapter a final subset of 10 ground motions are identified as candidate ground motions for use in the proposed study to investigate the adverse effects of vertical ground motions on bridge columns. These are identified in Table 2.6.

**Table 2-6: Selected ground motions for the experimental study**

GM	RSN	EQ Name	YYMMDD	Station	PGA [g] (unfiltered)	
					X	Z
1	126	Gazli, USSR	760517	Karakyr	0.61	1.26
2	495	Nahanni, Canada	851223	Site 1	0.98	2.09
3	752	Loma Prieta	891018	Capitola	0.53	0.54
4	825	Cape Mendocino	920425	Cape Mendocino	1.50	0.75
5	879	Landers	920628	Lucerne	0.73	0.82
6	982	Northridge-01	940117	Jensen Filter Plant	0.57	0.82
7	1051	Northridge-01	940117	Pacoima Dam (upper left)	1.58	1.23
8	1054	Northridge-01	940117	Pardee-SCE	0.66	0.38
9	1063	Northridge-01	940117	Rinaldi Receiving Station	0.83	0.83
10	1085	Northridge-01	940117	Sylmar-Converter Sta. East	0.83	0.38

The above candidate motions will next be assessed for their suitability to be reproduced on the UC-Berkeley shaking table particularly with respect to the frequency content in the desired range for both horizontal and vertical accelerations.

# 3 Design of Shaking Table Tests

## 3.1 Introduction

Dynamic testing is the most ideal method to replicate earthquake input motions. Due to limitation of facilities, only a few shaking table tests have been conducted to examine the effect of vertical acceleration on bridge columns, up to this date. To perform tests on the UC-Berkeley shaking table at the Richmond Field Station (RFS), quarter-scale bridge column specimens, necessary instrumentation and input loading sequence were prepared to investigate the response of a bridge column subjected to the horizontal and vertical dynamic excitations.

## 3.2 Description of the Shaking Table

The UC Berkeley shaking table, operated by the Pacific Earthquake Engineering Research (PEER) Center, is now the largest 6 DOFs table in the United States. The shaking table is stiffened by heavy transverse ribs and the eight horizontal hydraulic actuators (four in each direction) are attached to the ribs. The four vertical actuators are attached to the table by post tensioning rods at points located  $1.5 \text{ ft} \times 1.5 \text{ ft}$  ( $305 \text{ mm} \times 305 \text{ mm}$ ) from each corner. All 12 actuators are 75 kips (334 kN) capacity hydraulic actuators and connected to 1580 kips (7028 kN) reaction block. As a result, about 3g can be achieved with the empty table which weighs about 100 kips (445 kN). Decoupling of components is accomplished by the length of the actuators and the control system. A unique feature of the UC-Berkeley shaking table is that a 1.5 psi air pressure supports the total weight of the table and specimen while the table is in operation. This feature allows the hydraulic actuators to operate more efficiently during dynamic loading. Table 3-1 summarizes the characteristics of the UC-Berkeley shaking table. Fidelity tests, as discussed in the next section, were performed before the actual RC bridge column tests to confirm the performance of the shaking table.

## 3.3 Selection of Input Motion: Fidelity Tests

In the presence of a vertical excitation, the shaking table is governed by its own frequency and it is not possible to reproduce all frequencies of the input motion exactly. Therefore, some motions may not be possible to be reproduced. Performing fidelity tests is the considered approach to select suitable motions for the intended dynamic tests. On March 19, 29, and April 2, 2010, a total of 30 trials were conducted to check the table performance and feasibility of 4 different ground motions from the PEER NGA database [37]. These ground motions were selected from the motions discussed in Section 2.1.

**Table 3-1: Properties of superstructure and springs used to model the soil-foundation system for the Amador Creek Bridge**

Property	Value
Table dimensions	20 ft × 20 ft (6.1 m × 6.1 m)
Table weight	About 100 kips (445 kN)
Components of motion	6 DOFs
Displacement limits	horizontal limits are ±5 in (±127 mm) vertical limit is ±2 in (±50.8 mm)
Velocity limits	30 in/s (0.76 m/s) in all axes with an unloaded table
Acceleration limits	About 3g in all axes with an unloaded table

### 3.3.1 Fidelity Test Setup

To verify the shaking table performance, it is important to have the fidelity test setup similar to the intended dynamic test specimen. Even though it is practically not feasible to achieve the horizontal and vertical periods comparable to those of the real specimen, the over-turning moment due to the height of the center of gravity (C.G.) which is one of the main factors that affect the table performance under vertical and horizontal excitation inputs can be controlled by stacking mass blocks and supporting steel beams. The geometrical scale of the setup corresponds to the 1/4-scaled prototype. The total weight is 118 kips (525 kN) and the C.G. is 9 ft (2.74 m) above the table (Figure 3-1 and Figure 3-2). Locations of the instruments placed on the shaking table and the mass blocks are shown in Figure 3-3. Since the specimen is a 1/4-scale specimen (length scale =  $S_L = \text{prototype length}/\text{model length} = 4$ ), each ground motion is compressed in time using a factor of  $\sqrt{S_L} = 2$ .

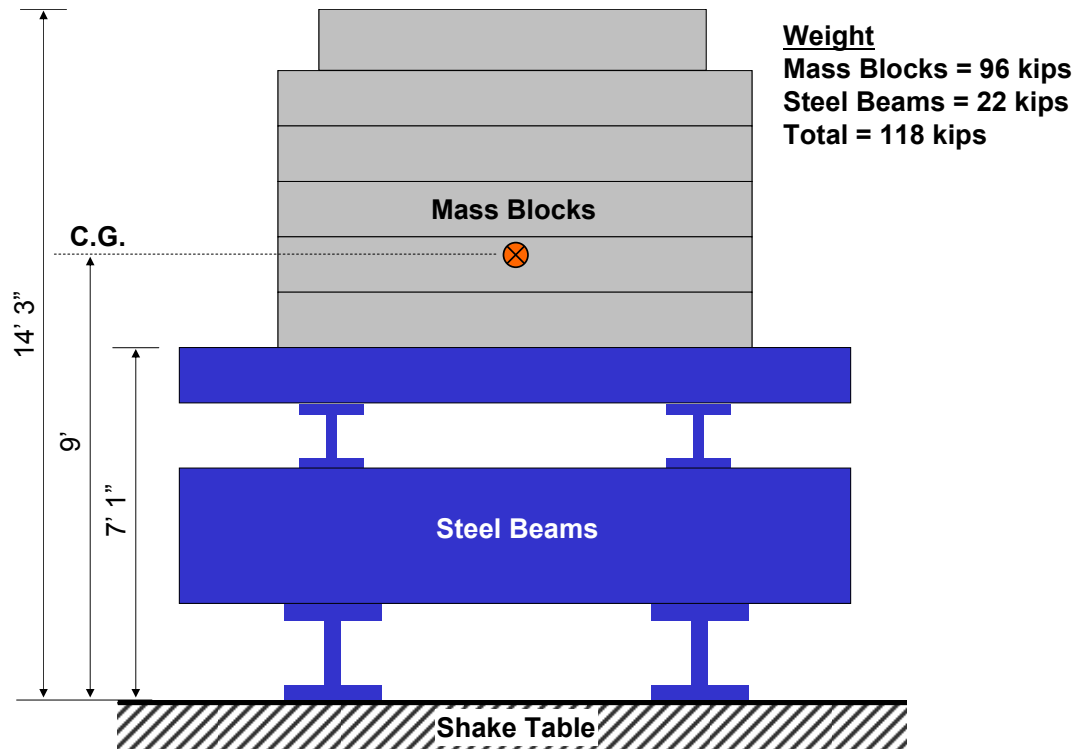


Figure 3-1: Schematic of the fidelity test setup



Figure 3-2: Photograph of the fidelity test setup

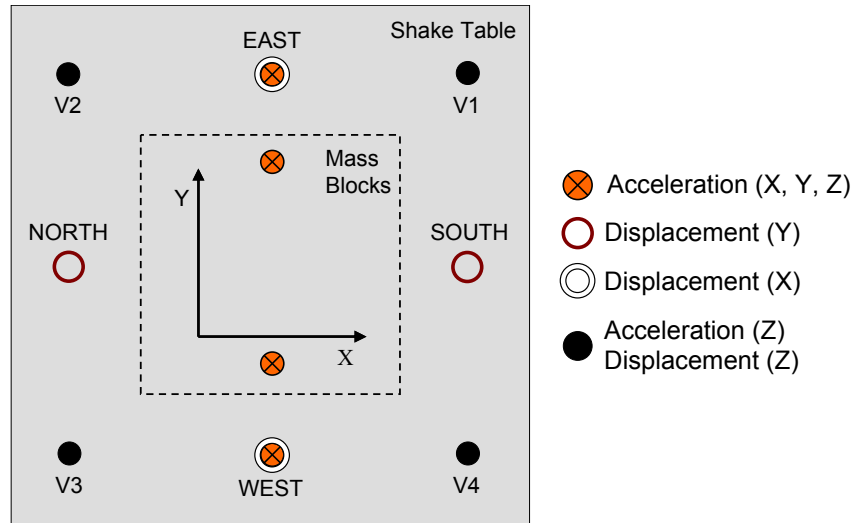


Figure 3-3: Shaking table plan, axes, and instrumentation for the fidelity tests

### 3.3.2 Input Ground Motion Candidates and Scale Factors

The selected ground motions for possible consideration in the shaking table tests were listed in Table 2.6 based primarily on the analysis using a full-scale single-column model with the aspect ratio of 3.5 (refer to Chapter 2). Additional considerations in the ground motion selection process have also been described in Chapter 2. Since the performance of the shaking table needs to be verified for the entire intensity level range which will be applied in the dynamic tests, magnitude scales for different intensity levels should be determined. These scales are calculated as follows based on the analyses results from the parametric study in Chapter 2:

1. Nonlinear time history analyses of the full-scale single-column are conducted using the full scale ground motions with the larger of the two horizontal components (referred to as X component) and the vertical (Z) component. The force reduction factor ( $R$ ) is calculated from the obtained ductility values,  $\mu$ , based on the equal energy assumption by Newmark and Hall [32], i.e.  $R = \sqrt{2\mu - 1}$ . The scale factor for ‘Yield Level’ is subsequently calculated as  $1/R$ .
2. Since significant strain hardening is expected, the maximum considered earthquake (MCE) level is assumed to correspond to ductility=2, hence the force reduction factor corresponding to MCE level ( $R_{MCE}$ ) is calculated as  $\sqrt{2 \times 2 - 1} = 1.73$ .
3. The scale factor for MCE is calculated as  $R_{MCE}$  multiplied by the scale of the yield level which is equal to  $1.73/R$ .
4. For simplicity and to preserve the basis of the selection criteria mentioned in Section 2.1, the scale factors determined for the horizontal components using the above procedure are utilized for the vertical components as well.

The scales determined using the assumption of ductility=2 (as mentioned in item 2 above) was sufficient to evaluate the table performance, since the scales determined in this manner resulted in accelerations close to the table limits.

After further elimination based on the demand and capacity histories, GM 1, 5, 7, and 9 (Table 2.6) were utilized in the fidelity tests with the determined scales (in terms of the target PGA after filtering, as mentioned below) listed in Table 3-2. As mentioned before, all ground motions are compressed in time using a factor of 2. The ground motions are filtered using a filter range of 0.6~30 Hz for the X components and 2~60 Hz for Z components to accommodate the displacement limits of the shaking table.

**Table 3-2: Properties of the finally selected four ground motions for the fidelity tests**

GM	RSN	EQ Name	Station	Target PGA [g] (filtered)			
				Yield Level		MCE Level	
				X	Z	X	Z
1	126	Gazli, USSR	Karakyr	0.48	0.96	0.83	1.66
5	879	Landers	Lucerne	0.41	0.64	0.71	1.11
7	1051	Northridge-01	Pacoima Dam (upper left)	0.98	0.78	1.70	1.35
9	1063	Northridge-01	Rinaldi Receiving Station	0.25	0.26	0.44	0.44

### 3.3.3 Fidelity Test Results

Typical results of the fidelity tests for 2 ground motions (GM1 and GM7) are shown in Figures 3.4 – 3.8. Among the four ground motions evaluated, GM7 seems to be the most suitable input given the shaking table performance. In these figures, the expected natural period range of the test specimens and its elongation due to damage is identified in terms of the important frequency range (in this study) using double headed horizontal arrows. In addition, the legend “f-measured” in these figures stands for the filtered measured data. As discussed, the shaking table does not reproduce frequencies over the entire range in the vertical direction. For example, for each ground motion, the response spectrum of the measured vertical acceleration has a sharp peak at 5~15 Hz and a valley at 15~30 Hz and another peak around 45 Hz. Therefore, ground motions with spectra like GM1 (Figure 3-4 and Figure 3-5) is not suitable to be replicated on the UC-Berkeley shaking table. In most cases, the measured horizontal acceleration spectra are much more similar to the target spectra, compared to the case of the vertical spectra.

Results of GM7 0.5-yield, yield, and MCE levels are shown in Figure 3-6, Figure 3-7 and Figure 3-8, respectively. The corresponding scale factors are 0.33, 0.66, and 1.14 compared to the originally recorded motion. In the important frequency range defined by the horizontal double headed arrow, the shaking table has an acceptable performance in matching the target spectra for yield and MCE levels of GM7 for both of the horizontal and vertical components. The basic information on GM7 is in PEER NGA database [37] and Appendix A shows the record and station information. The Northridge earthquake occurred on January 17, 1994 in the city of Los Angeles, California. The epicenter was in Reseda and the hypocenter latitude and longitude were 34.2057 and -118.554, respectively.

One cannot state that the GM7 obtained from the PEER NGA database [37] has higher frequency content compared to the other ground motions, i.e. GM1, GM5, or GM9. In particular, the frequency content of the vertical component of GM7 mostly leans towards lower frequency range compared to the other three ground motions.

**Table 3-3: GM7 Information**

Earthquake	Northridge-01 19940117 12:31
Moment magnitude	6.69
Seismic moment	1.2162+E26 dyne-cm
Mechanism	Reverse Fault Rupture
Hypocenter depth	17.5 km
Fault rupture length/width	18.0 km / 24.0 km
Average fault displacement	78.6 cm
Fault name	Northridge Blind Thrust
Slip rate	1.5 mm/yr
Station	CDMG 24207 Pacoima Dam (upper left abutment)
Instrument housing	Earth dam (abutment)
Mapped local geology	Granitic
Geotechnical subsurface characteristics	Rock
Preferred Vs30	2016.10 m/s
Epicentral distance	20.36 km
Hypocentral distance	26.85 km
Joyner-Boore distance	4.92 km
Campbell R distance	7.01 km
RMS distance	18.60 km
Closest distance	7.01 km

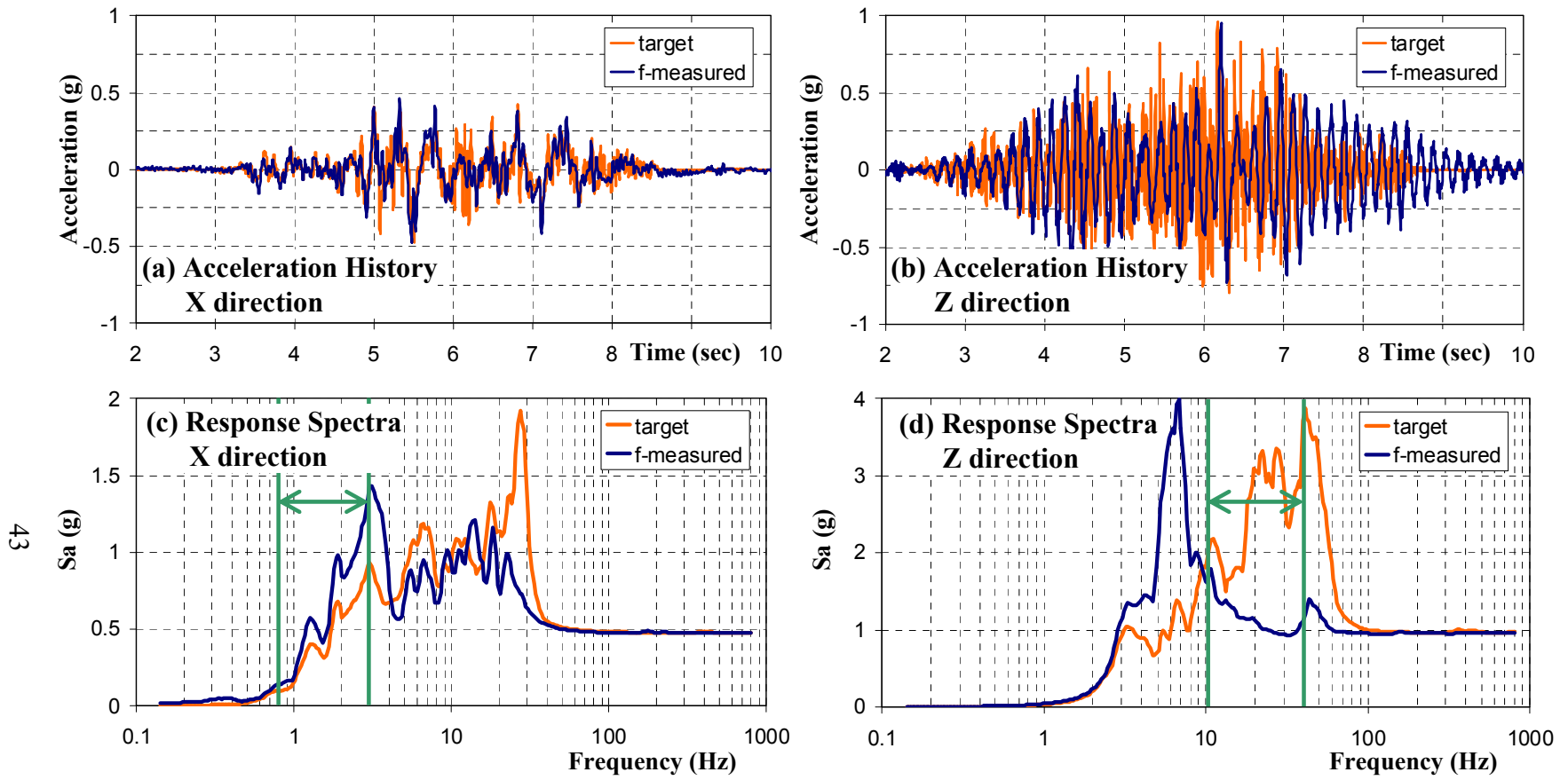


Figure 3-4: GM1 yield level

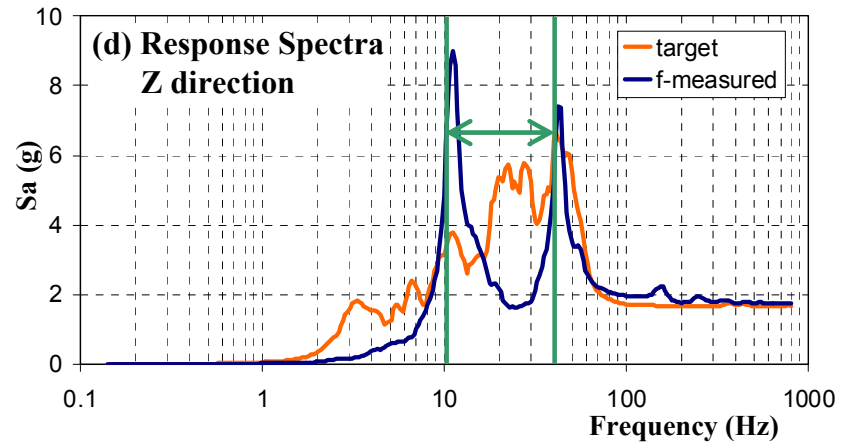
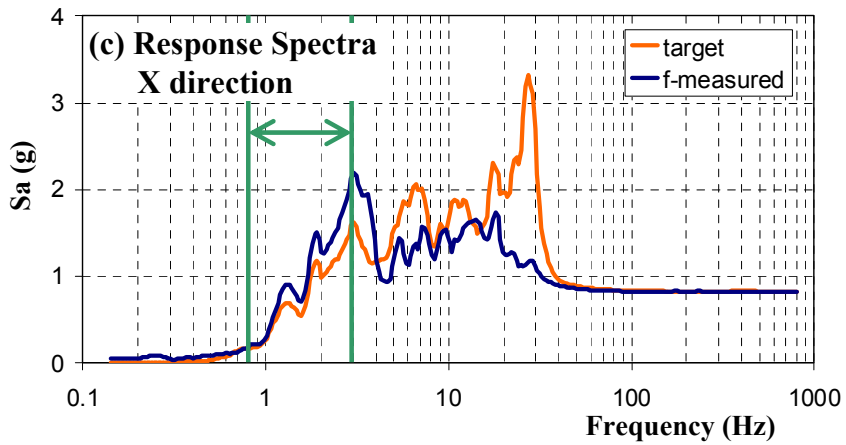
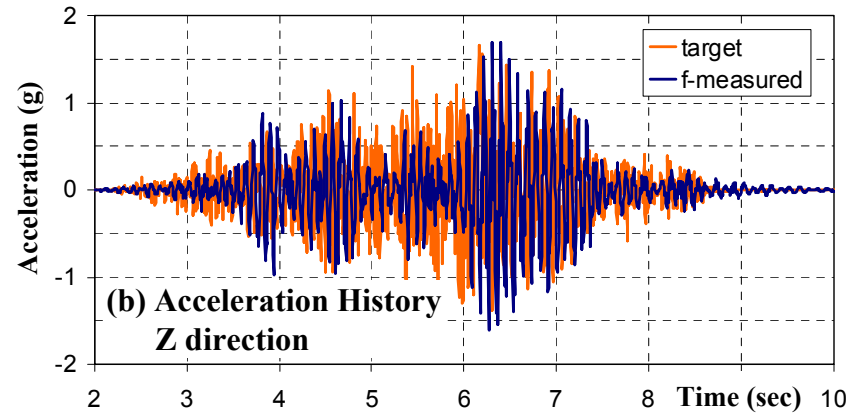
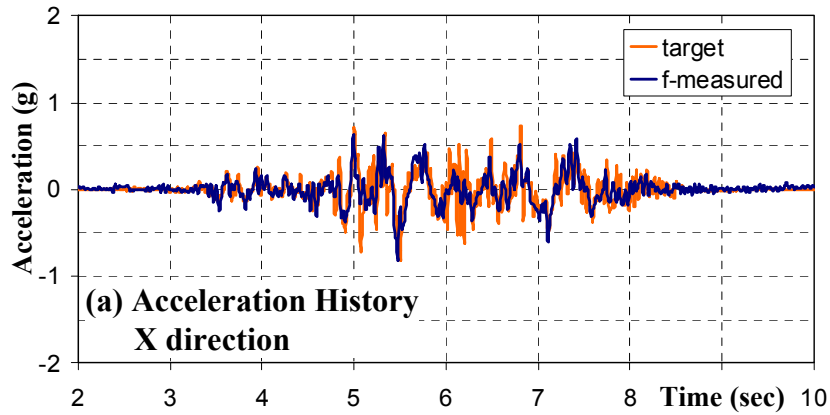


Figure 3-5: GM1 MCE level

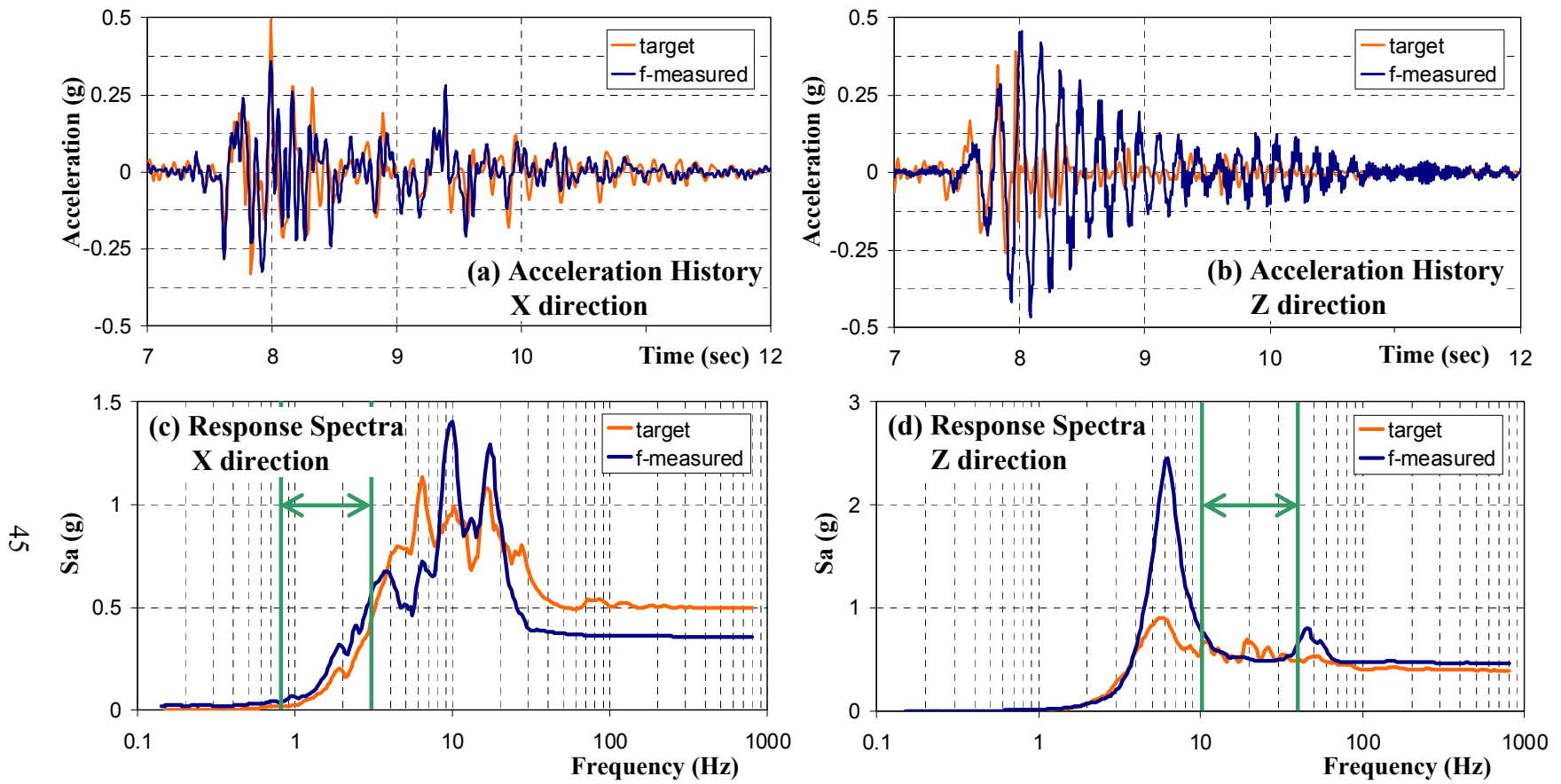


Figure 3-6: GM7 0.5-yield level

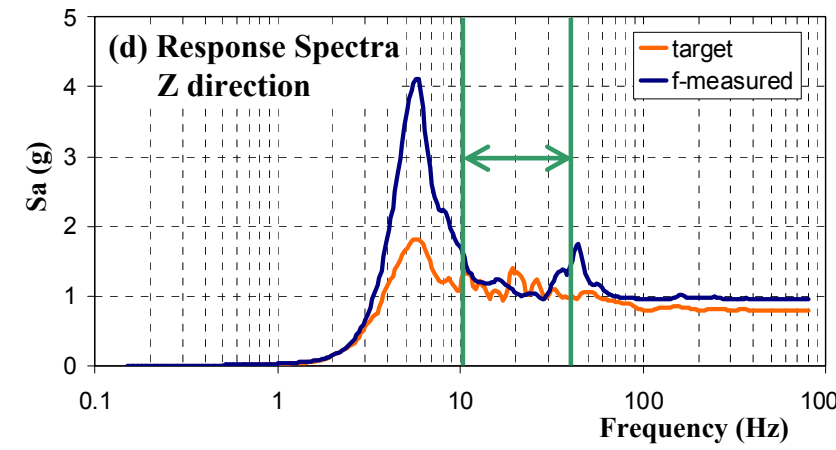
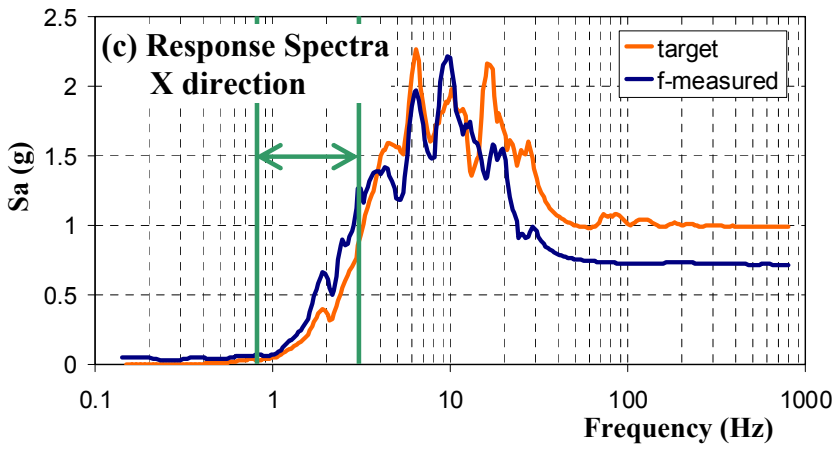
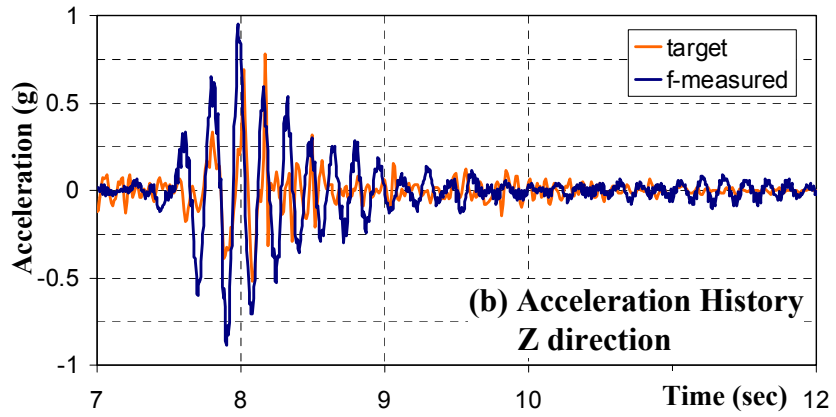
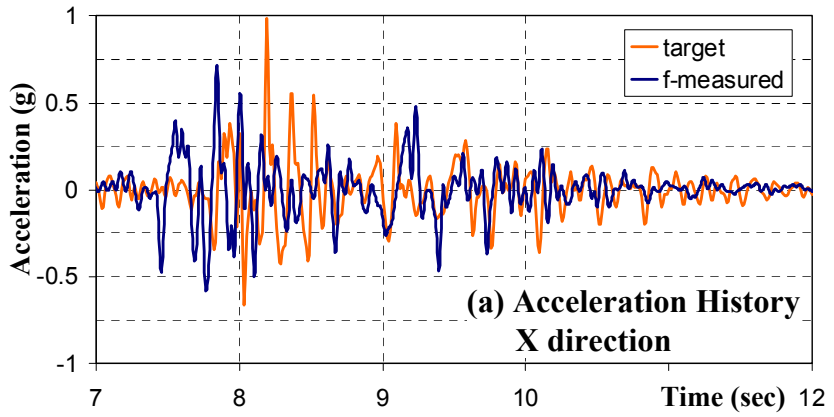


Figure 3-7: GM7 yield level

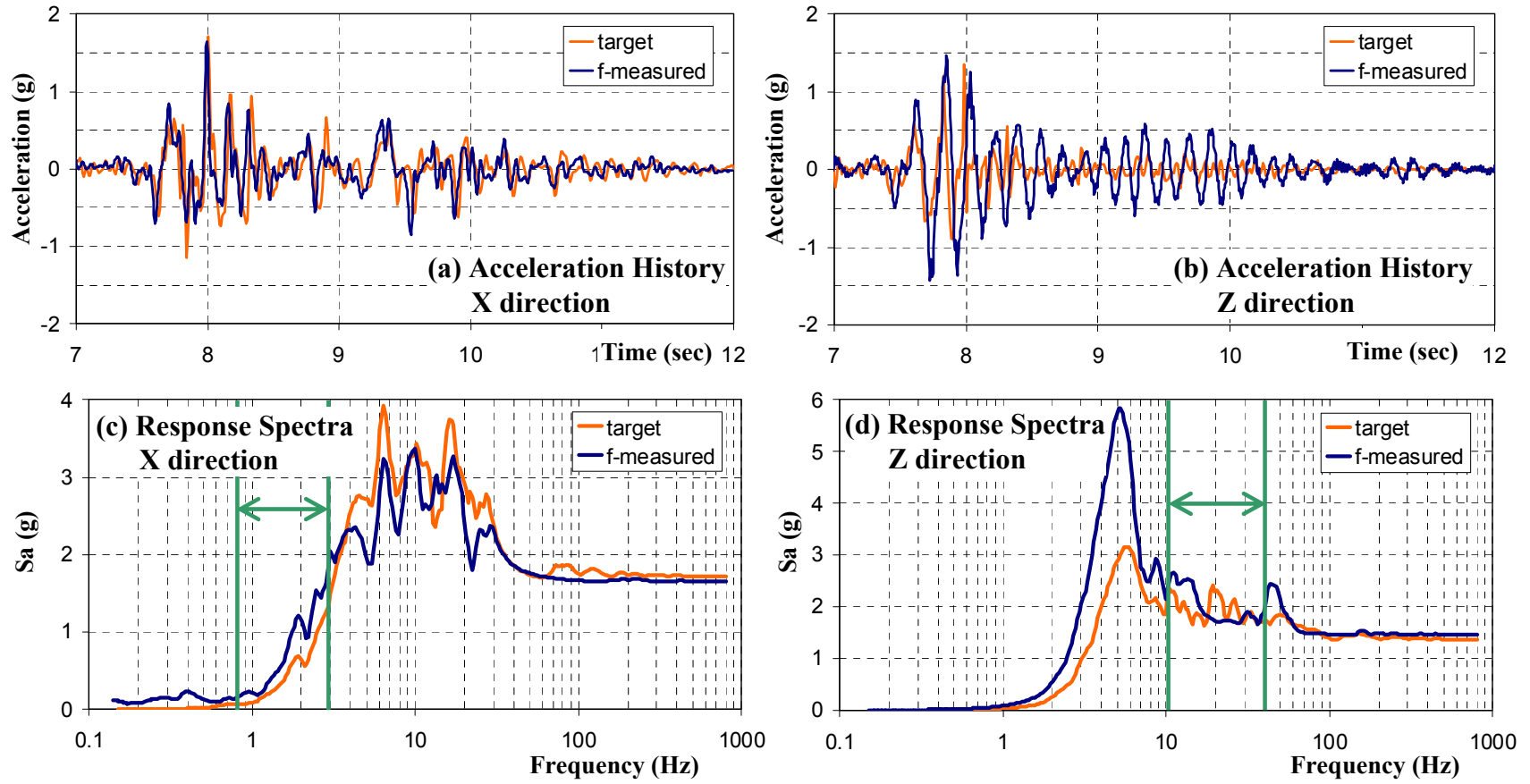


Figure 3-8: GM7 MCE level

### 3.3.4 Further Discussion about GM7

After the completion of the fidelity tests, MCE level is determined to be the highest intensity level that can be applied with acceptable shaking table performance. This determination is based on the following calculations. The capacity of a vertical actuator is given as 77 kips (342.5 kN). There are 4 vertical actuators and they should resist (a) the vertical force due to vertical acceleration applied on the shaking table and test setup and (b) that due to horizontal acceleration of the test setup, ignoring the damping force for simplicity. Considering the shaking table weight is about 100 kips (445 kN), it is reasonable to accept that the acceleration limit of the empty shaking table (i.e. without any test specimen) is about 3g (precisely,  $77 \times 4 / 100 = 3.08g$ ). The total fidelity test setup and shaking table weight is 218 kips (970 kN). Therefore, the maximum achievable vertical acceleration is  $77 \times 4 / 218 = 1.41g$ . Hence, for good performance of the shaking table in this study, MCE of GM7 for the specified mass and C.G. height of the test specimen is considered as the maximum excitation level that can be applied.

The fidelity tests revealed the following:

- The performance of the UC-Berkeley shaking table is acceptable with the proposed mass and C.G. height of the 1/4-scale test specimen. Therefore, the proposed 1/4-scale specimen is feasible unless bigger mass or higher C.G is utilized.
- Among the four ground motions which were selected based on the analytical study, GM7 is the most suitable for the dynamic tests with vertical excitation considering the shaking table characteristics.
- GM7 MCE level is the highest level that is applied in the fidelity tests and the response spectra suggest that the shaking table performance is still acceptable. However, this intensity level is found to be near the limits of the shaking table based on the measured vertical accelerations. Hence, sufficient performance is not expected if a stronger excitation is applied, or if a bigger mass or higher C.G is utilized. Therefore, GM7 MCE level and the fidelity setup mass and C.G height are considered as defining the upper limit for the excitation and specimen configuration in this study.

## 3.4 Specimen Design

The Plumas-Arboga Overhead Bridge (PAOB) is the selected prototype for designing the test specimens, since its aspect ratio is closer to the desired value than that of Amador Creek Bridge which was used in the preliminary parametric study. A column with a low aspect ratio ( $H/D$ ) is expected to show shear or flexure-shear behavior. As discussed in Chapter 2,  $Maxdcr$  tends to increase as the aspect ratio decreases. To represent a critical bridge column constructed in California with higher damage potential due to vertical motions, an aspect ratio of 3.5 is used in the test specimen for the dynamic tests.

The Plumas-Arboga Overhead Bridge (PAOB) is a two-bent, three-span RC bridge. It is designed by Caltrans according to post-Northridge design practice as the ACB. Its total length is

456 ft (139 m) and the spans connected to abutments are about 133 ft (40.5 m) each and the span between columns is about 190 ft (58.0 m). The heights of the two bents shown in Figure 3.9 were modeled as 29.7 ft (9.0 m). The aspect ratio along the ‘Bent center line’ (weak axis) is 3.58 and that along the ‘Bridge center line’ (strong axis) is 5.37. Tables 3.4 and 3.5 present properties of the elastic superstructure and properties of its original interlocking spiral column cross-section and the modified effective circular cross-section. This latter cross-section is used for the design of the shaking table test specimens.

**Table 3-4: Cross-section properties of the Plumas-Arboga Overhead Bridge superstructure**

Parameter	Value
$A$	6.73 m <sup>2</sup>
$I_x$	5.28 m <sup>4</sup>
$I_y$	70.09 m <sup>4</sup>
$J$	75.37 m <sup>4</sup>

**Table 3-5: Column cross-section properties of the Plumas-Arboga Overhead Bridge**

Parameter	Interlocking spiral cross-section	Modified effective circular cross-section
$A$	3.61 m <sup>2</sup>	3.14 m <sup>2</sup>
$I_x$	0.715 m <sup>4</sup>	0.788 m <sup>4</sup>
$I_y$	1.247 m <sup>4</sup>	0.788 m <sup>4</sup>
$J$	1.962 m <sup>4</sup>	1.575 m <sup>4</sup>

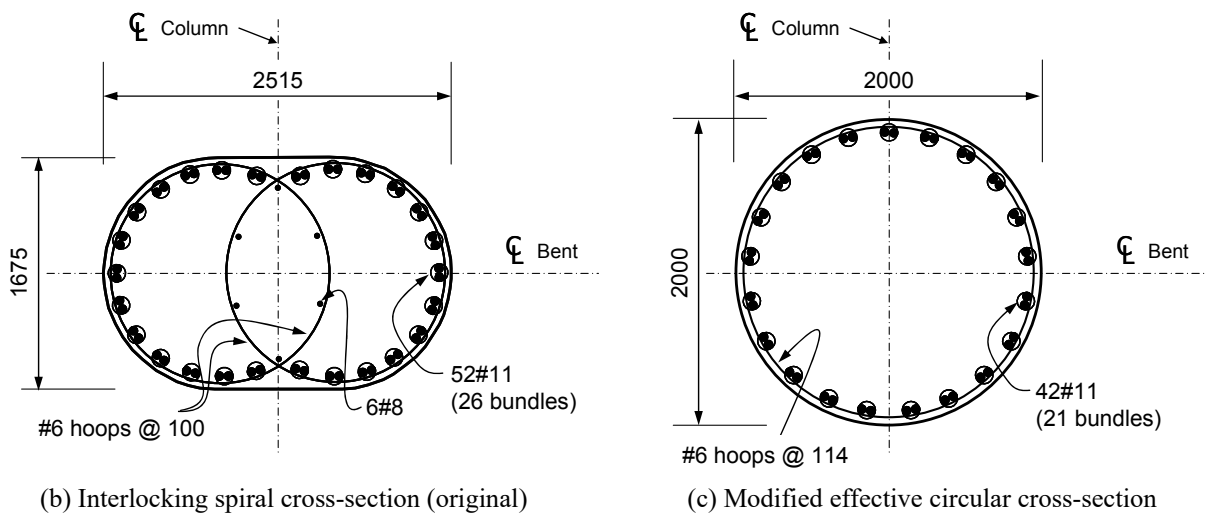


**Figure 3-9: Column cross-sections of the Plumas-Arboga Overhead Bridge (units: mm)**

### 3.4.1 Cross-Section Properties

Two specimens were designed and the design properties are identical except for the transverse reinforcement ratio. The comparisons of cross-section properties are summarized in Table 3.6. Section A is the cross-section of the PAOB. Sections B and C are the cross-sections of the 1<sup>st</sup> and 2<sup>nd</sup> specimens (SP1 and SP2), respectively. These cross-sections are illustrated in Figure 3-10.

Confined concrete properties (peak stress and strain,  $f'_{cc}, \epsilon_{cco}$ , respectively, and ultimate stress and strain,  $f'_{ccu}, \epsilon_{ccu}$ , respectively) for each cross-section are calculated based on Mander's model [29].  $M_{max}$  of each cross-section was calculated assuming the yield strength of the longitudinal and transverse reinforcing bars  $f_y, f_{yt}$ , respectively, of 60 ksi (413.7 MPa) and the aspect ratio (AR) of 3.5.  $V_s$  and  $V_c$  were calculated based on the ACI equations as defined in Chapter 2.

In Table 3.6, the concrete contribution to the shear capacity,  $V_c$ , for the 'maximum tension' and 'gravity only' are specified. Assuming the pseudo-acceleration of GM7 MCE level (corresponding to 114% of the original record) at 0.03 sec with 2% damping as 1.98g, the maximum tension was estimated. The vertical period, 0.03 sec, was calculated from the mass configuration described later and from axial stiffness  $EA/L$ .

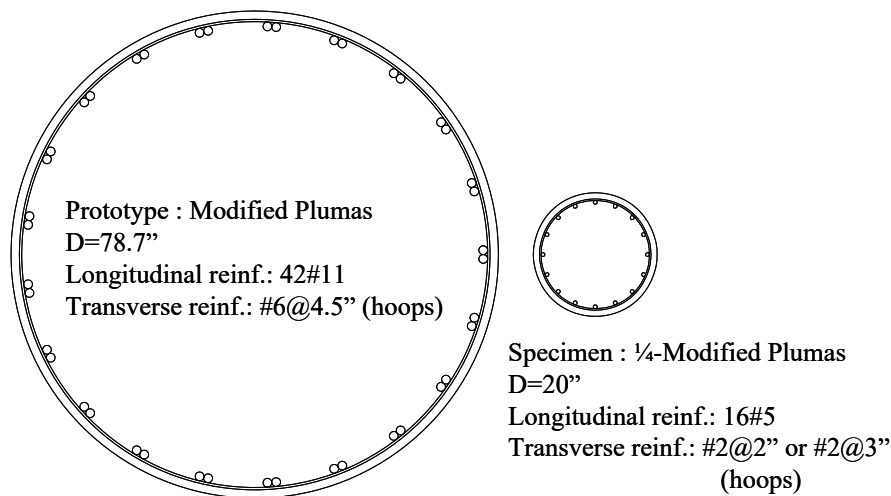


Figure 3-10: Prototype and test specimen column cross-sections

### 3.4.2 Mass and Mass Moment of Inertia

Mass at the top of the test specimen was determined to match 6.5% axial load ratio (ALR) as listed in Table 3.7. Mass moment of inertia (MMI) is calculated as 64.0 -m<sup>2</sup> (47.2×10<sup>3</sup> slug-ft<sup>2</sup>) by scaling MMI of the prototype column using similitude relationships as explained in Section 3.5.1.1. MMI of the prototype column is determined such that the lateral period of the column matches the lateral period of the full scale bridge system. Mass corresponding to 6.5% ALR is

used in both of the single column and bridge system models. By using the same mass and matching the modal properties, the best resemblance between the prototype column in the bridge system model and that in the single-column model was achieved. Finally, the calculated MMI for the prototype column and the test specimen are  $12.084 \times 10^6$  slug-ft<sup>2</sup> (16384 t-m<sup>2</sup>) and  $47.2 \times 10^3$  slug-ft<sup>2</sup> (64.0 t-m<sup>2</sup>), respectively. By a proper combination of concrete blocks, lead blocks, and steel beams on the test specimen, the desired weight for the intended ALR, MMI, and height of C.G. are achieved.

**Table 3-6: Cross-section properties**

Parameter	Unit	A. PAOB	B. SP1	C. SP2	A/B	A/C
Diameter, $D$	[in] ([m])	78.7 (2.0)	20 (0.508)	20 (0.508)	3.94	
Area, $A$	[in <sup>2</sup> ] ([m <sup>2</sup> ])	4869.5 (3.14)	314.2 (0.203)	314.2 (0.203)	15.50	
Height, $H$	[in] ([m])	275.6 (7.0)	70 (1.778)	70 (1.778)	3.94	
Longitudinal reinforcing bars		42#11	16#5	16#5	-	
Diameter, $d_{st}$	[in] ([mm])	1.41 (35.8)	0.625 (15.875)	0.625 (15.875)	2.26	
Bar Area, $A_{st}$	[in <sup>2</sup> ] ([mm <sup>2</sup> ])	1.56 (1007)	0.307 (197.9)	0.307 (197.9)	5.09	
Total Area, $A_s$	[in <sup>2</sup> ] ([mm <sup>2</sup> ])	65.52 (42310)	4.909 (3166.9)	4.909 (3166.9)	13.36	
Reinf. Ratio	[%]	1.348	1.563	1.563	0.862	
Transverse reinforcing bars		#6@4.5"	#2@2"	#2@3"	-	
Diameter, $d_{sh}$	[in] ([mm])	0.75 (19)	0.25 (6.35)	0.25 (6.35)	3.0	
Bar Area, $A_{sh}$	[in <sup>2</sup> ] ([mm <sup>2</sup> ])	0.44 (283.5)	0.0491 (31.68)	0.0491 (31.68)	9.0	
Spacing, $s$	[in] ([mm])	4.5 (114.3)	2 (50.8)	3 (76.2)	2.25	1.5
Vol. Reinf. Ratio	[%]	0.543	0.545	0.363	0.996	1.496
$A_v D/s, A_v = 2A_{sh}$	[in <sup>2</sup> ] ([mm <sup>2</sup> ])	15.39 (9929.2)	0.982 (623.4)	0.655 (415.6)	15.7	23.5
Confinement: $f'_c = 4$ ksi (27.58 MPa)						
$f'_{cc}$	[ksi]	4.98	5.02	4.68	0.992	1.064
$f'_{ccu}$	[ksi]	4.31	4.33	3.97	0.995	1.086
$\epsilon_{cco}$	-	0.00446	0.00456	0.00371	0.978	1.202
$\epsilon_{ccu}$	-	0.01187	0.01241	0.00961	0.956	1.235
Capacity (6.5% axial load)						
$M_{max}$	[k-ft] ([kN-m])	15047.2 (20404)	233.0 (316.0)	230.3 (312.3)	64.57	65.33

$V_s$	[kip] ([kN])	756.5 (3364.8)	46.5 (206.8)	31.0 (137.8)	16.27	24.42
$V_{c,min}$ (max tension)	[kip] ([kN])	307.7 (1368.8)	19.85 (88.29)	19.85 (88.29)	15.50	
$V_{c,max}$ (gravity)	[kip] ([kN])	709.0 (3153.4)	45.74 (203.45)	45.74 (203.45)	15.50	
$V_{n,min} = V_s + V_{c,min}$ , $V_{n,max} = V_s + V_{c,max}$	[kip]	1064.2, 1465.5	66.35, 92.24	50.85, 76.74	16.04, 15.89	20.93, 19.10

**Table 3-7: Mass of the 1/4-scale test specimen**

Item	Unit	SP1 and SP2		
Diameter	[in] ([m])	20 (0.508)		
Area	[in <sup>2</sup> ] ([m <sup>2</sup> ])	314.2 (0.203)		
$f'_c$	[ksi] ([MPa])	4.0 (27.58)		
$A_g f'_c$	[kip] ([kN])	1256.8 (5590.0)		
Axial Load Ratio (ALR)	[%]	4.5	5.0	6.5
ALR × $A_g f'_c$	[kip] ([kN])	56.6 (251.5)	62.8 (279.5)	81.7 (363.3)

### 3.4.3 Material Properties

For reliable estimation of the capacity of test specimens, material properties were obtained by conducting material tests for the standard concrete cylinders and samples of the reinforcing steel bars. These material tests were conducted in the material and structure laboratory, Davis Hall, UC-Berkeley.

#### 3.4.3.1 Concrete

The concrete mix was specified as normal weight concrete with the 28<sup>th</sup>-day design strength of 4 ksi (27.58 MPa). Detailed concrete mix design specifications are presented in Table 3-8. A total of 48 6"×12" concrete cylinders were prepared at the time of column casting. Three cylinders were tested on the 7<sup>th</sup>, 14<sup>th</sup>, 20<sup>th</sup>, 28<sup>th</sup> days, the day of preliminary stiffness tests (72<sup>nd</sup> day), the days of tests (93<sup>rd</sup> and 111<sup>th</sup> days), and the 406<sup>th</sup> day, as specified in Table 3-9 where  $\mu$  and  $\sigma$  represent the mean and standard deviation, respectively. Figure 3-11 presents the strength maturity curve based on these cylinder tests. The strength gradually increases until the 28<sup>th</sup> day, and the mean strength reaches 85% of the design strength.

American Society for Testing and Materials (ASTM) specifies the procedure for concrete cylinder preparation and testing. Specimen preparation procedure stated in ASTM C31 [8] was

followed in this study. According to ASTM C172 [7], concrete should be sampled from the middle of the truck load. At least three portions of discharge are necessary to obtain a representative sample since the first or last discharge portions from the load will not provide a representative sample. Using the last discharge might have caused the large deviations shown in Figure 3-11. In addition, the strength values on the 93<sup>rd</sup> day are clustered between 2.9 and 3.5 ksi. Their standard deviation is not as large as those on the 28<sup>th</sup> and 72<sup>nd</sup> days. This implies that there is a high probability there was a mistake in testing the cylinders on the 93<sup>rd</sup> day. Of course, the possibility of choosing three low-strength cylinders cannot be ignored.

**Table 3-8: Concrete mix specifications**

28 <sup>th</sup> day strength [psi]	4.0 (27.58 MPa)
Cement	ASTM C-150 TYPE II
Fly ash	ASTM C-618 CLASS F 15%
Admixture (water reducer)	ASTM C-494 TYPE A
Cementitious sacks/yd <sup>3</sup>	5.00
Maximum size aggregate [in]	¾ (19 mm)
Slump [in]	4 (102 mm)
Water/cement ratio	0.602

**Table 3-9: Strength properties of concrete**

Day	Compression strength [psi]	Tensile strength [psi]
7 <sup>th</sup> (Aug. 4, 2010)	1429, 1471, 1712	180, 154, 195
	$\mu = 1537, \sigma = 152.6$	$\mu = 177, \sigma = 20.7$
14 <sup>th</sup> (Aug. 11, 2010)	2009, 2447, 2104	258, 238, 242
	$\mu = 2187, \sigma = 230.6$	$\mu = 246, \sigma = 10.3$
20 <sup>th</sup> (Aug. 17, 2010)	2985, 3063, 2943	265, 265, 257
	$\mu = 2997, \sigma = 61.0$	$\mu = 262, \sigma = 4.5$
28 <sup>th</sup> (Aug. 25, 2010)	3572, 2978, 3657	361, 326, 347
	$\mu = 3402, \sigma = 370.0$	$\mu = 345, \sigma = 17.3$
72 <sup>nd</sup> (Oct. 8, 2010)	3897, 3057, 3196	N/A
	$\mu = 3383, \sigma = 450.6$	
93 <sup>rd</sup> (Oct. 29, 2010)	2909, 3365, 3435	278, 307, 263
	$\mu = 3236, \sigma = 285.6$	$\mu = 283, \sigma = 22.4$
111 <sup>th</sup> (Nov. 16, 2010)	4108, 4144, 3759	336, 356, 368
	$\mu = 4004, \sigma = 212.5$	$\mu = 353, \sigma = 16.1$
406 <sup>th</sup> (Sep. 7, 2011)	4669, 4750, 4693	N/A
	$\mu = 4704, \sigma = 41.7$	

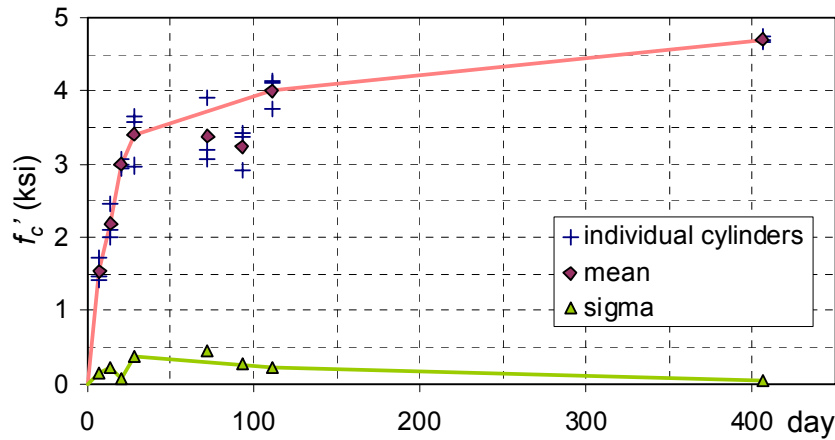


Figure 3-11: Concrete strength maturity curve

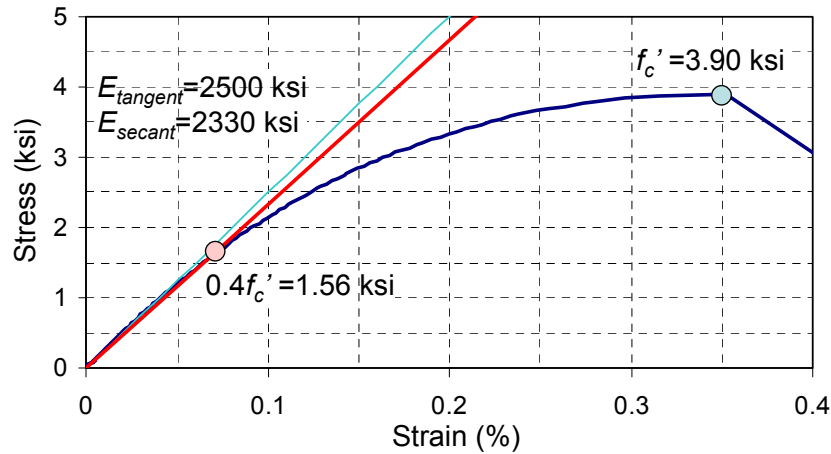


Figure 3-12: Example concrete stress-strain relationship on the 72<sup>nd</sup> day (1<sup>st</sup> cylinder)

A sample stress-strain relationship that is obtained from one of the tested cylinders is shown in Figure 3-12. From this figure, the obtained compressive strength is 3.9 ksi (26.89 MPa), the corresponding peak strain is 0.35%, and the initial tangent modulus is 2500 ksi (17.24 GPa). The secant modulus which connects the origin and  $0.4f'_c$  is 2330 ksi (16.06 GPa), as specified in Figure 3-12.

### 3.4.3.2 Steel Reinforcing Bars

Both longitudinal and transverse (i.e. hoops) steel reinforcing bars of the columns are tested. #5 bars were used as longitudinal reinforcement. Total of four tensile tests were conducted on September 28, 2011. In addition, four tensile tests were conducted to confirm the properties of the #2 reinforcing bars used as hoops on May 27, 2010, as shown in the photograph of Figure 3-13(d). Figure 3-13(a) and (b) show the obtained stress-strain relationships of the longitudinal and transverse reinforcement, respectively. One linear variable differential transformer (LVDT)

is used to measure the displacement between two points with 2 in (51 mm) gage length. For #2 bar, a strain gage is placed to measure strain at one point in the middle of the LVDT gage length. As shown in Figure 3-13(b), both stress-strain relationships are very similar. However, as shown in Figure 3-13(c), the strain from the LVDT has a slightly steeper slope and smaller strain after 5%-strain which corresponds to 87 ksi (599.84 MPa) in stress. This is due to the difference in measuring the strain, i.e. the strain from the strain gage near the necking point is larger than that obtained by the LVDT averaging over its 2 in (51 mm) gage length. Table 3-10 summarizes the properties of both reinforcing bars. The yield stress is calculated based on the 0.1% offset method [9].

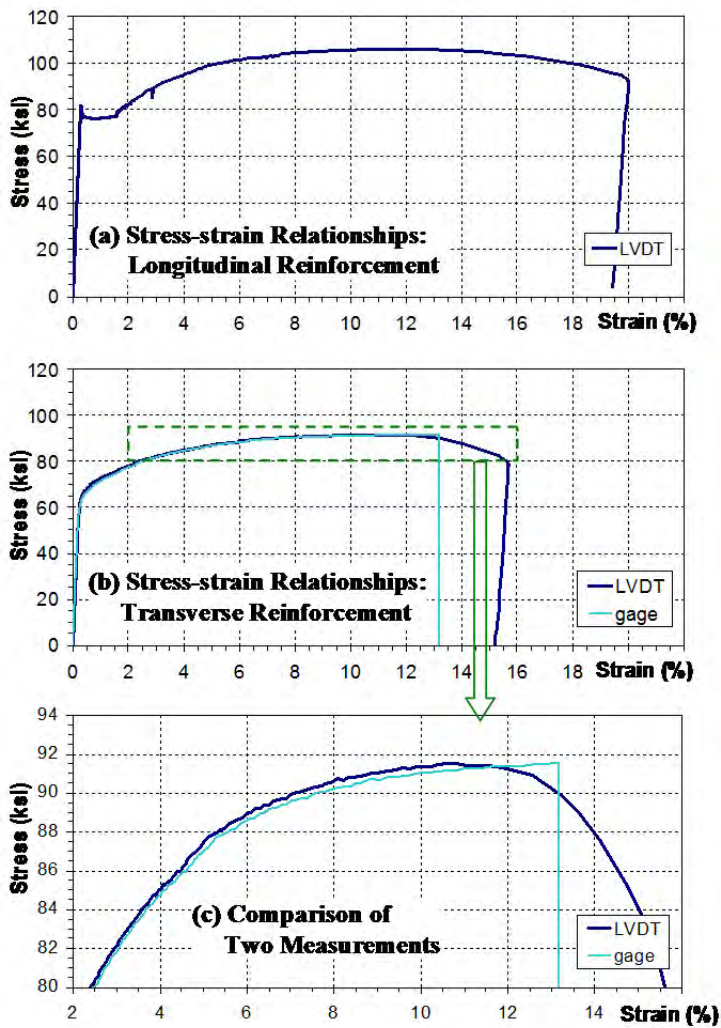


Figure 3-13: Testing longitudinal and transverse reinforcing bars (sample results and setup)

**Table 3-10: Average properties of the reinforcing bars**

Property	Longitudinal bars #5, from LVDT	Transverse bars #2, from LVDT
Yield stress, $f_y$ [ksi]	77.54	63.13
Ultimate stress, $f_u$ [ksi]	105.06	90.25
Yield strain, $\varepsilon_y$ [%]	0.27	0.22
Ultimate strain, $\varepsilon_u$ [%]	12.04	11.64

### 3.5 Experimental Setup and Test Program

Two shaking table tests were conducted at the Richmond Field Station Earthquake Simulator, at Richmond Field Station of UC-Berkeley. As shown in Figure 3-14(a), the specimen is placed at the center of the shaking table using a thick large transition steel plate,  $8' \times 8' \times 3.35''$  ( $2.44 \text{ m} \times 2.44 \text{ m} \times 85 \text{ mm}$ ), for better shaking table performance and control purposes which would otherwise be critical due to the large specimen weight. Steel chains shown in this figure are connected to the prestressing rods for the top concrete blocks to prevent collapse of the test specimen. The prestressing rods connect the steel beams and concrete blocks to achieve the stability and avoid any sliding of the mass system during the shaking tests.

#### 3.5.1 Dimensional Analysis

As mentioned previously, the test specimens are scaled from the prototype column by using a length scale of 4. Keeping the accelerations and stresses same for the prototype and the scaled columns lead to the following scale factors for time, mass and MMI.

Length:  $L = 1/4$

Acceleration:  $LT^{-2} = 1$ , therefore,  $T = 1/2$

Stress:  $ML^{-1}T^{-2} = 1$ , therefore,  $M = 1/16$

MMI:  $I = ML^2$ , therefore,  $I = 1/256$

where  $T$  and  $M$  are the scale factors for time and mass, respectively.

#### 3.5.2 Column

The test columns are 20 in (508 mm) in diameter and 70 in (1778 mm) in height. For longitudinal reinforcement, 16#5 bars are used for both specimens and the longitudinal reinforcement ratio is 1.563%. For transverse reinforcement, #2 hoops are used where the first specimen (SP1) has 2 in (51 mm) spacing and the second specimen (SP2) has 3 in (76 mm) spacing. For both specimens, the spacing is uniform over the entire column height. The

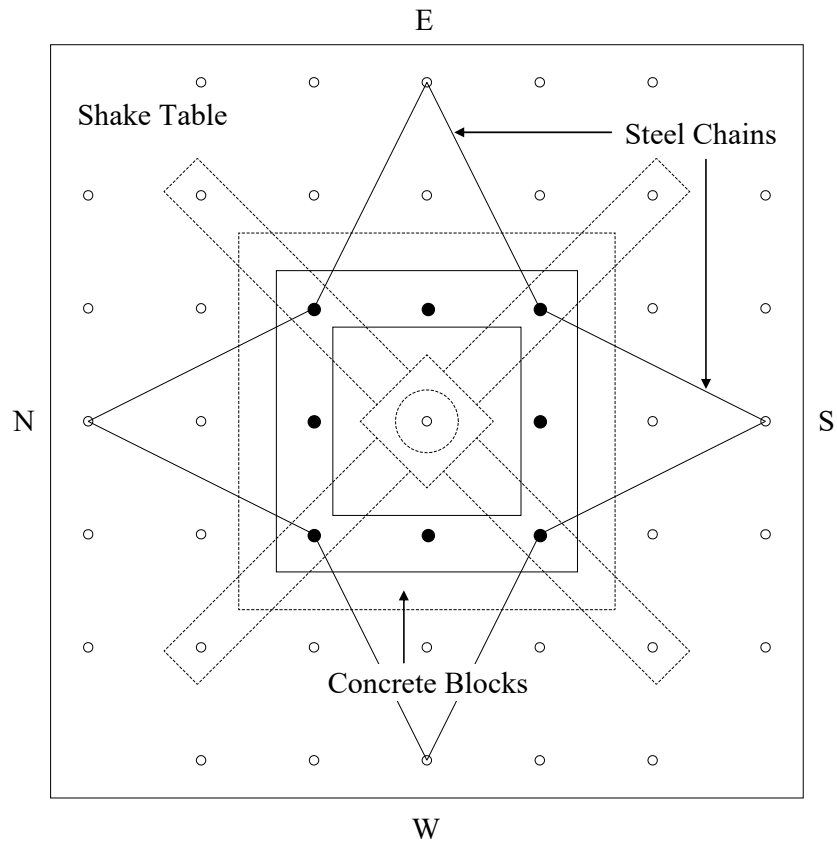
volumetric ratio of the transverse reinforcement is 0.545% for SP1 and 0.363% for SP2. Bridge Design Specifications (BDS) [12] by Caltrans provide the required minimum volumetric ratio as 0.468%. Therefore, SP1 satisfies the BDS while SP2 does not satisfy the BDS in terms of the transverse reinforcement. Finally, the weight of the column, except for the footing, is about 3.9 kips (17.35 kN). Complete set of drawings of the test specimens can be found in Appendix B.

### **3.5.3 Base Plate, Footing, and Top Steel Beams**

The base steel plate is designed to place the test specimen at the center of the shaking table. Nine 2.5" (64 mm) holes, to connect the plate to the shaking table, and 16 7/8" (22 mm) tap (threaded) holes, to connect the load cells to the plate, were drilled on the 8' × 8' × 3.35" (2.44 m × 2.44 m × 85 mm) base steel plate. Design details of the base plate are given in Appendix B.

The footing is designed to fix the column to the shaking table and it is 60 in × 60 in × 18 in (1524 mm × 1524 mm × 457 mm) in dimensions. It is reinforced with #6 deformed bars in both longitudinal directions and with #3 ties in the transverse direction. The footing is set on four load cells, one at each corner. The footing weight is about 5.7 kips (25.35 kN). Footing details can be found in Appendix B.

The top steel beams are designed to resist prestressing forces and to support inertia forces of the mass blocks which consist of two concrete blocks and 72 lead blocks. The four beam cross sections, HSS 20×12, are designed to have small deflection and enough flexural capacity. Figure 3-15 shows a plan view showing the layout of these four beams and the number of attached lead blocks. For more information, the design of steel beams is explained in details in Appendix B. The lead blocks are hung by four prestressing rods fixed at the tip of smaller HSS pipes as shown in the photograph of Figure 3-16. These HSS pipes were welded to the top of the four steel beams.



- Shake Table Anchor Point
- Concrete Block Anchor Point

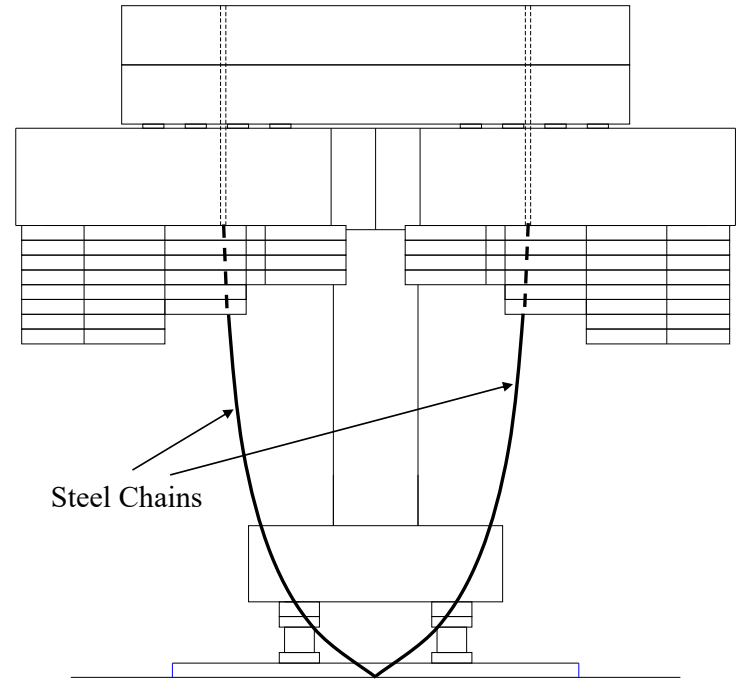


**Figure 3-14: Specimen location on the shaking table and the catching safety system (a) Plan view, (b) Elevation view**

### 3.5.4 Mass Blocks

The target ALR was 6.5%, but the additional weight of steel beams and miscellaneous items caused slightly heavier gravity load on the column. Finally, 6.8% ALR, i.e. about 85.6 kips, is achieved by two concrete blocks, 72 lead blocks on the column (Figure 3-15), monolithically cast top block with the column, and the tie assembly. The concrete blocks are identical in dimensions and weight. Each block is 10 ft×10 ft×14 in (3045 mm × 3048 mm × 356 mm) in dimensions and about 16.5 kips (73.4 kN) in weight, i.e. a total of concrete blocks weight of 33 kips (146.8 kN). The lead blocks are also identical. Each lead block is 27 in×21 in×3.5 in (686 mm × 533 mm × 89 mm) in dimensions and 0.5 kips (2.22 kN) in weight, i.e. a total of lead blocks weight of 36 kips (160.1 kN). As a result, the center of gravity (C.G.) is about 8.5 ft (2591 mm) above the shaking table as dictated by the test setup shown in Figure 3-16.

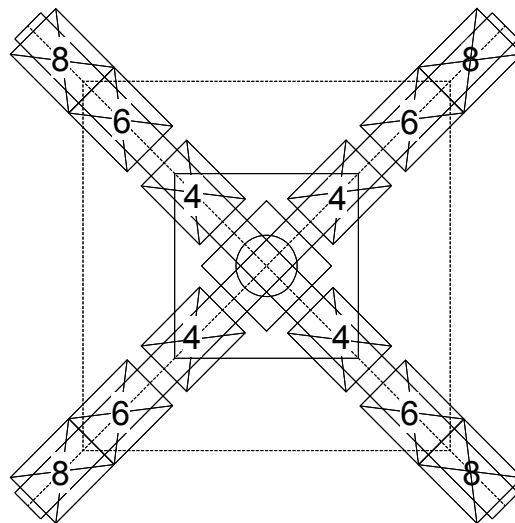


**Figure 3-15: Final mass configuration**



**Figure 3-16: Final test setup**

### **3.5.5 Instrumentation**

Total of 137 channels are used for each shaking table test and they are distributed as follows:

- 16 channels for monitoring accelerations and displacements of actuators under the table;
- 12 channels for tri-axial load cells monitoring restoring force of the specimen;
- 27 channels for nine 3D accelerometers and 9 channels for nine 1D accelerometers, monitoring the vertical acceleration at specific points of the test specimen;
- 38 channels for strain gages on the longitudinal and transverse reinforcing bars;
- 14 channels for Novotechniks (after the name of the manufacturer) and 2 channels for direct current differential transformers (DCDTs) monitoring local deformation of the test specimen; and
- 19 channels for wire potentiometers monitoring displacement at specific points of the test specimen.

The channel list and instrumentation drawings are presented in Appendix C.

### **3.5.6 Internal Instrumentation**

Total of 38 strain gages were installed on the reinforcing bars for each test specimen. 18 gages were installed on longitudinal bars (L) and 20 gages on transverse bars (H) at the following locations (defined by the column diameter,  $D$ , and the column height,  $H$ ):

- At 3D/2 and 2D from the bottom and D/2 from the top as shown in Appendix C: 2 gages (L) and 2 gages (H);
- At D/2 from the bottom as shown in Appendix C: 2 gages (L) and 6 gages (H);
- At D from the bottom and also from the top as shown in Appendix C: 4 gages (L) and 2 gages (H); and
- At mid-height (i.e. H/2) as shown in Appendix C: 2 gages (L) and 4 gages (H).

### 3.5.7 External Instrumentation

As shown in Appendix C, linear position transducers (Novotechnik), DCDTs, wire potentiometers, accelerometers, and load cells were installed to obtain local deformation, global displacement, acceleration, and restoring force, respectively. These instruments are installed in the following locations:

- **Novotechniks and DCDTs**

Total of 14 Novotechniks were installed to measure local deformation on the north and south sides of the column. They were mounted on threaded rods penetrating through the column in the horizontal loading direction, as shown in Appendix C. Total of six rods were kept unbonded from the surrounding concrete by the gap of 1/16" (1.6 mm) around the rod except at the center of the column. The bonded length is roughly 14" (356 mm). Each rod has a brace on each side to fix the Novotechnik and its wire. Locations of these measurements are given in Appendix C. From the Novotechnik data, one can calculate the strain at D/2, D, 3D/2, and 2D from the bottom and at D/2 from the top. These strains from the displacement measurements can be compared to the strains obtained directly from the reinforcing bar strain gages. In addition, section curvatures can also be obtained by using these computed strains on the north and south sides of the column. Moreover, two DCDTs were installed to capture the vertical displacement of the top concrete block. They were located 7" (178 mm) off from the east and west sides of the column.

- **Wire Potentiometers**

Total of 19 wire potentiometers were installed to measure displacement of the test specimen. They captured the displacement in the longitudinal (X), transverse (Y) and vertical (Z) directions. These measurements were arranged as follows:

- Column – 4 wire potentiometers in X and 4 wire potentiometers in Y direction;
- Footing – 2 wire potentiometers in X and 1 wire potentiometer in Y direction; and
- Mass – 2 wire potentiometers in X, 2 wire potentiometers in Y and 4 wire potentiometers in Z direction.

- **Accelerometers**

Total of 18 accelerometers were installed to measure acceleration at the following points. Four 3D accelerometers were located at each corner of the base plate, one below the top block, and four at each corner of the top of the concrete blocks. Eight 1D accelerometers to measure the vertical acceleration were attached along the height on the north side of the column, and one at the center on the top concrete block.

- **Load Cells**

Four tri-axial load cells support the specimen at the four corners below its footing. They measure axial load, and shear forces in the X and Y directions.

### **3.5.8 Test Sequence**

Two specimens are planned to follow identical test sequence. All excitations are scaled from 5% to 125% of the 1994 Northridge earthquake recorded at Pacoima Dam, and the upper limit is determined by the shaking table limits, as previously discussed. Since each specimen is subjected to irreversible inelastic behavior in medium or high-level tests, the intensity of excitation is increased gradually. The maximum curvature at the top of the column observed in the analysis is used as the basis for determining each intensity level. While conducting tests of SP1, the longitudinal strain near the base and the top of the column is checked. For SP2, the sequence of testing is almost the same as that for SP1.

## **3.6 Summary**

The dynamic tests to examine the effect of vertical excitation on shear strength of RC bridge columns were designed within the capacity limits of the UC-Berkeley shaking table in the Richmond Field Station. The geometric scale of the test specimens is selected as 1:4. To confirm the shaking table performance, fidelity tests were conducted with steel beams and concrete blocks stacked on the shaking table. Even though the periods were not comparable to those of the scaled prototype, the total mass (118 kips) and the center of gravity, 9 ft from the shaking table, were comparable to those of the test specimens. Four ground motions were selected from reduced subset of motions identified in Chapter 2. Total of 30 trials were conducted and the input motion was finalized. Also, the intensity limit of the applied motion was identified.

The specimens are designated as SP1 and SP2. Both SP1 and SP2 have longitudinal reinforcement ratio of 1.563% which is close to the prototype value. The transverse reinforcement ratio of SP1 is close to that of the prototype, but SP2 has 2/3 of that of SP1, achieved by adjustment the hoop spacing. The mass on the column was identical in both specimens. Assuming  $f'_c = 4$  ksi (27.58 MPa) and 6.5% axial load ratio and including miscellaneous weight, 85.6 kip-weight (38.83 ton) was placed on each column. Total weight on the table is slightly over 100 kips (45.36 ton). The center of gravity of the specimen was about 8.5 ft (2591 mm) above the table. A base plate and prestressing rods were placed to hold the specimen at the center of the shaking table. Steel chains hold the mass blocks to avoid unexpected movement which might cause safety concerns.

Total of 38 strain gages were installed on the reinforcing bars of each specimen. 18 gages were attached to the longitudinal bars and 20 gages were attached to the hoops. For external

instrumentation, 9 3D accelerometers, 9 1D accelerometers, 4 loadcells, 14 Novotechniks, 2 DCDT, and 19 wire potentiometers were used.

The input motion, the Northridge earthquake (1994) recorded at the upper abutment of Pacoima Dam, is selected to be applied to the test specimens with increasing intensity, varying in magnitude from 5% to 125%-scale. The 2D excitation in X and Z is planned in most cases, but 1D excitation in X was also applied in some cases as these 1D runs are helpful to observe the difference in responses due to the effect of the vertical excitation.

# 4 Results of Shaking Table Tests: Global and Local Responses

## 4.1 Introduction

A series of tests was conducted on the UC-Berkeley shaking table at Richmond Field Station (RFS) on two quarter-scale specimens (SP1 and SP2). The ground motion recorded at the Pacoima Dam station of 1994 Northridge earthquake (RSN 1051) was applied. One of the horizontal (X) and vertical (Z) components were utilized in most cases. X component is selected because it produces larger shear strength reduction than the Y component. Since the geometrical scale of the specimen corresponds to the 1/4-scale modified Plumas-Arboga Overhead Bridge (PAOB), each component of the ground motion was time-compressed by a factor of 2 as shown in Figure 4-1. It should be noted that the acceleration history in Figure 4-1 is 100% unfiltered input ground motion obtained from the PEER NGA database [37].

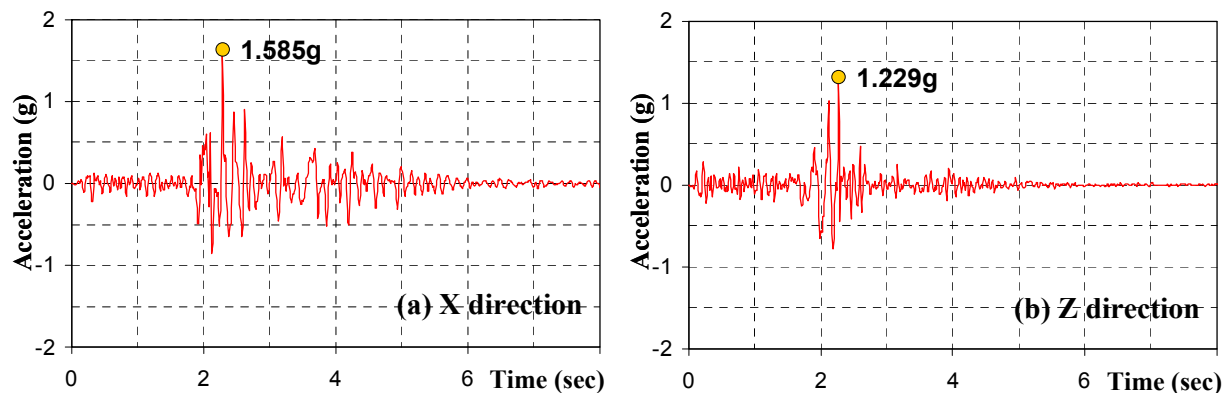


**Figure 4-1: Horizontal (X) and vertical components (Z) of 100% Northridge earthquake**

The ground motion was applied in increasing intensity levels and each intensity level was related to the expected curvature ductility (based on numerical simulations) at the top of the column. All tests are conducted with one of the horizontal and vertical components except the ones noted with 'X only' in . The low-level tests, from 5% to 25%-scale excitations, did not result in yielding of the cross-section at height  $h=60''$  (1524 mm) above the top of the footing, which corresponds to the mid-point of the plastic hinge at the top of the column, assuming a plastic hinge length equal to the diameter of the column,  $L_p = D = 20''$  (508 mm). The yielding at  $h=60''$  (1524 mm) occurs when 50%-scale motion is applied. Even though the maximum curvature of SP1 is larger than that of SP2 during the 50%-scale run, this can be considered as 'yield-level' for both specimens. After this yield-level, 70%, 95%, and 125%-scale motions are applied.

**Table 4-1: Test sequence**

SP	Run	Scale [%]	Ductility			Date	Notes
			Curvature		Displacement		
			$\phi/\phi_{ys}$ @ 60"	$\phi/\phi_y$ @ 60"	$\Delta/\Delta_y$ @ 70"		
1	1-1	5.0	-	-	-	Oct. 22	-
	1-2	12.5	-	-	-	Oct. 22	-
	1-3	12.5	-	-	-	Oct. 26	50% increased Z
	1-4	12.5	-	-	-	Oct. 26	Repetition of 1-2
	1-5	25.0	0.41	0.35	0.93	Oct. 26	Half-yield
	1-6	50.0	1.11	0.96	1.73	Oct. 27	Yield
	1-7	70.0	1.57	1.36	1.93	Nov. 1	Onset of shear cracks
	1-8	95.0	4.62	4.00	2.33	Nov. 1	Onset of cover spalling
	1-9	125.0	6.15	5.33	4.27	Nov. 1	-
	1-10	125.0	6.54	5.67	4.77	Nov. 2	X only
	1-11	125.0	7.31	6.33	5.47	Nov. 2	Repetition of 1-9
2	2-1	5.0	-	-	-	Nov. 16	-
	2-2	12.5	-	-	-	Nov. 16	-
	2-3	25.0	0.40	0.35	1.05	Nov. 16	Half-yield
	2-4	25.0	0.41	0.36	0.84	Nov. 16	Half-yield, X only
	2-5	50.0	0.92	0.80	1.43	Nov. 16	Yield
	2-6	50.0	0.99	0.86	1.27	Nov. 16	Yield, X only
	2-7	70.0	1.23	1.07	1.97	Nov. 18	Onset of shear cracks
	2-8	95.0	5.00	4.33	2.47	Nov. 18	Onset of cover spalling
	2-9	125.0	5.38	4.67	4.60	Nov. 18	-
	2-10	125.0	5.00	4.33	4.50	Nov. 18	X only
	2-11	125.0	4.23	3.67	4.77	Nov. 18	Repetition of 2-9

As can be identified from Table 4-1, tests without the vertical component are conducted for 125%-scale (run 1-10) for SP1 and 25%, 50%, and 125%-scales (runs 2-4, 2-6, and 2-10, respectively) for SP2 to examine the effect of vertical excitation. In Table 4-1, the curvature ductility,  $\phi_y = 3.0 \times 10^{-4} \text{ in}^{-1}$  ( $1.2 \times 10^{-5} \text{ mm}^{-1}$ ), is from the test data and  $\phi_{ys} = 2.6 \times 10^{-4} \text{ in}^{-1}$  ( $1.0 \times 10^{-5} \text{ mm}^{-1}$ ) is from the cross-section analysis. The curvature ductility at  $h=60''$  (1524 mm) can be considered as an adequate global response parameter. At  $h=70''$  (1778 mm), the yield displacement,  $\Delta_y = 0.3 \text{ in}$  (7.62 mm) for both SP1 and SP2, is estimated based on the shear force-lateral displacement responses presented later in this chapter.

## 4.2 Stiffness, Natural Frequency, and Viscous Damping

Before the main runs specified in Table 4-1, pullback and free vibration tests were conducted to obtain the stiffness and lateral and rotational vibration periods of each specimen. Obtained period and damping values were confirmed in part with the low-level tests, i.e. up to 12.5%-scale tests.

### 4.2.1 Pullback Tests

For SP1, total of five pullback tests were conducted as shown in Figure 4-2. Relative lateral displacement between the top of the footing and the column top (just below the monolithically cast RC block above the column) and absolute displacement (i.e. displacement between the column top and the top of the table) was measured. The difference between the absolute and relative displacements results from the rotation of the footing due to the axial flexibility of the load cells. For SP2, three pullback tests were conducted. The lateral stiffness obtained in each case is shown in Table 4-2. As specified, SP1 and SP2 have different stiffness values and the stiffness of SP2 is about 70% that of SP1, regardless of the displacement measurements. Lateral force-absolute displacement relationship in one case for each specimen is shown in Figure 4-3.



Figure 4-2: Photographs of the pullback tests without (left) and with (right) total mass

Table 4-2: Stiffness from pullback tests

Displacement measurements	Stiffness of SP1 [k/in]	Stiffness of SP2 [k/in]	Stiffness Ratio (SP2/SP1)
Relative	148.0, 150.0, 148.2	102.1	0.687
	Mean: 148.7		
Absolute	121.8, 116.3	82.1, 82.8	0.693
	Mean: 119.0	Mean: 82.5	

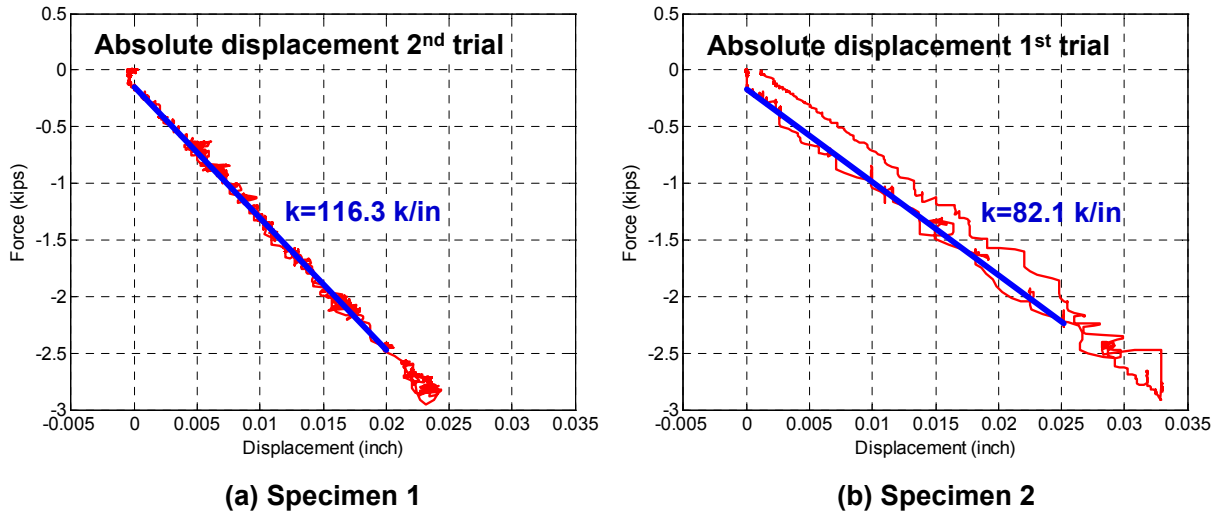


Figure 4-3: Estimation of lateral stiffness

## 4.2.2 Free Vibration Tests

After pullback tests, the lateral and rotational vibration periods of each specimen were estimated based on free vibration tests. Two tests were conducted for SP1 and three tests for SP2. Lateral periods of SP1 and SP2 were 0.43 and 0.47 sec, respectively. It should be noted that if mass moment of inertia provided by the mass assembly did not exist, the ratio of lateral periods would be expected to be the square root of the lateral stiffness, namely 0.83. However for the investigated columns, this ratio is 0.91 which is due to the coupling of the lateral and rotational modes. Lateral periods of the two specimens were much similar to each other during the 12.5% scale runs. Considering that cracks started to open and close during these excitations, it can be speculated that SP2 had some cracking prior to testing. During the 12.5% scale run, cracks initiated in SP1 and increased slightly for SP2 bringing the periods of the two specimens closer to each other. The damping corresponding to the lateral modes of vibration for SP1 and SP2 were calculated as 1.9% and 2.9%, using Eq. (4.1). Figure 4-4 shows the absolute lateral displacement measured at the top of the column and the theoretical displacement calculated by using the mentioned vibration period and damping values using an equivalent single degree of freedom (SDOF) system.

$$\zeta = (\ln(u_1/u_{j+1})) / (2j\pi) \quad (4.1)$$

In Eq. (4.1),  $u_1$  is the displacement at the first cycle peak and  $u_{j+1}$  is the displacement peak after  $j$  cycles.

From the Fast Fourier Transform (FFT) amplitudes, damping values were calculated as 2.2~2.5% (SP1) and 2.5~3.0% (SP2), respectively, using half-power bandwidth method [14]. In addition, the two specimens had the same rotational period of vibration, namely 0.096 sec as shown in Figure 4-5. This value was obtained from FFT amplitudes of the vertical acceleration at the top of the mass blocks and from the response spectra using the vertical acceleration measured on the

shaking table with 3% damping. Another peak observed in the response spectra of the shaking table, namely 0.027 sec, was the vertical period of vibration of the test specimen, as discussed in the next section.

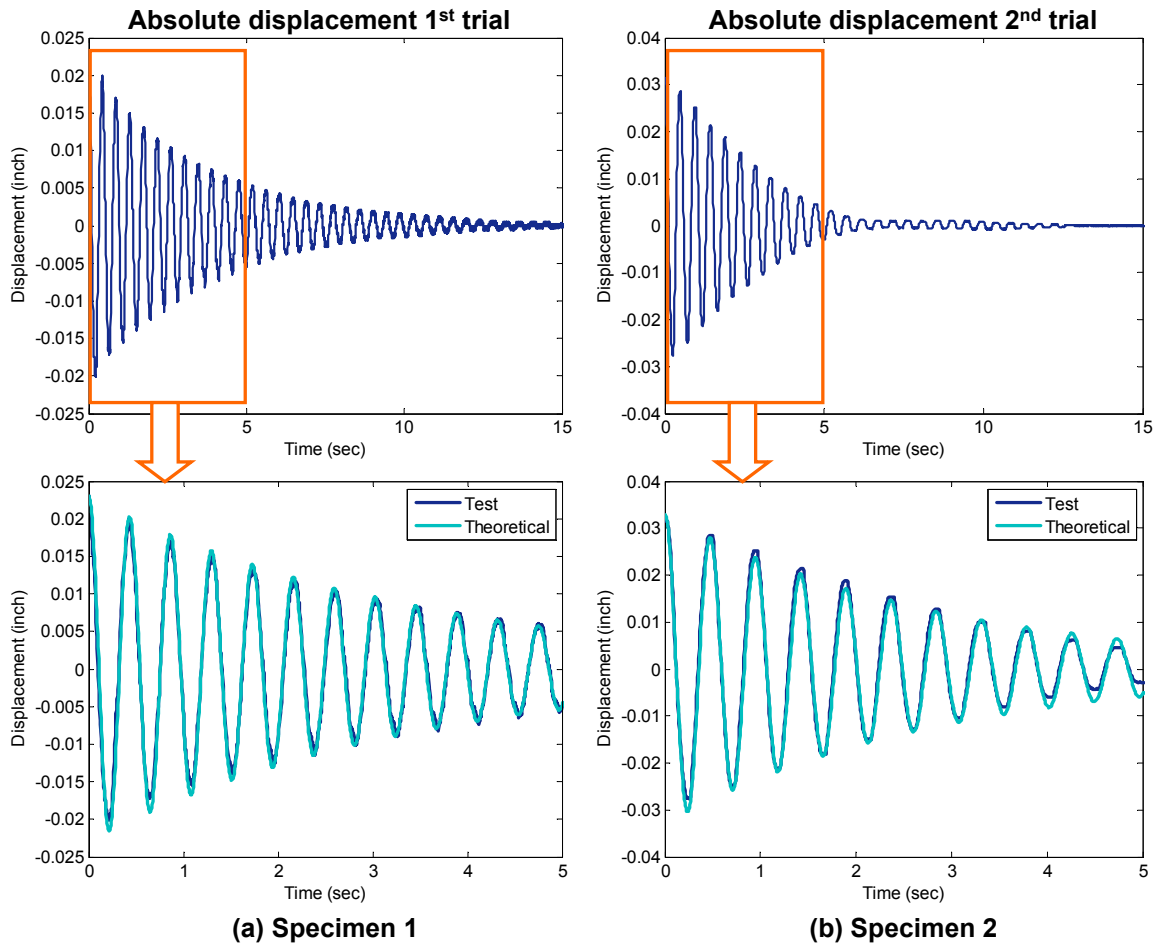
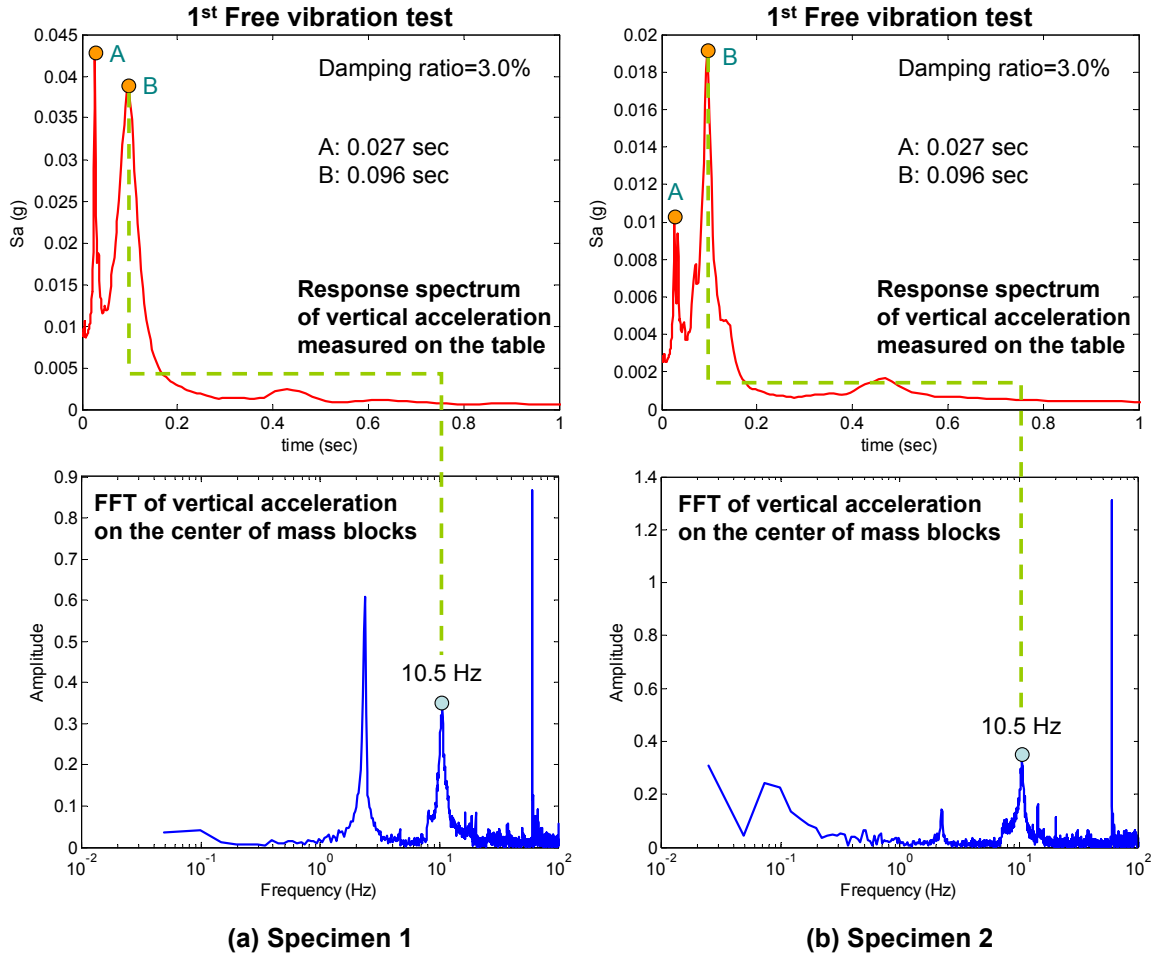


Figure 4-4: Absolute displacement measured in the free vibration tests

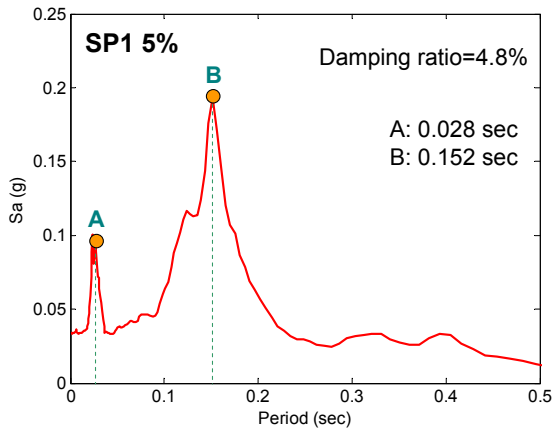
### 4.2.3 Estimation of the Vertical Period

Up to the 12.5%-scale runs, vibration periods did not change significantly. Hence, the periods obtained from FFT of the specimen response can be considered as reasonable estimation of the initial periods of vibration. It should be noted that the FFT peaks come from the response of the whole system including the shaking table. Figure 4-6 shows the response spectra using the vertical acceleration at different locations of SP1 under 5%- and 12.5%-scale motions. Except for the vibration period corresponding to peak A in Figure 4-6(a-2), which is 20% shorter than the others, the observed vertical period values are similar along the column under various intensity levels. The vibration period at peak B is the bending period of the shaking table. It should be noted that similar periods are observed for SP2.

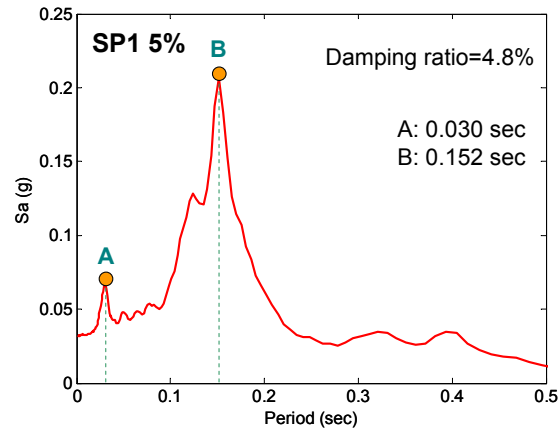


**Figure 4-5: Dominant frequencies of vertical acceleration measurements in free vibration tests**

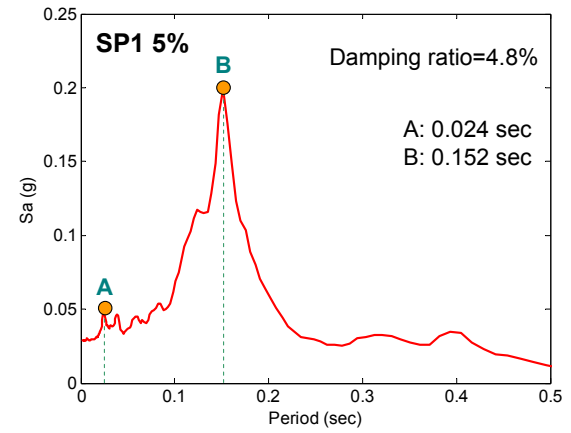
The shaking table effect appears in the case of the rotational period of vibration of the test specimen. When the table is flexing, it results in a rotational degree of freedom with relatively large mass moment of inertia, which increases the rotational period of the test specimen. In case of applying table motion, the vertical actuators induce bending of the table when they are trying to hold the table in the commanded vertical displacement. Therefore, the mass moment of inertia of the shaking table affects the rotational period of vibration. This does not occur in the free vibration test since the table is not flexing because the actuators are inactive and vertical restraint is provided by the large damping coefficient of the actuators. In this case, the boundary conditions of the test specimen are almost like four simple supports at the used four load cells. Therefore, the rotational periods obtained from free vibration tests can be considered as the rotational period of the specimen itself excluding the shaking table effect. For both specimens, the rotational period was approximately 0.1 sec.



(a-1) Table

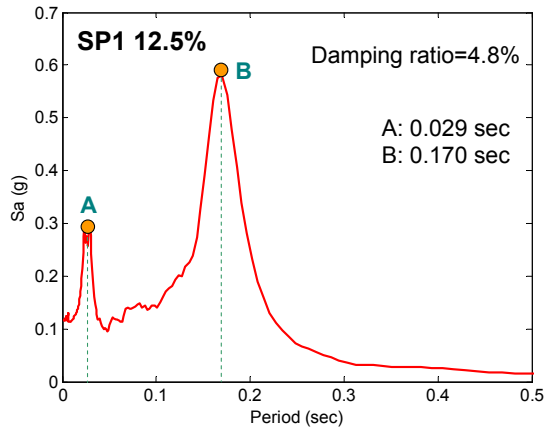


(a-2) Top of the column, East

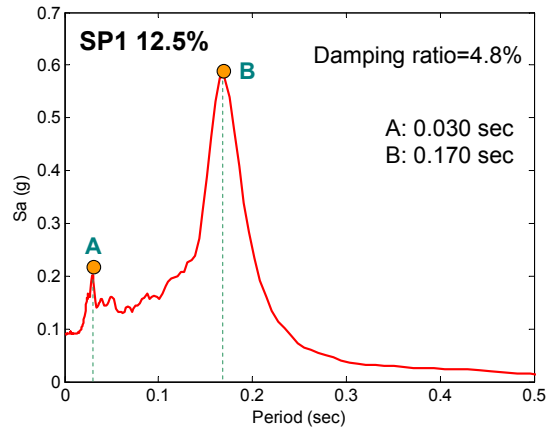


(a-3) Top of the mass blocks

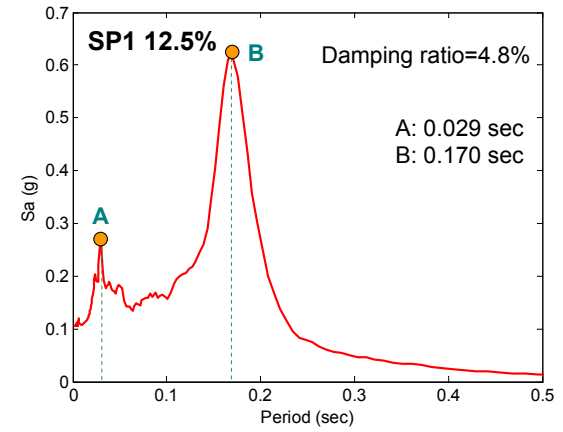
70



(b-1) Table



(b-2) Top of the column, East



(b-3) Top of the mass blocks

Figure 4-6: Response spectra using the measured vertical accelerations

**Table 4-3: Estimation of the periods of vibration of the test specimens**

SP	Test type	Horizontal [sec]	Rotation [sec]	Vertical [sec]
1	Free Vibration 1	0.43	0.10	0.027
	Free Vibration 2	0.43	0.10	0.027
	5% scale GM	0.43	0.15	0.028
	12.5% scale GM	0.49	0.15	0.029
2	Free Vibration 1	0.47	0.09	0.027
	Free Vibration 2	0.47	0.09	0.027
	Free Vibration 3	0.47	0.10	0.028
	5% scale GM	0.49	0.15	0.028
	12.5% scale GM	0.51	0.16	0.029

### 4.3 Table Accelerations

The acceleration response of the test specimen is closely related to the eigenvalues and inertia force of the system. The acceleration history is obtained directly from the accelerometers placed on the shaking table, specimen and concrete blocks. First, the shaking table acceleration is discussed and compared to the target acceleration. Second, the acceleration responses at the top of the column and on the concrete blocks are compared to the shaking table acceleration. Finally, a discussion about the acceleration differences at each location is presented.

Figure 4-7 and Figure 4-8 show the comparison of the time histories of the measured shaking table acceleration and the target acceleration, i.e. the original motion that is required to be reproduced using the shaking table. The table acceleration is the mean of acceleration values obtained from four accelerometers, one at each corner. In Figure 4-7(a), (b), and (c), horizontal and vertical components of the shaking table motion in 50%-, 70%-, 95%-scale tests for SP1 are respectively presented. The table replicates the horizontal (X) component with high precision in all three runs. Compared to the X-component, time history of the vertical (Z) component has discrepancies. Although the obtained peak acceleration is similar to that of the target, acceleration history after the peak does not resemble the target acceleration. This is observed in all three runs in Figure 4-7(a), (b), and (c). In spite of these differences after the peak in the acceleration history, the response spectra of both components obtained from the shaking table are comparable to those of the target, as already discussed in Chapter 3. Another observation is the delayed excitation in the Z direction. In particular, 70%- and 95%-scale Z-components were delayed about 0.2 sec and 0.3 sec, respectively. This is also observed in the 1<sup>st</sup> 125%-scale test shown in Figure 4-8(d) where the time lag was about 0.4 sec.

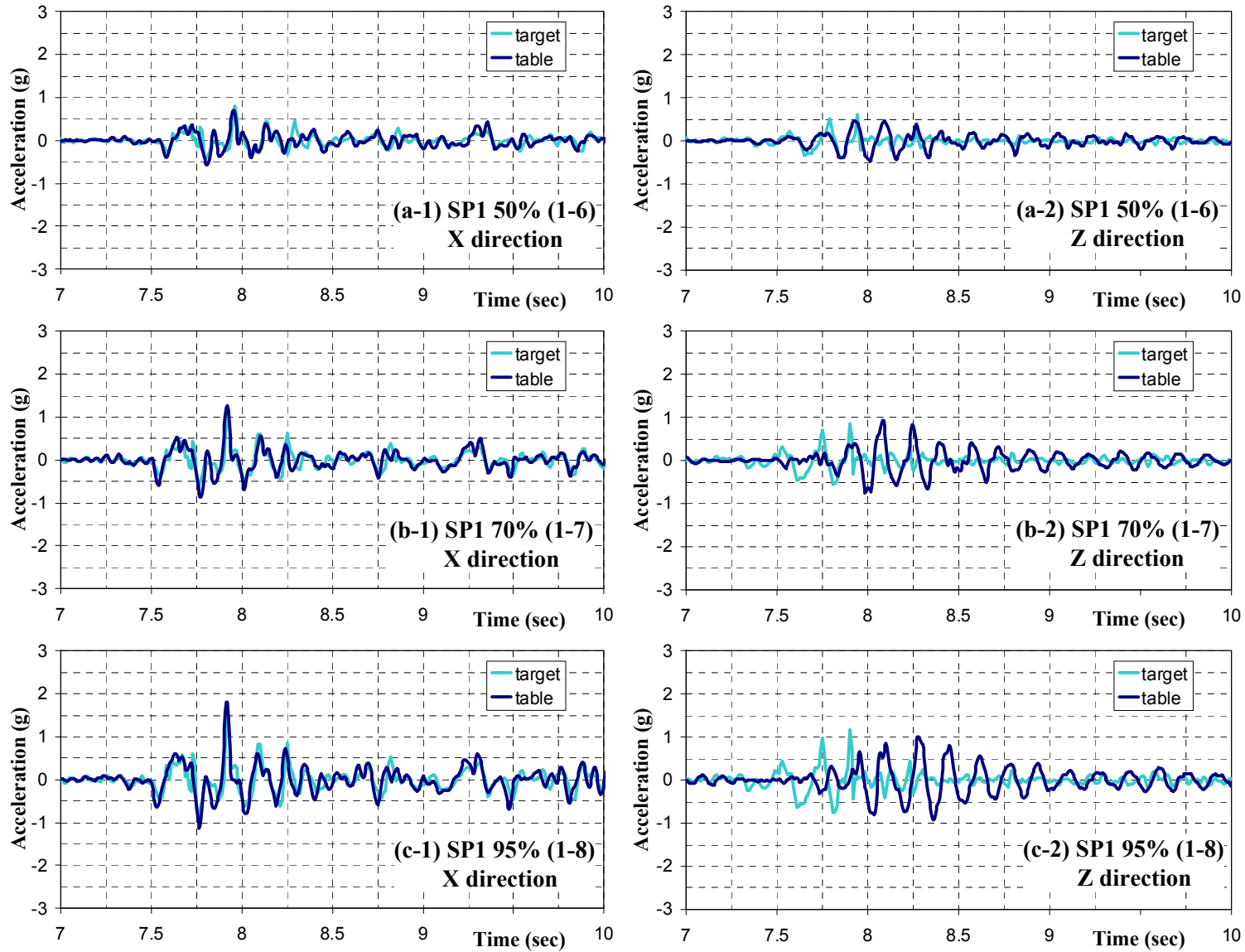


Figure 4-7: Shaking table acceleration history in SP1 tests

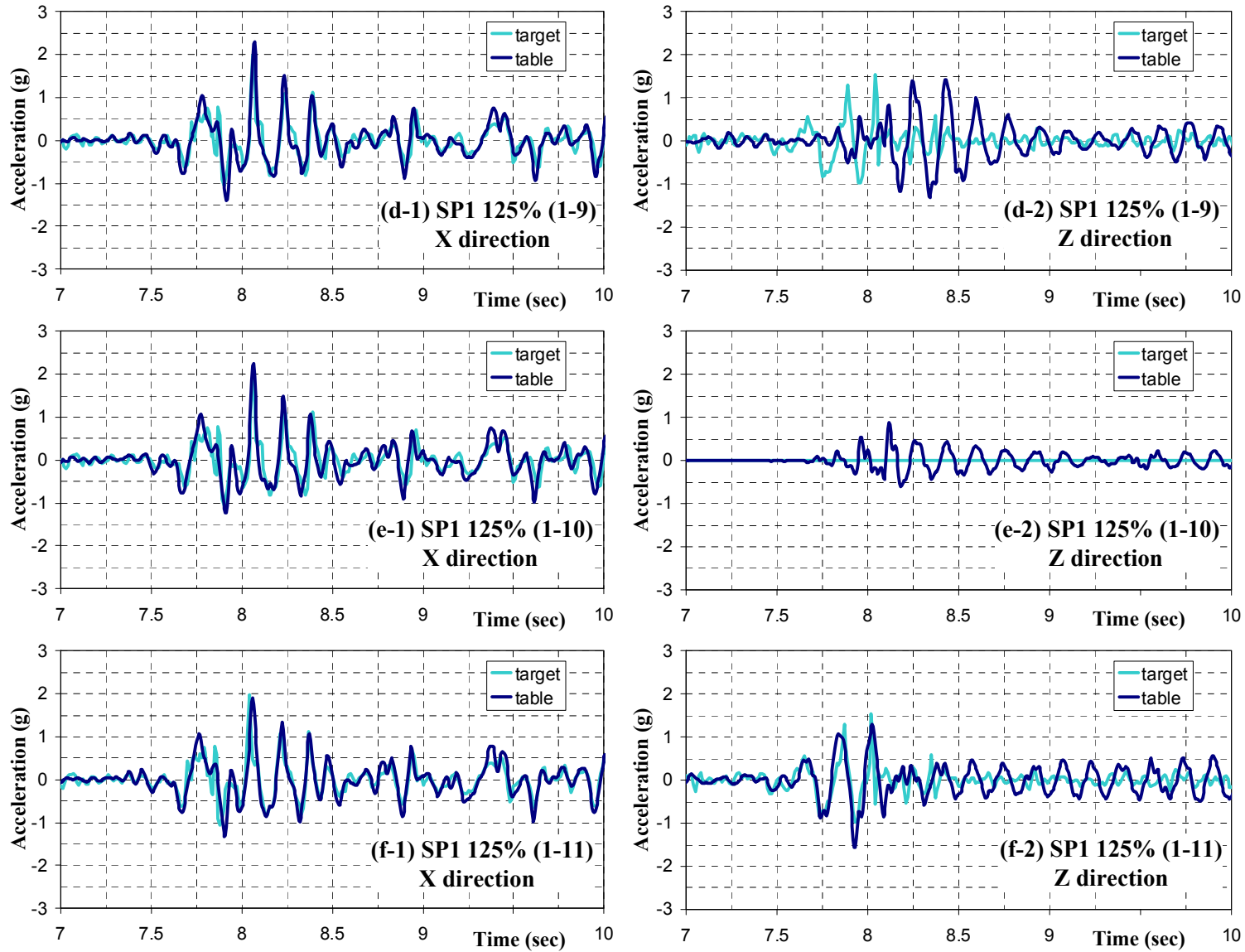


Figure 4-8: Shaking table acceleration history in SP1 tests (continued)

In Figure 4-8(d), (e), and (f), horizontal and vertical components of the shaking table motion for the 125%-scale tests for SP1 are presented. As mentioned in Table 4-1, the 2<sup>nd</sup> 125%-scale run was for X-component only. Therefore, Z-component in the 125%-scale ‘X only’ test is supposed to remain zero, but this is not the case as observed in Figure 4-8(e-2). The shaking table is controlled by vertical displacement at four points where the vertical actuators are connected. As a result, the vertical acceleration in the middle of the shaking table may not be zero during the horizontal excitation only because of the interaction of the vertical actuators which hold the vertical displacement at zero while balancing the forces due to the overturning moments caused by the horizontal acceleration.

The observations mentioned in the above paragraphs for specimen SP1 were also observed for specimen SP2.

### 4.3.1 Rotation of the Mass Blocks

The X-component of the acceleration on the mass blocks was significantly lower than that at the top of the column. This difference was due to the additional translational acceleration due to the rotation of the mass blocks. A quantitative explanation is presented in the following paragraphs.

The rotational acceleration is calculated by using the displacement measurements from the wire potentiometers connected to the south side of the mass blocks and the top of the column in X-direction (i.e. direction of the horizontal (north-south) acceleration component). Two wire potentiometers were connected to the south east and south west sides of the top concrete blocks. Hence, the mean of these two displacement measurements is calculated to obtain the displacement at point B in Figure 4-9 (d). Acceleration at point B is obtained through the double differentiation of the displacement time history at point B. On the other hand, acceleration at the top of the column (point A in Figure 4-9 (d)) was obtained from accelerometer measurements. It can be observed in Figure 4-9 (c) that the measured accelerations at the top of the column are very similar to the accelerations calculated from the measured displacements by double differentiation, validating the determination of accelerations at point B from the displacements where accelerometers were not present.

The acceleration difference between points B and A divided by the distance between these points ( $h_{AB}$ ) resulted in the rotational accelerations on the mass blocks. Additional acceleration on the mass block due to the rotation is equal to the obtained rotational acceleration multiplied by the distance  $h_{AT}$ . Then, acceleration at the top of the mass blocks is calculated with Eq. (4.2) by adding the additional acceleration to the measured acceleration at the top of the column.

$$\begin{aligned}
 a_{derived} &= a_{col-top} + a_{rotation} \\
 &= a_{col-top} + \left( \frac{a_{displ(B)} - a_{col-top}}{h_{AB}} \right) \times h_{AT} \\
 &= a_{col-top} + \left( a_{displ(B)} - a_{col-top} \right) \times r_h
 \end{aligned} \tag{4.2}$$

where  $a_{col-top}$  is measured acceleration at the top of the column,  $a_{displ(B)}$  is the acceleration calculated by differentiation of the mean displacement measured on the south side of the mass blocks,  $h_{AT}$  is the vertical distance from the column top to the accelerometers on the mass blocks, and  $h_{AB}$  is the vertical distance from the column top to the wire potentiometer targets.

It can be observed from Figure 4-9 (a) and (b) that the derived accelerations calculated with Eq. (4.2) matches well the measured accelerations. This matching of derived versus measured accelerations was also observed for the other runs and other test specimen (SP2). It should be noted that the shear force on the column was accordingly affected by the acceleration of this mass that depended on the rotation mentioned above. This is discussed further in the following section.

## 4.4 Forces

### 4.4.1 Shear and Axial Forces

Figure 4-10 presents the time histories for the axial and shear forces obtained from the load cells for specimens SP1 and SP2 subjected to 50%, 70%, and 95%-scale Northridge earthquake. The runs for these three levels are respectively denoted as 1-6, 1-7, and 1-8 for SP1 and 2-5, 2-7, and 2-8 for SP2 in Table 4-1. Figure 4-11 shows similar results for the 125%-scale Northridge input and the corresponding runs are denoted 1-9, 1-10, and 1-11 for SP1 and 2-9, 2-10, and 2-11 for SP2, respectively.

For levels below the 125%-scale motion, the axial force does not induce tension in the column in most cases. SP2 with 95%-scale motion (run 2-8, Figure 4-10 (c-2)) experienced very small peak axial tension (1.4 kips). As the intensity increased, the peak-to-peak amplitude of the axial force increased significantly. SP1 had peak-to-peak amplitude of 100.3 kips for axial force under 50%-scale motion, and it became 157.6 kips and 205.0 kips as the scale increased to 70% and 95%, respectively. Hence, under 95%-scale motion, the axial force amplitude was almost twice as large as that under 50%-scale. The peak-to-peak amplitude of the shear force for SP1 increased from 100.4 kips for 50%-scale to 130.3 kips and 165.1 kips for 70%- and 95%-scales, respectively. Similarly, the peak-to-peak amplitude of SP2 changed as follows: 101.8→162.5→198.9 kips (axial force) and 96.8→133.1→149.6 kips (shear force) for scales of 50%→70%→95%, respectively. The fact that the shear strength increase is less than that observed for axial forces is attributed to the fact that the shear forces at these intensities were no longer in the linear range, approaching the shear strength of the test specimens. It was also observed that the minimum axial force, i.e. minimum compression (positive) or maximum tension (negative), took place before the maximum shear force except for the cases of SP1 with 95%-scale and the first 125%-scale motions (runs 1-8, Figure 4-10 (c-1) and 1-9, Figure 4-10 (d-1), respectively). This observation for the 95%-scale and the first 125%-scale of SP1 is attributed to the somewhat large time lag of the vertical motion between the target acceleration and the shaking table acceleration.

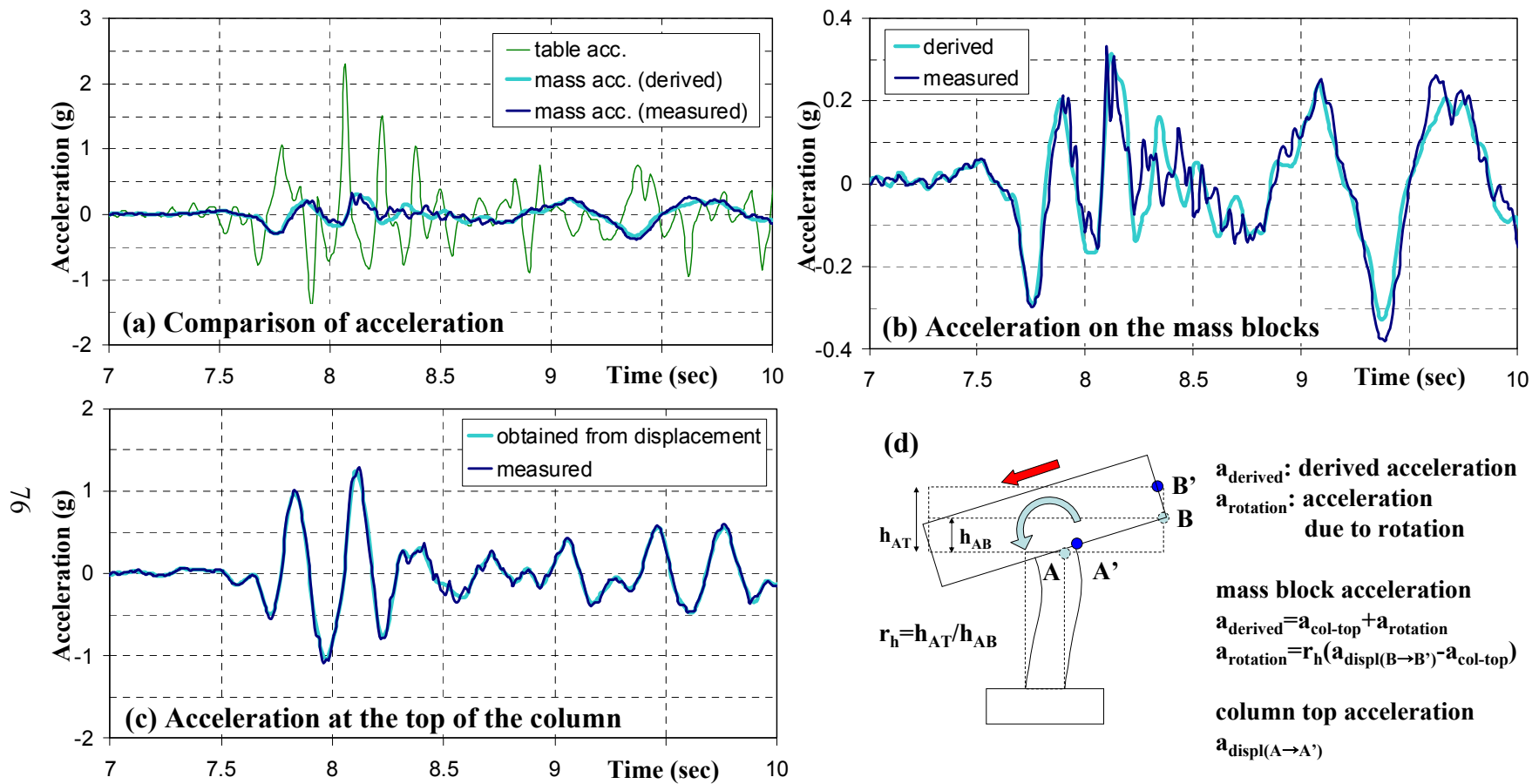


Figure 4-9: Comparison of measured and derived accelerations (specimen SP1, run 1-9)

Total of three 125%-scale tests were conducted for each specimen (Figure 4-11). As mentioned, the vertical component was not applied in the second of these three runs for each specimen (runs 1-10, Figure 4-11 (e-1), and 2-10, Figure 4-11 (e-2)). It was mentioned previously that vertical acceleration was measured on the shaking table even if the vertical component was not applied because vertical excitations were generated due to the interaction between the horizontal and vertical actuators. However, the axial force due to such inevitable vertical acceleration had relatively small compression values with limited effect on the RC column shear capacity. The peak axial and shear forces for the three runs with 125%-scale changed as follows: 252.8→144.5→208.4 kips (axial force, shown with triangle markers in Figure 4-12) and 91.4→92.6→88.3 (shear force, shown with square markers) for the respective runs 1-9→1-10→1-11 for specimen SP1 and 227.2→142.8→231.6 kips (axial force) and 77.4→80.9→77.2 kips (shear force) for the respective runs 2-9→2-10→2-11 for specimen SP2. For both specimens, the positive and negative shear force peaks are seen to change when the vertical component of ground motion is included, particularly the positive peak noticeably decreased after significant tension in the column (57.9 kips for SP1 and 63.3 kips for SP2). The positive shear peak (Figure 4-12, line with square markers) decreased from 92.6 kips to 80.5 kips in SP1 and from 80.9 kips to 67.0 kips in SP2. Considering that the shear forces were similar prior to significant tension for the 'X only' run, where for SP1, this force was 91.4 kips for run 1-9 and 92.6 kips for run 1-10 and for SP2, it was 77.4 kips for run 2-9 and 80.9 kips for run 2-10, the decrease of the positive peak shear force can be explained partly as a result of the vertical excitation, causing axial tension in the column. The reduction in shear force can be attributed to the reduction in the contribution of the concrete to the shear force capacity.

Considering the three 125%-scale tests together as a continuous test, it can be speculated that the reduction in the shear peak was due to degradation caused by the occurrence of two successive large axial tensile forces. For SP1, the positive peak shear forces after the first axial tensile peak (-65.8 kips in run 1-9) were 91.4 kips (run 1-9) and 92.6 kips (run 1-10) and they were reduced to 80.5 kips (run 1-11) after the second axial tensile peak (-57.9 kips in run 1-11). For SP2, the positive peak shear forces after the first axial tensile peak (-61.6 kips in run 2-9) were 77.4 kips (run 2-9) and 80.9 kips (run 2-10) and they were reduced to 67.0 kips (run 2-11) after the second axial tensile peak (-63.3 kips in run 2-11). Hence, the positive peak shear force reduced after the second axial tensile peak for both specimens. On the other hand, the peak axial tensile force in the 2<sup>nd</sup> X+Z tests did not affect the negative peak shear force (88.3 kips in SP1 and 77.2 kips in SP2). This can be explained by the duration of wave propagation in the vertical direction considering that the time between the peak axial tensile force and the negative peak shear force was about 0.04 sec only.

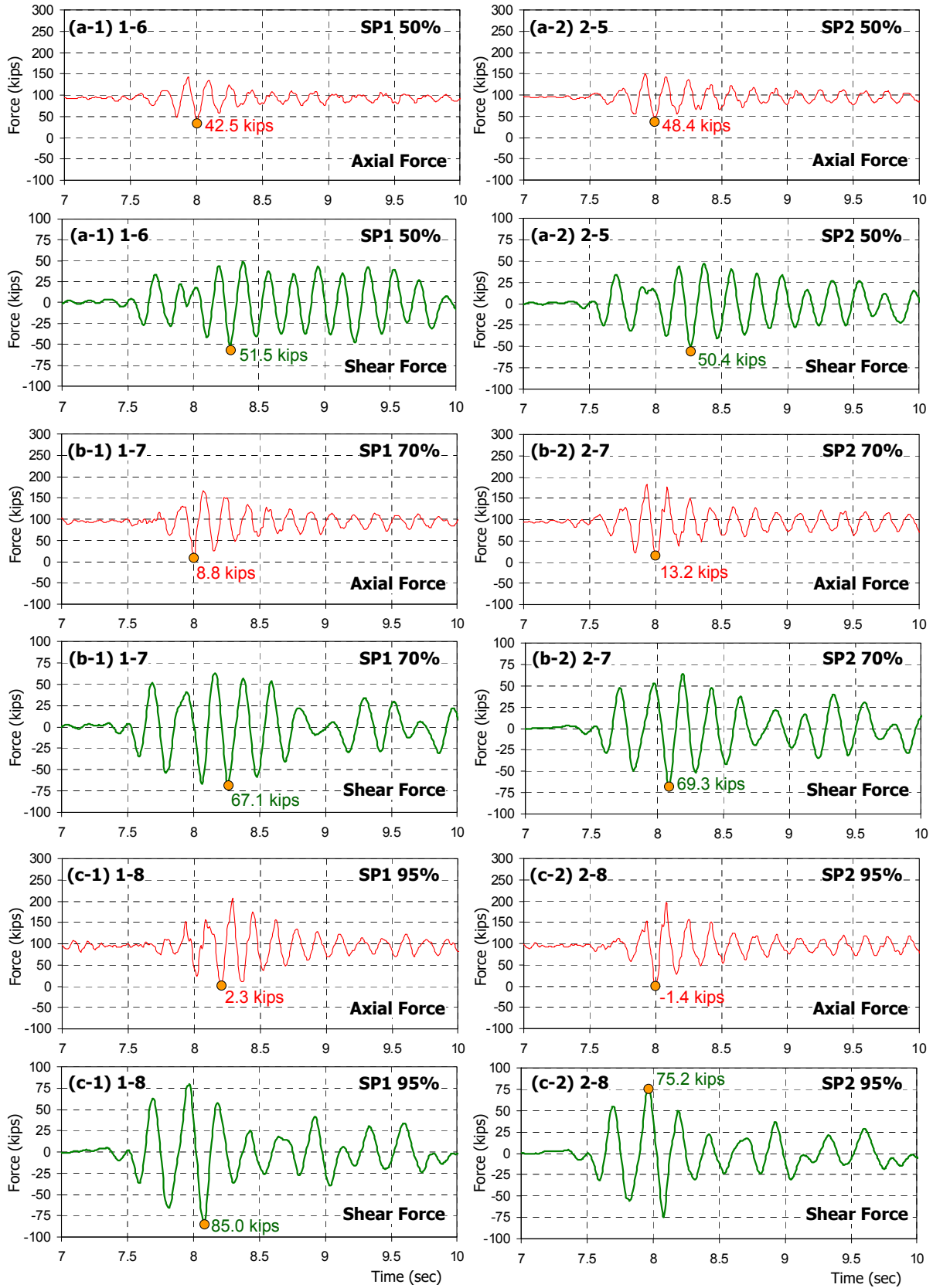


Figure 4-10: Axial force and shear force history

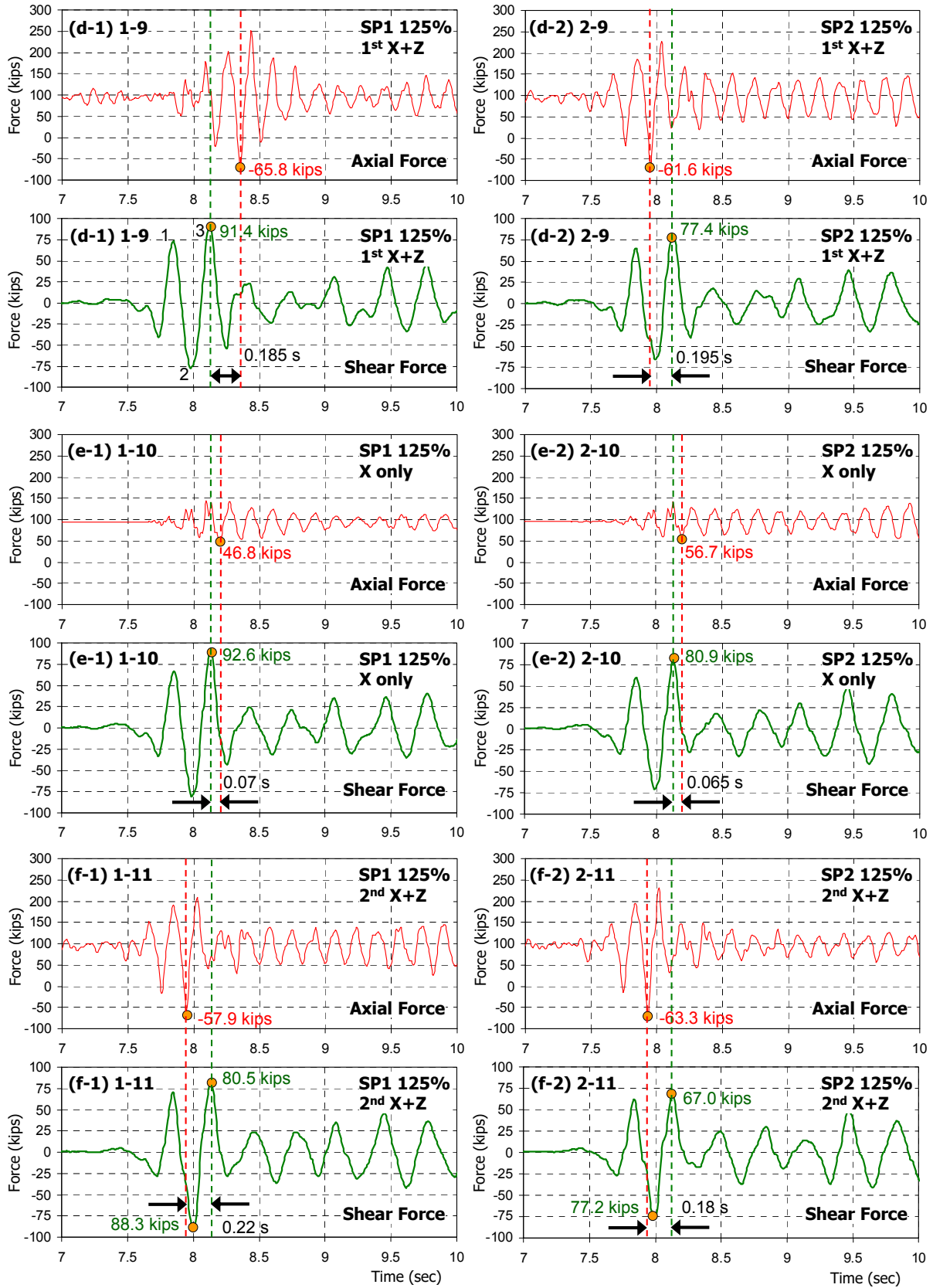
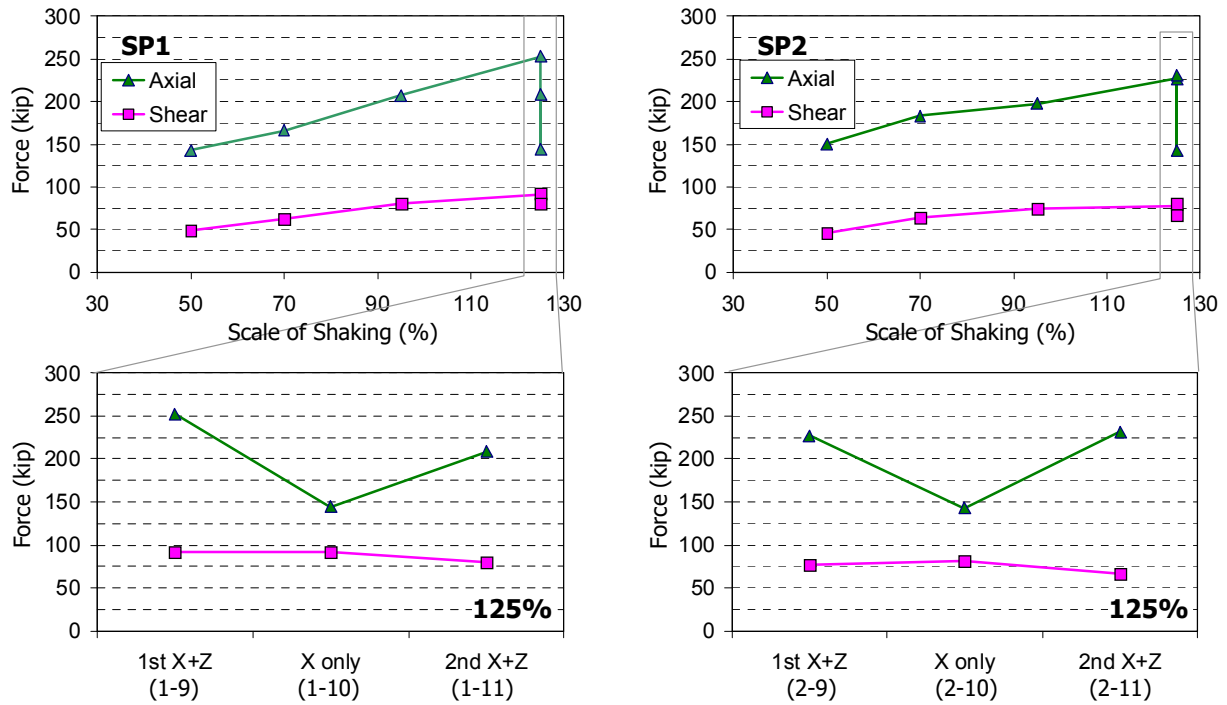


Figure 4-11: Axial force and shear force history (continued)



**Figure 4-12: Positive peak axial and shear forces with increasing intensity of shaking**

Table 4-4 compares the axial force at the maximum positive shear force in each test. Even though the decrease of the maximum positive shear force may have partly resulted from the decrease in axial compression, this cannot explain the difference between ‘X only’ and ‘2<sup>nd</sup> X+Z’ compared to the difference between ‘X only’ and ‘1<sup>st</sup> X+Z’. In particular, comparing runs 2-9 and 2-10, it was observed that the large difference in the axial force at the maximum positive shear force did not affect the magnitude of the shear force significantly. On the other hand, the maximum tension force and corresponding degradation, as discussed in the previous paragraphs, were more appropriate causes for the shear force difference between ‘X only’ and ‘X+Z’ runs.

**Table 4-4: Comparison of axial force at the maximum positive shear force**

SP	Run	(a) Axial [kips]	(b) Shear [kips]	(c) Axial ratio compared to ‘X only’ [%]	(d) Shear ratio compared to ‘X only’ [%]
1	1 <sup>st</sup> X+Z (1-9)	108.4	91.4	77.7	98.7
	X only (1-10)	139.5	92.6	100.0	100.0
	2 <sup>nd</sup> X+Z (1-11)	71.4	80.9	51.2	87.4
2	1 <sup>st</sup> X+Z (2-9)	43.8	78.0	30.7	96.4
	X only (2-10)	142.8	80.9	100.0	100.0
	2 <sup>nd</sup> X+Z (2-11)	73.5	67.1	51.5	82.9

## 4.4.2 Bending Moments

Bending moment is calculated from the axial and shear forces recorded using the load cells installed between the footing and the shaking table. Figure 4-13 (a), (b), and (c) show the bending moment at the base of the column,  $h=0''$  and at the top,  $h=70''$ , subjected to the 50%, 70%, and 95%-scale motions, respectively. Before 10 sec, shear and axial forces were significant. Subsequently, the axial force variation was minimal after 10 sec, and only the shear force governed the bending moment history. In all cases, the peak bending moment at the top was larger than that at the base. Moreover, the bending moment at the top and that at the base were out of phase before 9 sec (double curvature). After 10 sec, when the strong part of the horizontal motion ceased, they became in phase (single curvature) and the peak bending moment at the base exceeded that at the top. Therefore, it can be stated that the bending moments at the top and at the base were dominated by the rotational mode before 9 sec, whereas they were dominated by the translational mode after 9 sec. Figure 4-14(d), (e), and (f) compare the bending moments at the base,  $h=0''$ , and at the top,  $h=70''$ , subjected to the 125%-scale motions.

Table 4-5 compares the maximum values obtained in all the test runs. The absolute values are shown in columns (a) and (b) and the relative values compared to the capacity  $M_{max}$  (3327.5 kip-in for SP1 and 3300.1 kip-in for SP2), which is modified from the value in Table 3-6 to account for actual material properties and axial load, are shown in columns (c) and (d). The bending moment values for SP1 and SP2 exceeded  $M_{max}$  at the top during the 125%-scale tests. However, the bending moment at the base never exceeded  $M_{max}$  for all runs for both specimens. The variation in the peak bending moments as a function of shaking intensity is shown in Figure 4-15

**Table 4-5: Comparison of the maximum bending moment at the base and top of the column**

SP	Run	(a) Base [kip-in]	(b) Top [kip-in]	(c) Base [% of capacity]	(d) Top [% of capacity]
1	50% (1-6)	2029.62	2712.92	61.00	81.53
	70% (1-7)	1899.07	3531.06	57.07	106.12
	95% (1-8)	2459.33	3551.27	73.91	106.72
	125% '1 <sup>st</sup> X+Z' (1-9)	2910.17	3916.73	87.46	117.71
	125% 'X only' (1-10)	3153.47	4110.33	94.77	123.53
	125% '2 <sup>nd</sup> X+Z' (1-11)	2747.91	4046.68	82.58	121.61
2	50% (2-5)	1499.59	2431.99	45.44	73.69
	70% (2-7)	1854.07	3151.16	56.18	95.49
	95% (2-8)	2127.74	3199.51	64.48	96.95
	125% '1 <sup>st</sup> X+Z' (2-9)	2442.27	3627.92	74.01	109.93
	125% 'X only' (2-10)	2736.16	3669.18	82.91	111.18
	125% '2 <sup>nd</sup> X+Z' (2-11)	2343.11	3691.44	71.00	111.86

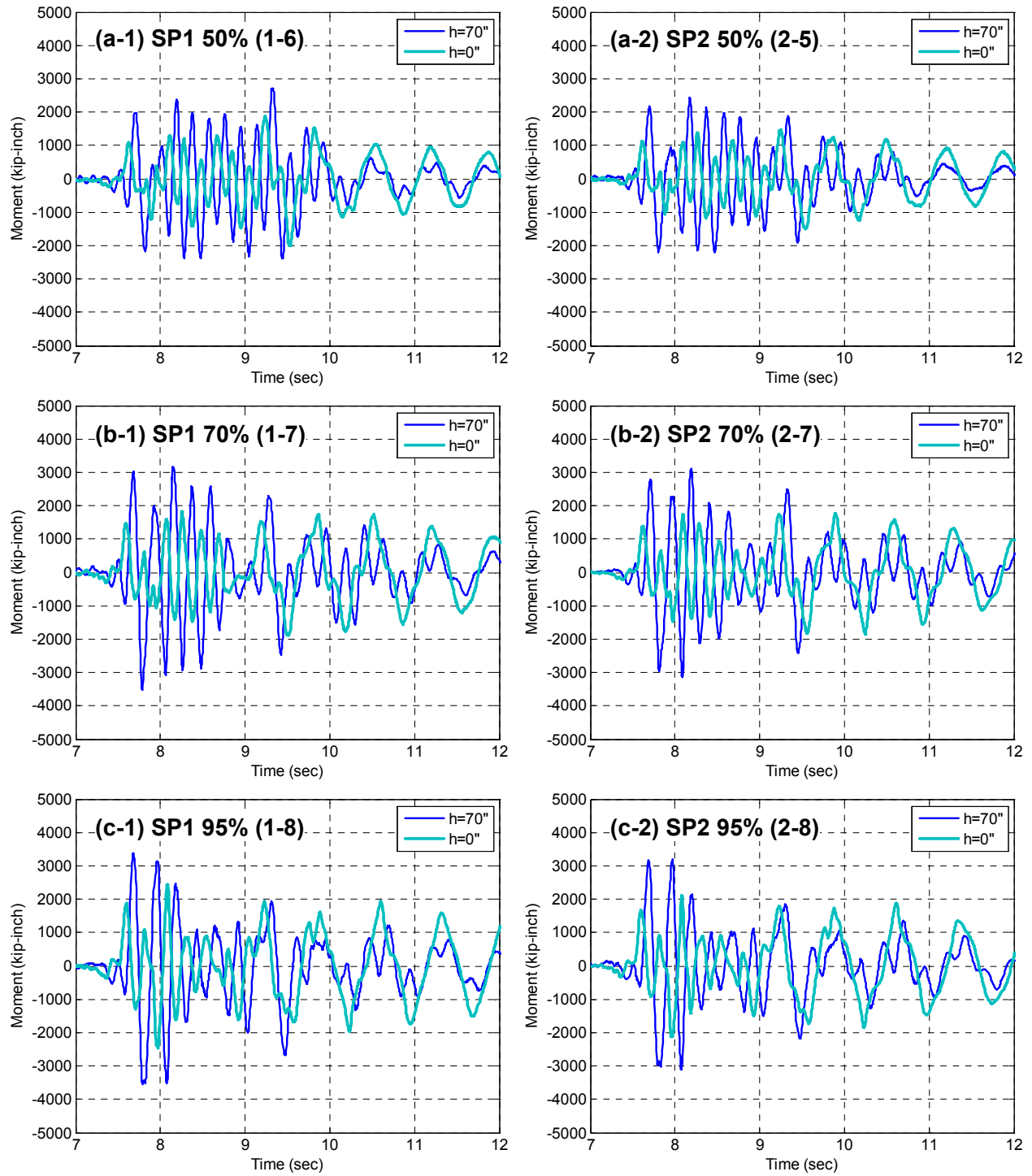


**Figure 4-13: Bending moment history at the top and base of the test specimens**

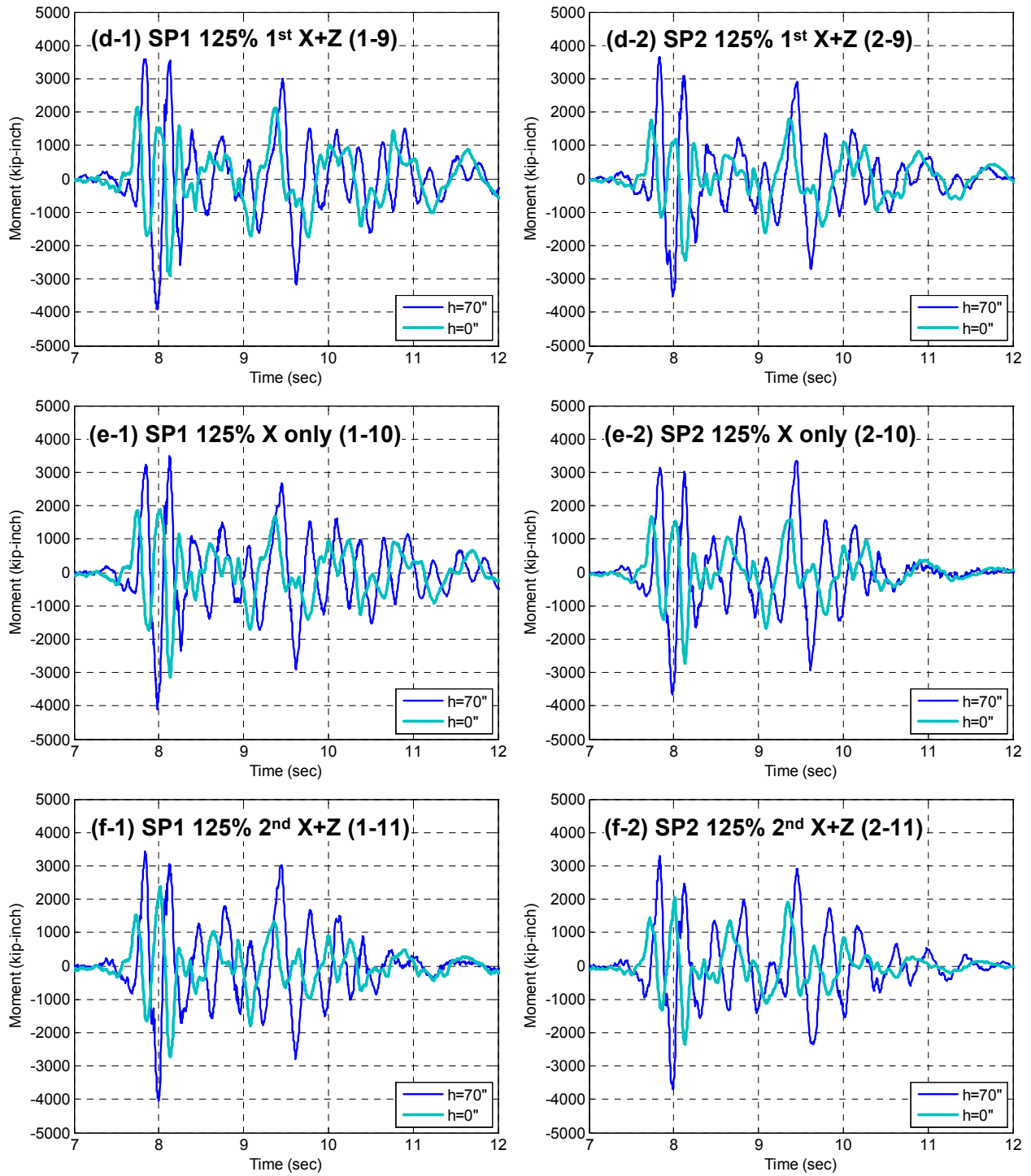


Figure 4-14: Bending moment history at the top and base of the test specimens (continued)

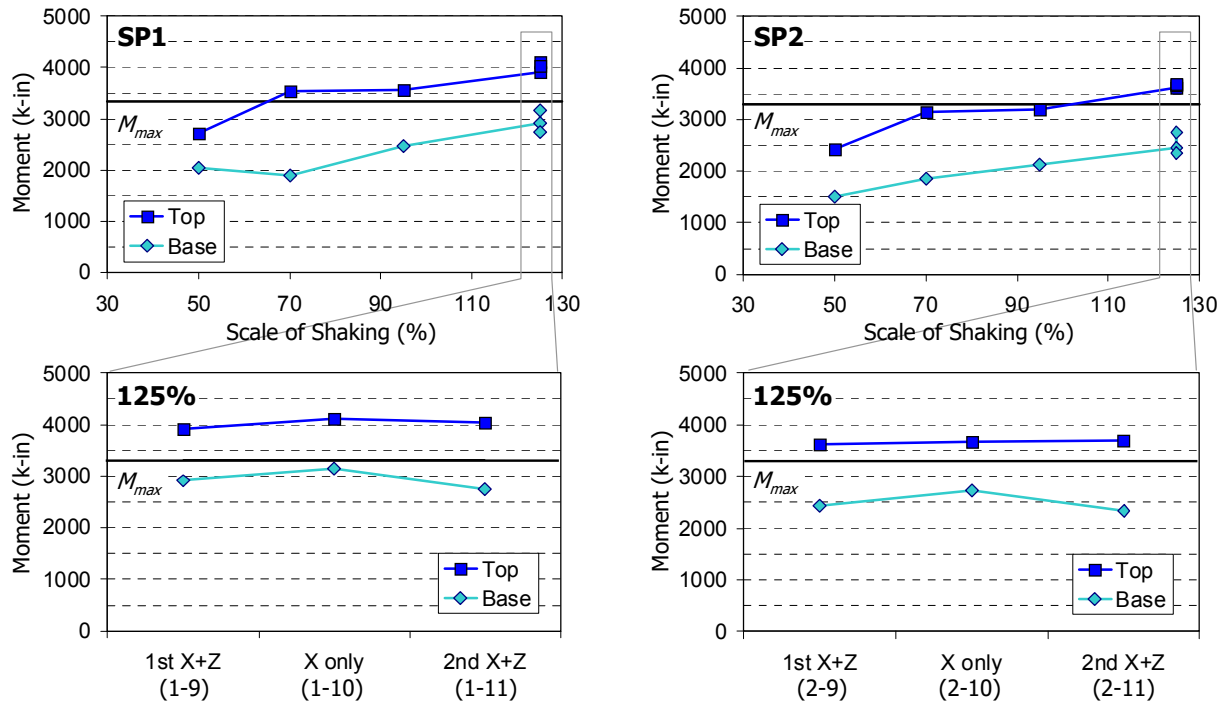


Figure 4-15: Peak bending moments at the top and base of the test specimens

## 4.5 Lateral Displacements

In this section, relative lateral displacement in the X direction is investigated. The lateral displacement histories were obtained from the wire potentiometers and the DCDTs. The locations are presented in Appendix C. Since absolute displacement was obtained from the wire potentiometers, each history was modified by subtracting the displacement at the footing to calculate the relative values. All the displacement histories presented in Figure 4-16 are in the X direction, in which the horizontal excitation was applied. Total of four wire potentiometers were connected to the south side of the column and the locations were at  $h=15''$ ,  $35''$ ,  $55''$ , and  $70''$  above the footing top. Hence, the lateral displacement variation along the column height can be examined.

The relative lateral displacement histories subjected to 50%- , 70%- , and 95%-scale motions are shown in Figure 4-16 (a), (b), and (c), respectively. In 50%- and 70%-scale tests, both specimens have the peak lateral displacement after 9 sec, i.e. after the main excitation. However, in the 95%-scale test, both specimens have the peak lateral displacement just before 8 sec. In Figure 4-17(d), (e), and (f), the displacement histories for the 125%-scale tests are shown. The peak displacement occurred around 8.14 sec, at which there was a clear 3<sup>rd</sup> peak of the shear force, refer to Figure 4-11(d), (e), and (f). It is to be noted that the displacement occurred on the positive side, which means the column deflected more toward the north side, where there was residual displacement.

compares positive (North) and negative (South) peaks before and after 9 sec. This demarcation was made since the main excitation ended roughly at 9 sec. Positive and negative values mean the top of the column deflected to the north and south sides, respectively. The positive peak was larger than the absolute value of the negative peak in most cases, and this difference increased as the intensity of the excitation increased. Except for the case of the 125%-scale '2<sup>nd</sup> X+Z' test of SP2, the positive peak increased or almost did not change for all the 125%-scale runs. The second-order approximation clearly fits well the 'North' peaks in Figure 4-18(a) and (b), but the first-order (linear) approximation is reasonable for the other cases.

The residual displacement increased at the end of every subsequent run. The residual displacement of specimen SP1 was 0.330 inch and of specimen SP2 was 0.220 inch at the top after the 125%-scale '2<sup>nd</sup> X+Z' test. At the other locations, the residual displacement was less than at the top of the column. In SP1, after the 3<sup>rd</sup> 125%-scale test, the residual displacement values were 0.044, 0.110, and 0.180 inch at  $h=15''$ ,  $35''$ , and  $55''$ , respectively. In SP2, the corresponding values were -0.005, 0.030, and 0.079 inch, respectively.

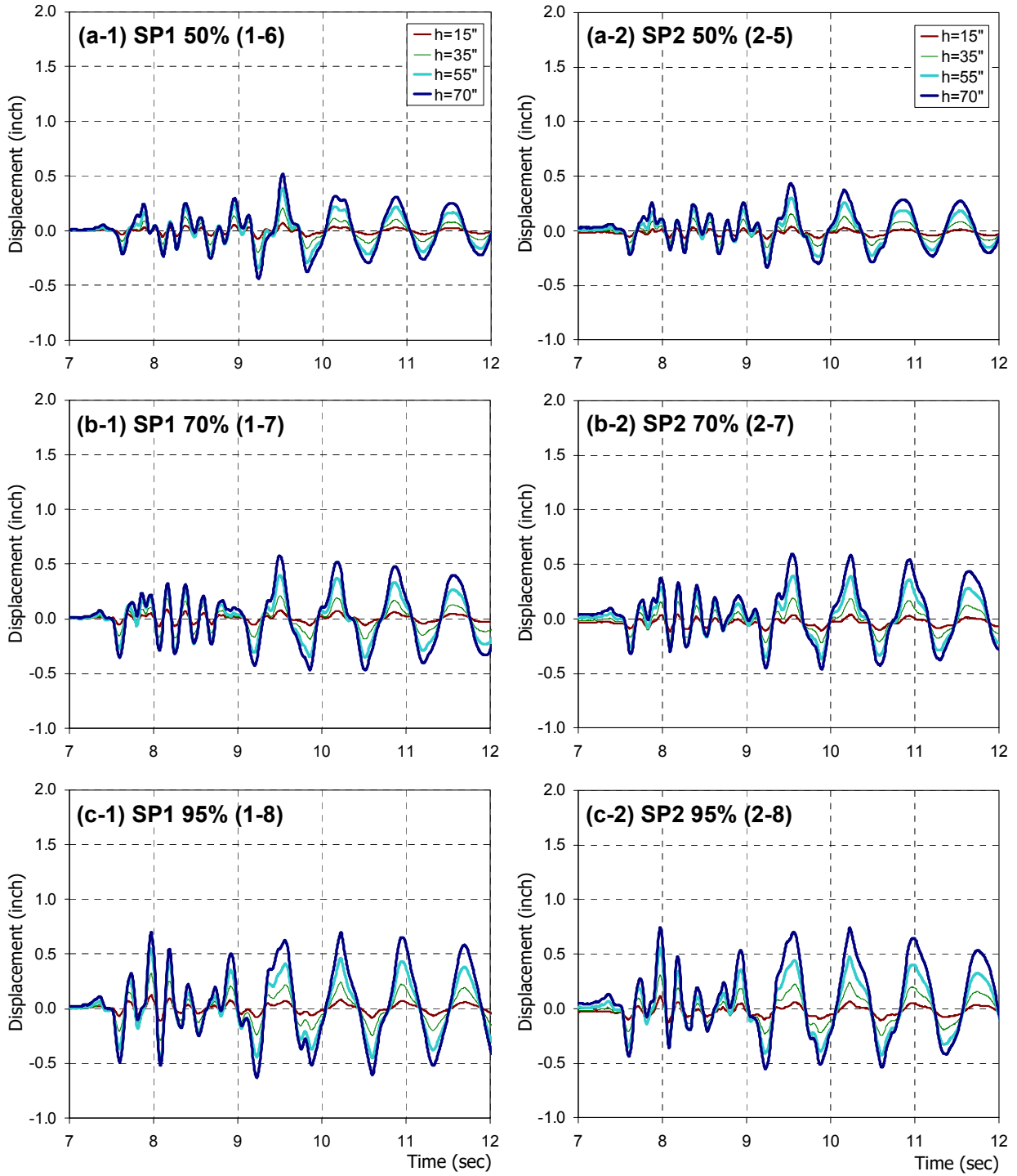


**Figure 4-16: Relative lateral displacement history**

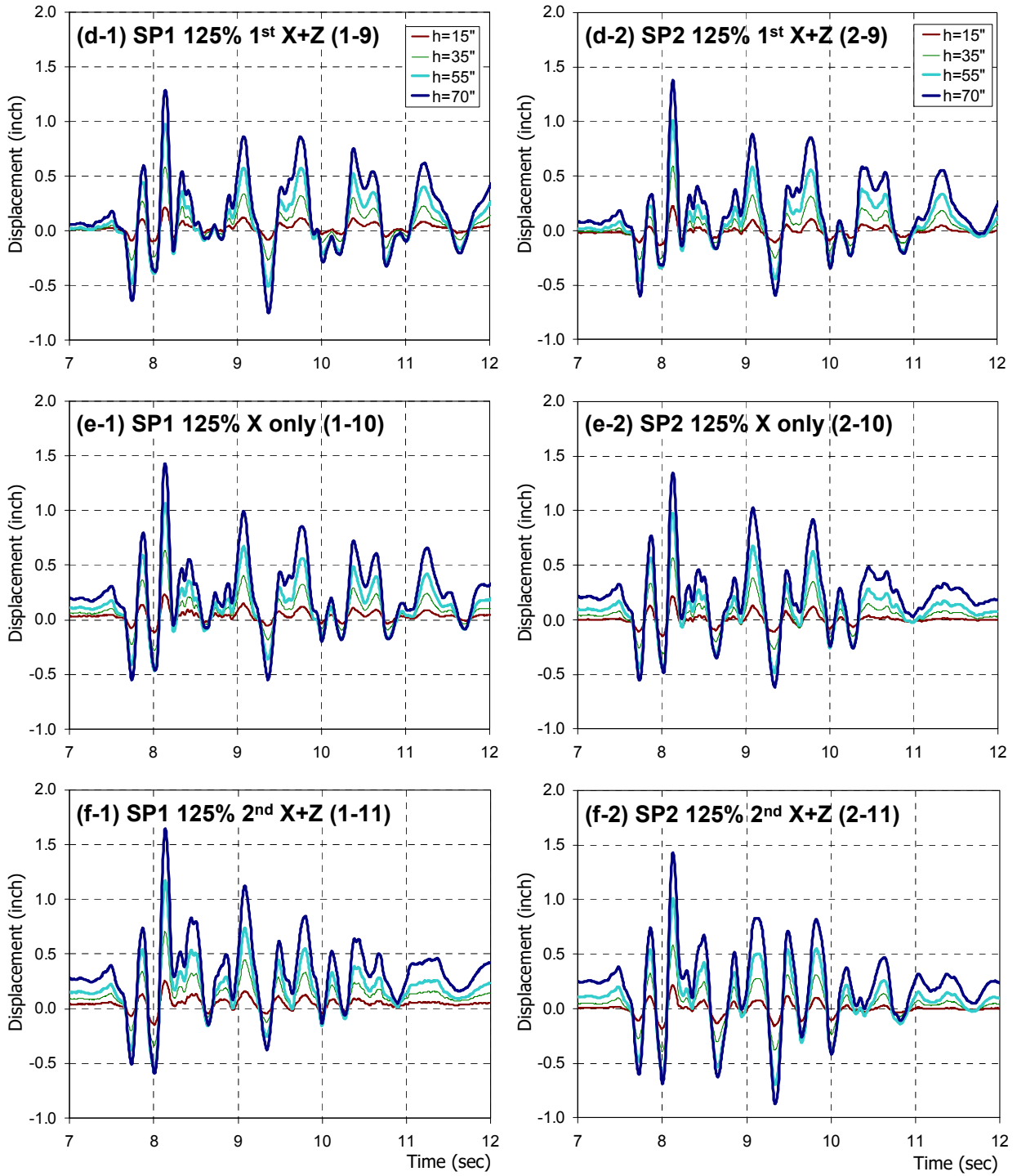
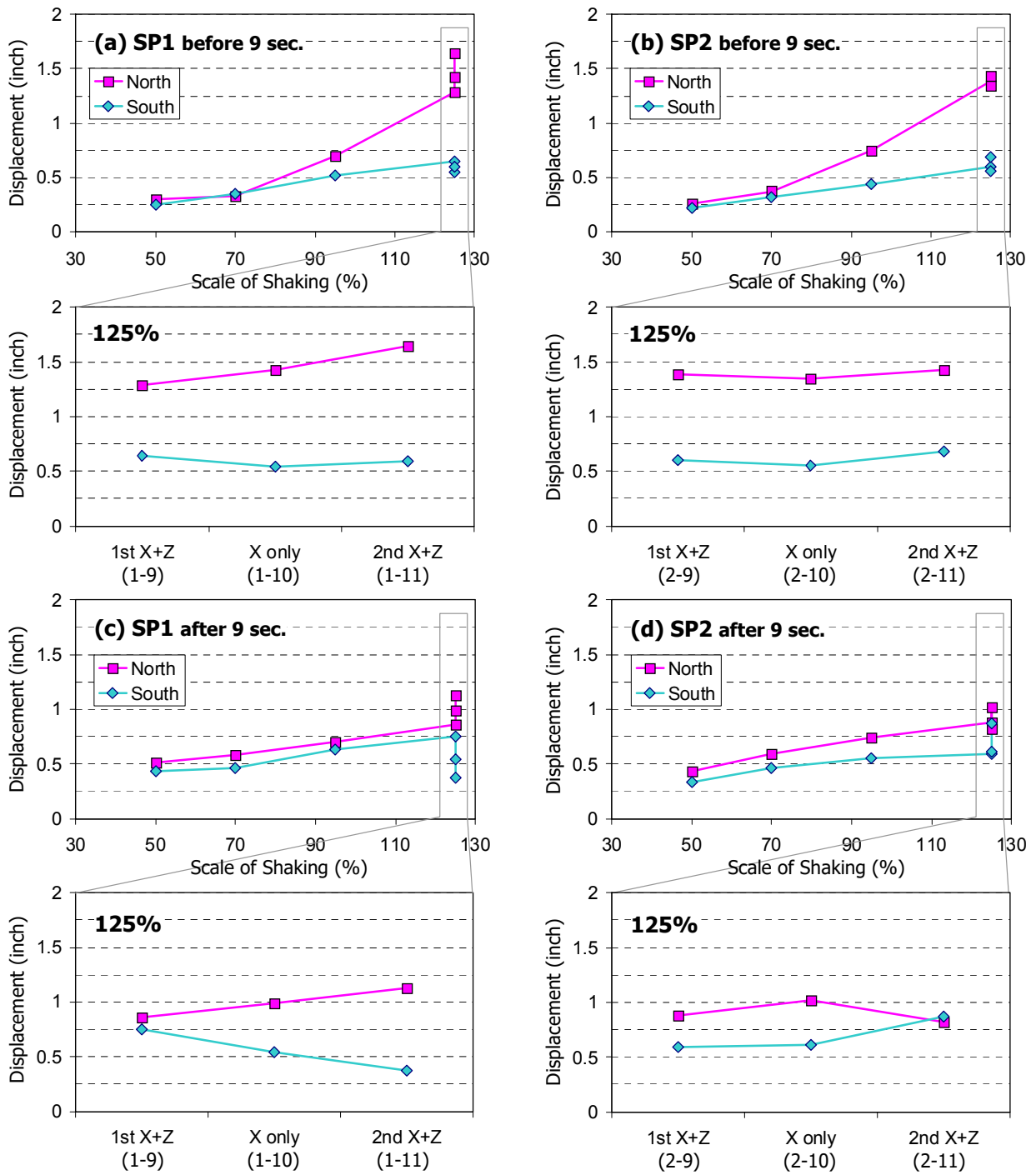


Figure 4-17: Relative lateral displacement history (continued)



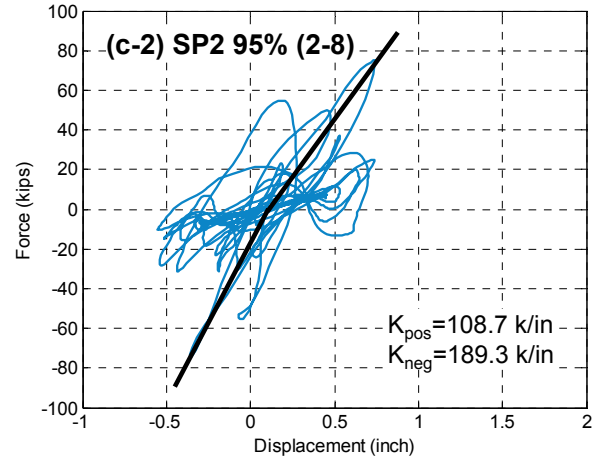
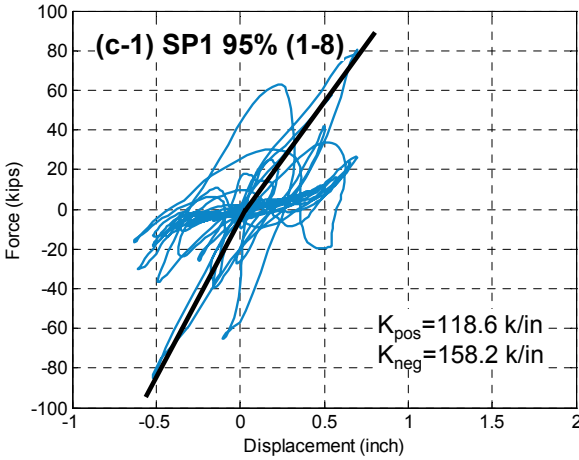
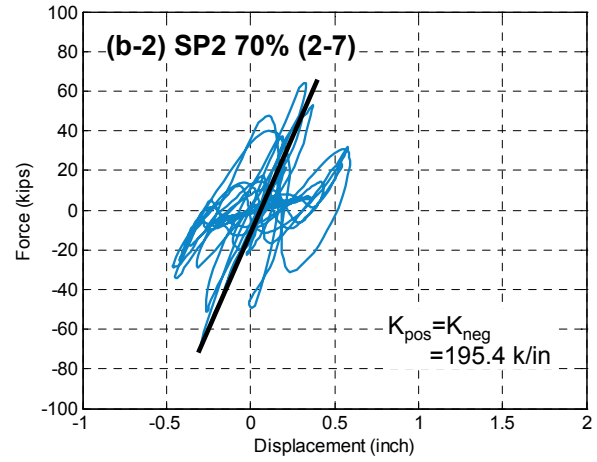
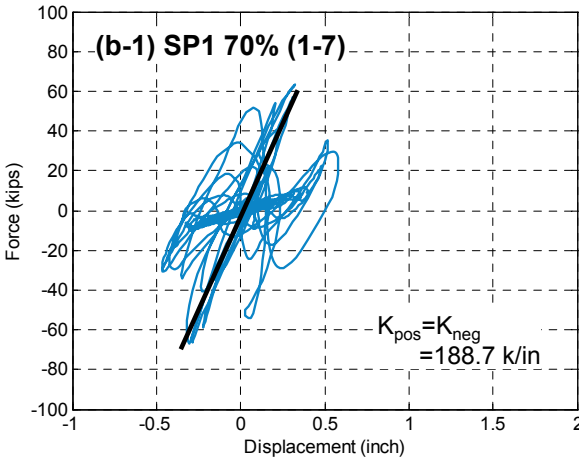
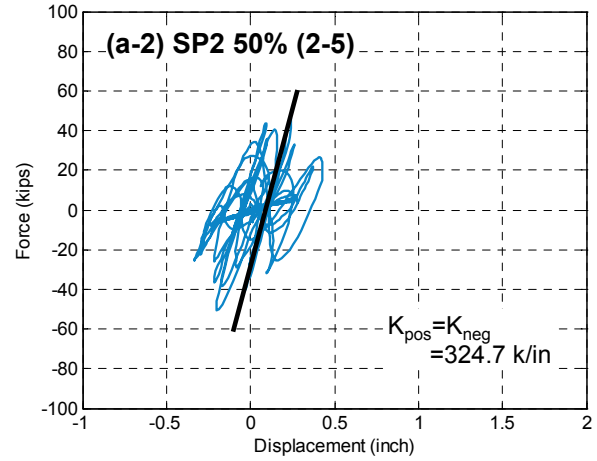
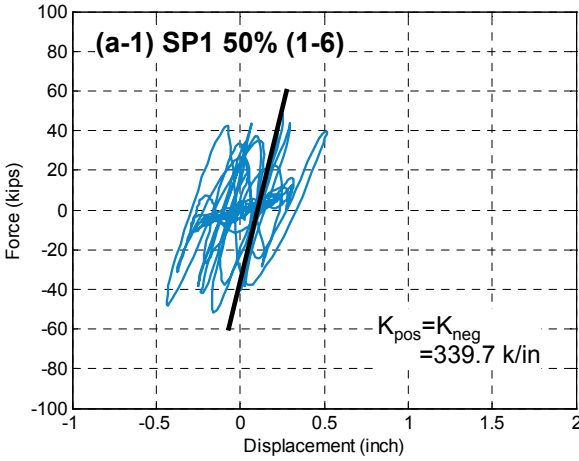
**Figure 4-18: Peak relative lateral displacement at the top of the test specimens**

## 4.6 Force-Displacement Responses

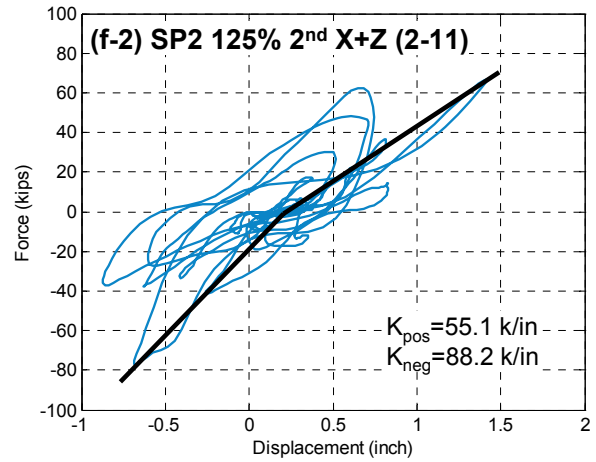
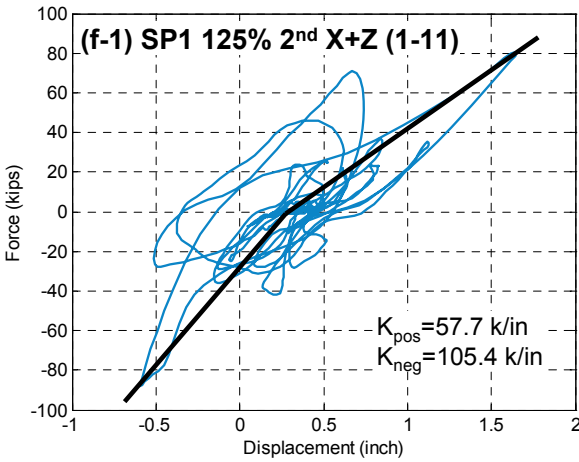
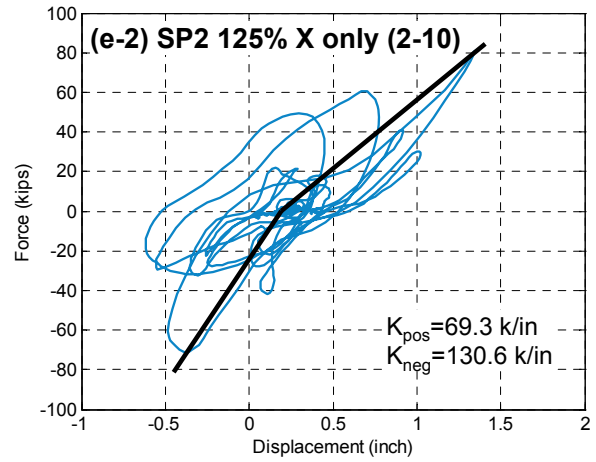
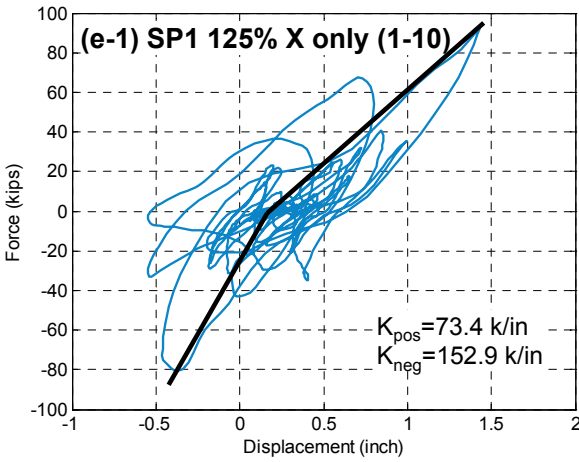
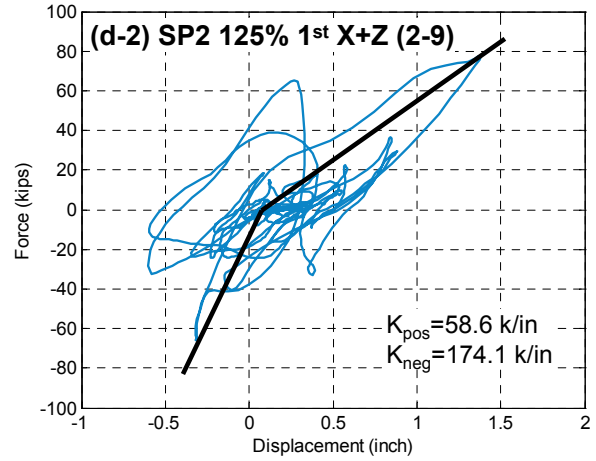
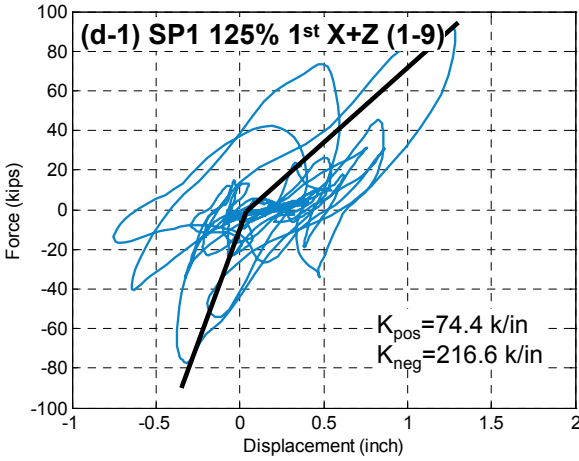
The base shear versus lateral displacement responses are shown in Figure 4-19 and Figure 4-20, and the axial force versus axial deformation responses are shown in Figure 4-21 and Figure 4-22. Note that the axial force is positive in compression and negative in tension and the axial displacement is positive in elongation and negative in shortening.

Figure 4-19 (a), (b), and (c) present the shear force-lateral displacement relationships of SP1 and SP2 subjected to the respective 50%-, 70%-, and 95%-scale motions (runs 1-7, 1-8, and 1-9 for SP1 and 2-7, 2-8, and 2-9 for SP2). Figure 4-20 (d), (e), and (f) are for the 125%-scale motions (runs 1-10, 1-11, and 1-12 for SP1 and 2-10, 2-11, and 2-12 for SP2). The decrease in the lateral stiffness with increasing damage was observed as the intensity of the ground motion increased. In addition, the stiffness on the positive force and displacement quadrant was smaller than that on the negative side, which was a consequence of the pulse in the ground motion resulting in asymmetric displacements and accordingly asymmetric damage distribution. As mentioned previously, the decrease in the maximum positive force in the 125% '2<sup>nd</sup> X+Z' test with respect to the 125% 'X only' test can be partly attributed to the decrease in shear force capacity due to the presence of axial tension. In addition, it should be noted that the maximum positive and negative shear forces of SP2 (95%- and 125%-scale tests) were smaller than those of SP1 since SP2 had lower shear capacity due to transverse reinforcement with wider spacing.

Figure 4-21 (a), (b), and (c) present axial force-vertical displacement relationships of SP1 and SP2 subjected to the respective 50%-, 70%-, and 95%-scale motions (runs 1-7, 1-8, and 1-9 for SP1 and 2-7, 2-8, and 2-9 for SP2). It can be confirmed that the column was not under significant tension before the 125%-scale motion was applied. It should be noted that the gravity load was about 100 kips from the load cells measurements, which represents the origin of the force in the axial force-deformation relationships. It was observed that the axial elongation was almost eight times the axial shortening due to the opening of the cracks. From Figure 4-22(d), (e) and (f), it can be confirmed that the vertical component of the 125%-scale motion caused tension and significant compression in the column as discussed previously. The axial force due to the excitation with horizontal component only was between 50 and 150 kips (the axial force variation under only horizontal component was due to the presence of vertical acceleration on the shaking table resulting from the interaction of the vertical and horizontal actuators to balance the overturning moment), but that subjected to both horizontal and vertical components was between -70 and 250 kips.



**Figure 4-19: Shear force-lateral displacement response**



**Figure 4-20: Shear force-lateral displacement response (continued)**

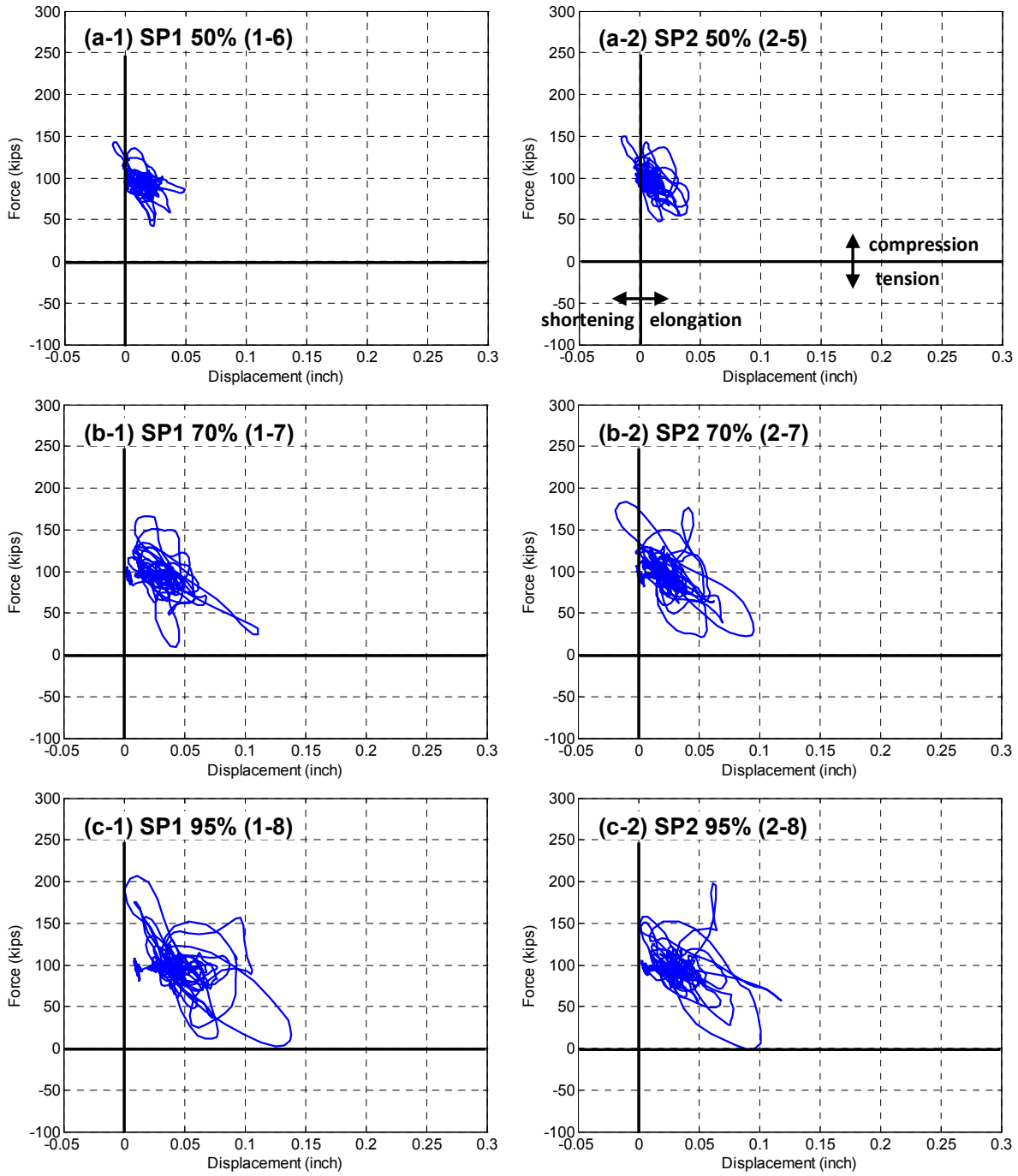


**Figure 4-21: Axial force-verticle displacement response**

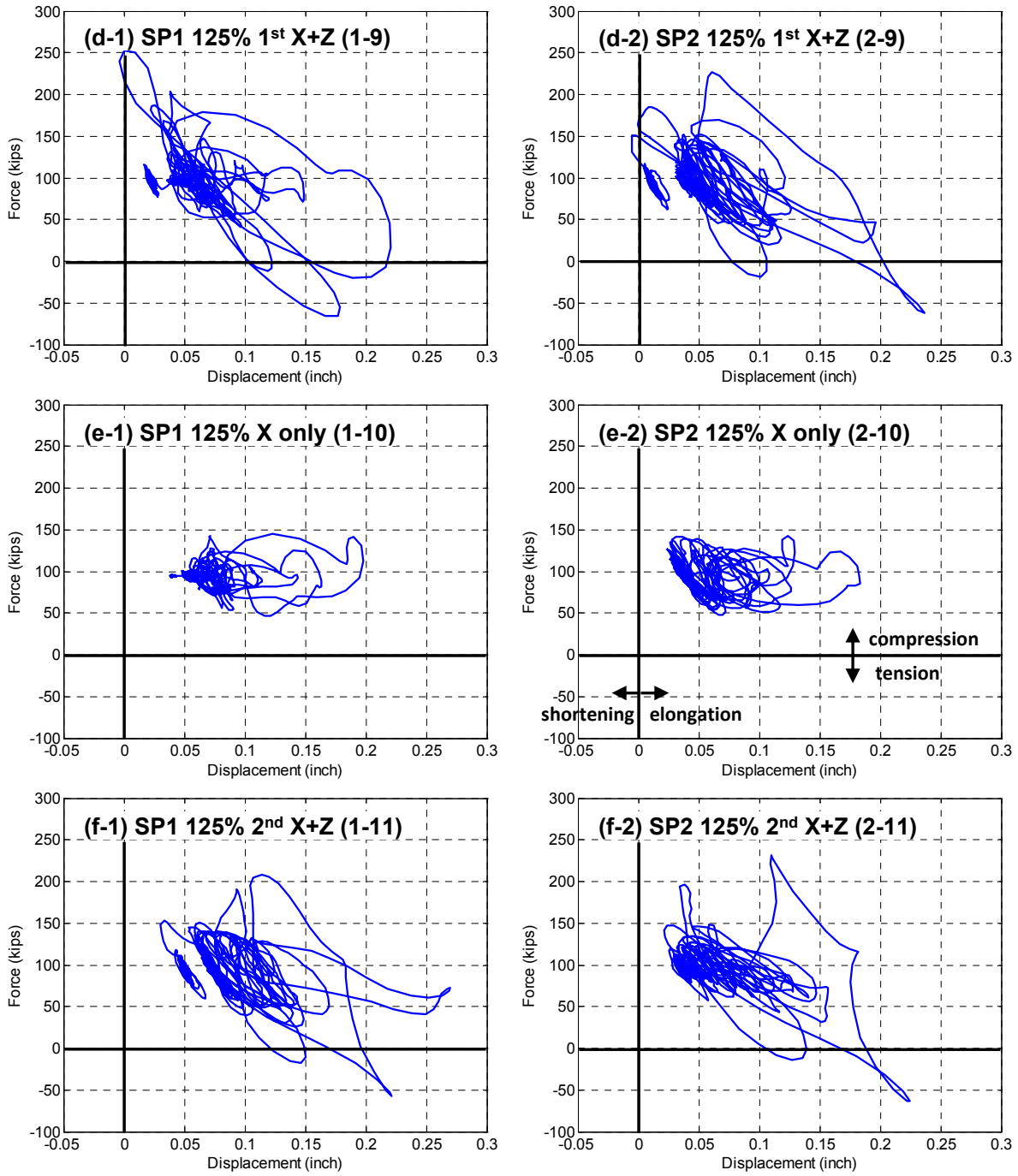


**Figure 4-22: Axial force-vertical displacement response (continued)**

The straight lines in Figure 4-19 and Figure 4-20 show the effective (secant) lateral stiffness of each test. The stiffness was calculated based on the maximum shear force on the positive and negative sides and the corresponding lateral displacement. Up to 70%-scale test, the stiffness value on the positive side was identical to that on the negative side. However, as the intensity level increased, the stiffness decrease in the positive side was more significant. During the 125% '1<sup>st</sup> X+Z' and the subsequent tests, the stiffness change was not remarkable on the positive side (positive was defined as the direction from south to north) but the decrease continued on the negative side. This trend implied that more damage initially occurred on the south side of the column. Subsequently, the damage extended to the north side of the column. These observations were consistent with the crack propagation patterns presented in the following section. It should be noted that the stiffness values were different from those obtained from the pullback tests where the column was predominantly deflecting in the 1<sup>st</sup> translational mode. However, during the ground excitations, the column deflected in a shape which was a combination of translational and rotational modes. Hence, stiffness values calculated from the force-displacement relationships up to 95%-scale tests were on average larger than the lateral stiffness from the pullback test.

## 4.7 Crack Propagation

Crack initiation and propagation of specimens SP1 and SP2 are shown in Figure 4-23 through Figure 4-28. It should be noted that thicker lines represent new cracks which did not exist in the previous runs. After the 50%-scale test, only three or four cracks appeared near the top on the south and north sides of SP1 while SP2 had more cracks in the upper part and the first shear crack appeared near  $h=60''$ . The lower part of each test specimen experienced less cracks than the upper part. Finally, SP2 had the first vertical crack near  $h=40''$  on the north side. After the 70%-scale test, several shear cracks appeared near the top on the east and west sides of the column. They were near or above  $h=50''$  in SP1 and some shear cracks appeared even between  $h=35''$  and  $50''$  in SP2. In addition, SP2 had a significant number of vertical cracks above  $h=20''$  on the north side. Cover spalling started at the top on the north and south sides and shear cracks appeared near the bottom on the east and west sides after 95%-scale test (runs 1-8 for SP1 and 2-8 for SP2). As a result, there were several shear cracks along the height of the columns except the regions between  $h=25''$  and  $35''$  on the east and west sides of SP1 and between  $h=20''$  and  $35''$  of SP2. SP1 had vertical cracks above  $h=30''$  on the north and above  $h=20''$  on the south. SP2 had similar cracks above  $h=10''$  on the north and between  $10''$  and  $30''$  on the south. As the intensity increased, cracks extended over the column. In particular, the shear cracks were visible clearly after 125%-scale motions except for the middle of SP1 ( $h=30''$  to  $40''$ , i.e. 1.5D to 2.0D). Compared to the 125%-scale 'X+Z' tests, the 'X only' test produced significantly less shear and vertical cracks. This observation is consistent with the reduction of shear strength at '2<sup>nd</sup> X+Z' test with respect to the 'X only' test. After the 125%-scale '2<sup>nd</sup> X+Z' test, the vertical cracks extended over the column, except for the region between  $h=10''$  and  $20''$  of SP1. In addition, it is observed that the crack distribution of SP2 was denser than that of SP1 subjected to the same intensity level due to lower shear capacity of SP2 compared to SP1. Photographs showing the final damaged state of the specimens is presented in Figure 4-29.

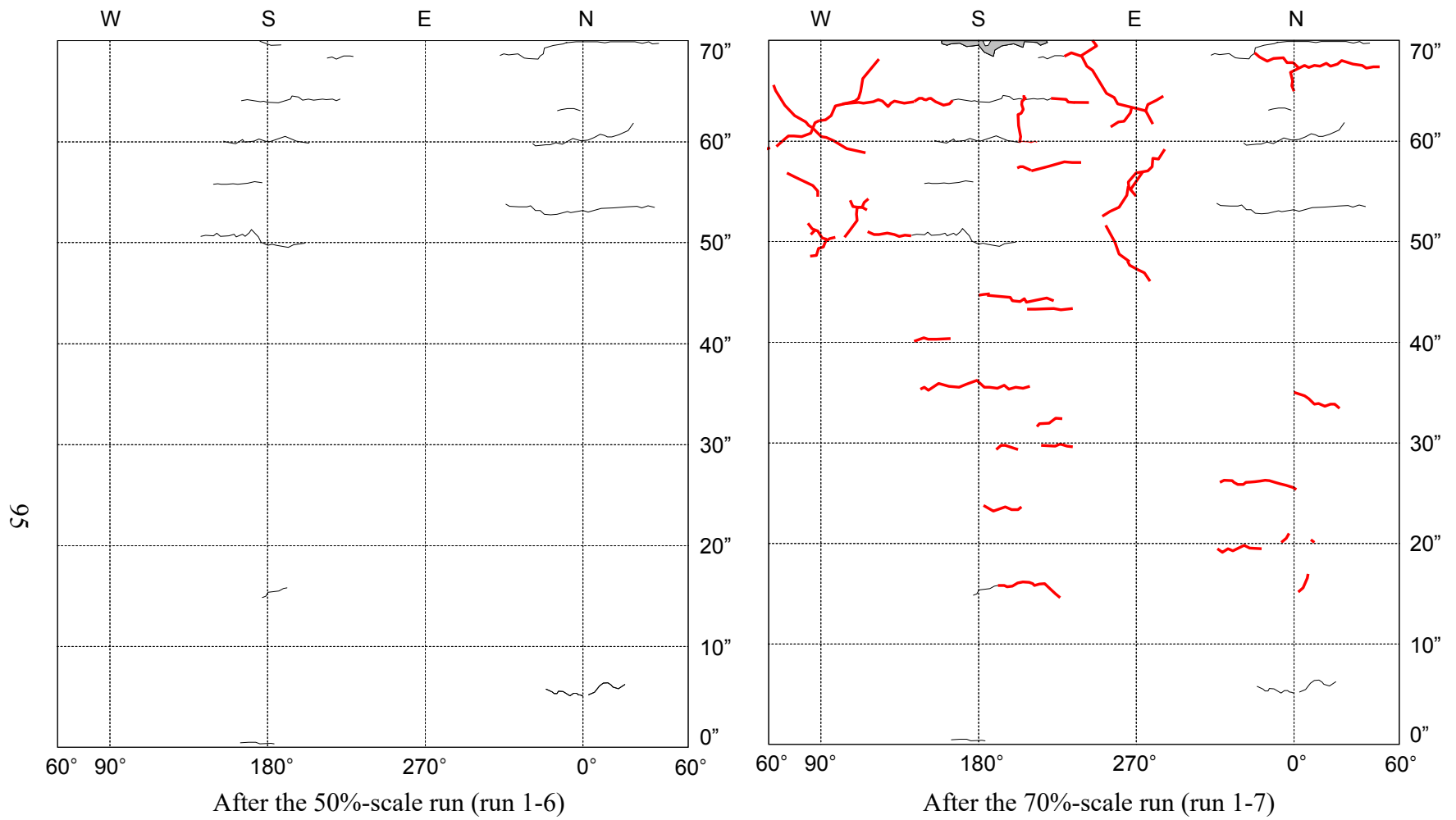


**Figure 4-23: Crack propagation of SP1**

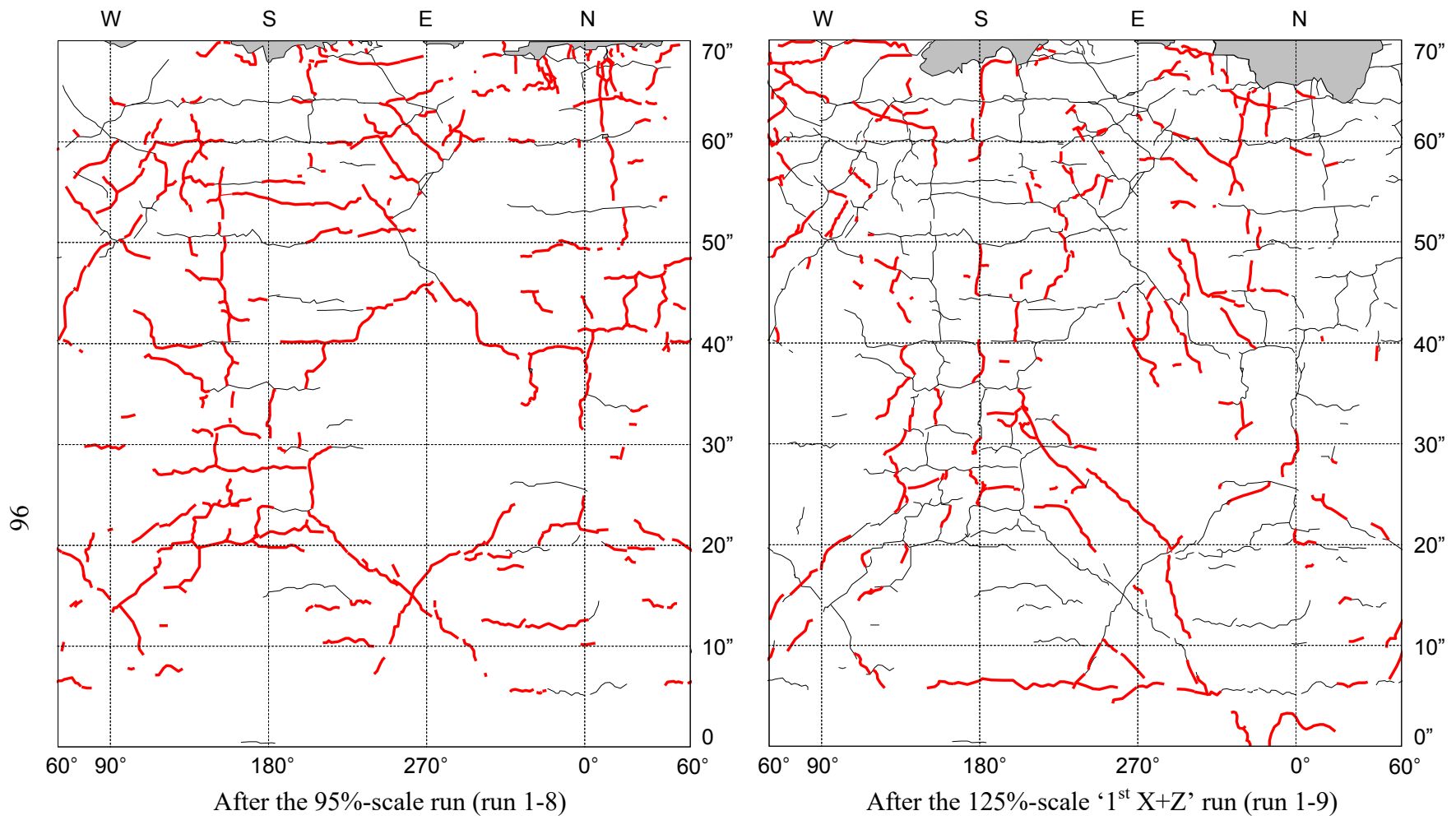


**Figure 4-24: Crack propagation of SP1 (continued)**

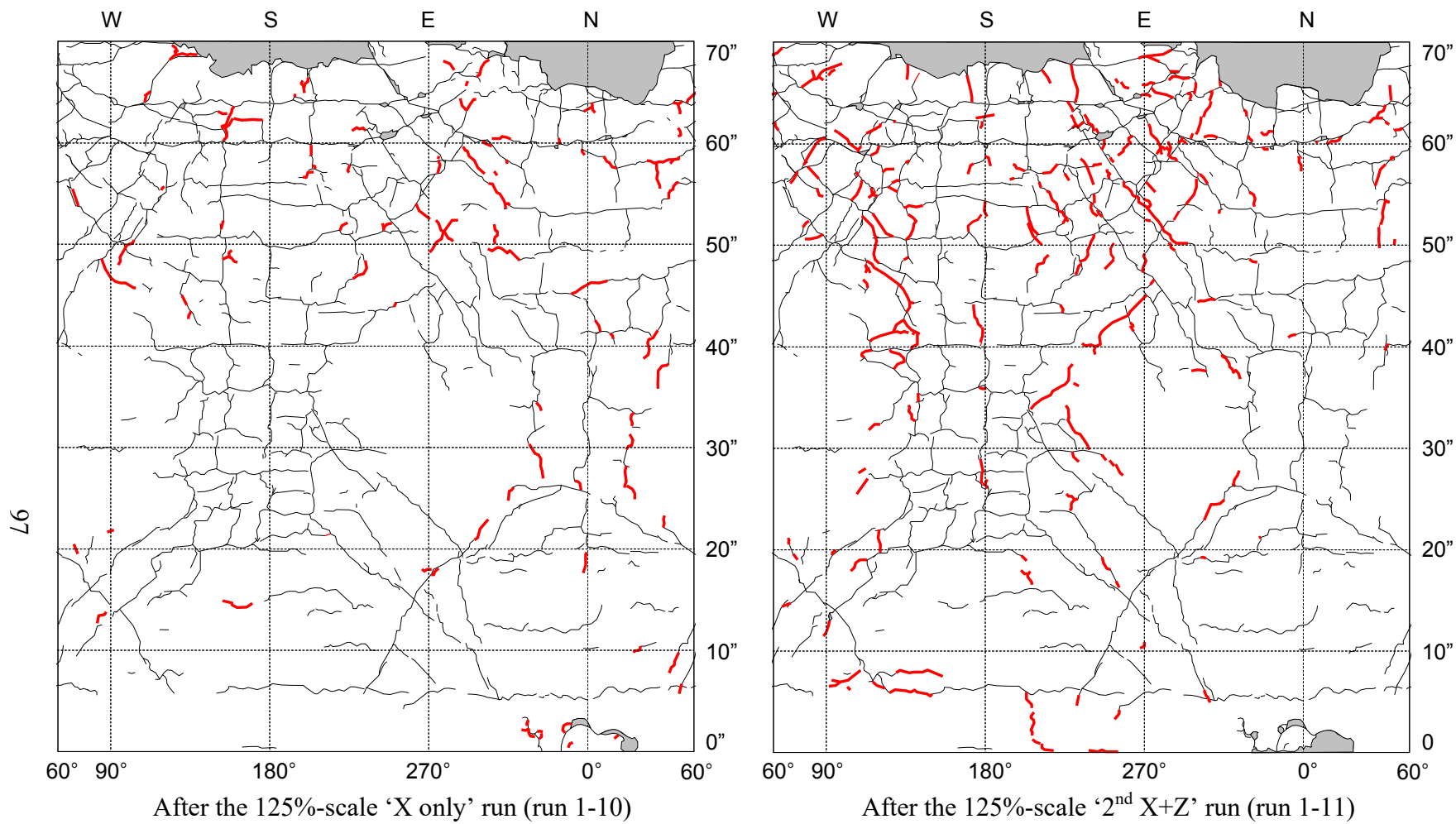


**Figure 4-25: Crack propagation of SP1 (continued)**

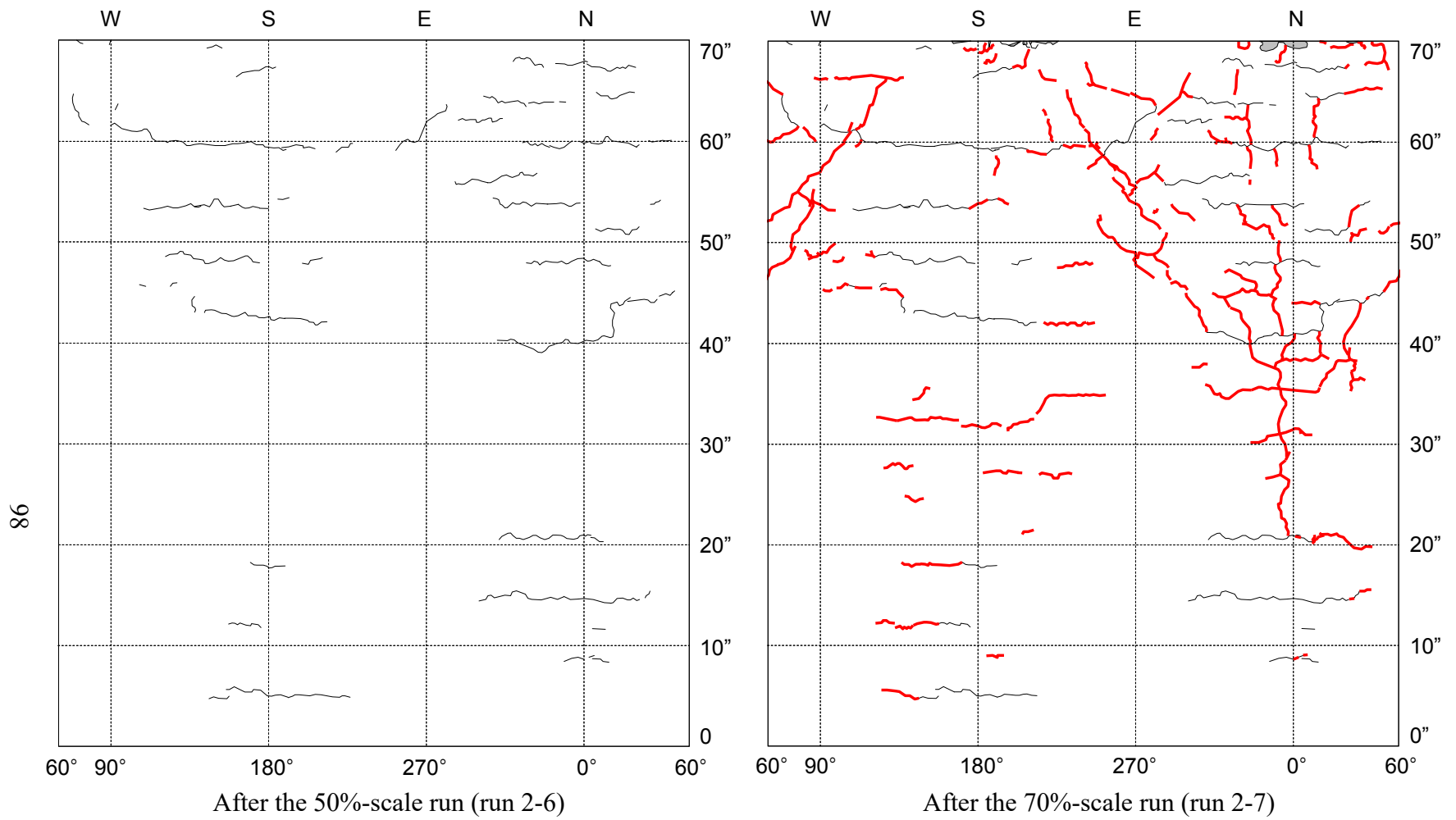


**Figure 4-26: Crack propagation of SP2**

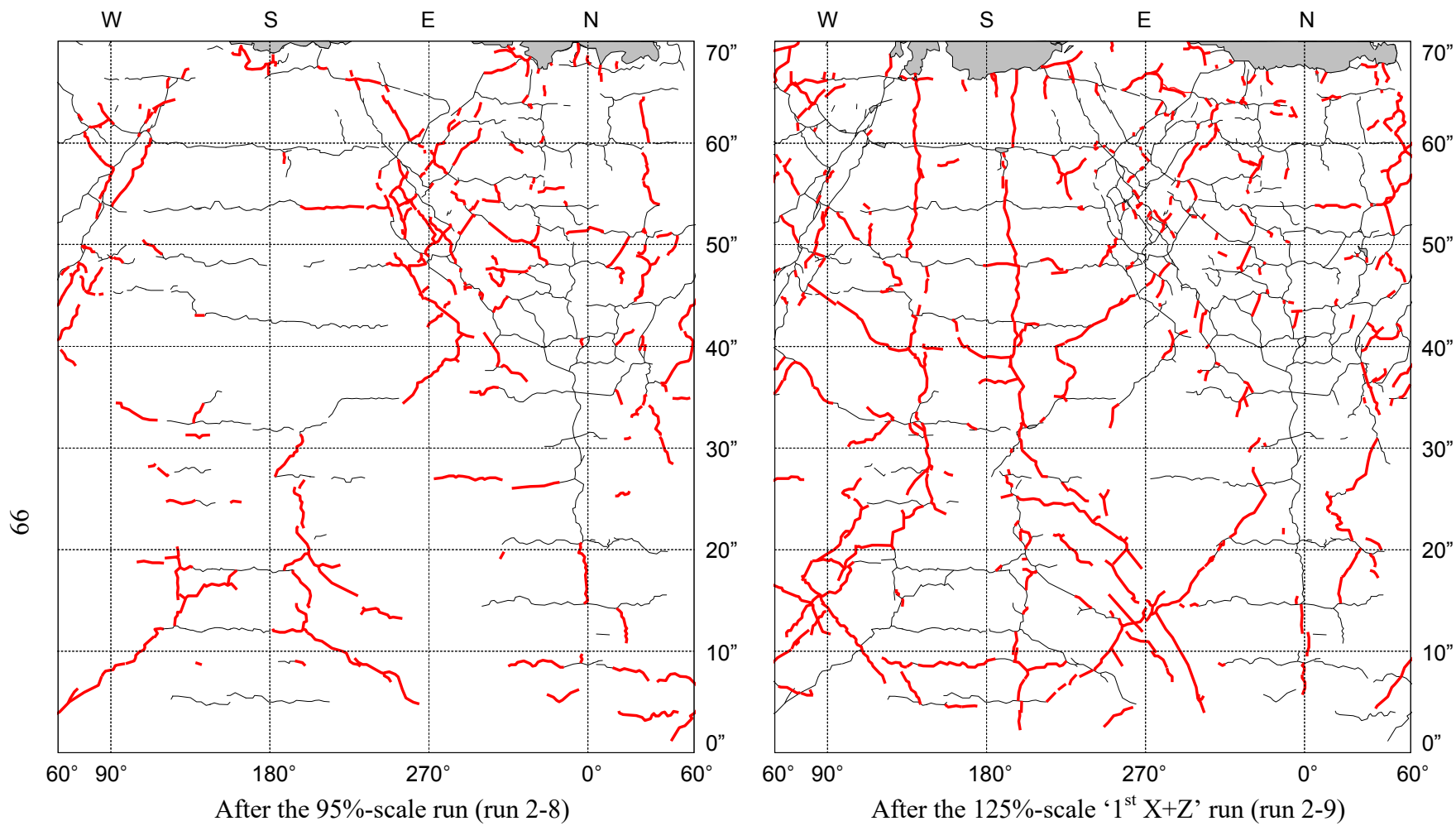


**Figure 4-27: Crack propagation of SP2 (continued)**

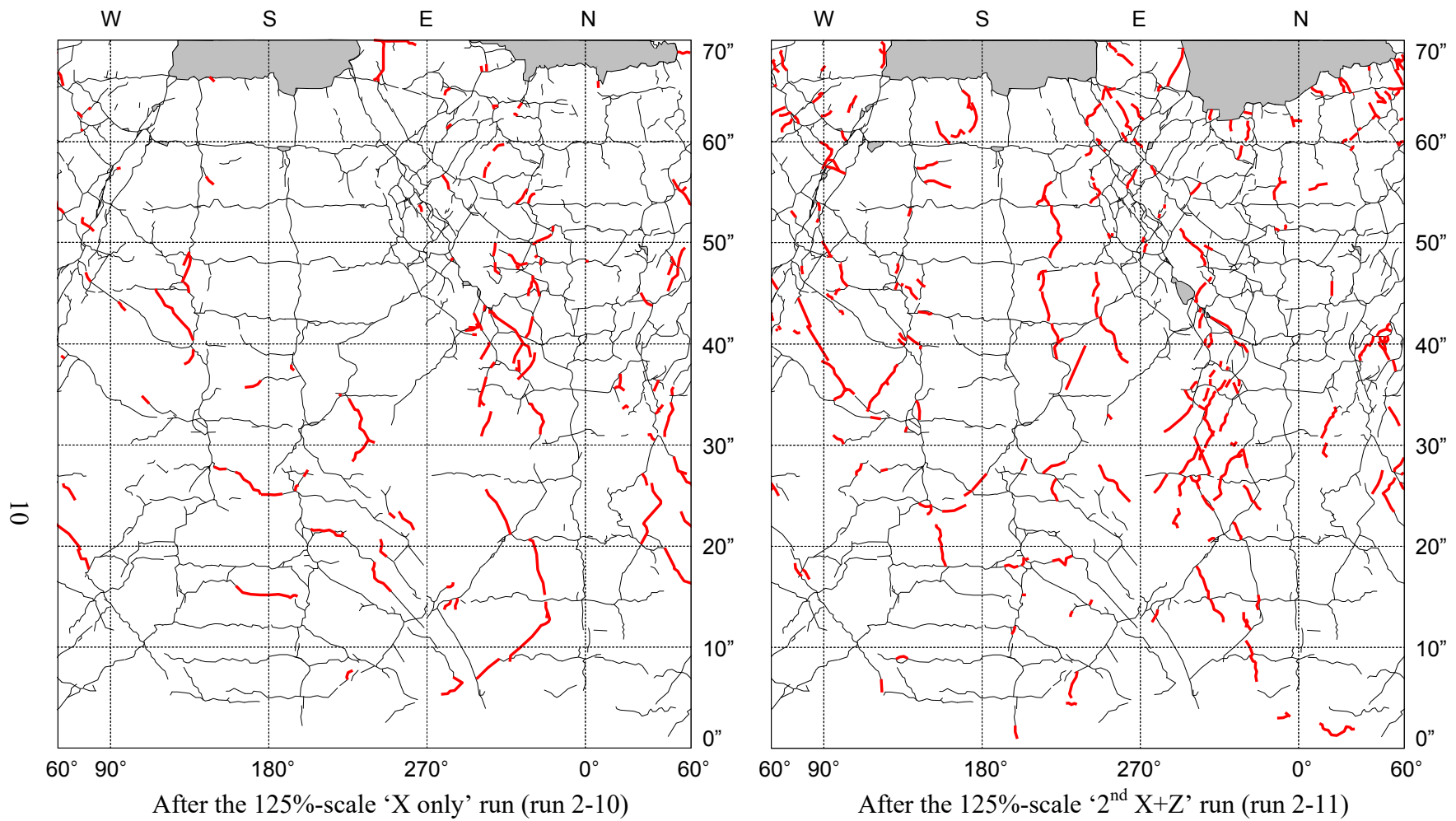


**Figure 4-28: Crack propagation of SP2 (continued)**

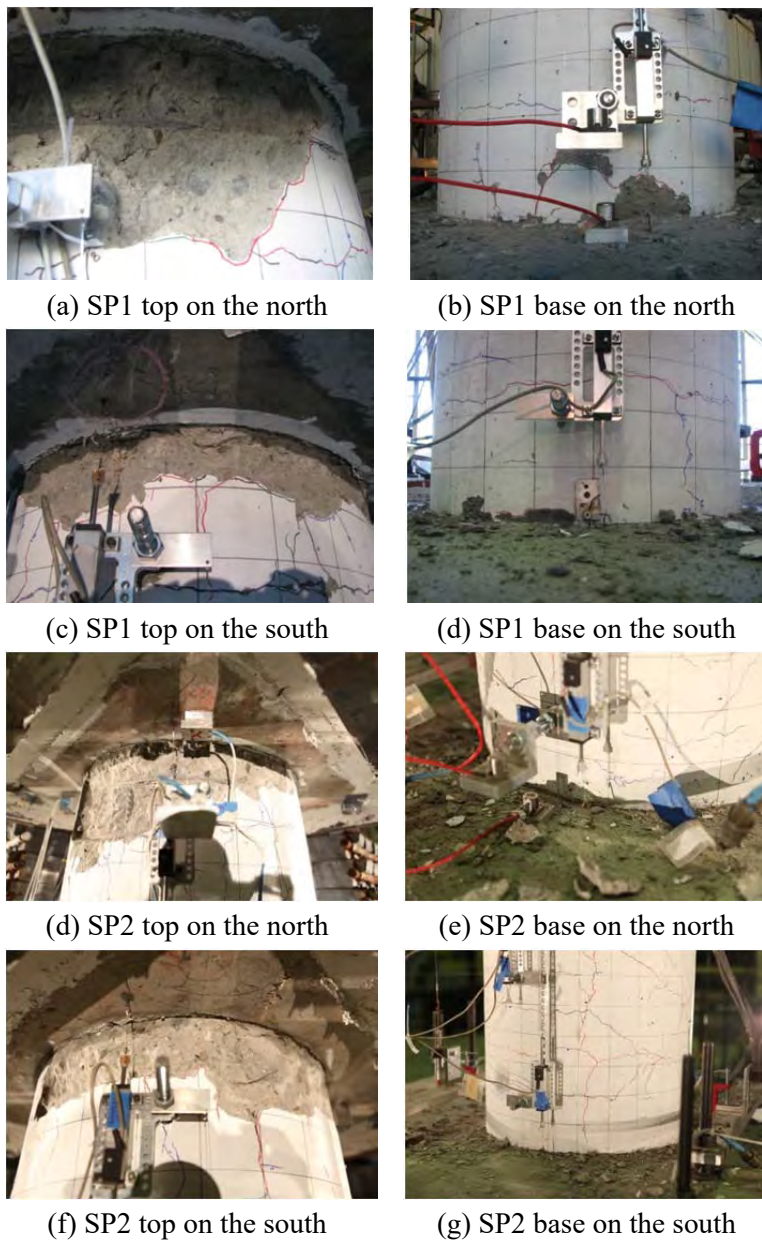


**Figure 4-29: Test photographs of the top and base of column, after 125%-scale tests (Runs 1-11, 2-11)**

## 4.8 Local Member Responses

Local response measures were gathered during the tests by means of 38 strain gages in each specimen. Locations of these gages are specified in Appendix C. They provide information on the sectional response during the test. The recorded curvatures, longitudinal and transverse

strains are presented in this chapter. In addition, the relationships of each response quantity and the force histories discussed in Chapter 4 are investigated.

#### 4.8.1 Section Curvatures

To measure the curvature at certain points on the north and south sides of the column, LVDTs were installed on the instrumentation rods and the locations of these LVDTs are shown in Appendix C. As an alternative to the calculation of the curvatures using the LVDTs, the longitudinal reinforcement strain data obtained from the strain gages can also be used. Theoretically, the curvatures from the LVDTs and from the strain gages should be the same if they were installed at the same height. However, differences exist because of the averaging effect of the LVDT measurements compared to the point-wise strain gages measurements. Since the strains obtained from the gages were less noisy, and were not affected by averaging, the curvatures presented in this section were computed using the strain measurements along the longitudinal reinforcing bars. Sign convention for curvature is such that it is positive when  $(\varepsilon_{SL} - \varepsilon_{NL})$  is positive, where  $\varepsilon_{NL}$  and  $\varepsilon_{SL}$  are the longitudinal strain on the north and south bars, respectively. This convention results in consistent signs for displacements and curvatures, i.e. when displacement is positive, curvature is also positive.

Up to the 70%-scale motion, both specimens had similar curvature time histories. Also, the curvatures of both specimens remained within  $\pm 0.5 \times 10^{-3} \text{ in}^{-1}$ , and no residual curvature was detected. The first noticeable difference of the magnitude of curvatures for the two cross-sections (top and bottom) appeared during the 95%-scale motion. The curvature at  $h=60''$  had residual curvatures of  $-0.41 \times 10^{-3}$  and  $-0.28 \times 10^{-3} \text{ in}^{-1}$  for SP1 and SP2, respectively. Under the same motion, there was no residual curvature at the cross-section at  $h=10''$ . It should be noted that the curvature of the cross-section near the top of the column was influenced more by the higher modes of vibration than that of the cross-section near the bottom of the column. This was manifested in the form of superposed small amplitude high frequency oscillations in the curvature time history of the cross-section near the top of the column due to the effect of the rotational mode of vibration.

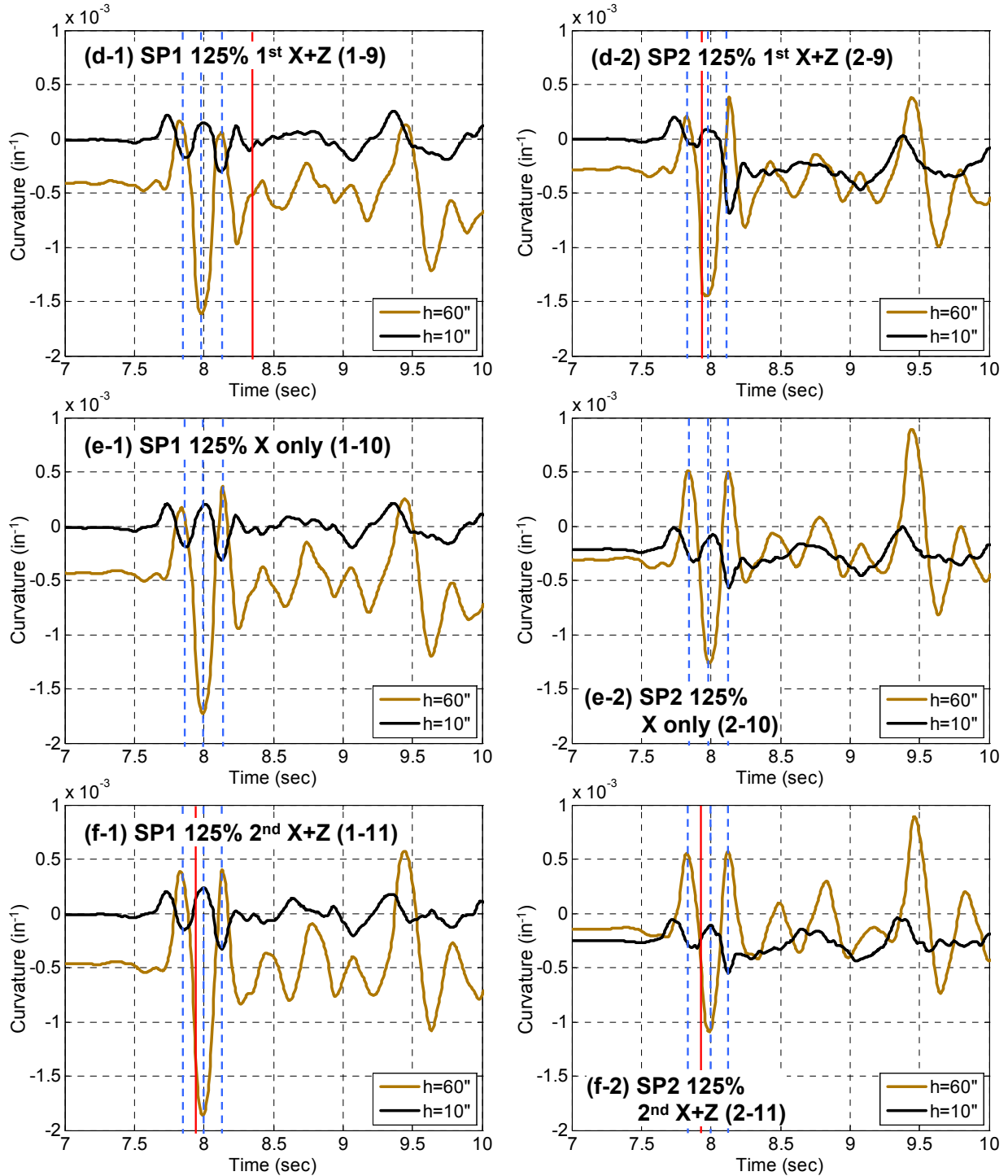


**Figure 4-30: Curvature response history at column bottom ( $h=10''$ ) and top ( $h=60''$ )**

In the 125%-scale tests, as shown in Figure 4-30, SP1 and SP2 experienced different curvature demands. In these figures, three dashed vertical lines indicate the time of the shear peaks and the solid vertical line indicates the time of the axial tension peak which is over 50 kips. The main

shear peaks, i.e. two positive and one negative shear peaks, appeared between 7.8 and 8.2 sec of each test, as discussed in the previous chapter. First, specimen SP1 did not experience any residual curvature while specimen SP2 had a residual curvature of approximately  $-0.25 \times 10^{-3} \text{ in}^{-1}$  at  $h=10''$  at the end of the 2<sup>nd</sup> X+Z test. Second, the curvature at  $h=60''$  increased as the 125%-scale runs were repeated with the residual curvature approaching zero, from  $-0.31 \times 10^{-3} \text{ in}^{-1}$  (run 1-9) to  $-0.14 \times 10^{-3} \text{ in}^{-1}$  (run 1-10) to  $-0.08 \times 10^{-3} \text{ in}^{-1}$  (run 1-11). Also, the peak-to-peak amplitudes in SP1 increased significantly as the 125%-scale runs were repeated, but they did not in SP2. The column was in double curvature during the strong motion part of the excitation between 7.5 and 8.5 sec, and large curvature peaks occurred at the shear peaks. However, after 9.5 sec, the column experienced a more complex curvature pattern due to the large curvature peaks and concentration of damage at  $h=60''$  unlike the responses at smaller intensities. In general, the curvature at the top cross-section of the column was at least three times higher than that at the bottom cross-section at shear peaks when tensile strain occurred at the top.

## 4.8.2 Moment-Curvature Response

The recorded moment-curvature responses of the two specimens subjected to the 125%-scale motions are presented in Figure 4-31. As noted earlier, the bending moment at the top was larger than that at the base. This was consistent in all the tests and the moment peaks at  $h=60''$  were larger than the peaks at  $h=10''$  by up to 90%. In the lower intensity tests (up to 70%-scale), both specimens had almost linear moment-curvature relationship. Nonlinear response was evident at  $h=60''$  under the 95%-scale motion and the tangent of the moment-curvature relationship at  $h=60''$  started to degrade; however, the moment-curvature relationship remained linear at  $h=10''$  and the maximum values were similar to those in the smaller intensity level tests.

In 125%-scale tests, the two specimens had different moment-curvature responses. Due to different residual curvature, the relationships at the same height,  $h=10''$  or  $h=60''$  did not have the same origin. For example, the residual curvature for specimen SP1 at  $h=10''$  remained zero for all tests, but that of SP2 became roughly  $-3.0 \times 10^{-5} \text{ in}^{-1}$  after the 125%-scale '1st X+Z' test, i.e. SP2 experienced more damage at  $h=10''$  than SP1.

The initial tangent of the moment-curvature relationship at  $h=60''$  of both specimens, as shown by the superposed straight lines decreased by about 17% in 'X only' test compared to '1st X+Z' test, but remained almost the same in the '2nd X+Z test'. Finally, due to less damage of the column bottom cross-section compared to that of the column top cross-section, the reduction of the initial tangent at  $h=10''$  was not as noticeable compared to that at  $h=60''$ .

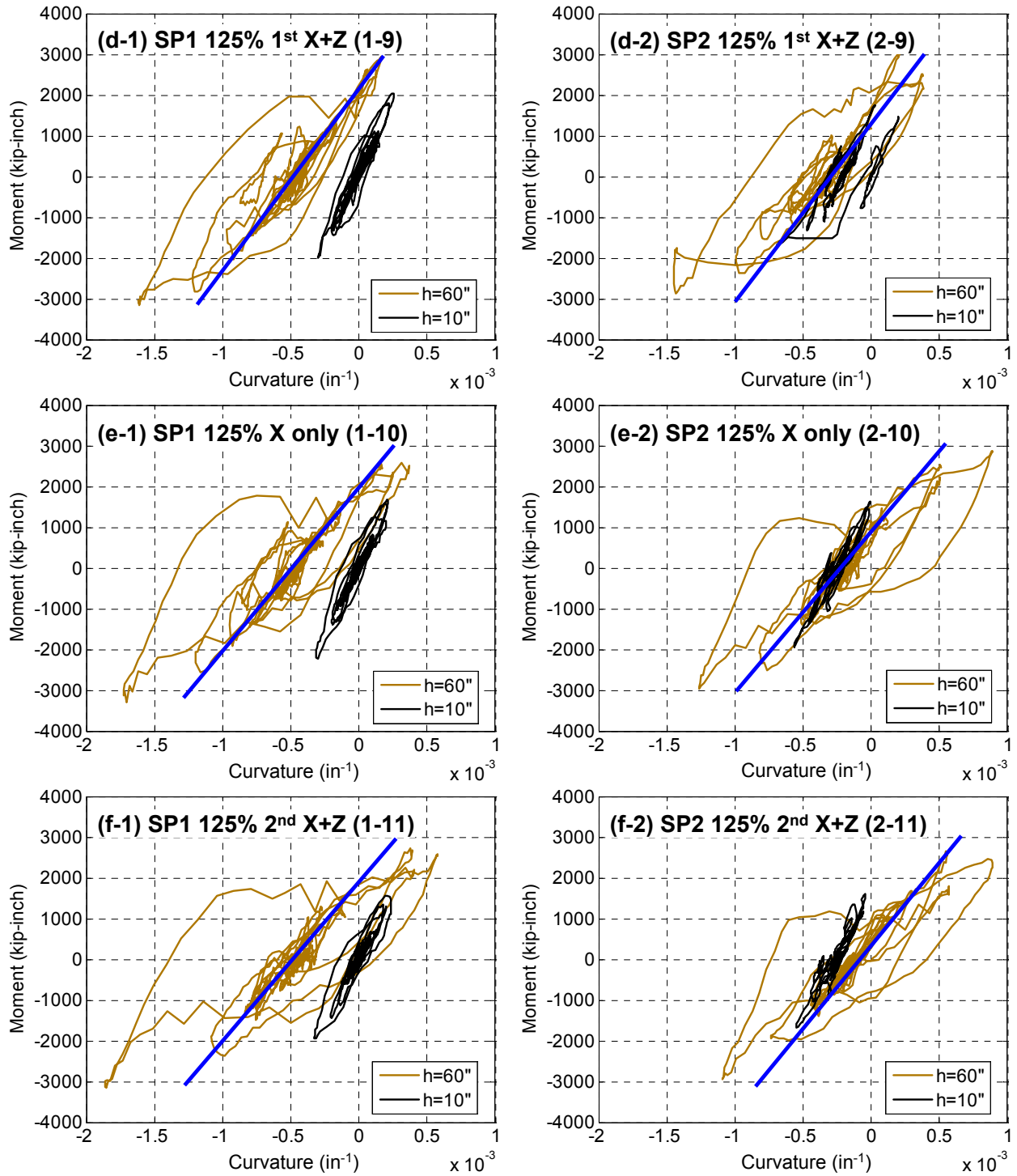


Figure 4-31: Moment-curvature response at  $h=10''$  and  $h=60''$

### 4.8.3 Longitudinal Strains

Basic characteristics of the recorded strains in the longitudinal bars are summarized in this section. Full details of the recorded longitudinal strain histories during the three 125%-scale tests are reported in Appendix D. Note that positive strain indicates shortening (compression) and negative strain indicates elongation (tension). To observe the response at the times of the axial tension and shear peaks, one solid line (for axial tension) and three dashed lines (for shear) are superposed on the time histories.

There was a remarkable difference in the strain history along the height. For example, the strain at NL1 indicated compression at the first shear peak, but the strain became tensile as the height increased and NL6 showed a tensile strain peak at that point. This behavior was observed at other shear peaks and on the south side as well. This behavior implies that the test specimen was in double-curvature as evidenced by the bending moments and curvatures discussed in previous sections.

Figure 4-32 and Figure 4-33 present the peak-to-peak amplitude and the maximum (in an absolute sense) tensile strains on the north and south sides. Note that the tensile strain is negative but the absolute values are used in these plots. Since the strain can stay negative from the beginning (due to residual strains) to the end of a run, it is possible that the maximum tensile strain is larger than the corresponding peak-to-peak amplitude.

The longitudinal strain near the top had the largest tensile value in most runs with the exception of the strain recorded at NL6 for specimen SP1. In specimen SP1, the elongation measured at location SL6 was the largest and increased as the runs were repeated. Compared to SL1, the strains at SL6 were about 5 times larger in peak-to-peak amplitude and 7 times larger for the maximum tensile strain. The strain at NL6 of SP1 also increased with repeated runs and it was 4 times larger than at other locations for the '2nd X+Z' test. In case of specimen SP2, NL6 and SL6 remained the largest on each side, but they did not increase with repeated runs. T

Figure 4-34 shows schematics of the deflected shapes of the test specimens. As discussed above, the nature of the strain responses near the top and the base were different (compression vs. tension) at each shear peak during the main excitation. This is expected because the bending moment histories at the top and the base also show the responses to be out-of-phase as discussed previously. During the 1<sup>st</sup> and 3<sup>rd</sup> shear peak, the top on the north side was in tension while the base on the north side was in compression. These directions (signs) of the straining actions were reversed during the 2<sup>nd</sup> peak.

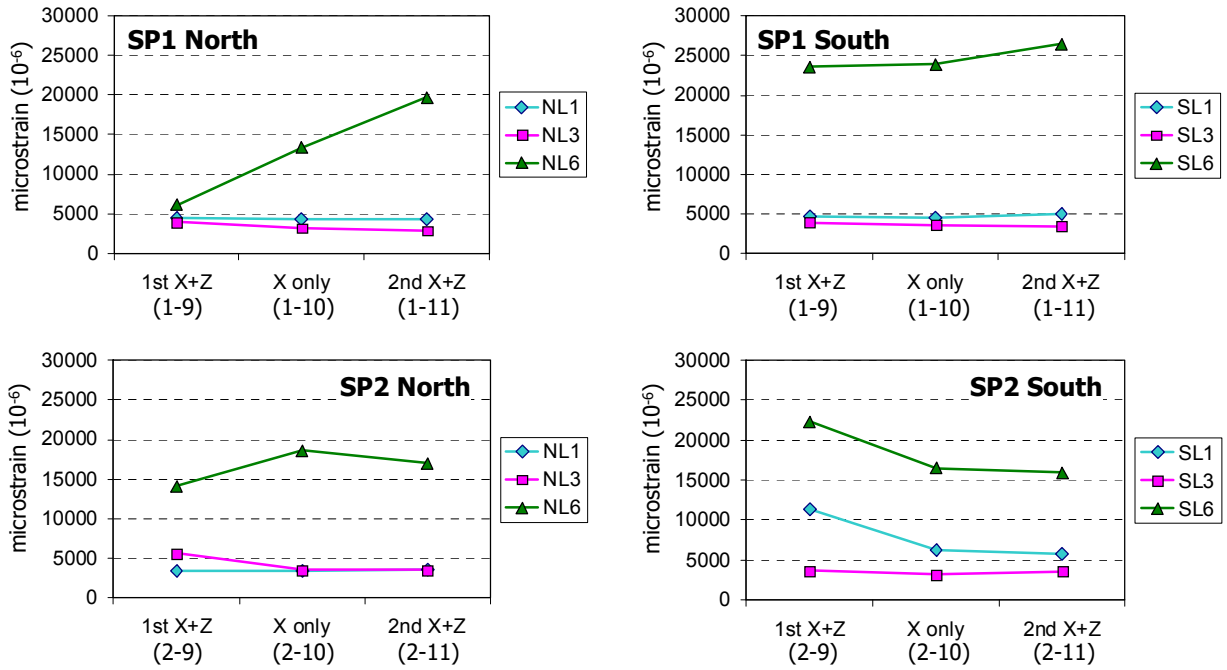


Figure 4-32: Peak-to-peak strain amplitudes recorded at north-south sides in the 125%-scale tests

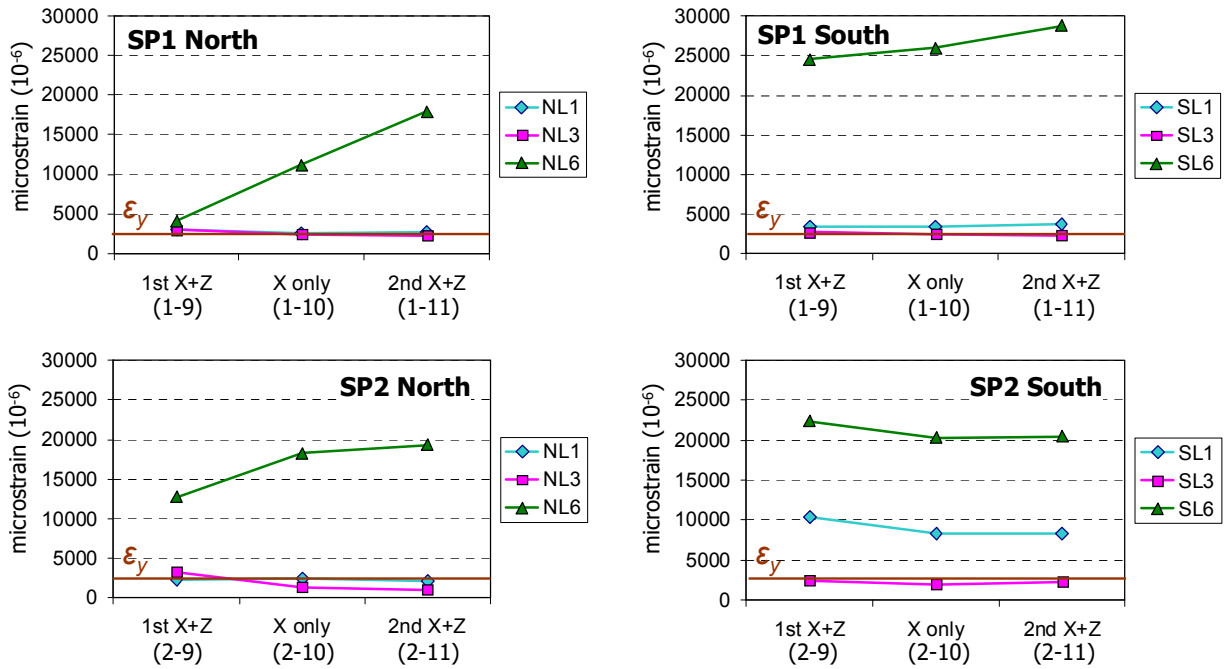


Figure 4-33: Peak tensile strains recorded at north-south sides in the 125%-scale tests

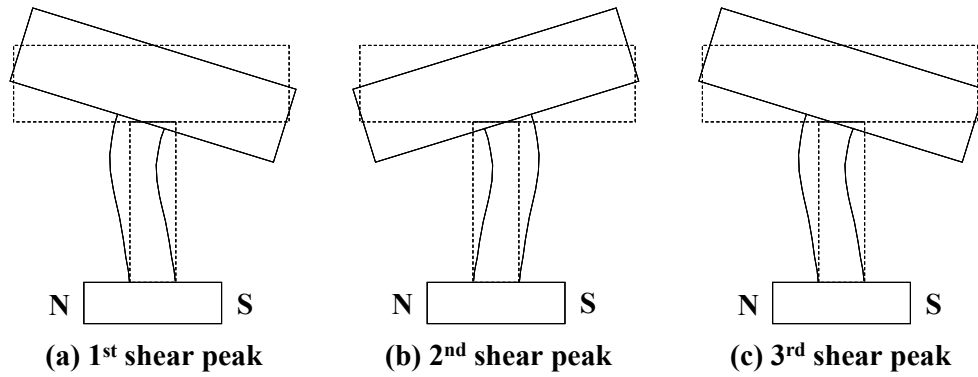


Figure 4-34: Schematic deflected shapes of the test specimens at shear peaks

Longitudinal strains were also recorded in the East-West direction at three locations as identified in the plots shown in Appendix D. All recorded strain values were less than those on the north and south sides. Maximum tensile strain at WL1 was less than 80% of that at NL2, both of which were at the same height. The strains remained negative, i.e. tensile, in most locations and runs except at EL3 partly due to the initial strain of EL3. This implies that the force distribution was not uniform on the east and west sides suggesting the presence of biaxial bending. This was confirmed by the difference in strains between EL and WL at the same height. Figure 4-35 and Figure 4-36 present the peak-to-peak amplitude and the maximum tensile strains on the east and west sides for the 125%-scale tests.

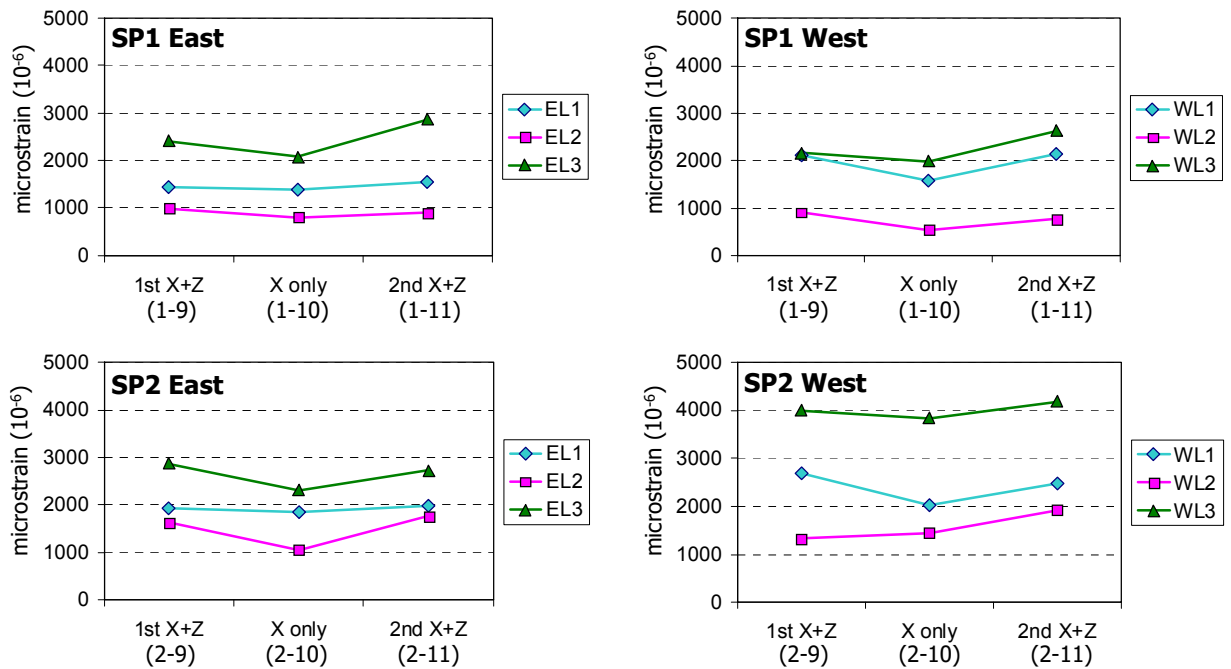


Figure 4-35: Peak-to-peak amplitudes of recorded strains on east-west sides in the 125%-scale tests

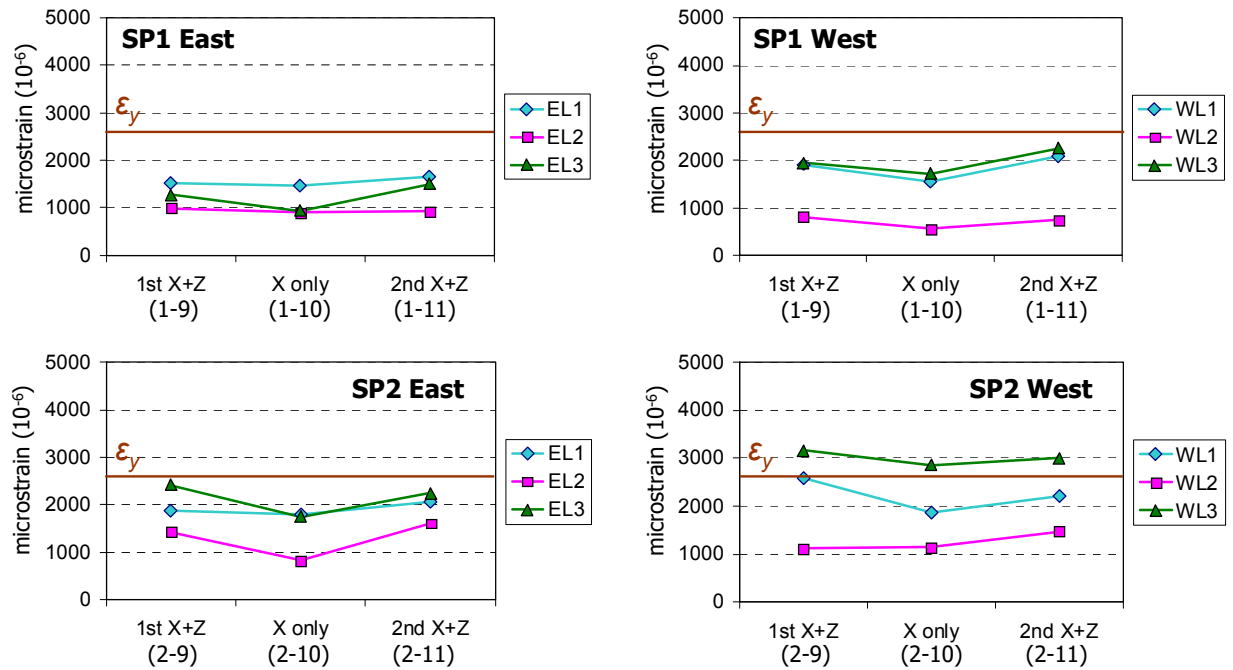


Figure 4-36: Peak tensile strains recorded on east-west sides in the 125%-scale tests

#### 4.8.4 Transverse (Hoop) Strains

Total of 14 strain gages were installed on the hoops on the north and south sides of the columns. The recorded strain histories during the 125%-scale tests are reported in Appendix D. Similar to the longitudinal strains, the transverse strains had peaks at the instant of the shear peaks and the tension peaks. The hoop tensile strain increased near the column top (i.e. at NH5, NH6, SH6, and SH7). This was expected since the compressive uniaxial stresses and accordingly the lateral strains and stresses were larger at the top due to the presence of larger bending moments. The peak-to-peak amplitude and the maximum tensile strain at  $h=10''$ ,  $40''$ , and  $60''$  for the 125%-scale tests are shown in Figure 4-37 and Figure 4-38. In specimen SP1, three different sections had similar peak-to-peak amplitude on the north side, but they differed on the south side. In particular, SH6 was about three times larger than SH1 and SH4. In general, the peak hoop strains increased as the runs progressed. Recorded hoop strains in specimen SP2 was typically larger than those recorded in specimen SP1.

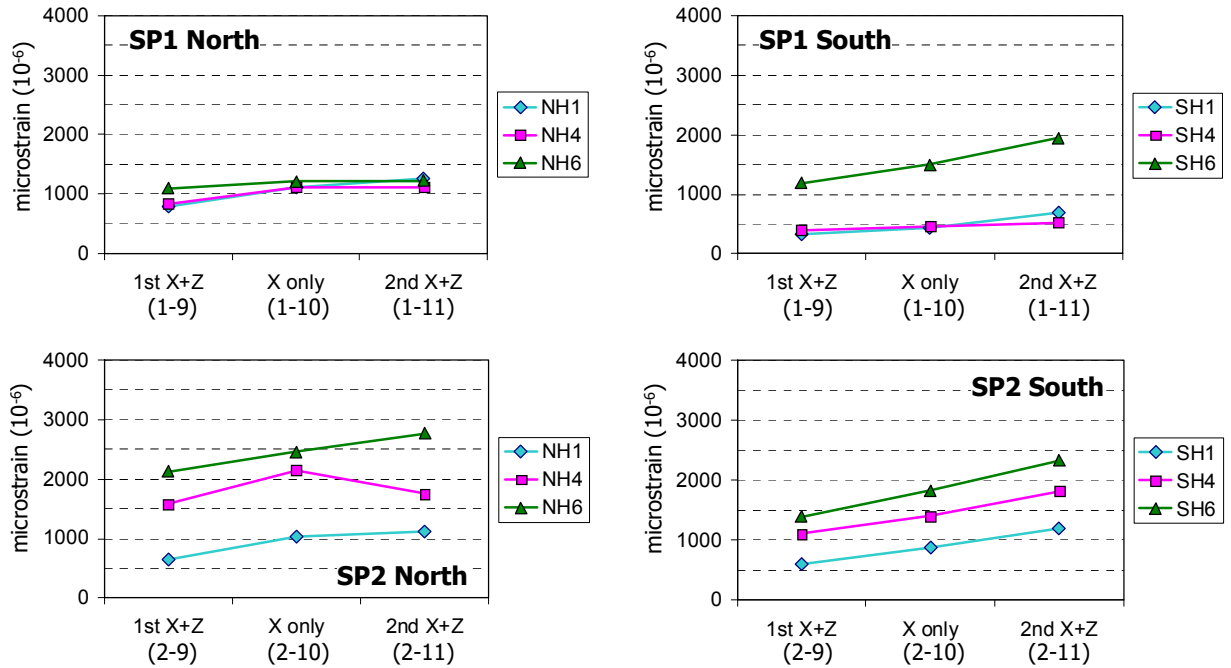


Figure 4-37: Peak-to-peak hoop strain amplitudes on the north-south sides in the 125%-scale tests

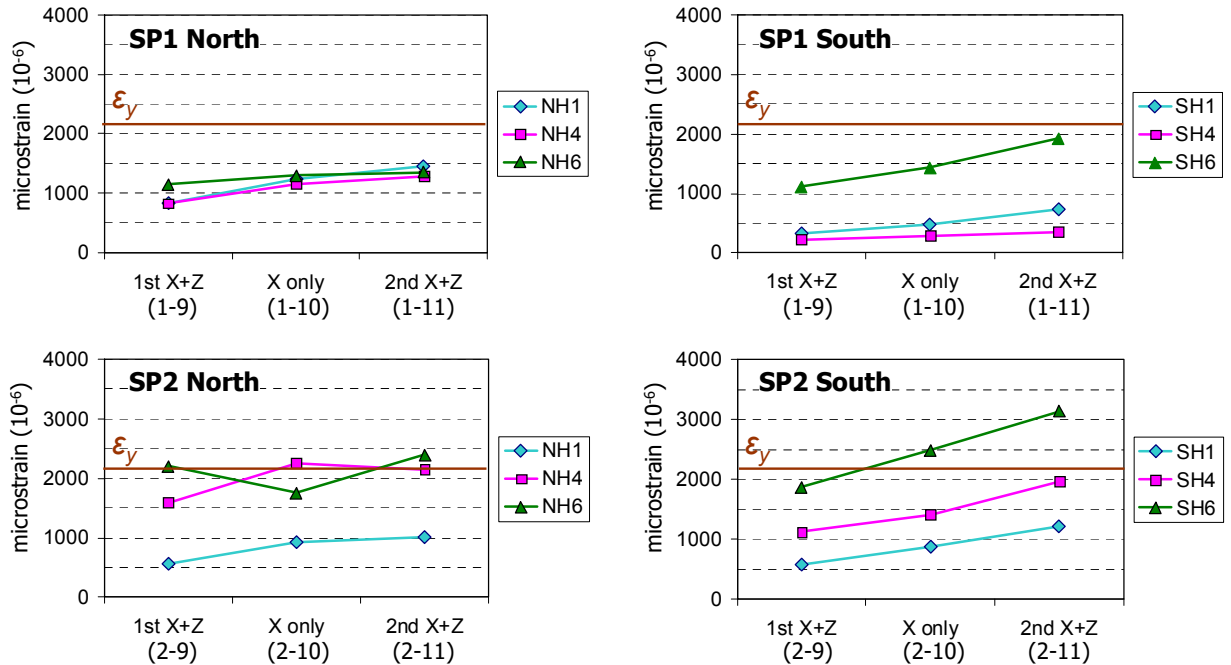


Figure 4-38: Peak tensile strains on the north-south side of specimens in the 125%-scale tests

## 4.9 Summary

The primary global and local responses obtained from the shaking table tests were examined in this chapter. Before the main dynamic tests, pullback and free vibration tests were conducted to determine the initial lateral stiffness and period of each specimen. SP1 was initially stiffer than SP2. Discrepancies between the calculated and observed fundamental period based on stiffness estimates was due to the fact that the tested column represented a two degree of freedom system in the lateral direction, with coupling between the translational and rotational modes. During the low-intensity excitations, the periods of both specimens became close to each other. Based on this observation, it is speculated that SP2 had some cracking before the tests.

Shaking table flexibility had a pronounced effect on the vertical response. The dynamic mode that was introduced by the table stiffness (in the vertical direction) and table mass governed the response in the vertical direction. In the horizontal direction, the acceleration recorded on the mass had a low frequency content and low amplitude compared to that at the top of the column or on the table which was due to the rigid body rotation of mass blocks.

The maximum acceleration at the top of the column or on the mass blocks did not increase linearly with the imposed table accelerations or the input intensity due to two reasons First, the lateral stiffness of the column decreased with increasing level of intensity and secondly, base shear capacity of the column was reached at the higher intensity levels. On the contrary, the acceleration histories in the Z direction were almost the same on the table, along the column height and on top of the mass blocks. The maximum values linearly increased with the input intensity, since axial forces were in the linear range and therefore axial stiffness variation was minor.

Similar to the accelerations, the maximum shear force did not increase linearly with the input intensity, but the maximum axial force did. The peak shear force in 125%-scale 'X only' test was larger than 125%-scale 1<sup>st</sup> or 2<sup>nd</sup> 'X+Z' test for each specimen, where the peak force was determined by the shear strength at this intensity. Considerable tensile force was induced on the test column due to vertical excitation. Tension in the columns resulted in degradation of shear strength, which is mainly due to the degradation of concrete contribution to shear strength.

Comparison of bending moment histories at the base and top of both of the specimens indicated that they were opposite in sign during the strong part of the excitation for all the intensity levels suggesting that the columns were in double-curvature. It is also noted that three 125%-scale resulted in similar maximum moment values suggesting that the axial force variation did not affect the bending moment noticeably.

The residual lateral displacement increased with the increased intensity of ground motions. The change of lateral stiffness is observed in the shear force-lateral displacement relationship. Beginning with the 95%-scale tests, the decrease in lateral stiffness was different on the positive and negative quadrants of the force-deformation response. This implies that the damage was not symmetric on the north and south. In the last 125%-scale test, stiffness in the positive direction was about 17% of that in 50%-scale test. In the axial force-vertical displacement relation, no significant decrease in stiffness was observed.

Flexural damage occurred both at the top and base of the column as the intensity of the ground motion increased, and the flexural damage at the top of the column occurred before that at the base since the moment at the top was larger. This was a result of the large mass moment of inertia at the top of the column. Reduction of the acceleration on the mass block due to the rotations contributed to this situation as well. As a result of flexural yielding both at the top and bottom of the column in double curvature, dynamic shear force reached the shear capacity which would not be the case if yielding occurred at the bottom and the moment at the top was smaller than the yield moment.

The progress of shear-induced damage was visible in the crack patterns. Both specimens started to have diagonal cracks near  $h=50''\sim 65''$  on the east and west sides during 70%-scale tests. They spread over the east and west sides except in the region  $h=25''\sim 35''$ . Also, there were vertical cracks as well as horizontal cracks on the north and south sides. SP2 had more cracks than SP1, since SP2 had wider hoop spacing. It should also be noted that the diagonal cracks during 125% 'X only' test was minimal compared to the 125% 'X+Z' tests supporting the observation that the concrete contribution to shear strength was reduced due to the presence of axial tension.

With respect to local section responses, it can be stated that the observed double-curvature response (noted for the bending moments) was confirmed by the longitudinal strain distribution across the height of the column on the north and south sides. The largest longitudinal strain was detected near the top of the column. This was followed by the value near the base and finally the middle had the smallest strain value. For the east and west sides, an abrupt change in tensile strain due to axial tension was remarkable. It was more significant than that on the north and south sides. The axial force significantly affected the strain histories on the east and west as evidenced by the peak strains occurring at the peak tensile forces in the column. Finally, based on observed results, the effect of vertical excitation on transverse strains was not significant.

# 5 Testing of Repaired Columns

Repair of Reinforced Concrete (RC) bridge columns damaged in earthquakes is often necessary to restore the system to functionality, particularly if the sustained damage is not severe or if the proposed repair method can provide adequate strength and deformability to resist the next design-level event. In this project, since the two columns sustained major damage following the imposed horizontal and vertical excitations, the feasibility of using FRP jacketing to restore the strength and deformability of the bridge columns is investigated.

Fiber Reinforced Polymer (FRP) composite laminates are commonly used for retrofit and repair of RC columns. This method has many advantages for seismic application, especially bridge columns, e.g. high strength-to-density ratio, ease to form into complex shapes, and resistance to fatigue. This chapter presents an experimental study carried out to evaluate the confinement effectiveness and shear strength and ductility enhancements of RC circular bridge columns repaired with FRP laminates as continuous confining media.

The two pre-damaged Reinforced Concrete (RC) circular bridge columns that were tested in the previous experimental phase of the project were retrofitted using Glass and Carbon Fiber Reinforced Polymer (GFRP and CFRP) jackets. The goals of this experimental study were:

- (1) To investigate response of repaired RC circular bridge columns subjected to series of horizontal and vertical ground motions;
- (2) To compare the response of repaired and as-built specimens

## 5.1 Details of Repaired Test Specimens and Repair Procedure

Both specimens tested in the previous experimental phase of the project developed shear and flexure cracks, the damage being more severe in as-built test specimen SP2 compared to SP1. The FRP, epoxy, mortar and corrosion protection system used in the repair were provided by Linford (product literature available from Linford).

Using the sounding hammer test, loose and unsound concrete was mechanically removed from the columns surface. Using wire brushes the exposed parts of the reinforcing bars were cleaned of any rust. Injection ports were installed in all cracks at adequate spacing. LinShield™ BC020 bonding and protection system were applied on cleaned concrete and reinforcement surfaces. Voids wider than  $\frac{3}{4}$  in. were patched using LinForce™ SM020 structural mortar and those smaller than  $\frac{3}{4}$  in. were cap sealed using LinForce™ GS100 gel/paste epoxy system. After the cap seal and patch material were cured, LinForce™ RN151 structural epoxy system was injected in all cracks. Multiport injection system was used with relatively low pressure to prevent further damage to cracked concrete. The procedure followed is displayed in Figure 5-1 and Figure 5-2 for the 2 specimens.



**Damage state of as-built specimen SP1**



**Epoxy and Gel coating**



**Multiport injection system**

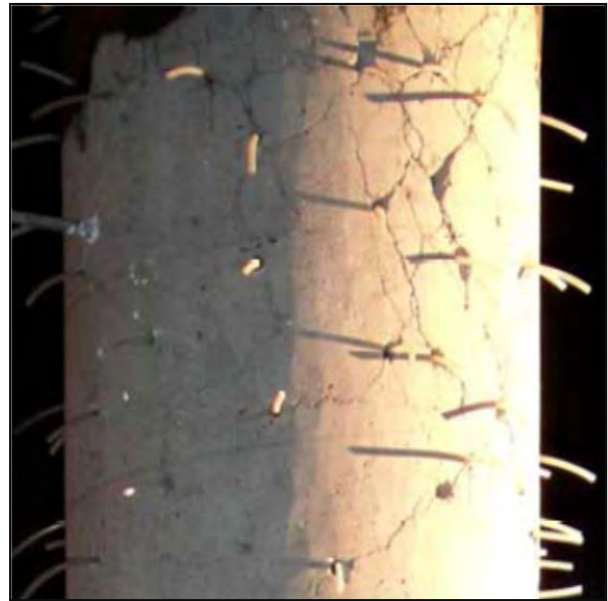


**GFRP repaired SP1**

**Figure 5-1: Repair of test specimen SP1**



**Damage state of as-built specimen SP2**



**Injection ports in damaged regions**



**Multiport injection system**



**CFRP repaired SP2**

**Figure 5-2: Repair of test specimen SP2**

When injection resin was cured, specimen surfaces were grinded to remove cap seal material and injection ports. Surface was then cleaned of any dust debris and one coat of LinForce™ RN075 prime was applied on it. Four layers of LinForce-E™ FRP composite system were installed on damaged specimen SP1. LinForce-E™ is an FRP composite system comprised of LinForce™ FE261 unidirectional Advantex glass fiber fabric impregnated with LinForce™ RN075 structural epoxy system. On the other hand, two layers of LinForce-C™ FRP composite system were installed on damaged specimen SP2. LinForce-C™ is an FRP composite system comprised of LinForce™ FC061 unidirectional carbon fiber fabric impregnated with LinForce™ RN075 structural epoxy system. LinShield™ PT006 temporary polyvinyl compression/curing tapes were wrapped on the installed FRP for the repaired columns and were discarded after 2 months. The process is shown in Figure 5-1 and Figure 5-2 for specimens SP1 and SP2, respectively.

### **5.1.1 Unidirectional Glass Fiber Fabric**

LinForce™ FE261 structural fabric was installed on damaged as-built test specimen SP1. This unidirectional fiber fabric is constructed with Owens Corning Advantex® glass fiber which is a high tensile strength material. This fiber was impregnated with LinForce™ RN075 fiber impregnation resin to achieve a strong FRP composite laminate. Average laminate tensile strength was 90.76 ksi with rupture strain of 2.3%. Thickness of plies was 0.04 in.

### **5.1.2 Unidirectional Carbon Fiber Fabric**

LinForce™ FC061 structural fabric was installed on damaged as-built test specimen SP2. This unidirectional carbon fiber fabric was impregnated with LinForce™ RN075 fiber impregnation resin to achieve a strong FRP composite laminate. Average laminate tensile strength was 143.95 ksi with an average tensile modulus of 9000 ksi. Thickness plies was 0.04 in.

## **5.2 Instrumentation**

The test specimens were instrumented both internally and externally using strain gages, displacement transducers, accelerometers and wire-potentiometers. Some strain gages, installed on the longitudinal and transverse reinforcing bars, were damaged during the tests of the as-built specimens and the repairing process leaving 29 out of 61 and 18 out of 50 strain gages to use for SP1 and SP2, respectively, refer to Appendix C. Total of 14 vertical displacement transducers, 9 3-D and 10 1-D accelerometers, and 20 vertical and horizontal wire-potentiometers were installed on both repaired test specimens. Locations of vertical displacement transducers, accelerometers and wire-potentiometers were the same for both specimens. In addition, 32 horizontal strain gages were installed on the FRP jackets of both test specimens along their height. Seven vertical displacement transducers were installed on the North and South faces (note that direction of applied horizontal ground motion was North-South), to measure curvatures along the height of the test specimen.

Four 3D accelerometers were installed on the steel plate attached to the shaking table to measure the accelerations in two horizontal directions (X and Y) and vertical (Z) direction. Nine 1D vertical accelerometers were installed along the tested column height from the footing to the top block to measure the vertical accelerations at different column cross-sections at 0 in., 10 in., 20 in., 30 in., 35 in., 40 in., 50 in., 60 in., and 70 in. One 3D accelerometer was installed on the East side of the top block of the column to measure X, Y, and Z components at height 70 in. At the middle of the top mass block, 1D accelerometer was used to measure the North-South acceleration. Finally, four 3D accelerometers were attached to the four corners of the top concrete slab.

### 5.3 Loading Protocol

For testing of the two specimens SP1 and SP2, the same set of horizontal and vertical ground motions were selected as used in testing of as-built specimens. Testing runs comprised of the same set of ground motions that were used for testing the as-built specimens. Table 5-1 gives the details of loading protocol. It is noted that the as-built test specimen SP1 was not tested for EQ4 and EQ6.

**Table 5-1: Ground motions for shaking table testing**

<b>Test</b>	<b>Earthquake</b>	<b>Station</b>	<b>Scale Factor</b>	<b>Components</b>
EQ1	Northridge	Pacoima Dam	0.050	Horizontal and vertical
EQ2	Northridge	Pacoima Dam	0.125	Horizontal and vertical
EQ3	Northridge	Pacoima Dam	0.250	Horizontal and vertical
EQ4	Northridge	Pacoima Dam	0.250	Horizontal only
EQ5	Northridge	Pacoima Dam	0.500	Horizontal and vertical
EQ6	Northridge	Pacoima Dam	0.500	Horizontal only
EQ7	Northridge	Pacoima Dam	0.700	Horizontal and vertical
EQ8	Northridge	Pacoima Dam	0.950	Horizontal and vertical
EQ9	Northridge	Pacoima Dam	1.250	Horizontal and vertical
EQ10	Northridge	Pacoima Dam	1.250	Horizontal only
EQ11	Northridge	Pacoima Dam	1.250	Horizontal and vertical

## 5.4 Experimental Results

This section presents the experimental results of the two repaired test specimens and their comparison with the responses of the as-built test specimens. Calculations of shear force are performed from the data obtained using the load cells attached to the specimens footings. Relative displacements were calculated from the wire-potentiometers data, after proper verification. Drift ratio was calculated as the ratio of measured displacement to the height of the test specimen. Plots of strain profiles measured from strain gage data and vertical displacement transducers are also presented.

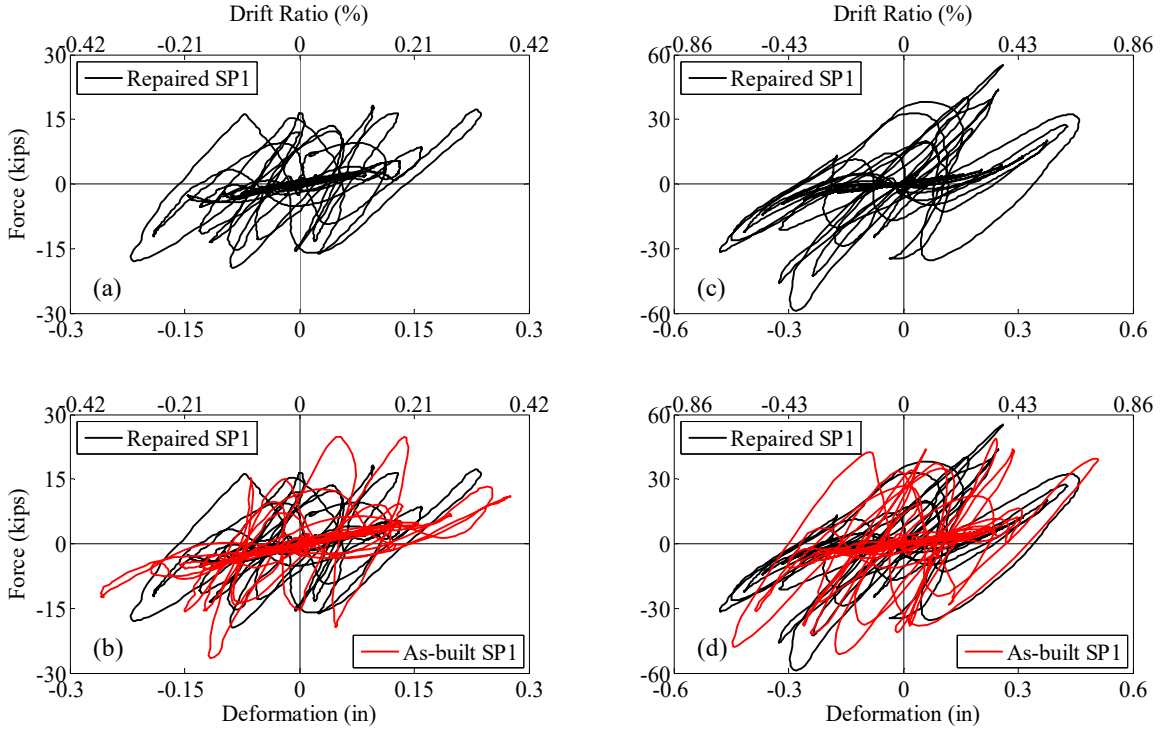
The FRP repair jacket of both test specimens was intact during the entire testing runs. The comparison of the force-deformation plots of the repaired and as-built specimens is presented and it is clearly observed that the repaired test specimens resisted more shear force compared to the as-built test specimens. Both repaired specimens showed improved stiffness.

### 5.4.1 Test Specimen SP1

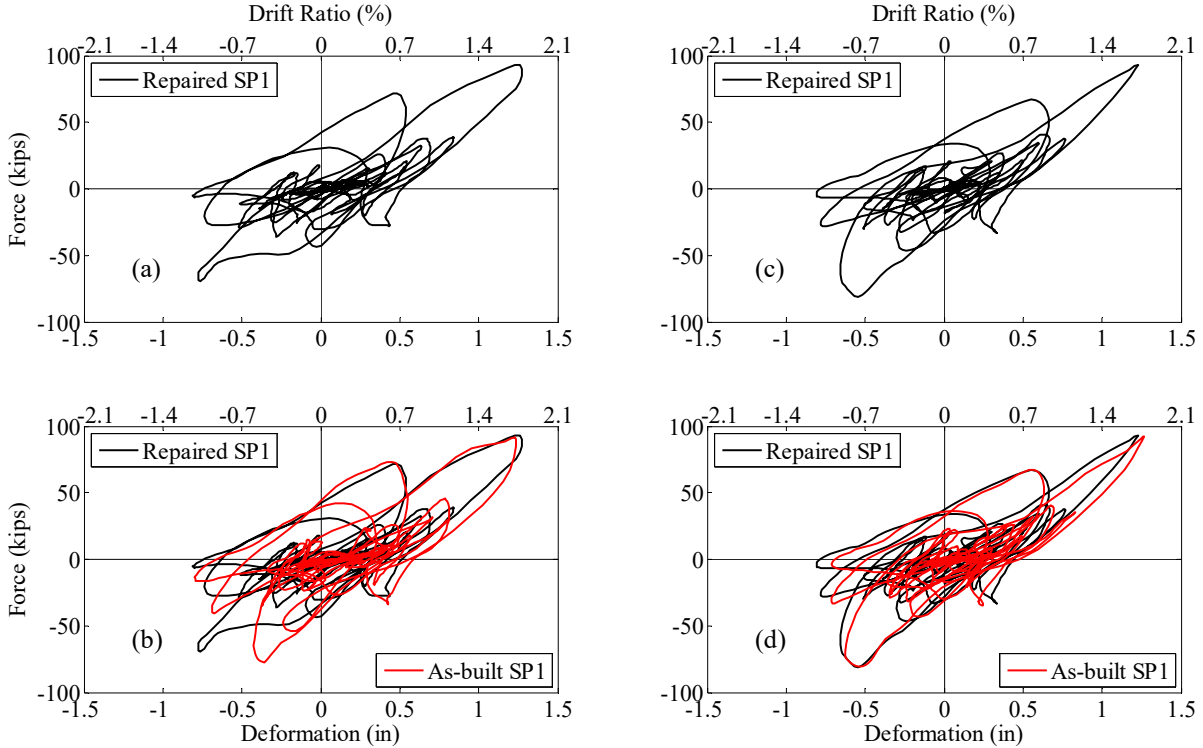
Figure 5-3 and Figure 5-4 show the force-deformation response of specimen SP1. Four main ground motion cases are chosen for discussion in this section. These cases are selected (based on the scale factor) to give a general idea of the response. Figure 5-3 shows the force-deformation response of the repaired specimen SP1 subject to EQ3 and EQ5. A comparison plot between repaired SP1 and as-built SP1 is also shown directly below. The maximum drift ratio attained by the as-built SP1 was slightly higher than that of the repaired SP1. For the same drift, the repaired SP1 resisted more shear force compared to the as-built SP1. Similar behavior was observed for the testing under ground motion EQ5. The behavior of the repaired SP1 was generally more stable compared to that of the as-built SP1 because of better confinement.

The effectiveness of confinement was more obvious for the ground motions with higher scale factors. Figure 5-4 shows the force-deformation response of the repaired SP1 subjected to EQ9 and EQ10 as well as the comparisons with the as-built SP1. Under both of these high ground motions, the repaired SP1 was stiffer than that of the as-built SP1 and was able to resist slightly higher shear forces. Response results of both repaired and as-built SP1, under all ground motions, are tabulated in Table 5-2.

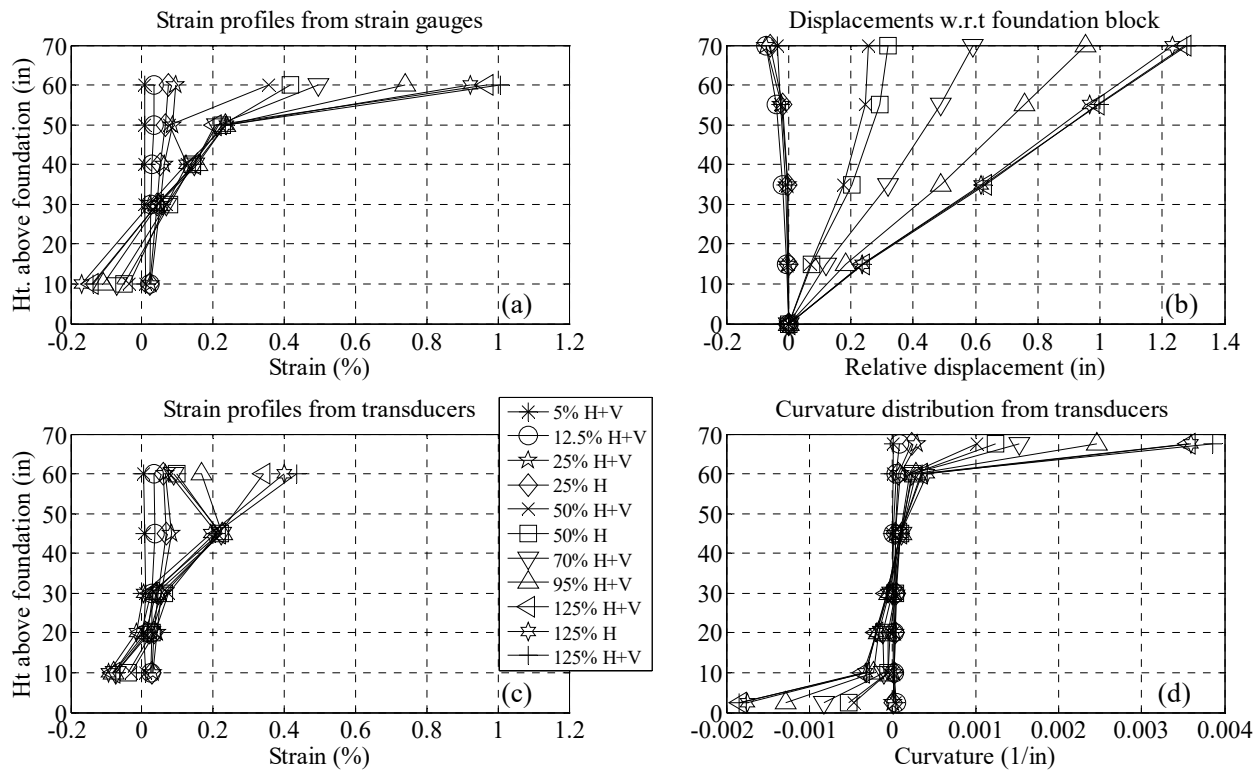
Figure 5-5 shows the strain profile on the North face of the repaired SP1. The shown plots are based on the measurements made using strain gages. The strain profile corresponds to the time when the strain at height 60 in. above the footing, was maximum. For ground motions up to EQ4, measured strains were below yield strain (approximately 0.21%) of the steel reinforcing bars. Based on the strain measurements, the first yielding of the reinforcing bars occurred during ground motion EQ5 near the top of the column. For all subsequent ground motions, peak strain values exceeded yielding at height of 60 in. and yielding started to spread along the column height. In the last ground motion (EQ11), all the strain gages above the mid-height of the column measured strains greater than the yield strain of the steel reinforcement.



**Figure 5-3: Force-deformation response of repaired specimen SP1 (above) and comparison to as-built specimen (below) for 2 excitations: EQ3 (left) and EQ5 (right)**



**Figure 5-4: Force-deformation response of repaired specimen SP1 (above) and comparison to as-built specimen (below) for 2 excitations: EQ9 (left) and EQ10 (right)**



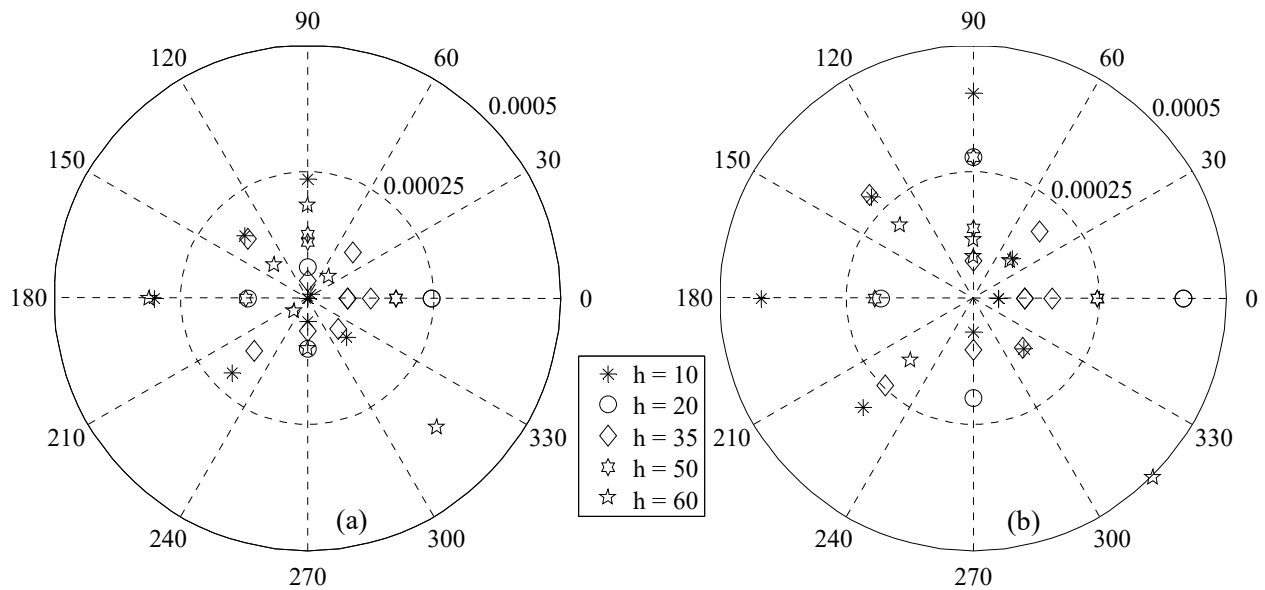
**Figure 5-5: Local responses of repaired SP1: (a) strain profile from strain gauges on the North face, (b) displacement profiles from wire-potentiometers along the height, (c) strain profile from the curvature data obtained using vertical transducers, (d) curvature**

Figure 5-5 also shows the curvature data at the time when the maximum strain was measured at height 60 in. above the footing. For the high intensity ground motions, the curvature diagram suggests the double curvature behavior, which is supported by the measurements of the strain gages readings. For the high intensity ground motions, the longitudinal strains in the considered reinforcing bar were in tension above the mid-height of the specimen and they were generally in compression below mid-height.

Figure 5-6 and Figure 5-7 show the strain profiles measured using the strain gages attached on the GFRP jacket around the test specimen circumference. The markers shown on the plots correspond to the time when maximum strain was measured along the column height at any of the strain gage locations.

**Table 5-2: Maximum responses during testing specimen SP1**

Test	GFRP retrofitted test specimen SP1			As-built test specimen SP1		
	Top displacement (in.)	Shear force (kips)	Drift ratio (%)	Top displacement (in.)	Shear force (kips)	Drift ratio (%)
EQ1	0.038	3.1	0.05	0.026	2.3	0.04
EQ2	0.127	8.7	0.18	0.065	10.5	0.09
EQ3	0.237	19.5	0.34	0.275	26.5	0.40
EQ4	0.221	20.8	0.32			
EQ5	0.480	58.8	0.69	0.509	51.5	0.73
EQ6	0.447	63.0	0.64			
EQ7	0.591	72.9	0.84	0.569	67.1	0.81
EQ8	0.961	87.4	1.37	0.678	85.0	0.97
EQ9	1.274	93.2	1.82	1.239	91.4	1.77
EQ10	1.231	93.2	1.76	1.264	92.6	1.81
EQ11	1.304	87.6	1.86	1.402	88.3	2.00



**Figure 5-6: Strain profiles of repaired SP1 based on jacket strain gages corresponding to time when maximum strain occurs along the column height: EQ5 (left) and EQ6 (right)**

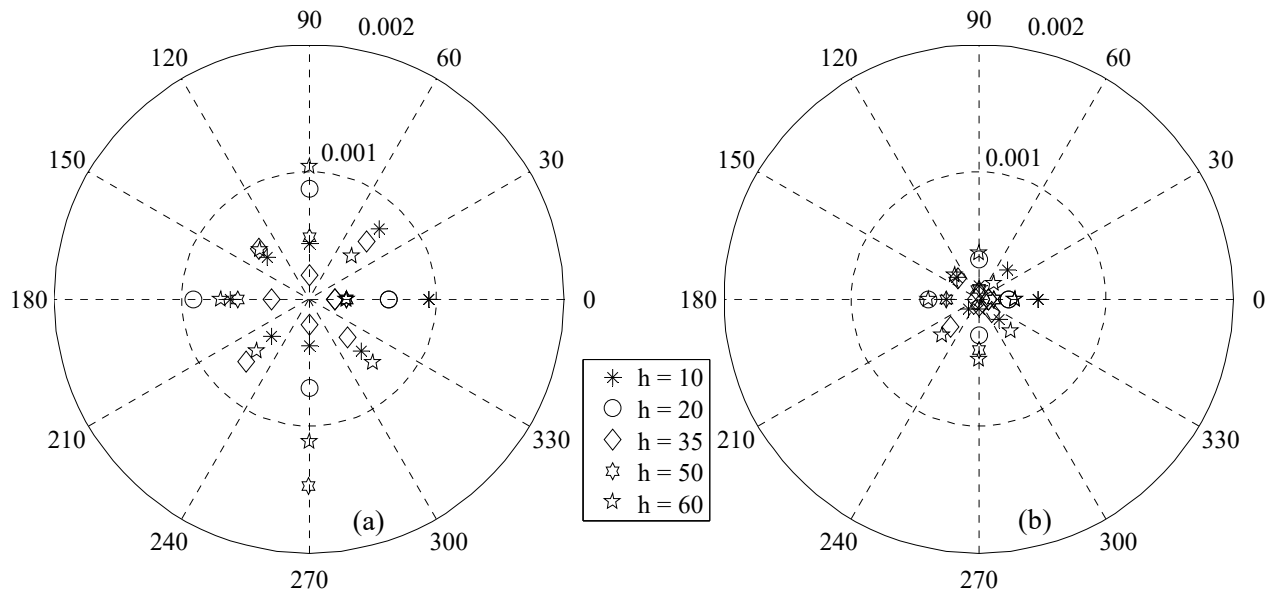


**Figure 5-7: Strain profiles of repaired SP1 based on jacket strain gages corresponding to time when maximum strain occurs along the column height: EQ9 (left) and EQ10 (right)**

#### 5.4.2 Test Specimen SP2

Force-deformation responses of repaired specimen SP2 are shown in Figure 5-8 through Figure 5-10. Figure 5-8 shows the response of repaired SP2 when subjected to EQ3 and EQ4. Due to the small intensity shaking, the responses for both “horizontal” (left) and “horizontal + vertical” (right) shown in Figure 5-8 is quite similar. The figure also shows the comparison plots of repaired and as-built SP2. Maximum drift ratio for the as-built SP2 was higher than that of the repaired SP2, while both specimens resisted approximately the same magnitude of shear forces. The responses of the as-built and repaired specimen subjected to EQ5 and EQ6 is displayed in Figure 5-9 where again the effect of the low-level vertical excitations are observed not to influence the response significantly. Figure 5-10 shows the force-deformation response of repaired and as-built SP2 under EQ9 and EQ10. Due to improved confinement configuration provided by the FRP jacket repair, the repaired SP2 was more ductile, had higher stiffness, and resisted higher base shear compared to the as-built SP2. Table 5-3 lists the maximum response variables for all the applied ground motions. The effect of the CFRP repair on enhancing the shear capacity of a column with relatively large hoop spacing is clearly observed.

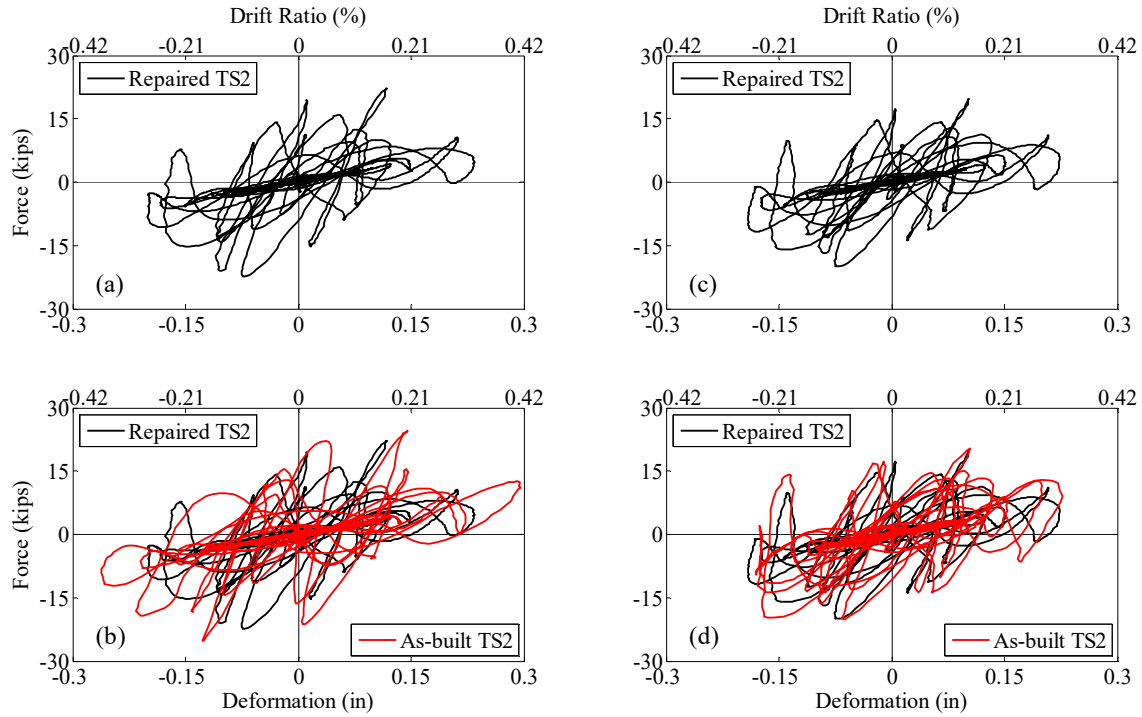


**Figure 5-8: Force-deformation response of repaired specimen SP2 (above) and comparison to as-built specimen (below) for 2 excitations: EQ3 (left) and EQ4 (right)**

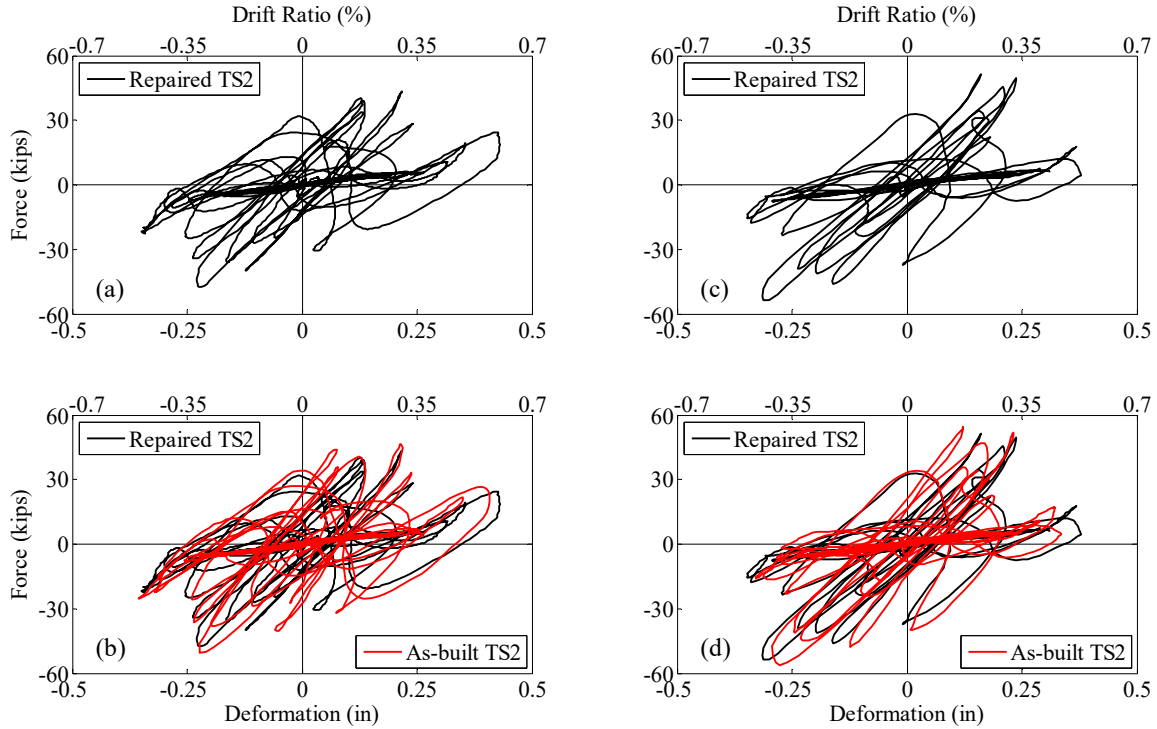


**Figure 5-9: Force-deformation response of repaired specimen SP2 (above) and comparison to as-built specimen (below) for 2 excitations: EQ5 (left) and EQ6 (right)**

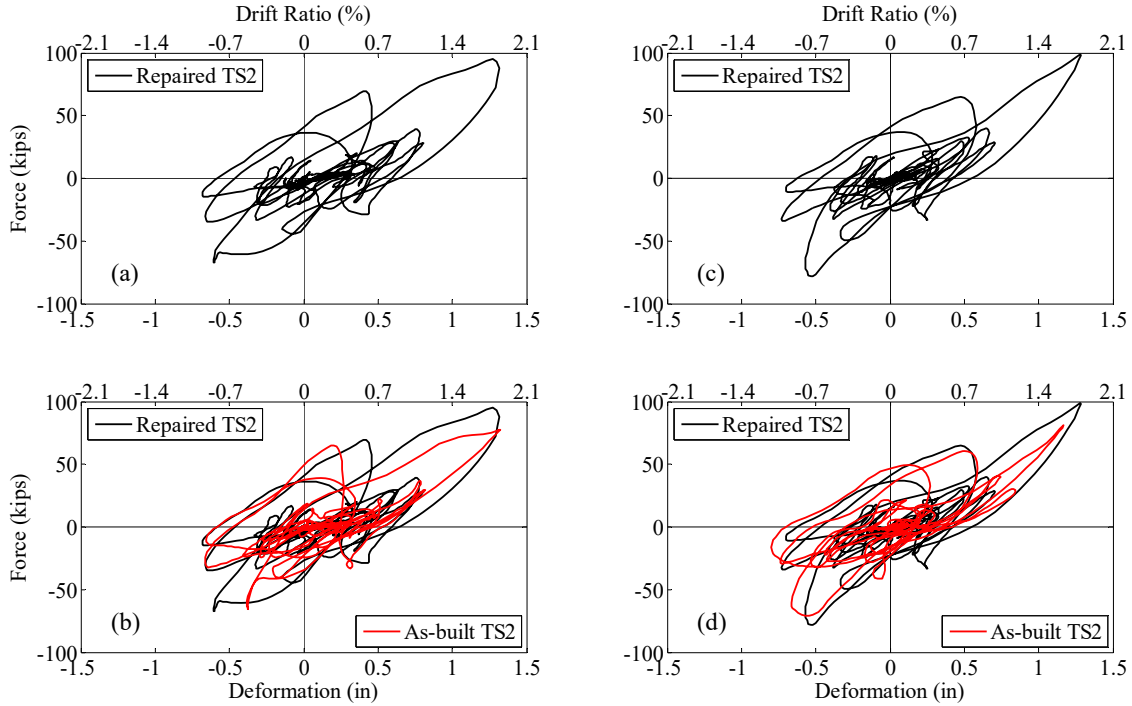


**Figure 5-10: Force-deformation response of repaired specimen SP2 (above) and comparison to as-built specimen (below) for 2 excitations: EQ9 (left) and EQ10 (right)**

Figure 5-11 shows the strain profile on the North face of the repaired SP2 based on strain gage measurements. Also shown in the same figure is the curvature distribution along the specimen height measured using the vertical displacement transducers. The behavior was similar to that observed for the repaired SP1. One main difference was that the first yield occurred at a location 60 in. above the footing during EQ6. The spreading of yield strain along the repaired SP2 height was gradual compared to the repaired SP1. However, both repaired specimens had comparable response for higher intensity earthquakes.

Figure 5-12 and Figure 5-13 show the strain profiles measured using the strain gages attached on the CFRP jacket around the test specimen circumference. The markers shown on the plots correspond to the time when maximum strain was measured along the column height at any of the strain gage locations.

It is generally observed that the FRP jackets remained intact in both of the repaired specimens with minor damage and the residual displacements were negligible.

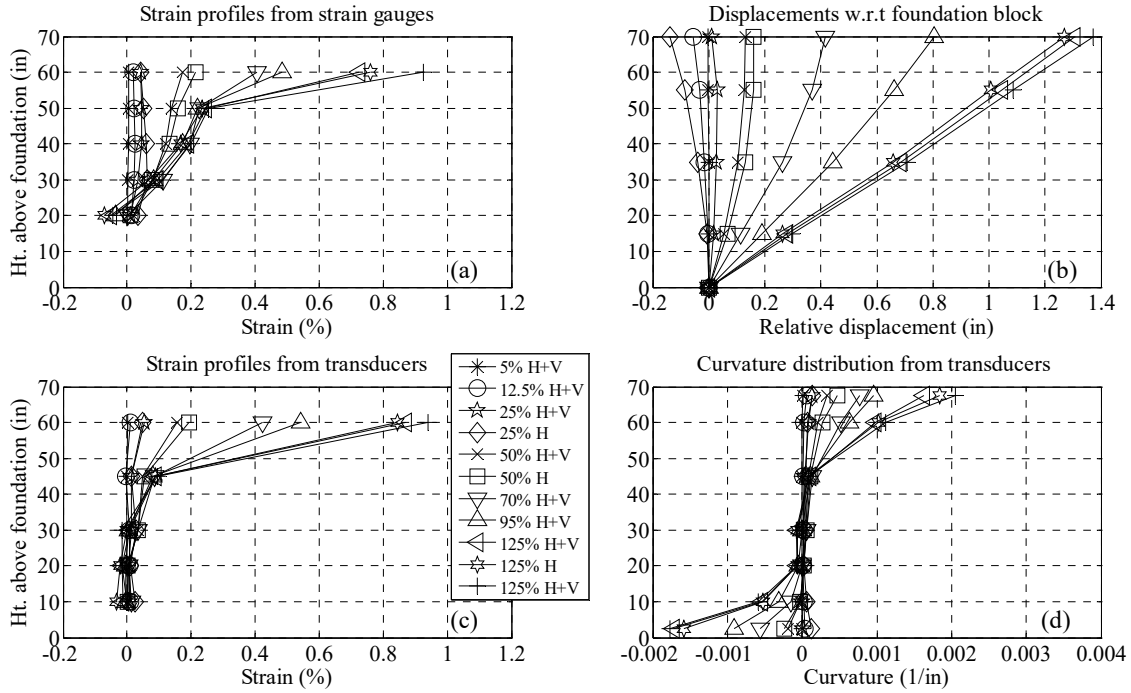


**Figure 5-11: Local responses of repaired SP2: (a) strain profile from strain gauges on the North face, (b) displacement profiles from wire-potentiometers along the height, (c) strain profile from the curvature data obtained using vertical transducers, (d) curvature**

**Table 5-3: Maximum responses during testing repaired specimen SP2**

Test	CFRP retrofitted test specimen SP2			As-built test specimen SP2		
	Top displacement (in.)	Shear force (kips)	Drift ratio (%)	Top displacement (in.)	Shear force (kips)	Drift ratio (%)
EQ1	0.031	2.1	0.04	0.023	1.7	0.03
EQ2	0.135	10.1	0.19	0.117	10.8	0.17
EQ3	0.233	22.4	0.33	0.295	25.4	0.42
EQ4	0.223	20.0	0.32	0.227	20.4	0.32
EQ5	0.430	47.6	0.61	0.410	50.4	0.59
EQ6	0.378	53.8	0.54	0.337	56.0	0.48
EQ7	0.631	69.1	0.90	0.550	69.3	0.79
EQ8	0.803	82.4	1.15	0.702	75.2	1.00
EQ9	1.317	94.9	1.88	1.320	77.4	1.89
EQ10	1.287	98.9	1.84	1.167	80.9	1.67
EQ11	1.383	90.2	1.98	1.223	77.2	1.75

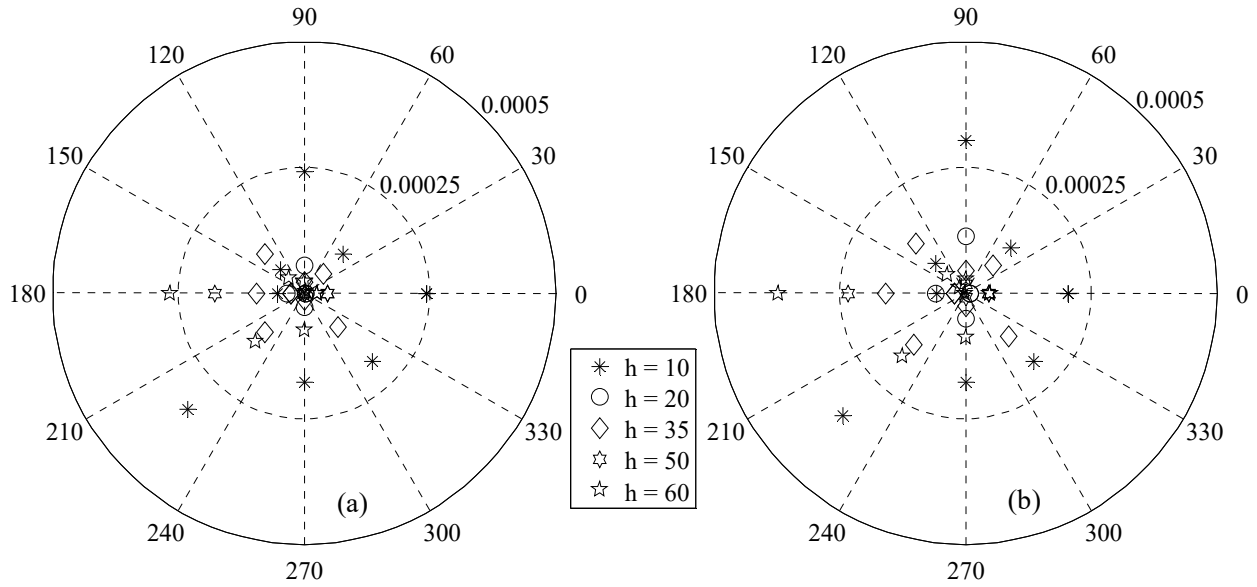


**Figure 5-12: Strain profiles of repaired SP2 based on jacket strain gages corresponding to time when maximum strain occurs along the column height: EQ5 (left) and EQ6 (right)**

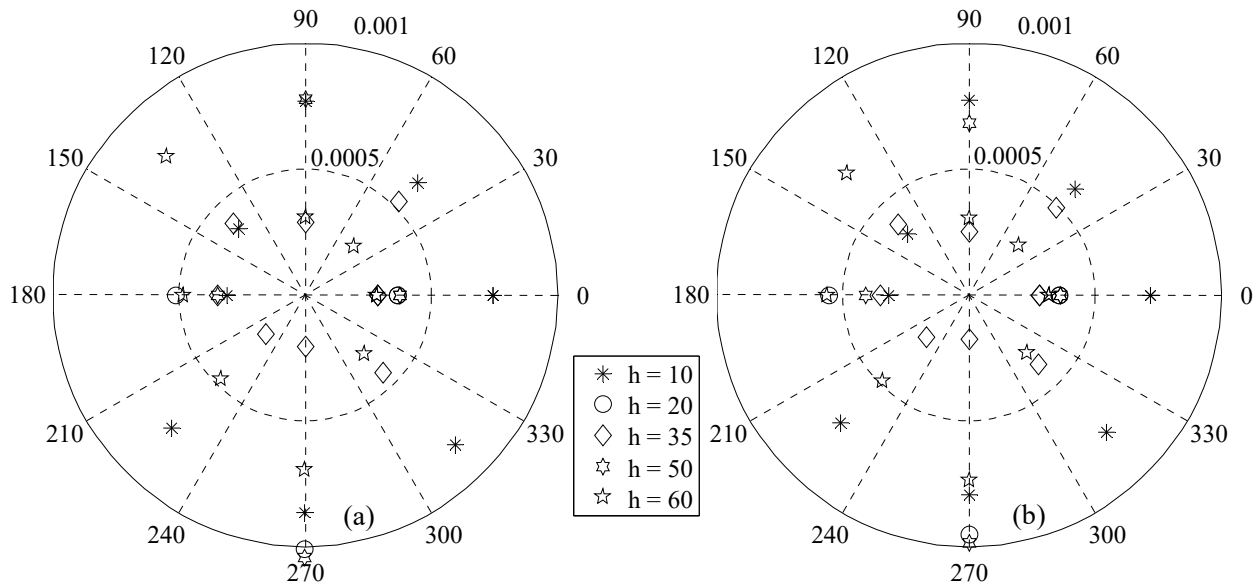


**Figure 5-13: Strain profiles of repaired SP2 based on jacket strain gages corresponding to time when maximum strain occurs along the column height: EQ9 (left) and EQ10 (right)**

# 6 Development and Evaluation of Computational Models

This chapter presents the computational models developed in order to predict the response of the tested bridge columns. In addition to the conventional modeling of RC columns, a new shear spring is developed and implemented in the computational platform, OpenSees [34], in order to incorporate shear strength estimation based on ACI [4] or Caltrans SDC [13] equations. Various response quantities obtained from the different models are compared with the test results to evaluate the developed computational models.

## 6.1 Development of OpenSees Element

OpenSees, a software framework for developing applications to simulate the performance of structural systems [34], provides a considerable number of material and element models for use in nonlinear seismic analysis. With particular reference to modeling inelastic shear, currently available options are limited.

Massone et al. [30] proposed and developed a beam-column element model that includes flexure and shear interaction in OpenSees. They modified the displacement-based element which already included linear curvature and constant axial strain distributions to include shear deformation. Based on linear interpolation of the curvature and constant axial strain, a third strain component was included to account for shear flexibility. The fiber discretization leads no longer to just uniaxial behavior, but rather a bidirectional response by incorporating a membrane material model based on simple uniaxial stress-strain relationships for concrete and steel. Although the material models can be cyclic, the element model formulation has been implemented and verified initially for monotonic static analysis. Unfortunately, ACI or Caltrans SDC based expressions for shear capacity cannot be represented with this element since it does not consider the effect of axial force in the shear strength estimation.

Elwood and Moehle [20] developed Limit State material models based on the existing Hysteretic material in OpenSees. Each Limit State material model can be interpreted as a spring in series with the nonlinear beam-column element. It captures the additional deformations, either shear or axial, that takes place after detection of failure. The Limit State material uses a drift capacity model to determine the point of shear or axial failure for a column and subsequently controls the post-failure response of the element resulting in strength degradation. The use of this drift capacity model is not applicable in this study since the model is derived from a database of tests with only axial compression and therefore does not represent the investigated axial tension effects caused by including the vertical acceleration component of the ground motion. Therefore, none of the existing models can be directly employed to model the variation of the shear capacity

as a function of the axial force or the ductility as implied by the code equations such as ACI or Caltrans SDC.

Incorporation of ACI and SDC code equations for shear capacity into OpenSees is achieved by proposing a new material model. Although the intended use of this new material is within a zero-length element connected to a beam-column element, it can be directly employed within a beam column element by aggregating the material into a section. The former approach is adopted in the analyses conducted within this study. Considered cases are designated as ‘ACI shear spring’ and ‘SDC shear spring’ in order to represent ACI and SDC equations, respectively. A bilinear force-deformation relationship is defined by the initial stiffness ( $K_{elastic}$ ), the yield force ( $V_y$ ), and the hardening ratio for post-yield stiffness ( $r$ ). Initial stiffness is the shear stiffness calculated as  $GA/L$ , where  $G$  is the shear modulus,  $A$  is shear area and  $L$  is the length of the column. Before yielding, the yield force is updated at each integration time step based on Eqs. (1.1) to (1.6) for ACI shear spring using the axial force at that time step and with Eqs (1.32) to (1.38) for Caltrans SDC shear spring using the displacement ductility and axial force at that time step. The displacement ductility is calculated as the displacement at a specified node (the top of the column in the present analyses) normalized by the yield displacement, both of which (the node number and the yield displacement) are input parameters to the new material model in OpenSees.

At the time step where the demand reaches the capacity, yielding takes place and the force-displacement relationship follows the post-yield behavior. The yield force is not updated and kept constant afterwards unless the column is subjected to any value of axial tension for the case of Caltrans SDC spring and a predetermined value of tension (specified as an input parameter) for the case of ACI spring. The yield force is kept constant after this final modification. The basis of this second modification is the significant change of the yield force as a result of axial tension. For the case of ACI spring, if the predetermined tension value occurs before any yielding, the yield force is not updated after reaching this predefined tension value. This option permits the investigation of the yielding situations in the close vicinity of the maximum axial tension. For example, if the maximum axial tension, which produces significant reduction in shear strength, takes place before a shear peak with a small time interval in between, and the demand does not reach the capacity, a potential yielding may not be captured unless the yield force is kept constant in this small interval. As mentioned in the previous chapter, it was observed that the shear strength degradation was due to the existence of previous tensile peaks during the tests. Such an option was not required for the SDC shear spring since the shear force is explicitly kept constant in the SDC equation in the aforementioned small interval due to the fact that the contribution of concrete to the shear strength is zero under any value of tension.

## 6.2 Simulation Model of Bridge Column

The specimen consists of a footing, a column, and a top block. Steel beams and mass blocks are placed on top of the test specimen and four load cells connect the specimen to the table below the footing. These features are expected to affect the dynamic and nonlinear responses of the test column. Hence, the whole setup above the table is modeled in this computational investigation.

The ‘Beam With Hinges’ (BWH) element is a commonly used force-based element to examine the nonlinear response of frame structures. Figure 6-1 shows the composition of a BWH element. It has localized plasticity at the ends, i.e. hinges, and the remaining part is kept linear elastic. The length of each hinge is defined by the user. Details of the BWH element implemented in OpenSees are described in the paper by Scott and Fenves [42].

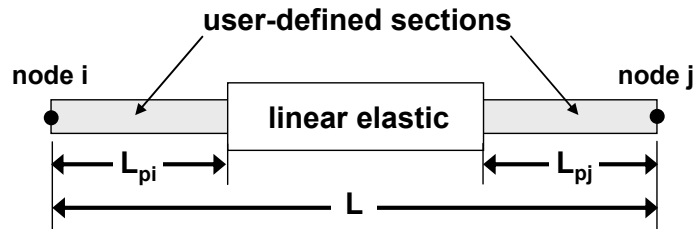


Figure 6-1: “Beam With Hinges” element [28]

Figure 6-2 presents the test specimen model using BWH element to represent the column. Two rigid elements at the top and the base are used for the top block and the footing, respectively. The nodal mass above the top rigid element has three translational and three rotational degrees of freedom, associated with the mass and mass moment of inertia of the mass assembly consisting of the top block, steel beams, lead blocks, and additional concrete blocks. A rotational spring is added below the rigid element at the base, because the specimen was placed on four load cells which were connected to the shaking table and they are not perfectly rigid. A shear spring is also incorporated into the element to investigate the effect of the code-based shear capacity prediction on the response of the column. ACI and SDC code equations are implemented in the spring and they are designated as “ACI” and “SDC”, respectively. It should be noted that the hardening ratio in the shear springs is set as  $r = 0.01$ . The hinge length is defined by Caltrans SDC 7.6.2. It is based on Paulay and Priestly [36] and specifies the plastic hinge length of RC columns as follows:

$$L_p = \begin{cases} 0.08L + 0.15f_{ye}d_{bl} \geq 0.3f_{ye}d_{bl} & (\text{in, ksi}) \\ 0.08L + 0.022f_{ye}d_{bl} \geq 0.044f_{ye}d_{bl} & (\text{mm, MPa}) \end{cases} \quad (6.3)$$

where  $f_{ye}$  and  $d_{bl}$  are respectively the expected yield stress and the nominal bar diameter of the column longitudinal reinforcing bars. Since the column with diameter  $D$  was in double-curvature

and had damage due to flexure at the base and the top, the same hinge length was assumed at both ends, i.e.  $L_{pi} = L_{pj} = L_p$ . The calculated  $L_p$  based on SDC is 14.5" (368 mm) which corresponds to  $0.725D$ , where  $D$  is the diameter of the column.

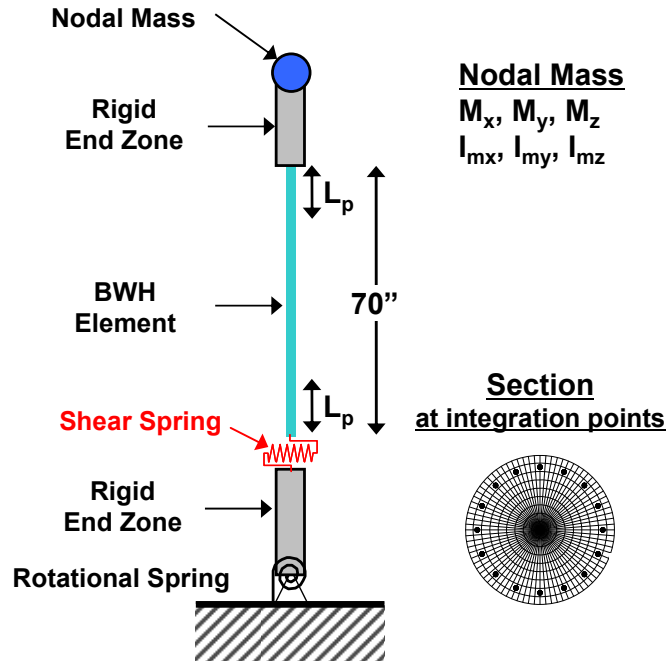


Figure 6-2: Specimen modeling

### 6.2.1 Material Modeling

For the core and cover concrete, the uniaxial material ‘Concrete02’ in OpenSees is utilized. The parameters which define this model are as follows:

- $f_{pc}$ : compressive strength
- $\epsilon_{psc0}$ : strain at compressive strength
- $f_{pcu}$ : crushing strength
- $\epsilon_{psu}$ : strain at crushing strength
- $f_t$ : tensile strength
- $E_{ts}$ : absolute value of tension softening stiffness
- $\lambda$ : ratio between unloading slope at  $\epsilon_{psu}$  and initial slope. The initial slope for this model is  $2f_{pc}/\epsilon_{psc0}$ .

Table 6-1 summarizes the parameters utilized for this concrete model in this study. Figure 6-3 presents the stress-strain relationship of ‘Concrete02’ material, where negative and positive stresses (and strains) represent compression and tension, respectively. Cover concrete properties are based on the material tests presented in Chapter 3. For core concrete, compressive strength and strain properties are calculated based on Mander’s model [29].

**Table 6-1: Concrete model parameters for numerical simulations**

Parameter	Units	Cover concrete	Core concrete	
			Hoops @ 2"	Hoops @ 3"
$f_{pc}$	[ksi] (MPa)	-4.1 (-28.0)	-5.12 (-35.3)	-4.77 (-32.9)
$\epsilon_{psc0}$	N/A	-0.003	-0.0069	-0.0056
$f_{pcu}$	[ksi] (MPa)	-0.41 (-2.80)	-3.51 (-24.2)	-0.37 (-2.53)
$\epsilon_{psu}$	N/A	-0.006	-0.0126	-0.0097
$f_t$	[ksi] (MPa)	0.41 (2.80)		
$\lambda$	N/A	0.8		

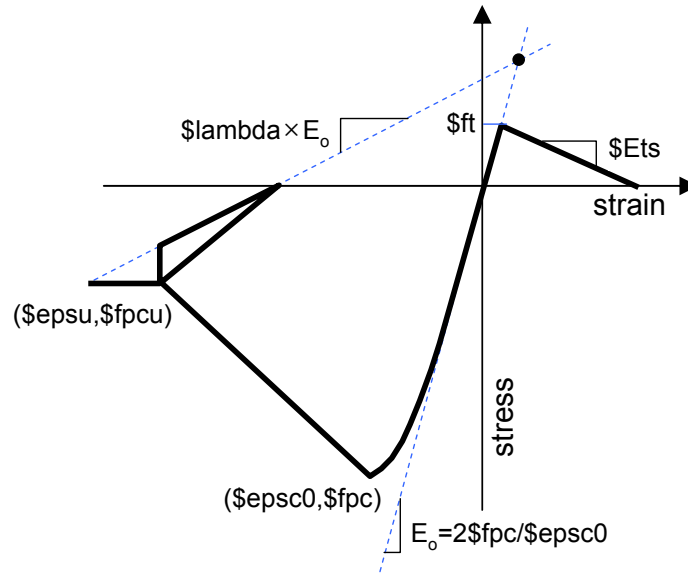


**Figure 6-3: Concrete02 model: material parameters [34]**

For reinforcing bars, the ‘Steel02’ model in OpenSees is used which is a uniaxial Giuffre-Menegotto-Pinto [31] steel material with isotropic strain hardening. For this model, the following parameters need to be defined:

- $F_y$ : yield strength
- $E$ : initial elastic tangent modulus
- $b$ : strain-hardening ratio (ratio between post-yield tangent and initial elastic tangent)
- $R_0, R_1, R_2$ : parameters that control the transition from elastic to plastic branches
- $a_1, a_2, a_3, a_4$ : isotropic hardening parameters

Table 6-2 summarizes the parameters utilized for this steel model in this study. Figure 6-4 presents the stress-strain relationship of ‘Steel02’ material. It should be noted that  $E_p$  is defined by multiplying two parameters,  $E$  and  $b$ . Based on the properties in Table,  $E_p$  for longitudinal and transverse reinforcement are 455.42 ksi (3140 MPa) and 580.15 ksi (4000 MPa), respectively.

**Table 6-2: Steel model parameters for numerical simulations**

Parameter	Units	(a) Longitudinal	(b) Transverse
$\$F_y$	[ksi] (MPa)	77.5 (534.3)	63.0 (435.3)
$\$E$	[ksi] (MPa)	29007.5 (200000)	
$\$b$	N/A	0.0157	0.0200
$\$R0, \$cR1, \$cR2$	N/A	Default	
$\$a1, \$a2, \$a3, \$a4$	N/A	Default (no isotropic hardening)	

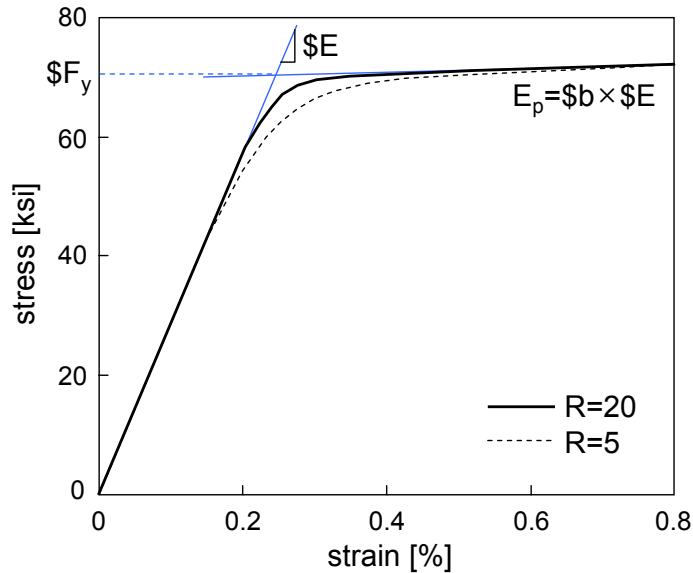


**Figure 6-4: Steel02 model: material parameters [34]**

## 6.2.2 Fiber Section Modeling

Fiber section modeling, which consists of subdividing a cross-section into discretized fibers with a finite area and uniaxial force-deformation relationship of the material associated with the fiber, is capable of representing the flexural behavior and its interaction with the axial force in beam-column elements. Therefore, this type of modeling is widely used in structural analysis applications. In this study, the core which is confined by hoops consists of 80 subdivisions in the circumferential direction and 80 subdivisions in the radial direction, as shown in Figure 6-5. The cover has 80 and 10 subdivisions in the circumferential and radial directions, respectively. The ‘Circular Layer’ command in OpenSees is utilized to construct a circular layer of reinforcing bars. 16 longitudinal bars are uniformly distributed along the circumference for the considered cross-section as shown in the figure.

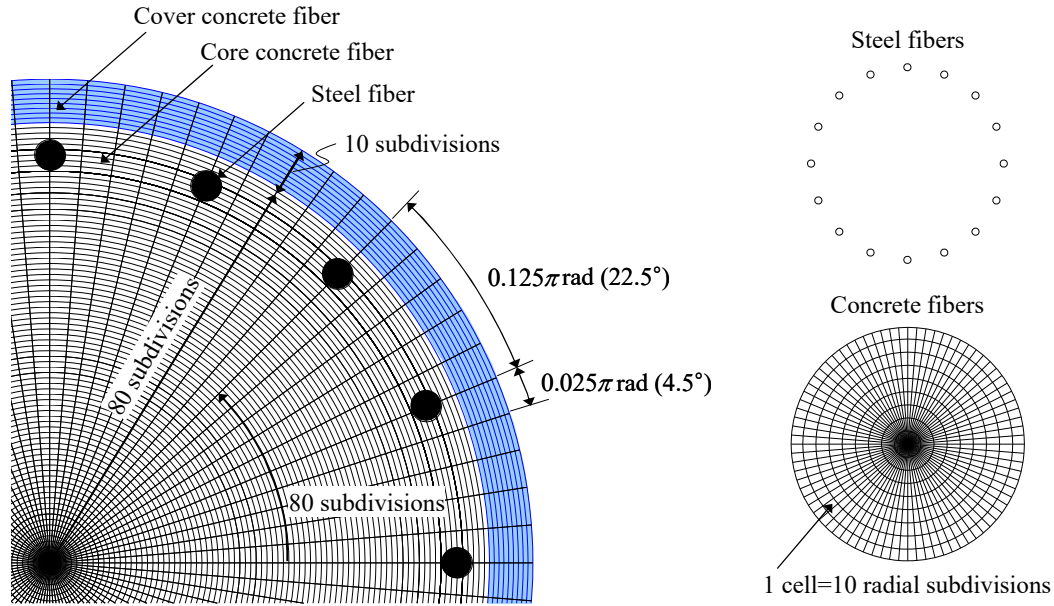
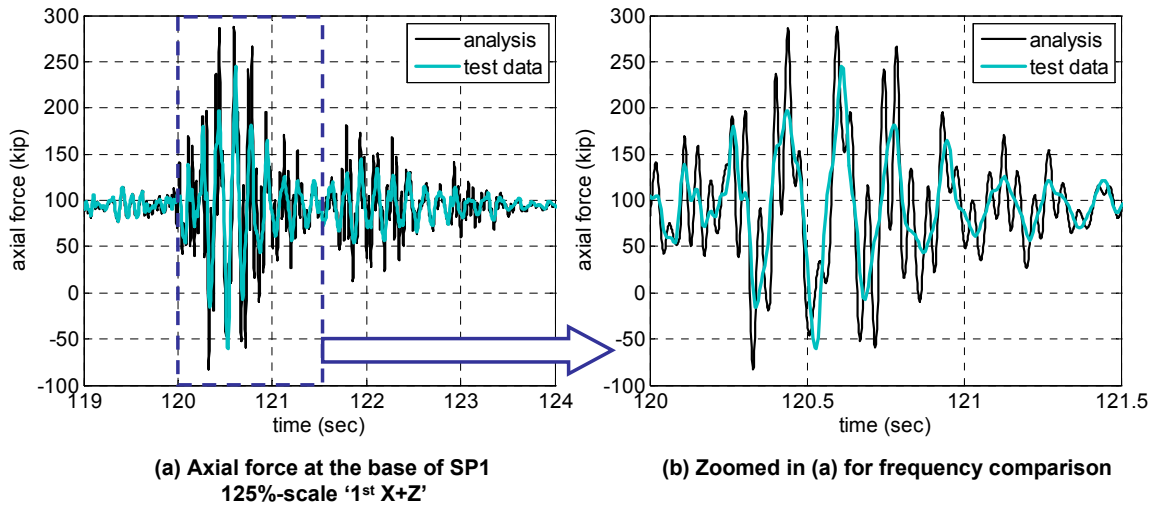


**Figure 6-5: Fiber section modeling**

### 6.3 Model Adjustment due to Shaking Table Effect

As mentioned in Chapter 4, the shaking table is not perfectly rigid. Its flexibility affects the response of the test specimen, especially in the vertical direction. The vertical natural period of the column is much shorter than that of the shaking table and the vertical period of the shaking table is dominant in the whole system (combined test specimen and shaking table as one system). If the shaking table effect is ignored and the vertical acceleration recorded on the shaking table is directly used as the input to the analytical model, acceleration history with higher frequencies is obtained at the top of the column. However, these high frequencies are not present in the test data (Figure 6-6) because of the dominant shaking table period in the vertical direction.

In order to demonstrate the shaking table effect on the vertical response, elastic dynamic analysis is conducted for the 2 DOF system presented in Figure 6-7(b) where  $\mathbf{u}_1$  and  $\mathbf{u}_2$  represent the vertical displacements of the shaking table and the test specimen, respectively, and  $\ddot{\mathbf{u}}_g$  represents the input target acceleration denoted as ‘target’ in Chapter 4. Since the effective mass and stiffness of the shaking table ( $\mathbf{m}_t$  and  $\mathbf{k}_t$ ) are not known accurately, they are varied as input parameters to match the vertical periods identified from the FFT plots of the measured acceleration. Based on the results of the analysis conducted with the selected Northridge ground motion, it is observed from Figure 6-7 that the acceleration histories at the shaking table level and at the top of the column are very similar and this is in agreement with the test data. It can be stated that the flexibility of the shaking table not only results in the modification of the target accelerations but also governs the test specimen response in the vertical Z-direction.



**]Figure 6-6: Axial force difference between numerical simulation and test data measured at the base of model SP1 under the 125%-scale '1st X+Z' motion**

Based on the issues discussed above, and keeping in mind that one of the main goals of the investigation in this study is the evaluation of the effect of axial tension (caused by the vertical acceleration of the ground shaking) on the shear capacity, it was concluded that imposing the measured axial forces directly in the simulation model is a more reasonable approach rather than modeling a complex table response with several sources of uncertainties and assumptions. Therefore, the recorded axial force history (from the load cells installed underneath the test specimen footing and above the shaking table) is directly applied to the column as an external force excitation in the conducted analyses. Accordingly, in order to equate the restoring forces to the external forces, model mass in the vertical direction is set to almost zero.

## 6.4 Other Considerations and Parameters for Numerical Simulations

Average of the accelerations recorded near the four load cells on the base plate underneath the test specimen is used as an input motion in the X and Y directions. The recorded accelerations are low-pass filtered with a cutoff frequency of 40 Hz. In the vertical direction, the recorded axial force time history filtered with a cutoff frequency of 30 Hz is used as external force excitation as discussed above. In order to be able to capture the correct accumulation of nonlinearity, such as the residual displacements, input for the different scale tests are combined into a single long acceleration record.

For the seismic simulation of the tested columns, mass-and-tangential stiffness proportional Rayleigh damping is used with constants calculated based on the 1<sup>st</sup> mode (translation in X) frequency of the numerical model and the vertical (translation in Z) frequency of the specimen. The damping assigned to the model is based on observed data. The conducted tests are classified into three groups (Table 6-3), where each group is assigned a different damping ratio ( $\zeta$ ) based on the measured data.

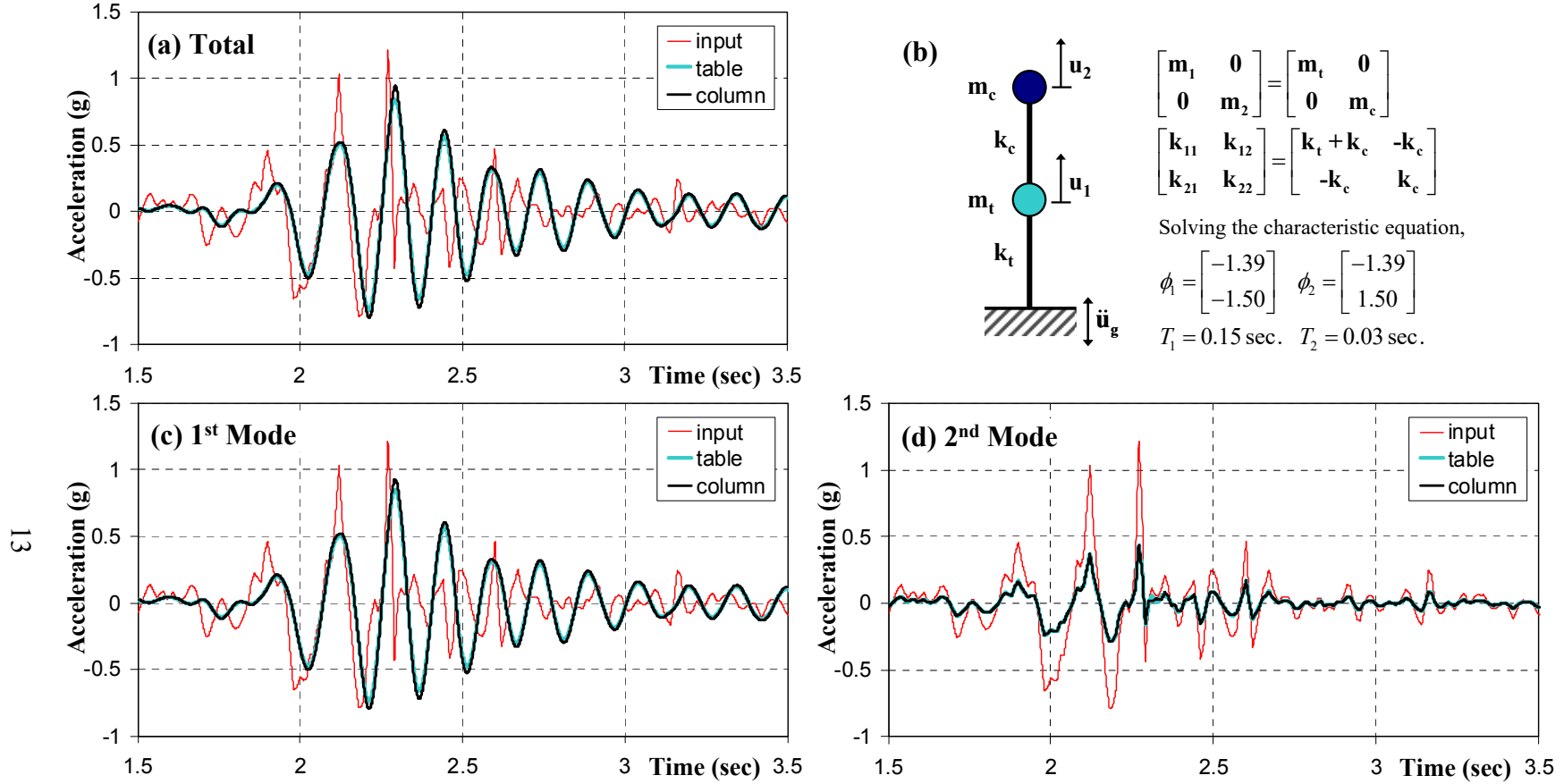


Figure 6-7: 2-DOF analysis for the shaking table and test specimen responses

**Table 6-3: Measured damping ratio**

Test	Damping ratio, $\zeta$ [%]
Free Vibration	2.0
5%-scale or 12.5%-scale	2.5
25%-scale or above	4.0

The damping ratio for the dynamic tests is calculated from the FFT of the horizontal acceleration measured on the top of the mass blocks using the half-power bandwidth method [14]. On the other hand, the damping ratio in the free vibration tests is estimated from the absolute lateral displacement history in the X-direction. Since the calculated damping ratios of SP1 and SP2 are similar, the same damping values are used in analysis of both specimens.

Considering that the test specimen experienced some cracking even before any shaking, a reduced stiffness (65% of  $E_c$ ) obtained from the cylinder tests is used to match the natural periods in the 50%-scale test, which were 0.63 sec for SP1 and 0.65 sec for SP2. The Newmark-beta method with parameters  $\gamma = 0.5$  and  $\beta = 0.25$  is used for time integration. Also, Newton-Raphson method with line search is used as the nonlinear solution algorithm.

## 6.5 Comparison of Numerical and Experimental Results

The responses of the specimens are simulated with sufficient accuracy by the model described above. Figure 6-8 shows the lateral displacement of both specimens from the free vibration tests. It is evident that the fundamental period of the system is adequately represented by the simulation model.

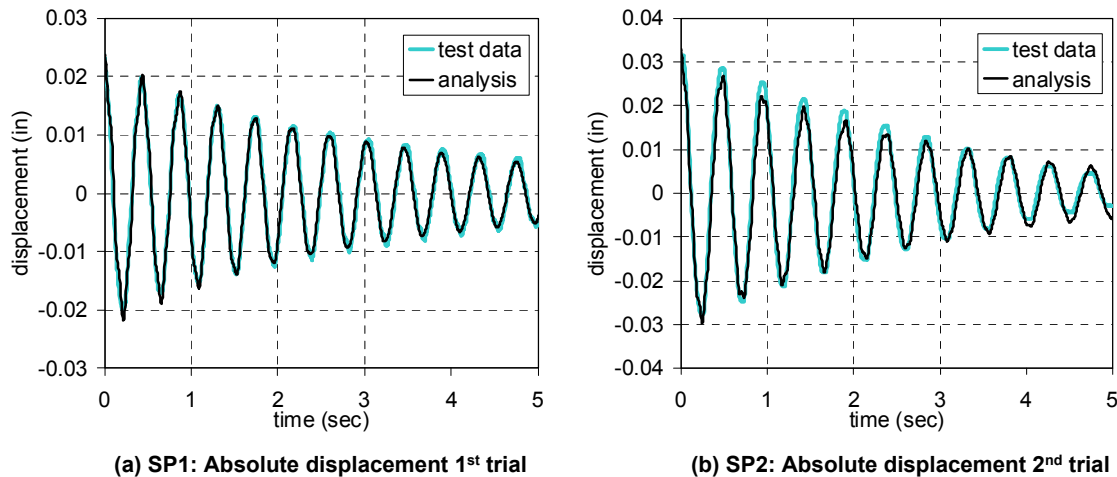


**Figure 6-8: Comparison of the numerical simulation and test results for free-vibration test**

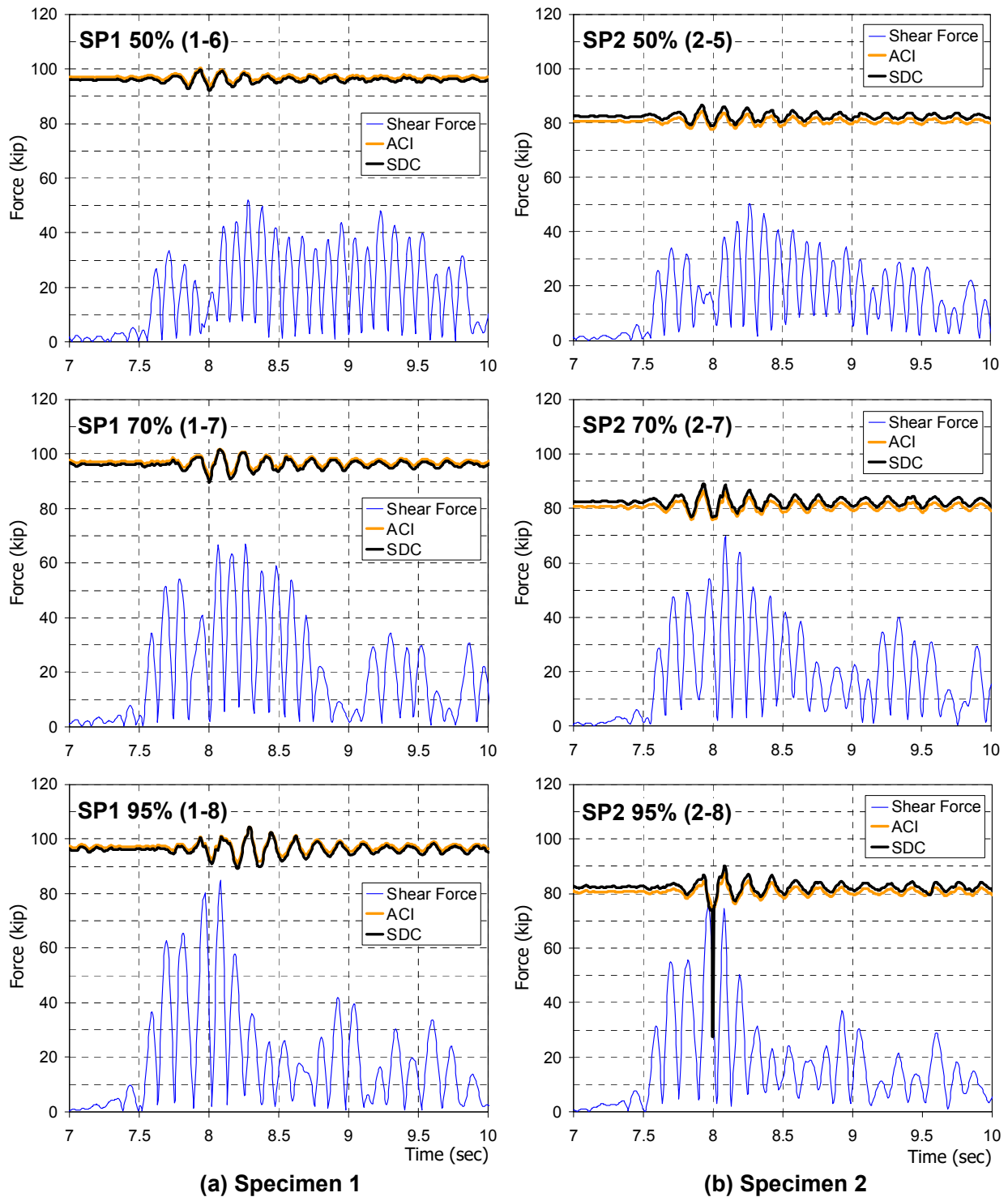
As discussed in Chapter 4, the specimens were not significantly damaged in the tests up to 25%-scale intensity level. In addition, the shear spring affects the response only for high-intensity level motions. Therefore, the behavior of the tested specimen is compared with the numerical simulations only for the tests with scales greater than 50% to examine the effect of vertical component of the ground motion.

### 6.5.1 Shear Force Demands

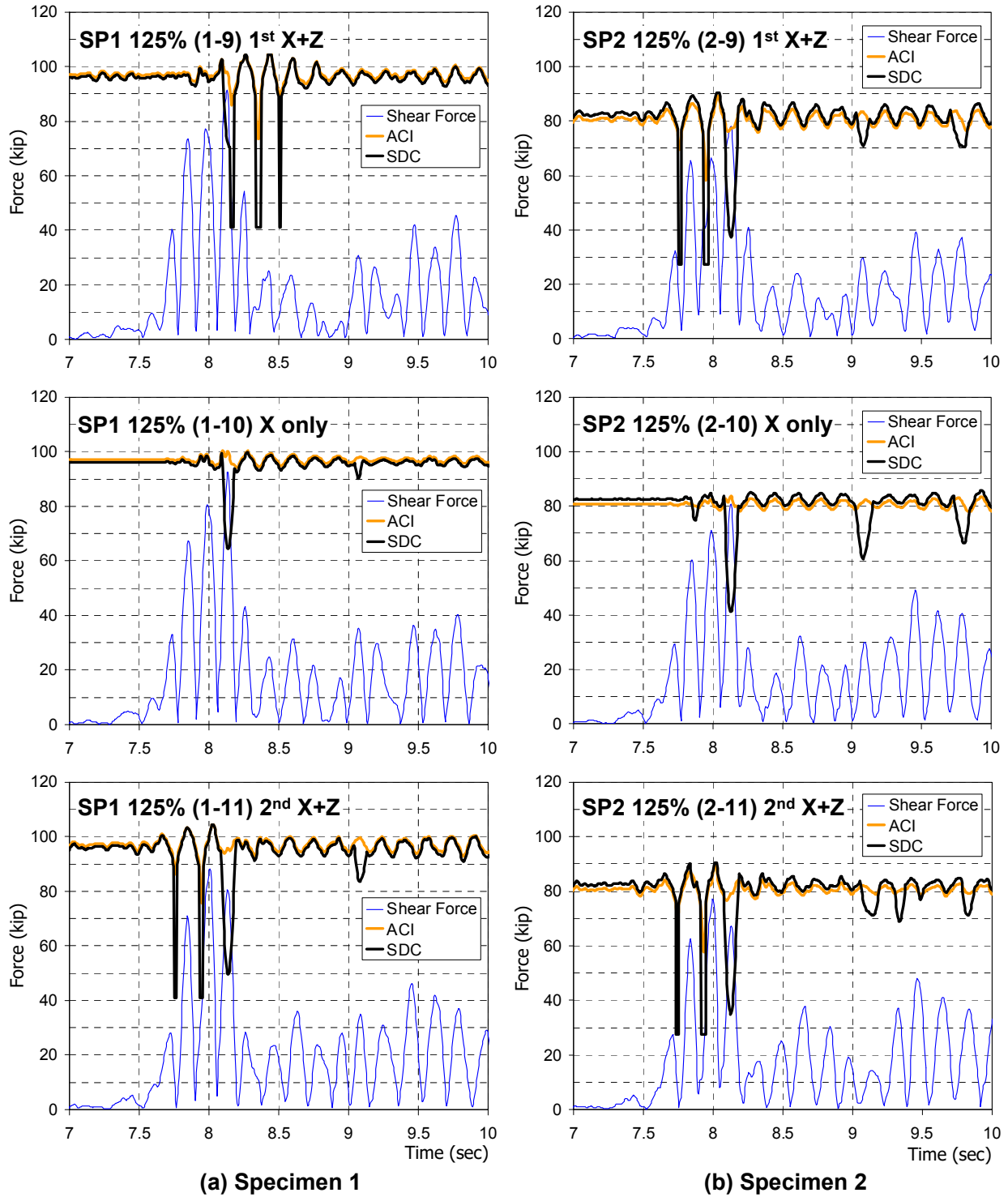
Figure 6-9 and Figure 6-10 compare the shear strength estimation of ACI and SDC equations with the absolute value of the shear force demand histories obtained from the test results. It should be noted that the axial forces and displacements gathered from the test results are used in these shear strength estimations. The two code equations provide similar estimations under compression, but they differ under tension. Up to 70%-scale SDC and ACI produce similar responses. In the 95%-scale run of specimen SP2, the first sudden decrease in shear strength takes place using the SDC estimation due to a small axial tension of 1.4 kips (6.2 kN). SDC and ACI estimations are considerably different under the 125%-scale motions for both specimens as shown in Figure 6-10. Since there is significant axial tension in the 1<sup>st</sup> and 3<sup>rd</sup> runs (Runs 1-9 and 1-11 for SP1 and Runs 2-9 and 2-11 for SP2), the SDC estimate reduces to  $V_s$  (shear strength provided by the hoops) only, i.e. 43.8 kips (194.8 kN) for SP1 and 27.5 kips (122.3 kN) for SP2, which correspond to 57.3% and 66.8% reduction compared to the initial full shear capacity, i.e.  $V_s+V_c$  where  $V_c$  is the shear strength provided by the concrete with no axial tension. Moreover, there are noticeable decreases in SDC estimation due to large ductility demands. As a result, SDC equation provides a more conservative estimation than ACI. Accordingly, the shear demands of SP1 and SP2 exceed the shear capacity estimated by SDC in all the 125%-scale tests, consistent with the observed shear damage described in Chapter 4. However the shear capacity estimates are overly conservative. The SDC shear capacity prediction is sometimes smaller than half of the shear force demand, as in runs 1-11 and 2-11. Noting that the shear forces are obtained from the test data, they should be bounded by the shear capacity values, signifying the underestimation of the shear strength by the SDC equation.

Figure 6-11 compares the shear force response histories of the numerical simulations with the recorded response from the experiments for specimen SP1 subjected to 50%, 70%, and 95%-scale excitations. The numerical simulations include both the ACI- and SDC-based models for estimating the shear capacity of the column. The response prediction using both ACI and SDC are almost identical for the 50%, 70% and 95%-scale tests since the shear springs do not yield at these levels. Figure 6-12 compares the shear force demands for specimen SP1 subjected to the 125%-scale excitations.

The simulation models are successful in matching the maximum shear forces at the peaks designated as 1, 2, and 3 for the first 125%-scale test (Run 1-9). The predicted shear peaks are lower than the experimentally recorded values for the remaining 2 tests (Runs 1-10 and 1-11). This is attributed to the conservative estimates of shear capacity for both the ACI and SDC-based models. Since SDC ignores the concrete contribution if the section is in tension the SDC-based model under-predicts the peak shears by a larger value than ACI.



**Figure 6-9: Comparison of shear force demand and shear strength estimation using ACI and SDC based on the data from 50%, 70%, and 95%-scale runs**



**Figure 6-10: Comparison of shear force demand and shear strength estimation using ACI and SDC based on the data from 125%-scale runs**

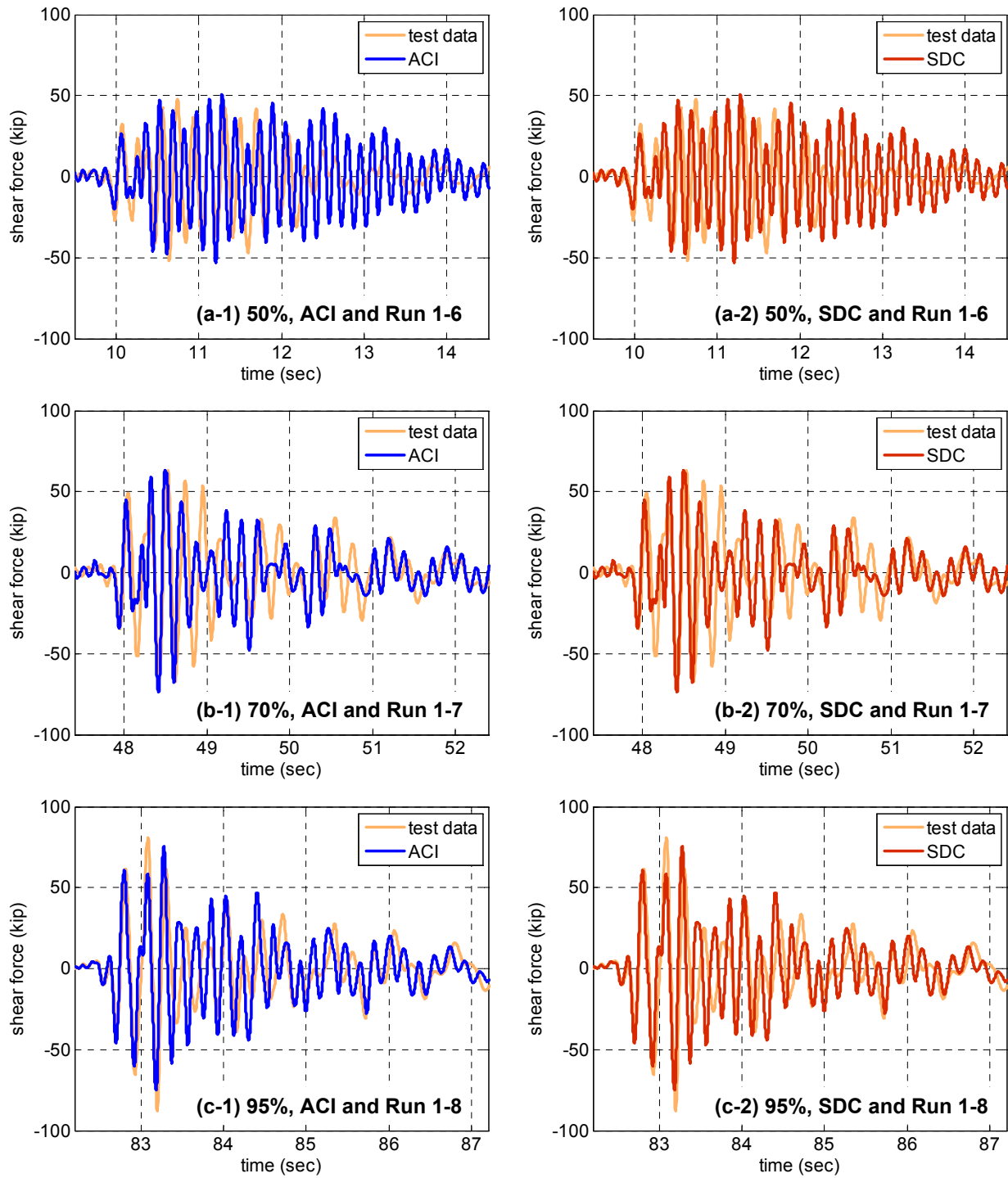


**Figure 6-11: Comparison of simulated versus recorded shear force histories of SP1 subjected to 50%, 70%, and 95%-scale motions**

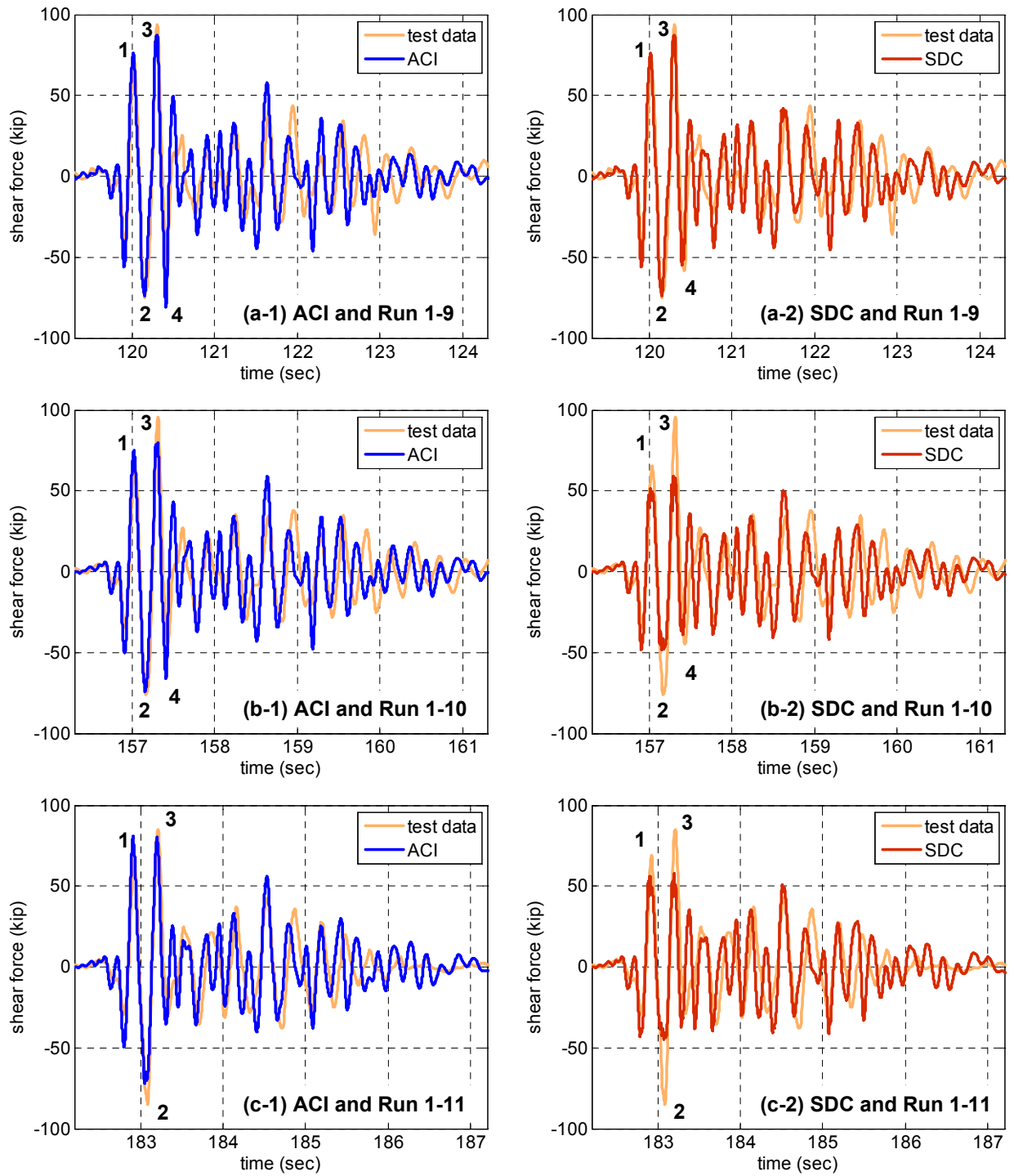


**Figure 6-12: Comparison of simulated versus recorded shear force histories of SP1 subjected to 125%-scale motions**

The simulated shear-force response histories under 50% to 125%-scale motions for specimen SP2 are presented in Figure 6-13 and Figure 6-14 and compared to the observed test data. The overall observations are very similar to those noted for specimen SP1. Just as observed in the response of specimen SP1, the maximum value of the shear is observed at the 3<sup>rd</sup> peak for all of the runs.

The ratio of the shear-force demands obtained from the simulation models to the shear-force obtained from test results at the 3<sup>rd</sup> shear peak, denoted as 'Response ratio' are presented in Figure 6-15 for the 125%-scale runs. In the case of specimen SP1, it is observed that both models predict the demands for the first test case (Run 1-9) with considerable accuracy. For Runs 1-10 and 1-11, the predictions are lower than the observed test results due to the conservative nature of the prediction equations in ACI and SDC. For specimen SP2 the predicted shear capacities of the column by both models for all 3 cases are quite similar (and conservative) since the tensile force in the column was large enough to cause both ACI and SDC to achieve their limit states. In general it can be stated that SDC estimates of the expected demands are more conservative than ACI.

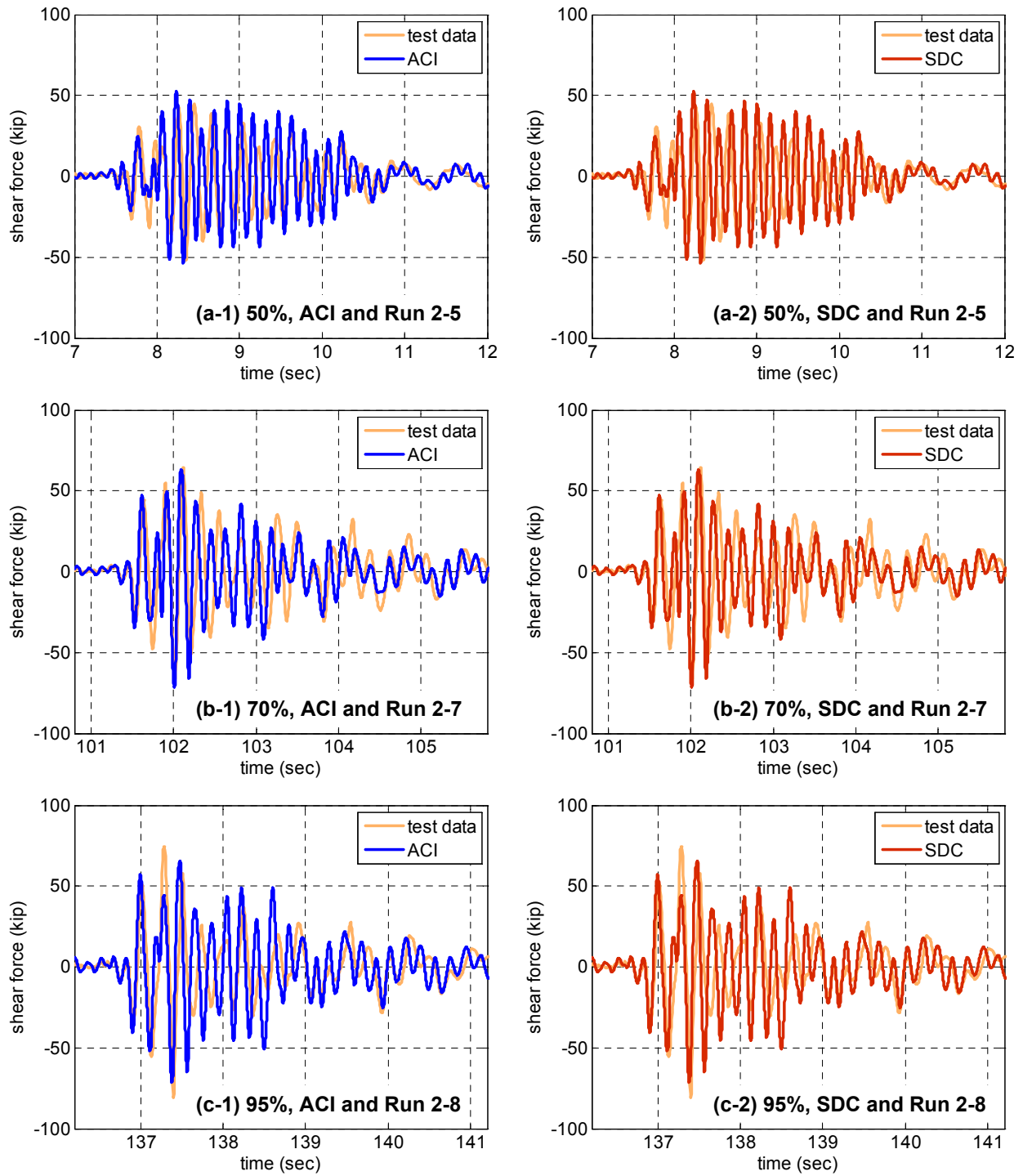


**Figure 6-13: Comparison of recorded versus simulated shear force histories of SP2 subjected to 50%, 70%, and 95%-scale motions**

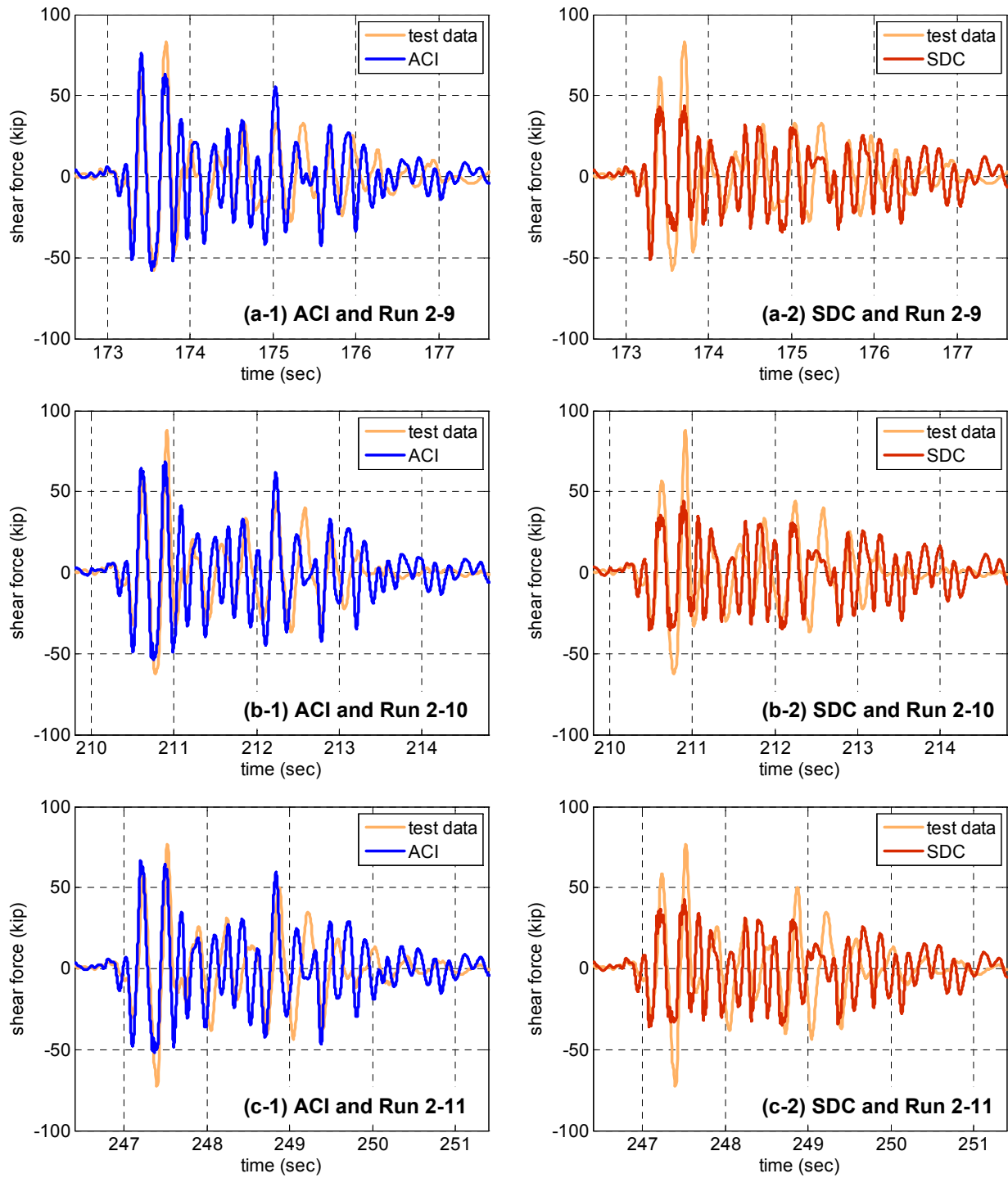


**Figure 6-14: Comparison of recorded versus simulated shear force histories of specimen SP2 subjected to 125%-scale motions**

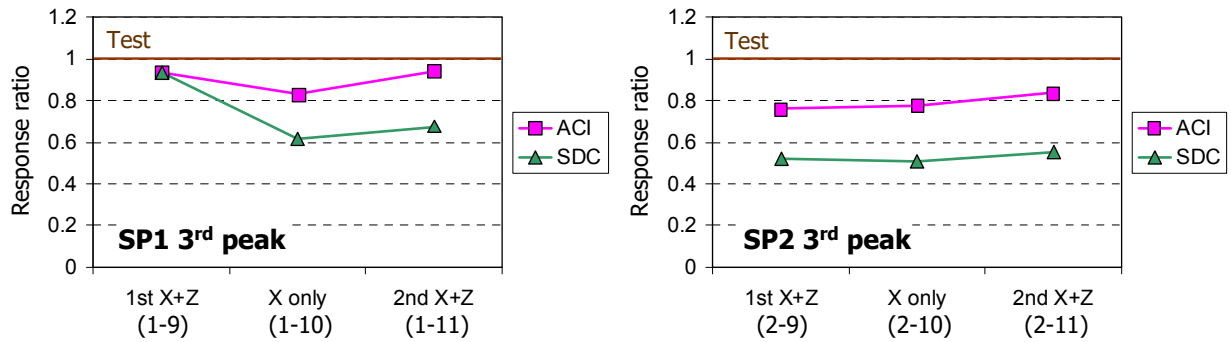
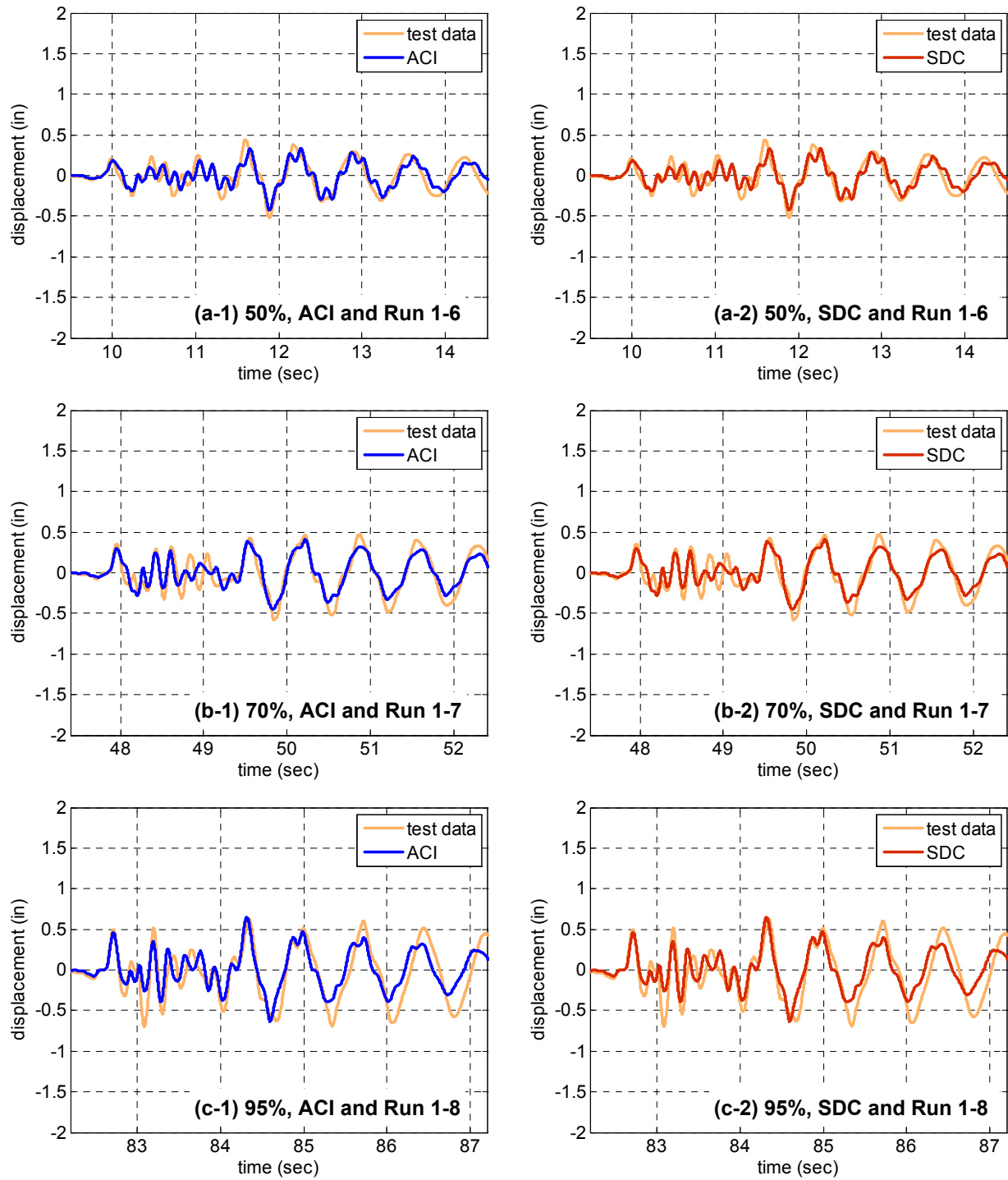


**Figure 6-15: Comparison of the computed to observed shear demands at the 3rd peak for both specimens using ACI and SDC models under the 125%-scale motions**

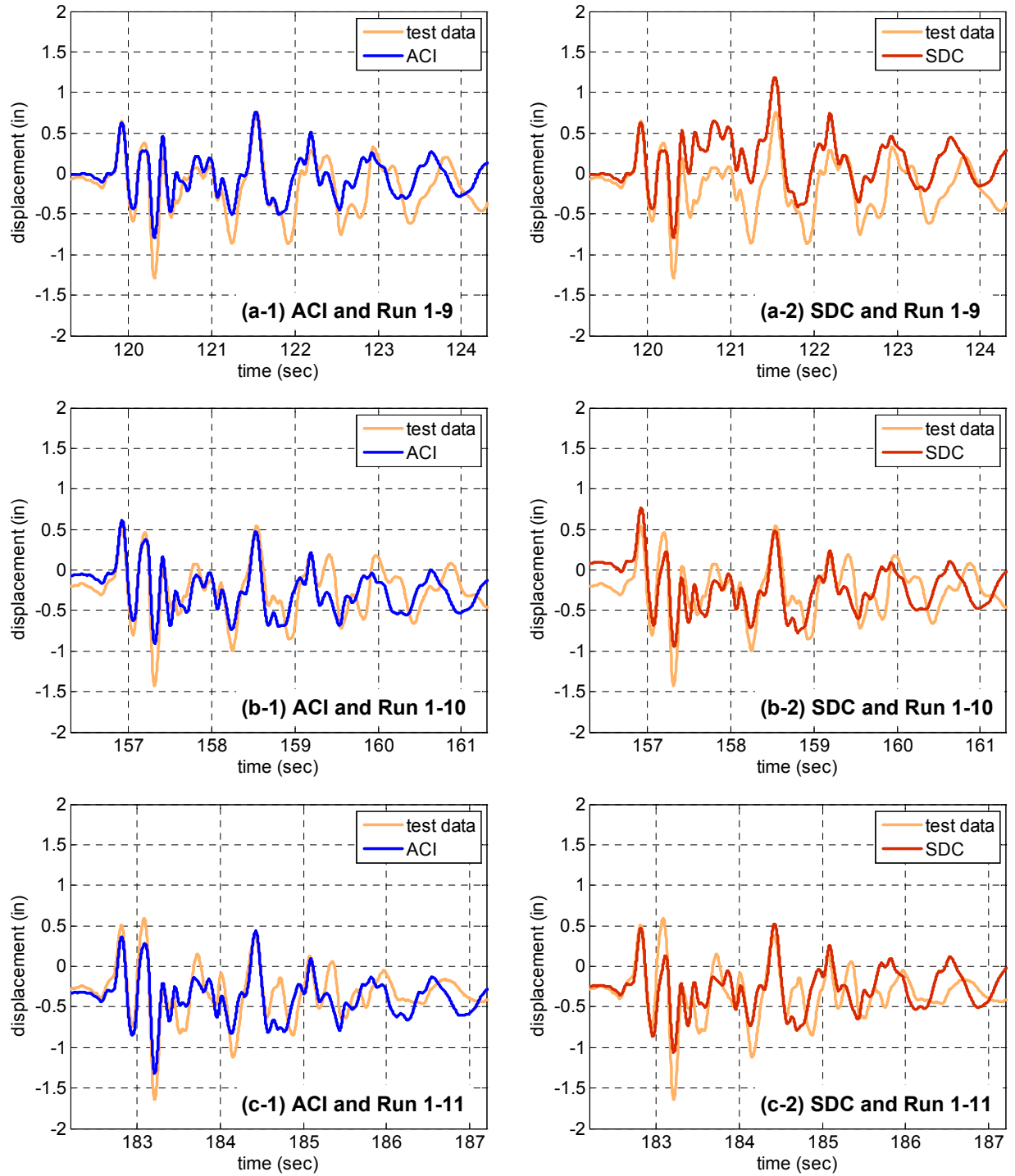
## 6.6 Lateral Displacement Demands

Figure 6-16 presents the lateral displacement histories of SP1 subjected to 50%, 70%, and 95%-scale motions and Figure 6-17 presents the displacement histories for the 125%-scale motions. Despite the slight frequency shift (indicating that the simulation model cannot fully capture the frequency of the mild to moderately damaged specimen) during the second half of motions 1-8 and 1-9 and some difference in the negative peak displacement of motion 1-9, the computed lateral displacement histories provide reasonable estimates of the maximum displacements. The discrepancies between observed and computed responses increase with increasing intensity.

Model predictions for specimen SP2 for motions 2-5 to 2-8 are shown in Figure 6-18 and for motions 2-9 to 2-11 are plotted in Figure 6-19. The observations made for specimen SP1 also apply to specimen SP2 with better predictions by both models for lower intensity motions.



**Figure 6-16: Comparison of computed and observed lateral displacement histories of SP1 subjected to 50%, 70%, and 95%-scale motions**



**Figure 6-17: Comparison of computed and observed lateral displacement histories of SP1 subjected to 125%-scale motions**

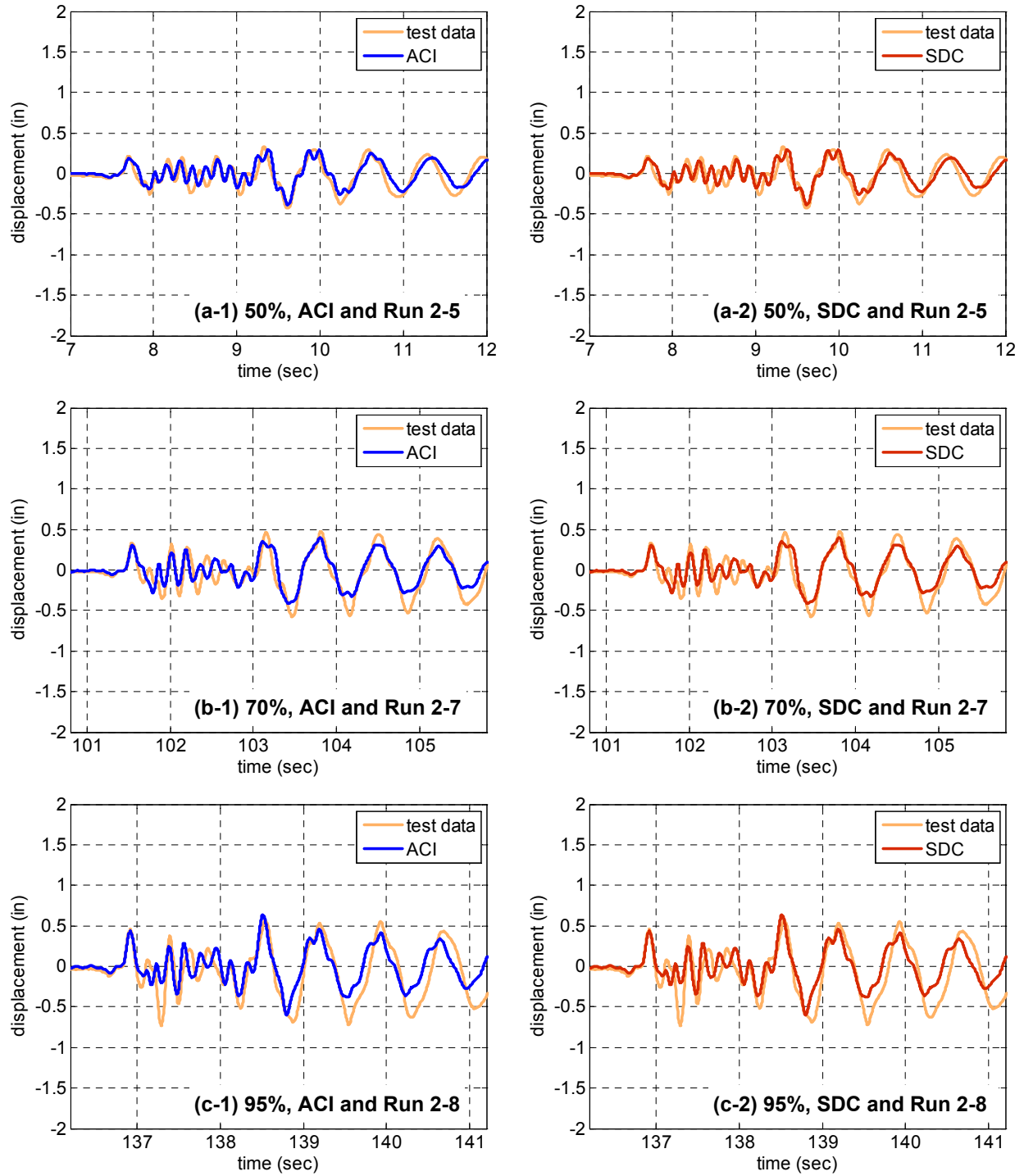


**Figure 6-18: Comparison of computed and observed lateral displacement histories of SP2 subjected to 50%, 70%, and 95%-scale motions**

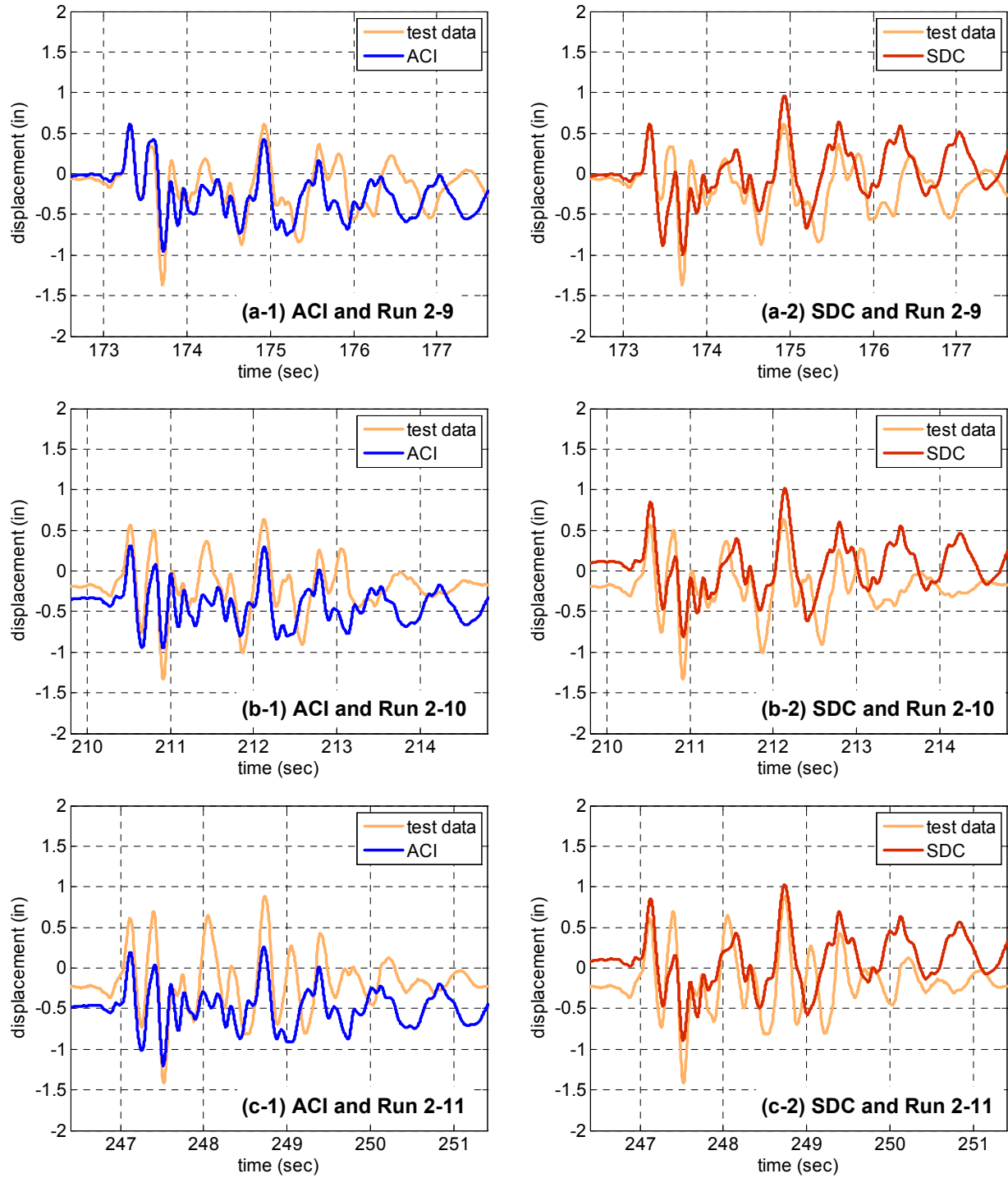


**Figure 6-19: Comparison of computed and observed lateral displacement histories of SP2 subjected to 125%-scale motions**

## 6.7 Summary

Since the existing elements in OpenSees are not suitable to incorporate the code-based shear strength estimation, two shear springs, which adopt the shear strength predictions by ACI and SDC equations, are developed. The force-displacement relationship of the proposed springs is based on a bilinear envelope which is defined by the initial stiffness, the yield force, and the hardening ratio for post-yield stiffness. The yield force is updated at each integration time step using the axial force and displacement ductility at that time step. The shear capacity (or yield force) is kept constant once yielding is initiated. For the input motion in X and Y directions, the acceleration histories recorded on the shaking table tests were used. For the Z direction, the axial force recorded by the load cells is used instead of vertical acceleration, due to considerations of the flexibility of the shaking table. The computational results are compared with those obtained from the tests.

It can be stated that the simulation models are generally successful in capturing the shear-force and lateral displacement history measured during the tests. The predictions of lateral displacements were more accurate for the lower intensity tests. Both shear springs provide results on the conservative side with ACI shear spring predictions being closer to the observed shear demands and the SDC shear spring predictions being much more conservative.

## 7 Concluding Remarks

The effect of vertical excitation on the seismic behavior of reinforced concrete (RC) bridge columns has been the subject of several previous investigations. Field evidence, analytical studies and static or hybrid simulations suggested that excessive axial tension or tensile strain of the column may lead to shear degradation and lead to possible shear failure. However, none of the studies to date has explicitly investigated the effects of vertical motions on shear demand and shear capacity through dynamic testing. Therefore, the objective of this project was to examine the effects of axial force variation in bridge columns due to strong vertical ground motions and the influence of these axial force fluctuations on shear strength degradation.

Two quarter scale specimens (SP1 and SP2) were constructed and tested on the UC-Berkeley shaking table at the Richmond Field Station. The two specimens have different transverse reinforcement ratio. Specimen SP1 satisfies the requirement of Caltrans Bridge Design Specifications. As a result of an extensive numerical investigation and preliminary fidelity tests, the 1994 Northridge earthquake acceleration recorded at the Pacoima Dam was selected as an input motion from among 3,551 earthquake acceleration records in the PEER NGA database. The chosen ground motion was applied to the test specimens at various intensity levels ranging from 5% to 125% of the actual recorded motion. The specimens were subjected to the combination of a vertical component and a single horizontal component in most of the cases. A single horizontal component was also applied in some of the cases to make a direct evaluation of the effect of the vertical excitation.

As part of the computational modeling, a new shear spring model is developed and implemented in the computational platform, OpenSees [34]. The model was developed in order to incorporate shear strength estimations based on ACI and Caltrans SDC equations addressing the effect of column axial load and displacement ductility on shear capacity of a column section.

### 7.1 Summary of Findings

#### 7.1.1 Experimental Findings

- The horizontal component of the acceleration on the mass blocks is significantly lower than that at the top of the column. This is a result of the rigid body rotation of the mass blocks due to the rotation at the top of the column. Reduction of the horizontal acceleration increases the bending moment at the top of the column relative to the bending moment at the base.

- The shaking table flexibility had a pronounced effect on the vertical response. The dynamic mode, which is introduced by the shaking table stiffness (in the vertical direction) governs the response in the vertical direction. Therefore, the response due to the column's axial mode is reduced compared to the case of a rigid shaking table. However, it should be stated that the flexibility of the shaking table did not affect the investigation since the mode introduced by the shaking table flexibility has a significantly larger period compared to the column's vertical period. As a matter of fact, the effect of the shaking table flexibility is analogous to the effect of the bridge girders in elongating the period of the bridge system compared to the period of a single bridge column.
- Strong vertical excitations were found to induce axial tension in the column which did cause marginal degradation of the shear strength (mainly due to the degradation of the concrete contribution to shear strength). The degradation did not adversely affect the performance of the column.
- Flexural damage at the top of the column takes place before the flexural damage at the base since the bending moment at the top is larger. This is a result of the large mass moment of inertia at the top of the column. Reduction of the acceleration on the mass block due to the rotations contributes to this situation as well.
- As a result of flexural yielding both at the top and base of the column (due to bending in double curvature), the induced shear force demand on the column attained the shear capacity which would not have been the case if yielding occurred only at the base. Significant shear cracking was observed as a result of this situation.

### **7.1.2 Findings from Numerical Simulations**

- The developed computational models are successful in capturing the shear force and displacement histories measured during the tests. They capture the rotational mode effect on the bending moment at the column top accurately.
- Due to the difficulty in modeling the shaking table stiffness which varies during a test, as well as between different intensity tests, measured axial force is directly applied to the computational models. This approach was accepted to fit well with the main purposes of this investigation, which are the evaluation of the axial tension on the shear capacity and the development of the corresponding computational modeling approach.
- Both ACI and SDC equations capture the shear strength degradation due to axial force. Both equations provide results on the conservative side with SDC estimates being more conservative due to the fact that concrete contribution to shear is ignored when the column is in tension. The shear strength reduction in the SDC expression due to ductility is much smaller than that due to axial tension.

## **7.2 Shear Demand versus Shear Capacity**

The primary objective of the project was to investigate if bridge columns designed to current Caltrans specifications had the ability to resist shear demands imposed by combined horizontal and vertical motions, particularly when the column is subjected to tension and when the column experiences high ductility demand.

Figure 7.1 summarizes the shear demands imposed on specimen SP1 for the 125% level tests (Runs 1-9 and 1-11) which represent the maximum intensity ground motions imposed on the specimens. Superimposed on these time history plots are the corresponding displacement ductility demands and axial force demands. It is seen that specimen SP1 experienced a peak ductility demand of 4.3 in Run 1-9 and is subjected to tension in the next immediate half-cycle whereas in Run 1-11, though the peak ductility demand is 5.5, the tension in the column occurs at lower ductility demands. Given the fact that axial force fluctuations occur at a high frequency, the column is not subjected to sustained tension. Hence axial-shear interaction effects could not be investigated adequately for the case of sustained tension during the dynamic testing.

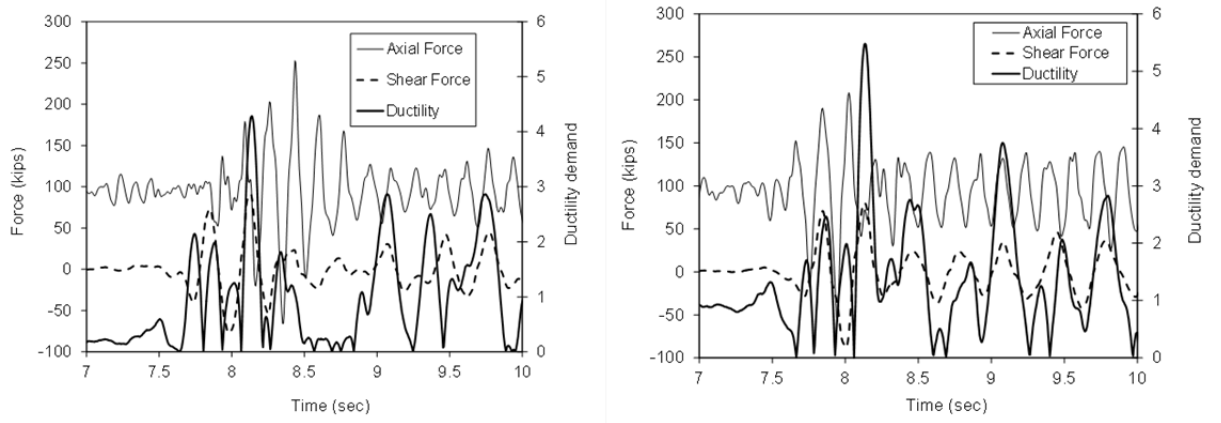
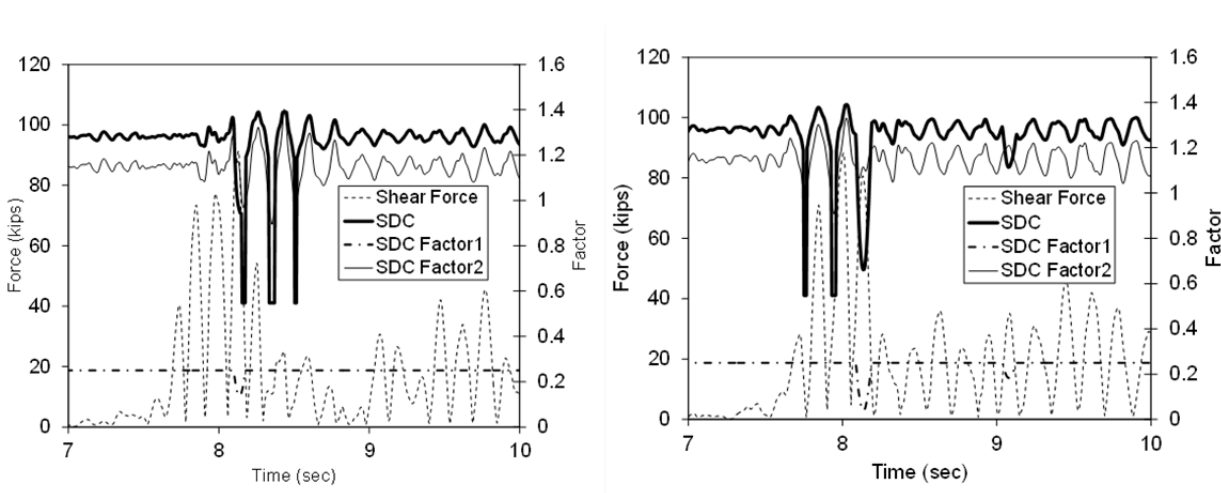


**Figure 7-1: Axial force, shear force and ductility demands on specimen SP1 during the maximum intensity horizontal + vertical motions (Left: Run 1-9; Right: 1-11)**

Figure 7.2 examines the variation of the two control parameters used in the SDC expression to estimate the shear capacity of the section. Recall from Section 1 that the contribution of concrete to shear strength is controlled by two factors:

$$0.3 \leq \text{Factor1} \leq 3$$

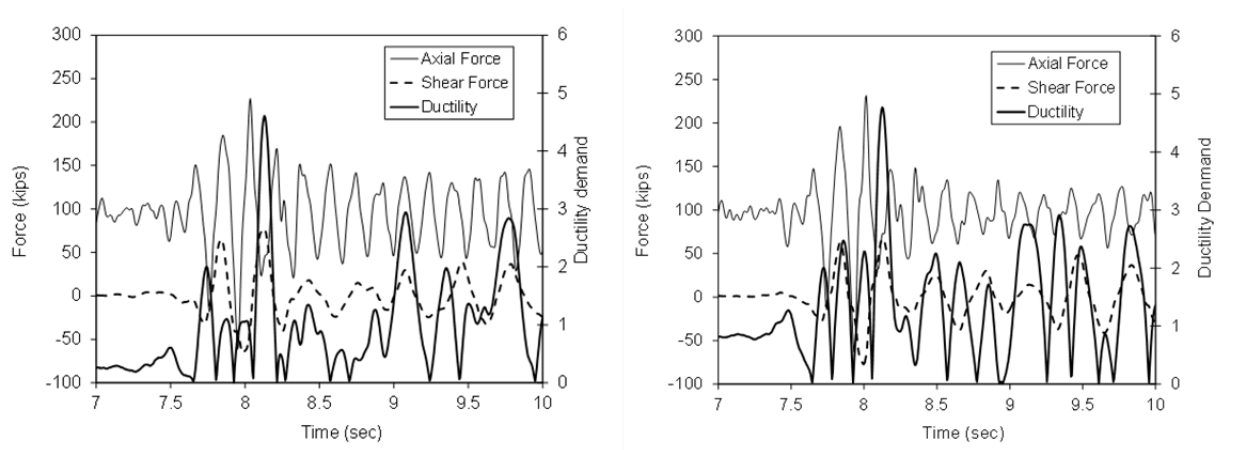
$$\text{Factor2} < 1.5 \text{ (Note however that this reduces to zero in the case of axial tension)}$$



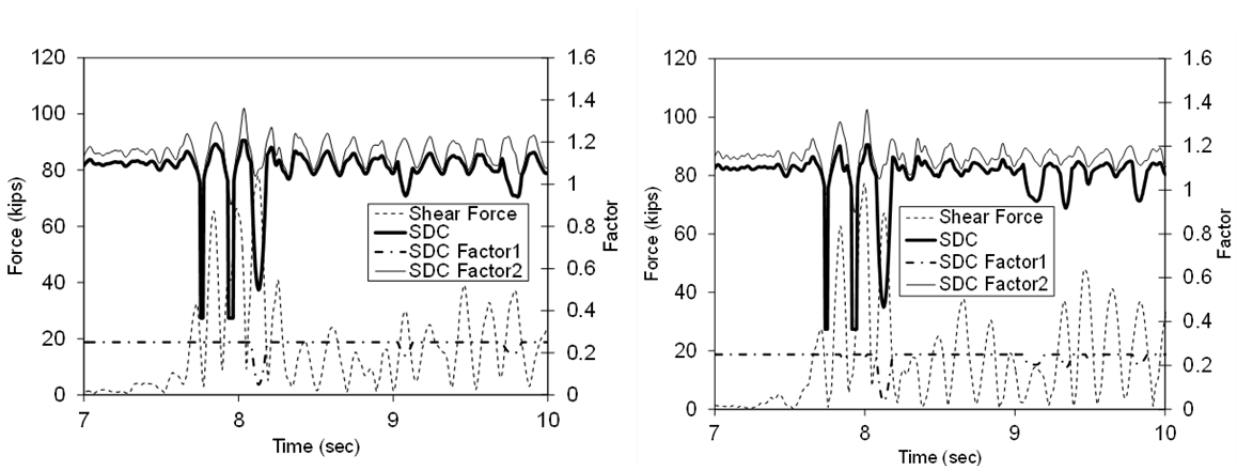
**Figure 7-2: Variation of control parameters in SDC shear capacity expression during the maximum intensity horizontal + vertical motions imposed on specimen SP1 (Left: Run 1-9; Right: 1-11)**

In Figure 7-2, Factor2 is computed independently as specified in SDC and not adjusted when the section goes into tension. Factor1 is a function of ductility demand whereas Factor2 is a function of axial force. When the section is in tension the contribution from concrete should be set to zero which implies that Factor2 = 0. It is evident from Figure 7.2 that Factor1 is essentially a constant except when the ductility demand is high. The intent of SDC is to limit the shear resistance of the section when axial tension occurs simultaneously with high ductility demands. In the case of specimen SP-1, it may be speculated that the column experienced significant ductility demand in Run 1-9 while the section was in tension; however, the state of tension was extremely brief to have any adverse impact on the performance of the column.

Similar plots are presented in Figures 7.3 and 7.4 for specimen SP2. The ductility demands on specimen SP2 are slightly lower than that imposed on specimen SP1. As discussed in Section 4, this specimen experienced higher shear degradation because it had a lower transverse reinforcement ratio. General observations noted for specimen SP1 with regard to axial tension, ductility demand and shear capacity are also valid for SP2.

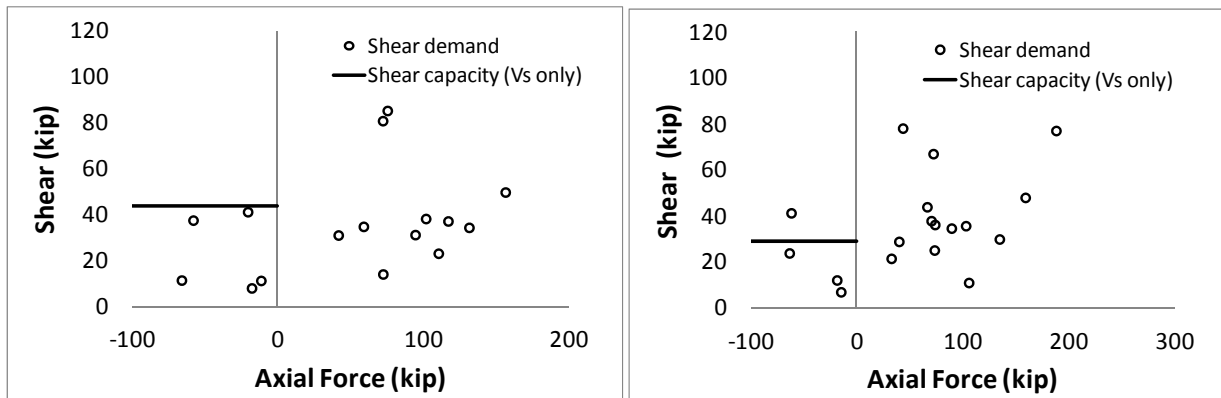


**Figure 7-3: Axial force, shear force and ductility demands on specimen SP2 during the maximum intensity horizontal + vertical motions (Left: Run 2-9; Right: 2-11)**



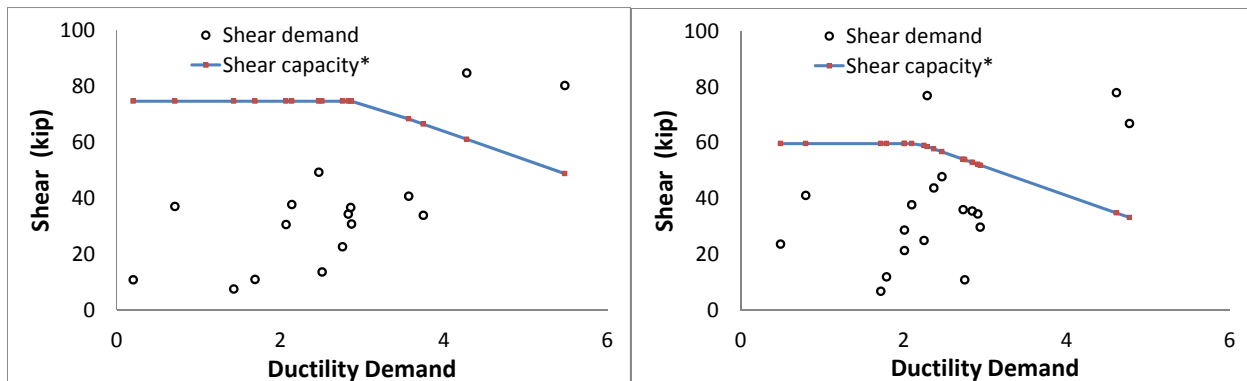
**Figure 7-4: Variation of control parameters in SDC shear capacity expression during the maximum intensity horizontal + vertical motions imposed on specimen SP2 (Left: Run 2-9; Right: 2-11)**

Figure 7.5 summarizes the shear demands experienced by the 2 specimens during ‘critical’ axial force and ductility levels. The plots also show the shear capacity provided by shear reinforcement only for the region controlled by axial tension. It is seen that the shear strength provided by transverse reinforcement (based on the SDC expression) is sufficient to resist the shear demand for specimen SP1 while it is inadequate (in one instant) for specimen SP2. However, specimen SP2 was fabricated with less transverse reinforcement than that required by SDC to investigate the consequences of tension on a column with inadequate shear reinforcement. The fact the column specimen SP2 performed adequately suggests that concrete contribution to shear resistance need not be ignored. It is reiterated that the state of axial tension was sustained for an extremely brief interval (less than 0.05 seconds). The SDC expression, however, is intended for cases of sustained axial tension (likely to occur in two-column bents).



**Figure 7-5: Shear demands in columns at instants of peak axial compression and tension: (a) Specimen SP1; (b) Specimen SP2 (Note: Solid line = contribution of shear reinforcement only)**

Figure 7.6 examines shear demand as a function of ductility demand. The demands are also compared to shear capacity based on the SDC expression with Factor2 set to unity. This assumption implies that there is no axial force in the column and may be considered a “conservative” mean axial force demand value. In both cases, it is observed that the shear demands exceed the available capacity. Since both specimens were able to sustain the imposed gravity loads at all demand levels, it may be concluded that the specimens had sufficient reserve strength and over-strength to safely resist the combined horizontal and vertical motions.



**Figure 7-6: Shear demands in columns as a function of lateral displacement ductility: (a) Specimen SP1; (b) Specimen SP2 (Note: Shear capacity was estimated assuming Factor2=1)**

### 7.3 Shear Demands in Two-Column Bents

A particular case of concern in the study of vertical excitations is the combined effect of overturning and axial force fluctuation in two-column bents. A supplementary numerical study was carried out to investigate this effect. A two-column bent as shown in Figure 7.7 was considered in the evaluation. The column height and superstructure spans are identified in Figure 7.8. The column diameter was 66 inch which resulted in a height-to-depth ratio of 3.5 and a shear span ratio of 1.75 (double curvature) which corresponds to the configuration of the single column that was experimentally investigated in this project. The column is reinforced with 36 # 11 bars and transverse reinforcement consisted of #6 bars at a spacing of 4.5 inch. Material properties are based on 4 ksi concrete (unconfined) and 60 ksi steel. The mass and foundation stiffness of the two-span bridge was adjusted to produce a system period of 1.2 sec in the transverse direction and a vertical period of 0.5 sec.

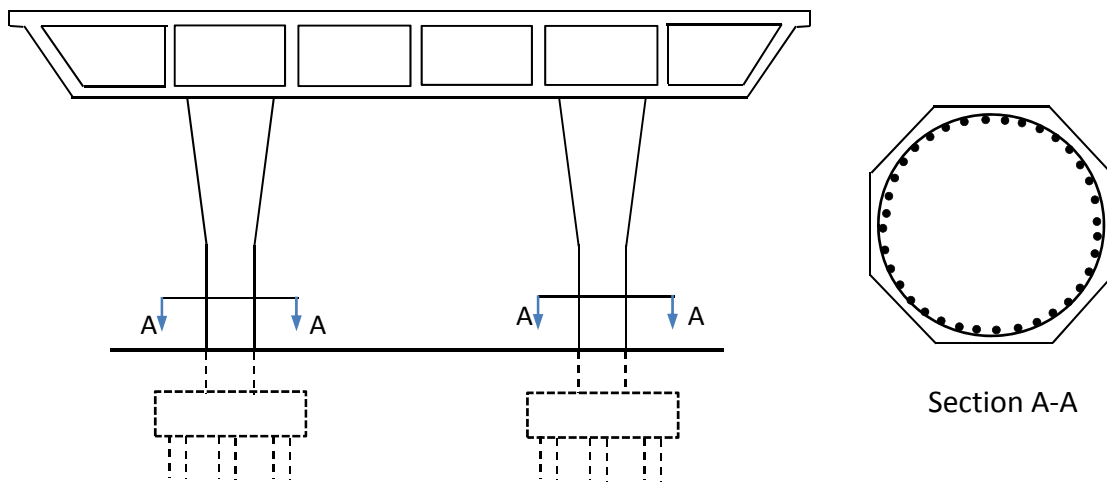


Figure 7-7: Configuration of two-column bent system investigated in the final phase of study

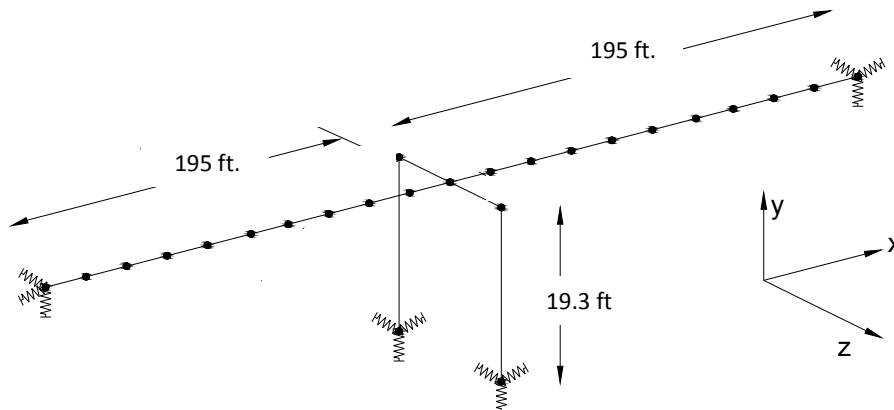
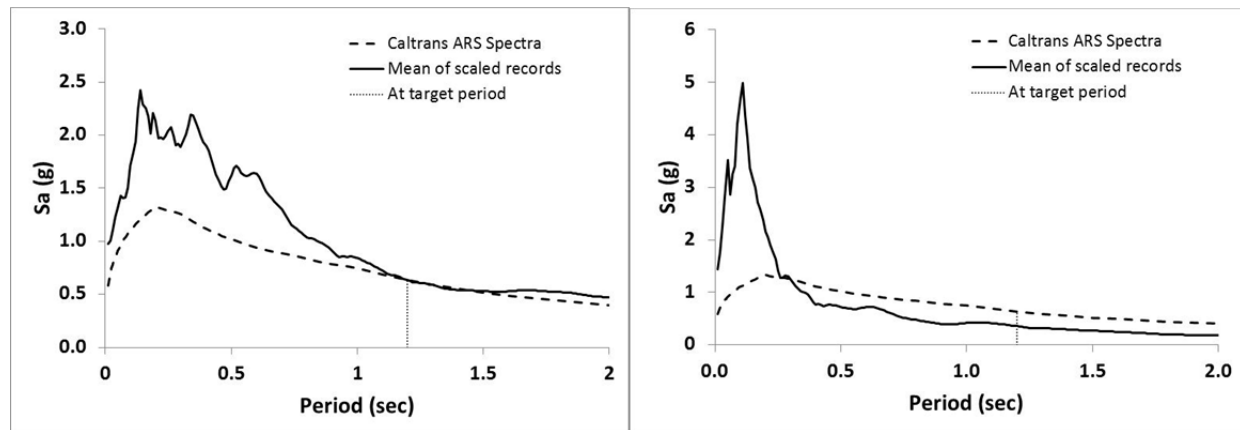


Figure 7-8: Simulation model of two-column bent

Seven ground motions (see Table 7.1) with high vertical-to-horizontal PGA ratios were selected for the study. The ground motions were scaled to match the Caltrans ARS spectra (for a site in San Francisco) at the fundamental transverse period. The same scale factor was applied to both horizontal and vertical motions. The mean spectrum of the seven scaled ground motions is displayed in Figure 7.9 along with the target ARS design spectrum for the site.

**Table 7-1: Selected ground motions for study of two-column bent**

No.	EQ Name	Station	V/H(PGA ratio)
1	Managua, Nicaragua-01	Managua, ESSO	0.89
2	Gazli, USSR	Karakyr	1.76
3	Imperial Valley-06	El Centro Array #6	3.77
4	Westmorland	Westmorland Fire Sta	1.69
5	Loma Prieta	UCSC Lick Observatory	0.82
6	Northridge-01	Canoga Park - Topanga Can	1.16
7	Northridge-01	Jensen Filter Plant Generator	0.81



**Figure 7-9: Mean spectrum of scaled ground motions**

Nonlinear time history analyses of the simulation model shown in Figure 7.8 were carried out using OpenSees and the shear demands in the columns were monitored at critical instants in the response. Figure 7.10 summarizes the shear demands in the columns at the instant of peak axial compression and tension as well as the instant of the highest ductility demand experienced by the column. It can be observed from the left plot of Figure 7.10 that the failure mode of the column is flexure as required by Caltrans SDC. Results indicate that neither axial force variations nor the imposed ductility demands are cause of concern in order to induce shear damage for this particular bent.

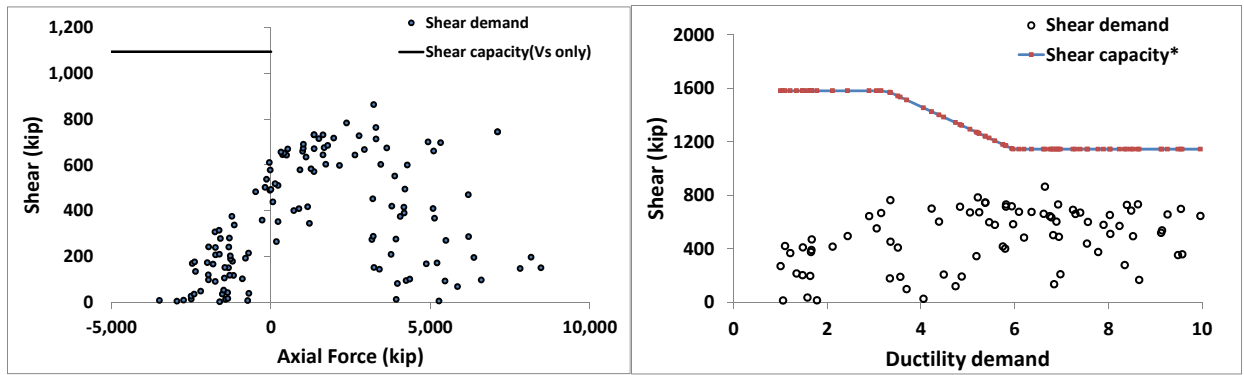


Figure 7-10: Shear demand versus capacity as a function of peak axial force and ductility demand

## 7.4 Final Comments and Recommendations

The experimental and computational investigation conducted in this study revealed that axial tension can be induced in bridge columns due to vertical ground motions. However, the frequency of axial force variations in bridges with single column bents (similar to the column investigated in this study) is extremely high and consequently the state of axial tension in the column is extremely brief. Though shear cracking was evident in the specimens subjected to severe horizontal and vertical motions, both specimens performed adequately and sustained the imposed gravity loads without severe damage.

1. Single column bents may be subjected to axial tension as a result of vertical excitation only. Since the vertical frequency of bridge columns is much higher than the transverse or longitudinal frequency, the imposed axial tension is sustained for very short durations. The effect of such transient axial tension on the shear capacity of bridge columns is not expected to be significant.
2. The present study of a single column bent suggests that ignoring the concrete contribution to shear capacity when the column is in tension is conservative. Given the fact that the shear capacity expression in SDC is specified to deal with cases of sustained axial tension, attention should be paid to the use of SDC expression in cases where axial tension occurs only due to vertical excitation.
3. The case of axial tension resulting from vertical vibrations of the superstructure due to vertical excitations was not specifically investigated. Single column bents that support long spans may experience out-of-plane superstructure vibrations that can put the column into sustained tension – which is different from the case investigated in this study. However, an earlier study (Kunnath et al. 2008) concluded that vertical excitations are critical only if the vertical period of the system is close to the predominant period of the vertical excitations. Since the predominant period of vertical excitations is much lower than that of the horizontal excitations, sustained tension in the column is unlikely. It may therefore be concluded that vertical excitations are not critical for single column bents from the perspective of shear demand and shear capacity.

4. Double-column bents with transverse periods that are significantly longer than the vertical period is likely to subject the column to sustained tension. Preliminary numerical studies of a typical two-column bent presented in Section 7.3 indicate that shear demands at critical points (at the instant of the peak ductility demand or the instant of maximum axial compression and tension) during the response, the available shear capacity is generally larger than the imposed demand. Even in cases when the column is in tension, the shear capacity of the transverse reinforcement is adequate to resist the shear demands in the column. However, experimental and additional numerical studies on two-column bents experiencing sustained axial tension is needed to resolve the issue of vertical excitation combined with over-turning effects.
5. Hybrid simulation where the column is tested experimentally and the rest of the bridge system is computationally modeled is a viable option for the evaluation of the column axial tension for a full bridge system. This approach has three advantages. First, the elongated vertical period due to presence of the bridge superstructure can be considered. Second, the elimination of a possible shaking table effect on the vertical response can be achieved. Third, the superstructure and supports can be modeled more accurately. The hybrid simulation test can be conducted by using three actuators, where one horizontal actuator is for the lateral degree of freedom and two vertical actuators are for the lateral and rotational degrees of freedom at the top of the column.

In conclusion it must be emphasized that the current experimental study investigated only a single near-fault ground motion in which significant vertical excitation was capable of inducing tension in the bridge column model. The permissible shear stress in the current SDC depends on concrete strength, transverse reinforcement ratio, axial force and ductility demand. Of the four main parameters, the issue of axial tension remains the most complex given the different frequencies at which horizontal and vertical motions impose the maximum demands. A dedicated experimental program that includes varying axial tension is needed to gain a more comprehensive understanding of axial tension on the shear demand and shear capacity of bridge columns, particularly for two-column bents which experience combined axial tension due to strong vertical motions and overturning effects from horizontal motions.

# References

- [1] AASHTO (2005), “LRFD Bridge Design Specifications, 3<sup>rd</sup> Edition, 2005 Interim Revisions,” American Association of State and Highway Transportation Officials, Washington, DC.
- [2] AASHTO (2010), “LRFD Bridge Design Specifications, 5<sup>th</sup> Edition, 2010 Interim Revisions,” American Association of State and Highway Transportation Officials, Washington, DC.
- [3] ACI Committee 318 (2005), Building Code Requirements for Structural Concrete and Commentary, ACI 318-05, American Concrete Institute, Farmington Hills, MI.
- [4] ACI Committee 318 (2008), Building Code Requirements for Structural Concrete and Commentary, ACI 318-08, American Concrete Institute, Farmington Hills, MI.
- [5] Alves, S. W. (2005), “Nonlinear Analysis of Pacoima Dam with Spatially Nonuniform Ground Motion,” Doctoral Thesis at California Institute of Technology, Pasadena, California.
- [6] Amirbekian, R. V. and Bolt, B. A. (1998), “Spectral Comparison of Vertical and Horizontal Seismic Strong Ground Motions in Alluvial Basins,” *Earthquake Spectra*, 14, pp. 573-595.
- [7] ASTM Standard C172/C172M (2010), "Standard Practice for Sampling Freshly Mixed Concrete," ASTM International, West Conshohocken, PA, 2003
- [8] ASTM Standard C31/C31M (2010), “Standard Practice for Making and Curing Concrete Test Specimens in the Field,” ASTM International, West Conshohocken, PA, 2003
- [9] ASTM Standard E8/E8M (2009), “Standard Test Methods for Tension Testing of Metallic Materials”, ASTM International, West Conshohocken, PA, 2003
- [10] Bentz, E. C., Vecchio, F. J., and Collins, M. P. (2006), “Simplified Modified Compression Field Theory for Calculating Shear Strength of Reinforced Concrete Elements,” *ACI Structural Journal*, 103, No. 4, pp. 614-624.
- [11] Bozorgnia, Y. and Campbell K. W. (2004), “The Vertical-to-Horizontal Response Spectral Ratio and Tentative Procedures for Developing Simplified V/H and Vertical Design Spectra,” *Journal of Earthquake Engineering*, Vol. 8, No. 2, pp. 175-207.
- [12] California Department of Transportation (Caltrans) (2010), “California Amendments to the AASHTO LRFD Bridge Design Specifications (Fourth Edition),” Sacramento, CA.
- [13] California Department of Transportation (Caltrans) (2010), “Seismic Design Criteria,” SDC-2010, Sacramento, CA.
- [14] Chopra, A. K. (2006), Dynamics of Structures, Theory and Applications to Earthquake Engineering, Pearson Prentice Hall, 3rd Edition, Upper Saddle River, NJ.
- [15] Collier, C. J. and Elnashai, A. S. (2001), “A Procedure for Combining Vertical and Horizontal Seismic Action Effects,” *Journal of Earthquake Engineering*, Vol. 5, No. 4, pp. 521-539.
- [16] CSA Committee A23.3. (2004), Design of Concrete Structures (CSA-A23.3-04), Canadian Standards Association, Rexdale, ON.

- [17] Elgamal, A. and He, L. (2004), "Vertical Earthquake Ground Motion Records: An Overview," *Journal of Earthquake Engineering*, Vol. 8, No. 5, pp. 663-697.
- [18] Elnashai, A. S. (1997), "Seismic Design with Vertical Earthquake Motion," Seismic Design for the Next Generation of Codes, eds. Fajfar, P. and Krawinkler, H. (Balkema, Rotterdam), pp. 91-100.
- [19] Elnashai, A. S. and Papazoglou, A. J. (1997), "Procedure and Spectra for Analysis of RC Structures Subjected to Strong Vertical Earthquake Loads," *Journal of Earthquake Engineering*, Vol. 1, No. 1, pp. 121-155.
- [20] Elwood, K. and Moehle, J. (2003), "Shake table tests and analytical studies on the gravity load collapse of reinforced concrete frames," PEER Report 2003/01, Pacific Earthquake Engineering Research Center, University of California, Berkeley, CA.
- [21] Eurocode 2. (2004), "Design of Concrete Structures," Part 1, CEN, European Standard ENV 1992-1-1, Brussels.
- [22] FEMA-356 (2000). Prestandard and Commentary for the Seismic Rehabilitation of Buildings. Report FEMA-356. Washington (DC): Federal Emergency Management Agency.
- [23] Fenves, G. L. and Mojtahedi, S. (1995), "Effect of Contraction Joint Opening on Pacoima Dam in the 1994 Northridge Earthquake," SMIP95 Seminar on Seismological and Engineering Implications of Recent Strong-Motion Data, p. 57 - 68.
- [24] Jeong, H., Mahin, S. A., Sasaki, T., and Kawashima, K. (2008), "Progress Report: Large-scale Tests of a US Bridge Column Using the E-Defense Shaking," April 2008.
- [25] Kawase, H. and Aki, K. (1990), "Topography Effect at the Critical SV-wave Incidence: Possible Explanation of Damage Pattern by the Whittier Narrows, California, Earthquake of 1 October 1987," *Bulletin of the Seismological Society of America*, 80, pp.1-30.
- [26] Kawashima, K., Ukon, H., and Kajiwara, K. (2007), "Bridge Seismic Response Experiment Program using E-Defense," *Proceedings of 39<sup>th</sup> UJNR Panel on Wind and Seismic Effect*, Technical Memorandum, Public Works Research Institute, Tsukuba Science City, Japan, No. 4075, pp. 57-66.
- [27] Kim, S. J. and Elnashai, A. S. (2008), "Seismic Assessment of RC Structures Considering Vertical Ground Motion," MAE Center report, No. 08-03.
- [28] Kunnath, S. K., Abrahamson, N., Chai, Y. H., Erduran, E., and Yilmaz, Z. (2008), "Development of Guidelines for Incorporation of Vertical Ground Motion Effects in Seismic Design of Highway Bridges," A Technical Report Submitted to the California Department of Transportation, University of California, Davis.
- [29] Mander, J. B., Priestley, M. J. N., and Park, R., "Theoretical Stress-Strain Model for Confined Concrete," *Journal of the Structural Division*, ASCE, Vol. 114, pp. 1804-1826
- [30] Massone, L. M., Orakcal, K., and Wallace, J.W. (2006), "Shear-Flexure Interaction for Structural Walls," *ACI Special Publication*, 236, pp. 127-150.
- [31] Menegotto, M., and Pinto, P. (1973). "Method of Analysis for Cyclically Loaded Reinforced Concrete Plane Frames Including Changes in Geometry and Non-elastic Behavior of Elements Under Combined Normal Force and Bending." *Proceedings. IABSE Symposium on Resistance and Ultimate Deformability of Structures Acted on by Well-Defined Repeated Loads*, Final Report, Lisbon.

- [32] Newmark, N. M. and Hall, W. J. (1982), "Earthquake Spectra and Design." Earthquake Engineering Research Institute, Berkeley, CA.
- [33] Newmark, N. M., Blume, J. A., and Kapur, K. K. (1973), "Seismic Design Spectra for Nuclear Power Plants," *Journal of Power Division*, ASCE, Vol. 99, pp. 287-303.
- [34] OpenSees (2009), <http://opensees.berkeley.edu/>
- [35] Papazoglou, A. J. and Elnashai, A. S. (1996), "Analytical and Field Evidence of the Damaging Effect of Vertical Earthquake Ground Motion," *Earthquake Engineering and Structural Dynamics*, Vol. 25, pp. 1109-1137.
- [36] Paulay, T. and Priestley, M. J. N. (1992), *Seismic Design of Reinforced Concrete and Masonry Buildings*, John Wiley and Sons, New York.
- [37] PEER-NGA Database (2011), <http://peer.berkeley.edu/nga/>
- [38] Priestley, M. J. N., Verma, R., and Xiao, Y. (1994), "Seismic Shear Strength of Reinforced Concrete Columns," *Journal of Structural Engineering*, ASCE, Vol. 120(8), pp. 2310-2329.
- [39] Priestley, M. J. N., Benzoti, G., Ohtaki, T., and Seible, F. (1996), "Seismic Performance of Circular Reinforced Concrete Columns under Varying Axial Load," Report-SSRP-96/04, Division of Structural Engineering, University of California.
- [40] Sakai, J. and Unjoh, S. (2007), "Shake Table Experiment on Circular Reinforced Concrete Bridge Column under Multidirectional Seismic Excitation," *Proceedings of the Research Frontiers*, SEI, May.
- [41] SAP2000 Manuals (2006). Computers and Engineering, Inc., Version 11, Berkeley, CA.
- [42] Scott, M.H. and Fenves, G.L. (2006), "Plastic Hinge Integration Methods for Force of Structural Engineering," ASCE, 132(2):244-252.
- [43] Silva, W. (1997), "Characteristics of Vertical Strong Ground Motions for Applications to Engineering Design," *FHWA/NCEER Workshop on the National Representation of Seismic Ground Motion for New and Existing Highway Facilities, Burlingame, CA*, Proceedings, Technical Report NCEER-97-0010, National Center for Earthquake Engineering Research, Buffalo, New York.
- [44] Talaat, M. M. and Mosalam, K. M. (2008), "Computational Modeling of Progressive Collapse in Reinforced Concrete Frame Structures," PEER Report 2007/10, Pacific Earthquake Engineering Research Center, University of California, Berkeley, CA.
- [45] Vecchio, F. J. and Collins, M. P. (1986), "The Modified Compression-Field Theory for Reinforced Concrete Elements Subjected to Shear," *ACI Journal*, 83, No. 2, pp. 219-231.
- [46] Walraven, J. C. (1981), "Fundamental Analysis of Aggregate Interlock," *Proceedings*, ASCE, V. 107, ST11, pp.2245-2270.